Permanent Magnet Servo Motors Design for Dynamic Loss Minimization and Self-Sensing Control

by

Huthaifa M. Flieh

A dissertation submitted in partial fulfillment of
the requirements for the degree of

Doctor of Philosophy
(Mechanical Engineering)

at the

University of Wisconsin-Madison

2019

Date of Final Oral Examination: 03/07/2019

The report is approved by the following members of the Final Oral Exam Committee:

Robert D. Lorenz, Professor Emeritus, Mechanical Engineering
Michael Zinn, Associate Professor, Mechanical Engineering
Eric Severson, Assistant Professor, Electrical and Computer Engineering
Daniel C. Ludois, Assistant Professor, Electrical and Computer Engineering
James Sember, Exexutive Director, Electrical and Computer Engineering

Abstract

Servo motors are widely used in industrial automation and robots. These motors allow precise position, speed and acceleration control, however,they require a special design to achieve the desired performance with low cogging and ripple torque. Typical servo motors are designed to provide the desired performance, without considering the dynamic loss behavior or self-sensing properties.

In this thesis, a methodology to design FI-SPMSM for servo applications with enhanced dynamic loss minimization and self-sensing performance is proposed. This helps in reducing the capital and operational cost of the servo drive system when it runs at high speed partial torque cycles. Furthermore, a methodology to design FW-SPMSM with attractive self-sensing properties without degrading the peak torque capability of the motor is also proposed. The designed motors can run at low speed full torque using injection based-self-sensing.

To achieve the above goals, a dynamic loss minimizing control algorithm is developed, this algorithm runs the motor at the optimum operating point without affecting the drive dynamics. A wide-speed range self-sensing algorithm with zero torque ripple is also developed. This helps in controlling the motor without any position sensor while maintaining high dynamic performance of the servo drive.

Since the dynamic performance is critical for servo motors, a methodology to estimate the dynamic shaft torque, including inertial torque component is developed. This leads to accurate transient loss measurements, leading to an accurate comparison for the designed motors during dynamic servo cycle operations.

Acknowledgements

I dedicate this thesis to Prof. Lorenz, who was an exceptional mentor and advisor. He spent his time caring about people and students and he treated us like his children. Without his encouragement, knowledge, ideas, and advice, I wouldn't be able to perform this research and achieve my goals.

I would like to thank my Ph.D. committee members, Prof. Jaal Ghandhi, Prof. Eric Seaverson, Prof. Daniel Ludois, Prof. Michael Zinn, and Jim Sember who have been knowledgeable advisers and teachers to me. I would also like to thank Prof. Neil Duffie, Prof. Thomas Jahns, and Prof. Bulent Sarlioglu who were a part of my Ph.D. preliminary exam committee for their support.

I would like to express appreciation for the opportunity to take classes and conduct research within the Wisconsin Electric Machines and Power Electronics Consortium (WEMPEC). I further thank Kyle Hanson, Kathy Young, and Helene Demont, for their kindness and continuous support and for being an integral part of my WEMPEC experience.

I thank Mitsubishi Electric Corp. and Delta Electronics Inc. for sponsoring a significant part of my research. and all members of the Mitsubishi and Delta team at WEMPEC, particularly, Eigo Totoki from Mitsubishi Electric, and Shao-Chuan Chien (Sean) and Li-Hsing Ku (Eick) from Delta Electronics for their help and support.

I thank Yuichiro Nakamura, Shinichi Yamaguchi, Toru Ogawa, Ariff Zaini, Mark Gries, Patrick Ozimek and Omid Shirazi who mentored me during the various internship opportunities I was encouraged to participate in via the WEMPEC program.

I would like to thank my WEMPEC peers for their overwhelming support and stimulating discussions. Thank you to the following good friends and fellow curious minds: Apoorva Athavale, Aditya Ghule, Baoyun Ge, Hao Jiang, Daniel Erato, Ryoko Immamura, Guangqi Zhu, Ruxiu Zhao, Yukai Wang, Tim Slininger, Marc Petit, Christoph van der Broek, Benjamin Grothmaan, Yuying Shi, Kang Wang, Narciso Marmolejo, Hasan Hakem, Hung-Yen Ou-Yang, Shang-Chuan Lee, Dheeraj Bobba, Renato Amorim Torres, Eugene rush, Jiejian Dai, Ju Hyung kim, Yingjie li, Le Chang, Zheng Gao, Muhammad Alvi, Ye Gu Kang, Peter Meyer, Minhao Sheng, Tim Polom, Yang Xu, Hao Zeng and all members of the CAST group from 2014-2019.

I also would like to thank my roommates in Madison, Raed Al Kontar and Amr Abdeen, I spent a wonderful time with you.

Finally, I would like to thank my family for their support and encouragement during this time. I could not have done this without my family support.

Table of Contents

List of Figures

List of Tables

Nomenclature

Symbol	Description
λ_{pm}	permanent magnet flux linkage
ω_r or ω_e	rotor electrical velocity
ω_m	rotor mechanical velocity
T_{em}	electro-mechanical torque
V_{dq}	stator voltage complex space vector
I_{dq}	stator current complex space vector
λ_{dq}	stator flux linkage complex space vector
R_s	stator resistance
L_d ,L_q	d- and q- axis stator inductance
P_{cu}	copper loss
P_{fe}	iron loss
K_{cu}	copper loss coefficient
K_{fe}	iron loss coefficient
K_T	torque constant
λ_{MTPA}	total stator flux linkage at rated current and maximum torque per amp
$\lambda_{dq\text{-}cm}$	stator flux linkage complex space vector estimated using current model

Superscripts

$(\ )^s$	stationary reference frame
$(\ )^r$	rotor reference frame
$(\ )^e$	excitation/synchronous reference frame
$(\ )^*$	commanded or reference quantity

Subscripts

$(\ )_e$	rotor electrical
$(\ )_m$	rotor mechanical
$(\ )_{dq}$	complex vector of the form $(\ )_d + j(\ )_q$

Abbreviations

EMF	electromotive force

MMF	magnetomotive force
FW	flux-weakening
FI	flux-intensifying
PM	permanent magnet
PMSM	permanent magnet synchronous machine
IPM	interior permanent magnet
FEA	finite element analysis
SPM	surface mounted permanent magnet
FSPM	flux switching permanent magnet
LMC	loss minimizing controller
HFFI	high frequency flux injection
HFI	high frequency injection
MTPA	maximum torque per ampere
MTPV	maximum torque per volt
MTPF	maximum torque per flux
MRAC	Model reference adaptive control

Introduction

This section provides research background and motivation, research overview, and a chapter-by-chapter list of material discussed herein.

Research Motivation

Servo motors are widely used in many automation and robotics application to allow precise control of the motor position, velocity, and acceleration. The majority of electrical machines used in servo applications are permanent magnet (PM) motors, due to high efficiency, power density, and dynamic performance. Different PM machine types are used in servo application, each having its pros and cons. To achieve the desired precise position control, these machines require special design.

The research motivation is to develop a servo drive system that is more efficient and reliable, with lower capital and operational cost, without sacrificing the high dynamic performance of standard servo drive systems.

To achieve the above goals, several motor designs and control methodologies are developed. This includes servo motor designs that have better dynamic loss minimization and self-sensing properties, dynamic loss minimizing control, and injection based self-sensing algorithm with zero torque ripple.

Transient performance is essential for servo motors. To evaluate different servo motor designs, techniques are developed in this thesis. Achieving the above goals leads to a lower cost, more efficient, more reliable, and smaller sized servo drive system.

Research Overview

This research evaluates the dynamic performance of standard servo motors found in the market (SPMSM and IPMSM). A methodology to design a new servo motor that has flux intensifying property and meets the desired servo requirements is then developed. The proposed (FI-SPMSM) design combines the benefits of both IPMSM and SPMSM designs and uses less magnet material reducing the drive cost while achieving lower energy loss in high-speed partial torque duty cycle servo applications. FI-SPMSMs are also suitable for injection based-self-sensing control, unlike standard SPMSMs.

A methodology to design flux weakening SPMSM (FW-SPMSM) that has attractive self-sensing features without sacrificing the peak torque performance of standard FW-SPMSMs is also proposed in this thesis. In the proposed design, the saliency of this motor improves with load, unlike standard FW-IPMSMs, in which the saliency degrades with load. The designed motor would achieve low losses for servo applications that require high-torque low-speed operation.

A methodology to evaluate motor losses during dynamic speed operations using standard drive sensors is also proposed in this research. This is done by developing a dynamic shaft torque observer, which allows estimating the motor losses during transient speed operations, which aids in understanding motor transient losses and the actual thermal limits of the motor.

To run the designed motors at the optimum operating point without affecting the drive torque dynamics, a methodology to design a dynamic loss minimizing control with DB-DTFC (LMC-DB-DTFC) is proposed. This algorithm selects the feasible optimum stator flux linkage to

minimize total motor loss every switching period. The proposed LMC-DB-DTFC operates even at the voltage limit during flux weakening operation.

A methodology for injection based self-sensing control with zero torque ripple is developed by utilizing the attractive independent control of the motor airgap torque and stator flux linkage feature of DB-DTFC. A high-frequency flux is injected along the torque line, while the position is estimated from the measured terminal currents, allowing the use of self-sensing techniques with inherently zero torque ripple. Back-EMF tracking self-sensing control is also used during medium and high-speed operation. A methodology for smooth switching between the injection based and the back-EMF tracking self-sensing is proposed. The proposed algorithm has good dynamic performance, which allows controlling the motor even during rapid speed transients.

Research Contributions

The following list summarizes the key contributions made by this research.

- Development of a methodology to design FI-SPMSMs, using a smaller amount of magnet, suitable for dynamic loss minimization and injection based self-sensing. This design is very efficient for servos that operate at high-speed partial torque cycles.
- Development of methodology to design bread-loaf and arc-shape FW-SPMSM with a symmetric structure to achieve the desired cogging and ripple torque requirements for servo applications and has enhanced self-sensing features. This design is very efficient for servos that operate at low-speed high-torque cycles.
- Development of a methodology to minimize total motor loss dynamically at the switching period level, without affecting the torque dynamics of the drive by taking advantage of the

torque and flux decoupling of DB-DTFC. The proposed algorithm works even at the voltage limit during flux weakening operation.

- Development of a methodology to accurately estimate the shaft torque components during both steady-state and dynamic speed operations, allowing accurate transient loss measurement.
- Development of a methodology to control the servo motor using self-sensing techniques at zero and low-speed operations with zero torque ripple. This is achieved by injecting a high-frequency flux (HFFI) along the torque line with DB-DTFC.
- Development of a methodology for a smooth transition between the HFFI and back EMF techniques. The proposed methodology requires low computational efforts in the DSP and has good dynamic performance, allowing usage in servo applications.
- Experimentally identified and evaluated the steady-state and dynamic performance of the developed HFFI-self-sensing control algorithm on flux intensifying and flux weakening permanent magnet motors.
- Development of scalable design methodology for FI-SPMSM and FW-SPMSM for servo applications with enhanced dynamic loss minimization and self- sensing properties.
- Development of methods to design SPMSMs and IPMSMs with very low cogging and ripple torque, then fairly compare the dynamic loss minimization and self-sensing performance for those motors.

Summary of Chapters

In Chapter 1, a state-of-the-art review is given on the performance requirements of servo motors, PM machine design for power conversion and self-sensing, techniques to achieve low cogging and ripple torque in PM motors, and control techniques for PM motors including current regulations, DB-DTFC, loss minimization, and self-sensing control.

In Chapter 2, method to design SPMSMs and IPMSMs with very low cogging and ripple torque is presented. The performance of these motors is compared and evaluated. Then a methodology to design FI-SPMSM servo motor with enhanced dynamic loss minmization perfromance is presented. The performance of the three motors is experimentally evaluated. Scalability analysis of this design methodology is also evaluated in this chapter.

In Chapter 3, a methodology to design FW-SPMSM servo motors with enhanced self-sensing properties is proposed. The proposed motor has a symmetrical rotor structure with lower losses for servo applications that run at high-torque low-speed operation. The self-sensing performance of the proposed motor improves with increasing the motor load, unlike standard FW-PMSM. The designed prototype power conversion and self-sensing performance are evaluated and compared with a designed FW-SPMSM with an asymmetrical rotor using shifted magnets. Scalability analysis of this design methodology is evaluated in this chapter.

In Chapter 4, a methodology to design a dynamic shaft torque observer is presented. This observer estimates the dynamometer shaft torque during steady-state and transient speed operation allowing the measurement of motor’s transient losses. The proposed technique works with standard dynamometer sensors. The proposed methodology is experimentally evaluated in this chapter.

In Chapter 5, a methodology to design dynamic loss-minimizing controller with DB-DTFC for PM servo motors is presented.

In Chapter 6, a wide-speed range self-sensing control algorithm is presented. First, a methodology to estimate the motor position at zero and low speed with zero torque ripple is presented. Then, a back-EMF self-sensing algorithm to control the motor at medium and high-speed operation is presented. This chapter also presents a methodology for a smooth switching between the previous self-sensing algorithms.

In Chapter 7, the key conclusions and contributions of this work are summarized. Recommendations for the future work are presented.

Chapter 1 State-of-the-Art Review

This thesis presents methodologies to design, model and control of a permanent magnet (PM) servo motors with enhanced dynamic loss minimization and self-sensing performance. The proposed methodologies will be evaluated during both steady-state and dynamic operations through developing several servo cycles.

This chapter presents a review of the performance requirements of a permanent magnet synchronous motors used in servo applications. The state-of-the-art techniques for the design of conventional permanent magnet synchronous machines are reviewed. The state-of-the-art control methods used for optimal utilization of the drive capability for high performance while minimizing losses are discussed. Next, state-of-the-art self-sensing techniques during zero, low-speed, and high-speed operation are discussed. Limitations of the found designs and algorithms when they applied to servo motors and applications are highlighted.

1.1 Applications and Performance Requirements for Servo Motors

Servo motors are widely used in industrial applications that require precise control of acceleration, speed, and position. They are used in industrial robots, rolling machines, printers, etc. Different types of servo motors are able to serve this purpose. Servo motors require high dynamic performance. Permanent magnet synchronous motors (PMSMs) achieve this and tend to have a high-power density and high efficiency. For these reasons, PMSMs are the most commonly used type of servo motors.

Different PMSM designs are used for servo applications, but the two main types are the surface PM (SPMSM) and the interior PM (IPMSM). Servo motor design is optimized to achieve

very low levels of ripple and cogging torque. For these reasons, an IPMSM servo motor generally has low reluctance torque (low saliency ratio). The main advantage of an IPMSM configuration compared to an SPMSM is that there is no need to use a sleeve for high-speed operation and can achieve lower dynamic losses during certain servo cycles.

1.1.1 Servo cycles

In general, servo cycles can be divided into two main categories according to the applications: point-point servo cycle and continuous operational servo cycle.

Point-to-point servo cycles or pick-and-place servo cycles are used in different applications like robots, printers, CNC machines, etc.; time span of these kinds of cycles is short, often only a few seconds. The servo motor used in these kinds of cycles requires precise position control at both starting and ending points. Fig. 1-1 shows a typical point to point servo cycles.

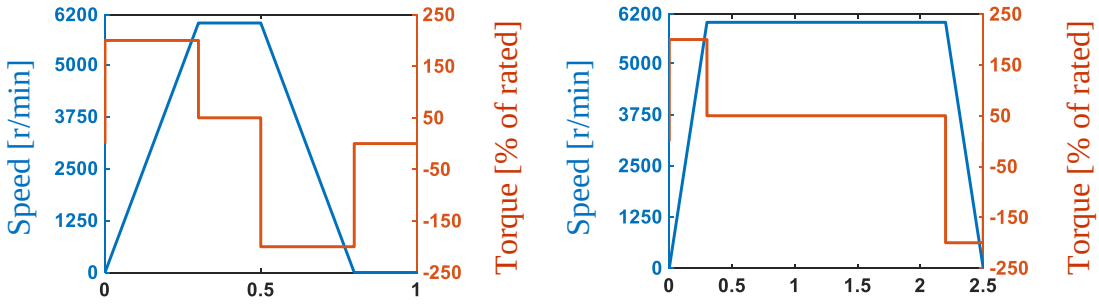

(a) short cycle (b) long cycle

Fig. 1-1 Typical servo cycle for point-to-point application

Continuous operational servo cycles are used in applications that require precise position and speed control all the time, used in rolling machines, aluminum foil manufacturing machines, painting robots, etc.; the time span for these kinds of cycles is longer than point-to-point cycles, typically measured in minutes. Fig. 1-2 shows a sample of continuous operational servo cycle.

Most of the servo applications run at high speed with partial rated torque as in Fig. 1-2-a. However, there are some direct drive servo applications that run at low-speed high torque operation as in Fig. 1-2-b.

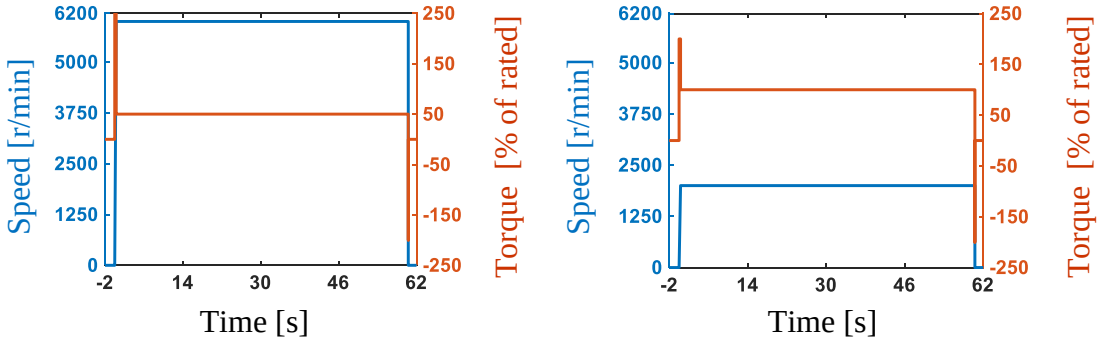

(a) high speed partial torque (b) low speed rated torque

Fig. 1-2 Typical continous servo cycle

In this research, continuous operational servo cycles will be studied. Energy loss in these kinds of cycles will be compared for different servo motor designs. Methodologies to design servo motors with enhanced self-sensing and dynamic loss minimization performance will be presented in this thesis.

1.1.2 Servo motor drive structure

The majority of electrical drives are supplied using PWM voltage source inverters. In these kinds of converters, the maximum output voltage is limited by the DC link voltage, which is determined by the grid voltage (rectified grid AC voltage). Fig. 1-3 shows the block diagram for voltage source converter.

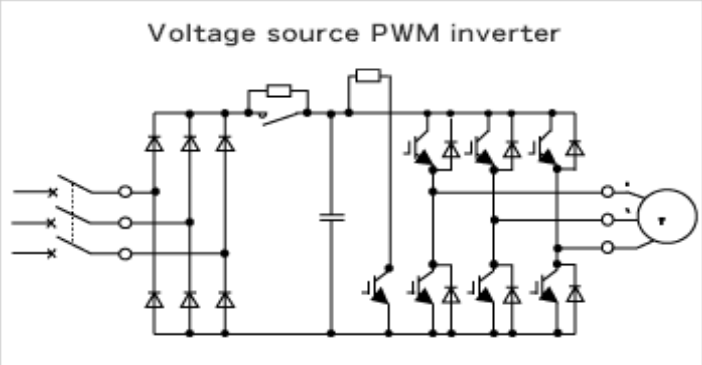

Fig. 1-3 Voltage source converter

In Japan, grid voltage is 200 $V_{L\text{-}L,\ RMS}$ rectifying this voltage using 3 phase uncontrolled rectifier will lead to 270 V DC link voltage as in equation(1-1). The maximum output voltage from the PWM inverter can be obtained using space vector modulation which is 172 V as in equation(1-2) [1].

In this research an external DC power supply is used to charge the inverter DC link with 270 V to emulate the target system.

$$V_{DC} = \frac{3}{\pi} * V_{L\text{-}L\ Peak} \tag{1-1}$$

$$V_{max} = \frac{2}{\pi} * V_{DC} \tag{1-2}$$

1.1.3 Cooging and ripple torque requirments

Servo motors are designed to achieve very low levels of cogging and ripple enabling smooth and precise speed, position, and acceleration control. Cogging and ripple torque requirements for servo application are summarized inTable 1-1. FEA requirements were set to be lower than the practical requirements to overcome the extra cogging and ripple torque due to the manufacturing process.

Table 1-1 Servo motor application requirements

Specifications	Practical requirement	FEA requirement
Cogging torque	<1.5%	<0.5%
Torque ripple	<4%	<2%

1.2 Design of Conventional PMSMs

Servo motors require high dynamic performance. This is achieved by PMSMs, which have a high-power density, high efficiency and low inertia. For these reasons, PMSMs are the most commonly used type of servo motors.

Servo motors require a high peak torque at low speed, to achieve a high acceleration rate. These motors typically run at medium speed (2000 – 8000 r/min). These motors didn't require wide constant power region like automotive applications. This makes PMSMs a very attractive choice for servo applications. Fig. 1-4 compares the high-efficiency region for different electrical machines types.

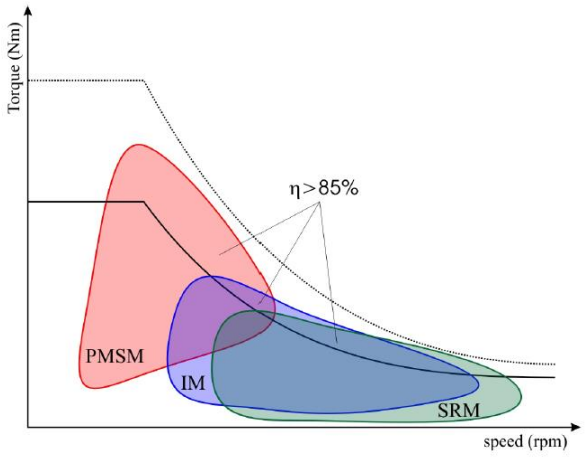

Fig. 1-4 High efficiency regions for conventional designs of PMSM, IM and SRM machine types with rated (solid lines), peak (dotted lines) torque-speed envelopes [2]

Conventional PMSMs can have a surface permanent magnet (SPM) topology, examples shown in Fig. 1-5, or an interior permanent magnet (IPM) topology, examples shown in Fig. 1-6.

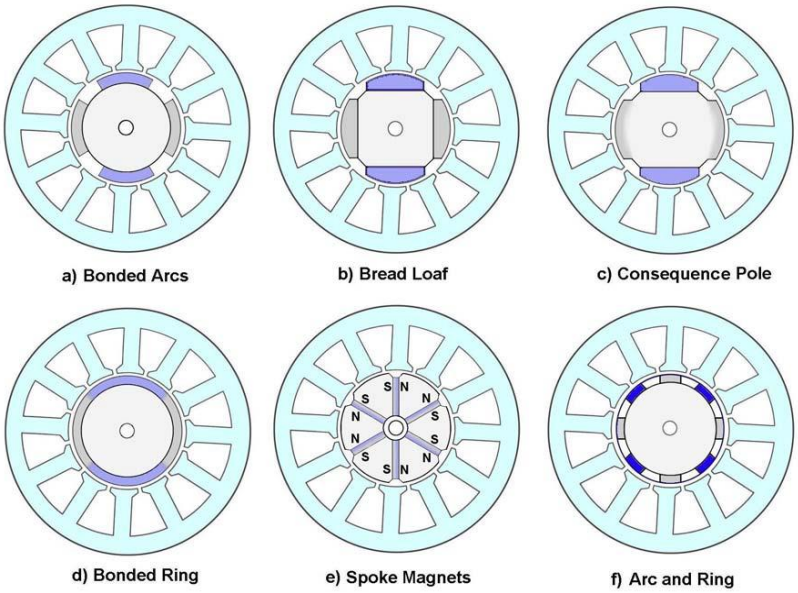

Fig. 1-5 Surface permanent magnet rotor topologies

The bonded ring magnet SPMSM has a trapezoidal back-EMF. This structure is very suitable for BLDC motors, in which a square wave back-EMF is desired [4] . To achieve a lower torque ripple, the magnet span is reduced. This structure typically called bonded arcs or arc and ring SPMSM. It has lower 3rd harmonic and lower fundamental back-EMF and is typically used in AC SPMSMs[4] . To achieve a very low cogging and ripple torque the magnet can be shaped to achieve sinusoidal back-EMF, as in bread-loaf SPMSM. This structure is very common in high-performance industrial servo motors.

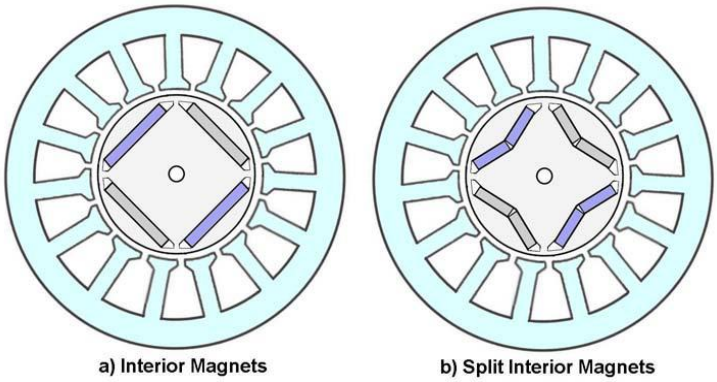

Fig. 1-6 Interior permanent magnet rotor topologies

IPMSMs have magnets inset or buried in the rotor. This allows running the motor in a high-speed operation without the need to use any sleeve to protect the magnet. Typically, IPMSMs are designed to utilize the reluctance torque component in addition to the magnet torque during high-speed operations.

Both SPMSM and IPMSM structures have their advantages in different applications. A basic performance comparison between each of them in terms of their electrical and mechanical features is listed in Table 1-2 [5] [6] [7] [8] .

SPMSM is commonly used in servo applications due the high peak torque perfromance, which reflectcs higher acceleration rate with lower copper losses. However, few companies start manufacturing IPMSM for servo applications due to a lower iron loss which becomes significant at high-speed operation.

This section will review the literature for the developed techniques to design PM motors with low ripple and cogging torque, with enhanced dynamic loss minimization performance, and with enhanced self-sensing performance.

Table 1-2 Performance comparisons between IPM and SPM machines [8]

Machine category	Electric features	Mechanical features
IPM machine	1. The combination of PM and salient-pole synchronous machine 2. This machine can achieve wide constant-power speed range	1. Magnets are embedded in the rotor and is suitable for high speed applications, such as hybrid electric vehicles 2. Iron lamination stacks are always required in the rotor which increase the difficulty of manufacture
SPM machine	1. The inductance is quite low because of the large air gap including the magnet height 2. The back-EMF voltage is directly proportional to the rotating speed	1. Magnets are glued on the rotor and is suitable for low speed applications, such as CNC milling and turning machines 2. Soft magnetic material can be used instead of steel lamination in the stator to reduce the cost

1.2.1 Design considerations of PM servo motor to achieve low cogging and ripple torque

Many techniques have been developed in the literature to reduce the cogging and ripple torque in PM motors. like shaping the magnet to reduce the airgap flux harmonics which helps achieving smooth torque [9] [11] [10] . Fig. 1-7 shows the magnetization patters and indicates the shape of back-EMF obtained from that pattern. Shaping the magnet can be done in the radial direction like in the bread-loaf configuration which can be easily done by performing 2D-FEA but requires complex magnet geometry.

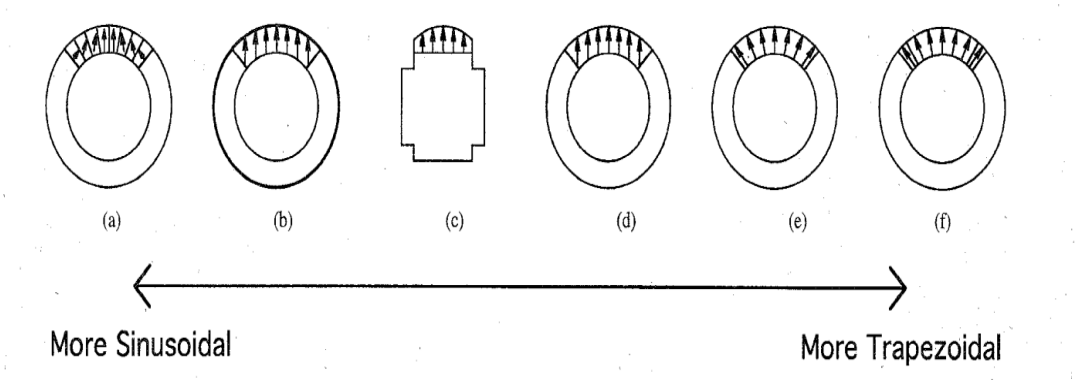

Fig. 1-7 Alternate means for obtaining sinewave and rectangular airgap flux distributions illustrated with four-pole motors. (a) blocked. (b) magnetic can. (c) tapered. (d) parallel. (e) radial. (f) interleaved. [9]

Cogging and ripple torque can be also reduced through shaping the magnet in the axial direction as in [13] and [14] . This requires performing 3D-FEA which is computationally intensive but allow using a simple magnet geometry. Fig. 1-8 shows the designed sinewave rotor.

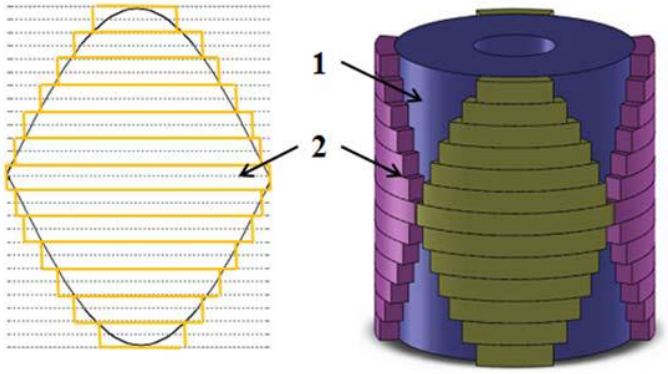

Fig. 1-8 SPMSM magnet shaping in the axial direction[14]

The authors of [14] compared different SPMSM topologies as in Fig. 1-9. They concluded that shaping the magnet to form a full or half sine wave would significantly reduce the 5^{th} and 7^{th} harmonics in the motor back-EMF as in Fig. 1-10. This helps in achieving a smoother torque.

DESIGN PARAMETERS OF ANALYSIS MODELS

Item	Unit	Model 1	Model 2	Model 3	Model 4
Rotor topology	-				
Magnet volume	cm^3	26.0	17.8	19.8	18.2
Rotor volume	cm^3	94.4	86.2	88.2	86.6
No. of coil turns	mm	125	146	146	154
Wire diameter	mm	0.6	0.55	0.55	0.55
Phase resistance	mm	2.5	3.5	3.5	3.8
Current density	A/mm^2	4.1	4.8	4.8	4.8

Fig. 1-9 Comparison between different SPMSM axial magnet shaping [14]

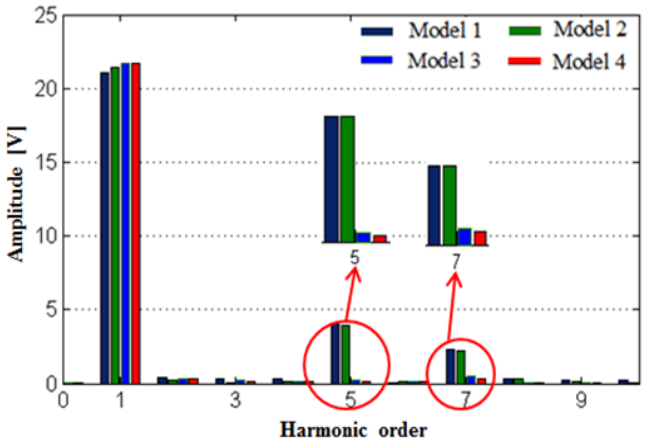

Fig. 1-10 FFT analysis of phase back EMF for a different SPMSM axial magnet shaping [14]

The other common technique used to reduce the ripple and cogging torque is skewing either the stator or the rotor. Skewing is very effective technique to reduce the cogging and ripple torque. On the other hand, skewing will lead to decrease the fundamental airgap flux and reduce the torque capability of the motor. The authors of [15] studied the impact of skewing on SPMSMs cogging and ripple torque. The different techniques to reduce the motor ripple torque were reviewed in [8] .

The authors of [18] proposed skewing the magnet in the SPMSM to reduce the cogging torque. They proposed a simple cogging torque equation as in (1-3).

$$T_{Cog} = -\frac{1}{2}\,\Phi_g^{\,2}\frac{dR_g}{d\theta} \qquad (1\text{-}3)$$

where $\frac{dR_g}{d\theta}$ represents the variation of air gap reluctance.

The purpose of the skew is to reduce the variation of air gap reluctance (reduce the reluctance torque) which reduces the cogging torque [15] . However, it may reduce the average torque of the motor. The skewing effect can be illustrated by a skew factor as in (1-4).

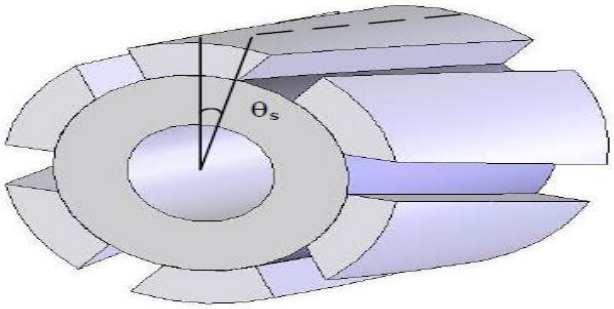

Fig. 1-11 Rotor geometry with skewed magnet

$$K_{skew} = 1 - \frac{\theta_s}{2\pi} \quad \text{and} \quad T_{skew} = K_{skew} * T_{avg} \qquad (1\text{-}4)$$

where K_{skew} is the skew factor ($K_{skew} \leq 1$), θ_s is the skew angle in radians as shown in Fig. 1-11, T_{skew} is the average torque after skewing.

Skewing the motor can be used to reduce the cogging torque. However, it is hard to adopt this technique to achieve very low cogging and ripple torque required for servo applications due to complexity of the rator and the manufacturability issues.

Similar methodology was proposed in [16] . The authors proposed using dual stator Flux Switching PM (FSPM) motor as in Fig. 1-12-a. One of the stators is shifted, this can achieve harmonic cancellation when adding the back-EMF from the two stators and reduce the resultant

back-EMF harmonics as shown in Fig. 1-12-b. Reducing the back-EMF harmonics helps in achieving lower cogging and ripple torque.

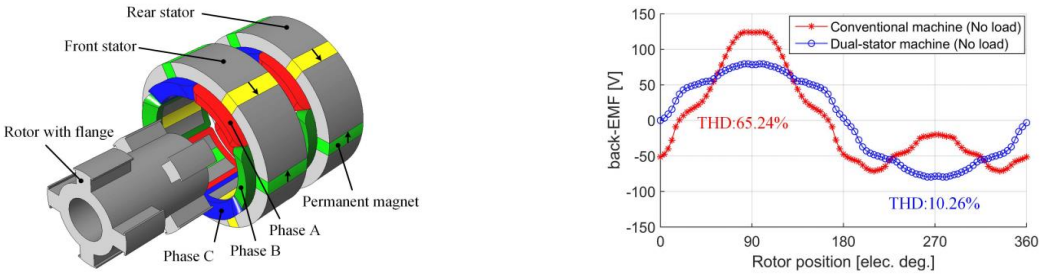

(a) Geometry (b) Baeck-EMF comparison

Fig. 1-12 FSPM motor with dual stator, and back-EMF comparison between dual stator FSPM and single stator FSPM [16]

Shifitning the PMS ploes are also a good way to reduce the cogging and ripple torque in SPMSMs [10] , [11] , [12] . Fig. 1-13-a shows the SPMSM that is designed by [12] . Shifting the PMs pole requires complicated mechanical design for the rotor to shift the center of mass to match with the center of rotation. This is done by adding holes to the rotor. This technique is very effective in reducing the cogging torque and can be used to design SPMSM for servo applications with using a simple ring-shaped magnet as in Fig. 1-13-b. This methodology will be further investigated later in chapter 3 of this thesis.

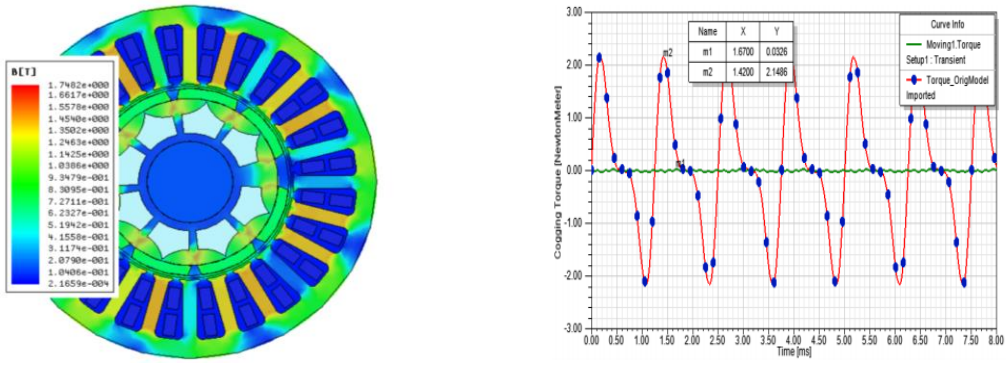

(a) Geometry (b) Cogging torque comparison

Fig. 1-13 SPMSM with shifted PMs (asymmetric design) and the reduction of cogging torque compared to the symmetric design [12]

Stator winding type and slot-pole combination also affect the motor ripple and cogging torque. This will be discussed in the following subsection.

1.2.2 Stator winding configurations of PMSMs

In general, electrical machine windings can be divided into two main types, concentrated and distributed windings [19] . Distributed windings are generally used in large machines in which, several stator teeth are wound and combined into one phase. Through this winding type, the stator MMF can be designed to achieve a smooth back EMF [20] . Distributed winding machines can be designed to produce higher torque, through having larger saliency ratio (achieved through shaping the flux path), and larger reluctance torque compared to the concentrated winding type. However, distributed winding machines have longer end-windings which increase the copper losses and affect the motor efficiency [21] . For these reasons, distributed winding motors are preferred for high-torque applications.

The other winding type is concentrated windings machines. This type of machine has short end- windings, which reduces the copper losses and achieves higher efficiency. However, this type of windings has lower armature flux linkage, which might affect the torque density of the motor [22] . Concentrated winding motors are easier to manufacture (automated winding procedure). These machines are commonly used in high-efficiency low-power motors. Fig. 1-14 shows both concentrated and distributed winding motors.

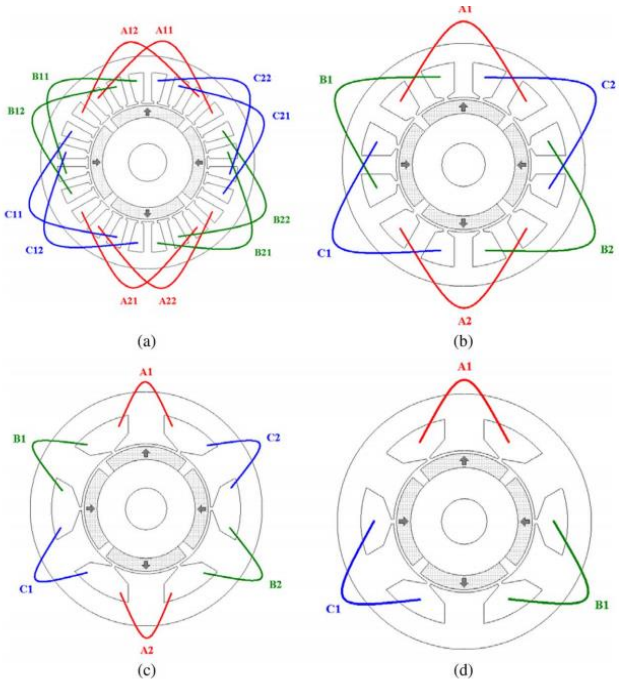

Fig. 1-14 Typical stator winding configurations (four pole) [1]. (a) Twenty-four slot, overlapping (distributed). (b) Twelve slot, overlapping (concentrated). (c) Six slot, non-overlapping, all teeth wound. (d) Six slot, nonoverlapping, alternate teeth wound.[23]

Recently, low power SPMSM for servo applications with concentrated windings have been adopted by the majority of the servo motors manufacturer. This happens due to many reasons which are summarized as follows:

a) Concentrated windings motors have shorter end windings, this reduces the copper volume used in these motors, and reduces the copper losses. This type of winding is easier to fabricate compared to the distributed winding this drives the manufacturing cost down compared to distributed windings [24] [25] .

b) High slot fill factor (the ratio of winding area to the slot are) can be achieved with concentrated windings motors, through using a soft magnetic composite. For example, 78% slot fill factor was achieved by [26] and 75% was achieved by [27] . The authors used segmented stator components.

c) Similar number of slot and pole combination can be used with concentrated windings. This can be used to achieve a very low cogging torque in the motor [28] .

Different concentrated winding topologies were reported in the literature. The main classification of the concentric windings is done according to the number of coils per slot and classified to all teeth wound windings (two coils occupy one slot) as in Fig. 1-15 (a), and alternative teeth wound windings(one coil occupy one slot) as in Fig. 1-15 (b). Detail comparisons between these two configurations have been reported in [29] , [34] .

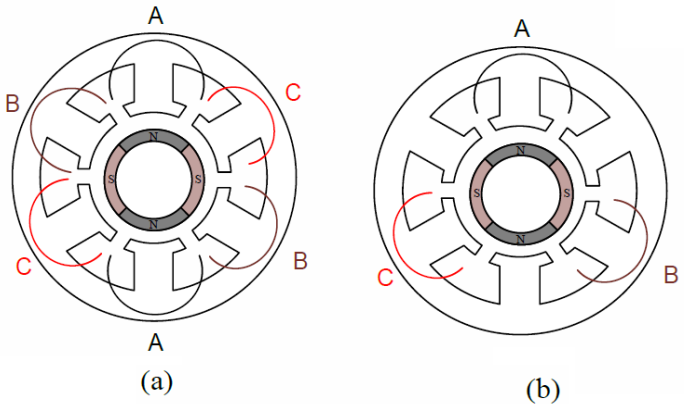

Fig. 1-15 Example of winding layout with (a) all teeth wound concentrated winding (6slots/4poles) and (b) alternative teeth wound concentrated windings (6slots/4poles) [8]

PM machines with alternative teeth wound concentric windings produce higher self-inductance and lower mutual-inductance than that with all teeth wound windings. This configuration can also achieve higher output torque; however, torque ripple might be a considerable issue and the MMF harmonics are also higher than all teeth wound design, which leads to higher rotor eddy current loss [29] [34] .

In this thesis, both winding configurations will be used. Concentric winding will be used with the designed small size servo motor, while distributed winding will be used with the designed high-power servo motor.

1.2.3 Slot-pole combination design

Distributed winding machines tend to have a high number of stator slots compared to the number of poles, the coil span for a full pitch winding is 180°. While in case of a concentric winding configuration, the coil has 120° span. This might lead to a poor torque production. This can be avoided by adequately selecting the slot pole configuration. Similar number of stator slots and rotor poles forms attractive combinations [25] [26] [32] .

Three main factors are typically used to select the proper slot, pole combination. These factors are the number of slot per pole per phase, winding factor, index factor, and the great common multipler factor.

- Slot per pole per phase (N_{spp}) can be calculated as in (1-5).

$$N_{spp}= \frac{N_s}{2pN_{ph}} \quad (1\text{-}5)$$

where Ns is the number of stator slots, p is the number of pole pairs, and Nph is the number phases.

The machine is called fractional slot machine if N_{spp} is not an integer number. Fractional slot motors with a similar number of poles and slots ($N_{spp}<1$) tends to have low cogging and ripple torque compared to traditional fractional slot motors [31] .

- Winding factor (Kw) for concentrated winding machines can be calculated as in (1-6).

$$K_{w}= \left|E_{phase}\right| \frac{N_{ph}}{N_s} \quad (1\text{-}6)$$

where E_{phase} is the phasor back-EMF per phase caused by the winding element. Increasing the winding factor reflects increasing of the motor torque density[34] .

- Index factor (C_T) which can be calculated as in (1-7).

$$C_{T=}\frac{2pN_s}{N_c} \quad (1\text{-}7)$$

where N_c is the least common multiplier (LCM) of the number of poles and slots. Smaller index value (higher LCM value) factor indicated smaller amplitude of cogging torque [34] .

- Great common divider (GCD) for the number of slots and poles can be used to pick the right slot-pole combination that achieves low radial forces, by selecting an even GCD number.

These factors are summarized in tables which simplifies selecting the appropriate slot-pole comination. Table 1-5 shows the winding factor values for different slot-pole cobinations. Table 1-4,Table 1-5 shows the calculated least common multipler and great common divider calculated for different slot-pole combination respectively. [35][36].

Table 1-3 Winding factors calculated for different slot/pole combinations [8]

N_s \ N_p	2	4	6	8	10	12	14	16
3	c 0.866	c 0.866	×	×	×	×	×	×
6	d 1	c 0.866	×	c 0.866	c 0.5	×	c 0.5	c 0.866
9	d 0.945	d 0.945	c 0.866	c 0.945	c 0.945	c 0.866	c 0.616	c 0.328
12	d 0.966	d 1	×	c 0.866	c 0.933	×	c 0.933	c 0.866
18	d 0.96	d 0.945	d 1	d 0.945	c 0.735	c 0.866	c 0.902	c 0.945
24	d 0.958	d 0.966	×	d 1	d 0.925	c 0.866	c 0.76	c 0.866
36	d 0.956	d 0.96	d 0.966	d 0.945	d 0.924	d 1	d 0.898	d 0.945

c: Concentrated windings d: Distributed windings
For concentrated windings, only dbl k_w is shown

Table 1-4 Least common multipler calculated for different slot/pole combinations[5]

S \ 2p	2	4	6	8	10	12	14	16	18	20	22	24
3	6	12		24	30		42	48		60	66	
6	6	12		24	30		42	48		60	66	
9		36	18	72	90	36	126	144		180	198	72
12	12	12		24	60		84	48		60	132	
15				120	30		210	240		60	330	
18			18	72	90	36	126	144		180	198	72
21				168	210		42	336		420	462	
24		24		24	120		168	48		120	264	

Table 1-5 Great common divider calculated for different slot/pole combinations

S \ 2p	2	4	6	8	10	12	14	16	18	20	22	24
3	1	1		1	1		1	1		1	1	
6	2	2		2	2		2	2		2	2	
9		1	3	1	1	3	1	1		1	1	3
12	2	4		4	2		2	4		4	2	
15				1	5		1	1		5	1	
18			6	2	2	6	2	2		2	2	6
21				1	1		7	1		1	1	
24		4		8	2		2	8		4	2	

In this thesis, 10 poles,12 slots concentric winding is chosen for the high-speed low power servo motor. This configuration achieves high winding factor with low cogging and ripple torque. For the low speed, high power motor 24 slots, 8 poles distributed winding configuration is selected due to a high winding factor which maximizes the motor peak torque, this configuration achieves low cogging and ripple torque as well.

1.2.4 Design considerations of PM motors to achieve good dynamic loss minimization performance

Classical machine designers tend to design the machine based on the rated operation (at the rated speed and torque). They try to achieve the highest efficiency at that point. However, for

many applications that use adjustable speed drives like automotive and servo applications, the motor runs at different operating speed and torque (duty cycle applications). For these applications, the peak torque is required for a short period of time only during the acceleration/deceleration periods. Then the motor runs at high speed with partial load.

The fluctuation of rare earth magnet prices in the past decade encouraged motor designers to design new motors with a smaller amount of magnet material, to reduce the price of the servo drive. Several PM motor designs were proposed for automotive applications, and those designs use less magnet material in order to reduce the total cycle loss of the electrical drive. A FI-IPMSM motor for automotive applications is proposed in [37] . This motor has an inverted saliency using q-axis flux barriers and lower magnet volume. This can improve the high-speed operation performance but will decrease the peak torque. Fig. 1-16 shows the baseline FW-IPMSM and the proposed FI-IPMSM. Fig. 1-17 compares the performance of these two designs. FI-IPMSM achieves lower peak torque compared to FW-IPMSM, due to using less magnet material. However, this motor has higher efficiency during the high-speed medium torque operation.

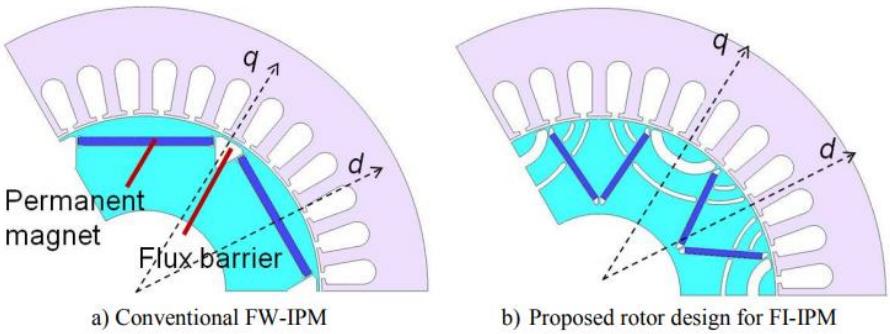

Fig. 1-16 Rotor designs for the conventional FW-IPMSM and FI-IPMSM designs[39]

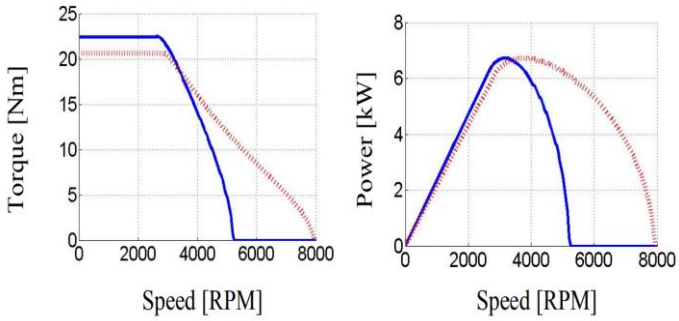

a) toque, power Vs speed comparison for the FW-IPMSM and FI-IPMSM

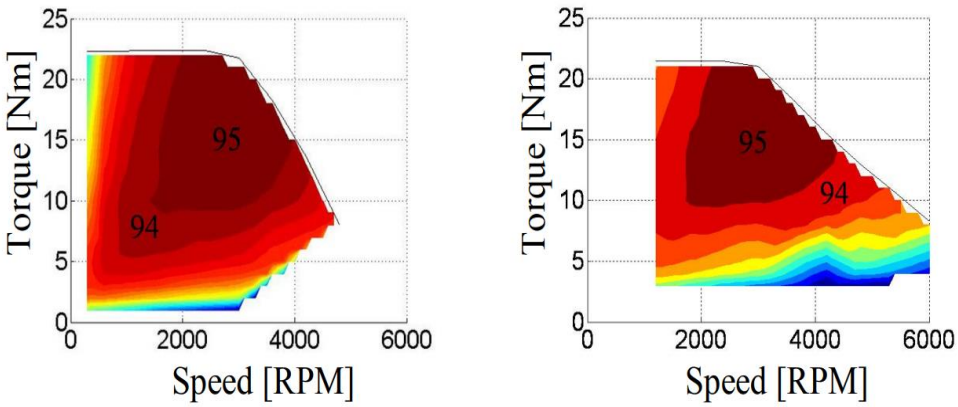

b) simulated efficiency maps for the FW-IPMSM and FI-IPMSM

Fig. 1-17 Performance comparison for FW-IPMSM and PI-IPMSM designs[39]

The authors of [40] propose using a FI-IPMSM structure for a variable gear electric vehicle drive. The authors use less magnet material, and they add q axis flux barriers to invert the motor saliency. This motor achieves a good efficiency through reducing the iron loss and improving the motor efficiency during the high-speed operation. In [41] an outer rotor FI-IPMSM is proposed; The proposed design can improve the torque under flux intensifying conditions and can operate for an extended speed range.

The authors of [42] propose a variable flux FI-IPMSM for automotive applications. They used a low coercive magnet to change the magnetization state of the magnet; with that, they

could save a significant amount of energy for the automotive cycle. Similar work was done by the authors of [43] and [44]. The authors of [45] show that there is a significant torque ripple associated with changing the magnetization state at high speeds, but the torque ripple only exists for few milliseconds. They claimed that this ripple will be filtered out by the vehicle inertia. Changing magnetization state has an extra loss, thus variable magnetization state motors are not suitable for high-performance servo applications.

The FI-IPMSM motor can achieve lower cycle loss for automotive cycles. However, these motors achieve a lower peak torque. This limits the acceleration rate of the motor or requires oversizing the inverter. The designed FI-IPMSM for automotive applications has hiher ripple and cogging torque and cannot be used in servo applications.

In summary, prior research shows the significance of reducing the magnet volume used in PM motors. This reduces the motor cost and improves the high-speed efficiency and performance. This was demonstrated using FI-IPMSMs, however, these motors have lower peak torque compared to FW-IPMSMs. The reduction of peak torque would be significant if the FI-IPMSM is compared with SPMSM. The reported designs were optimized for automotive applications and have relatively high cogging torque, which prevents using these designs in servo applications. At this time, there is still no appropriate PM motor design that improves the dynamic loss minimization performance through using a lower amount of magnet (flux intensifying PM motor) when it is used in servo applications and can achieve the required peak, ripple and cogging torque for servo applications.

1.2.5 Design considerations of PM servo motors to achieve good self-sensing control performance

Self-sensing techniques gains significant attention in the past few decades. Through these techniques, the motor can be controlled without any physical position sensor. This improves the reliability of the motor, achieves smaller size and reduces its cost.

Controlling the motor using self-sensing methods at zero and low speed is done through tracking the motor saliency. Using these techniques requires designing the motor to have a detectable saliency for the desired operating condition. Methodologies to modify the induction machine design to improve self-sensing performance were reported in [46]-[49].

In [37] the authors proposed the FI-IPMSM design for automotive application. The authors claim that this design would achieve better self-sensing performance. The authors of [50] compare the FW-IPMSM self-sensing properties with an inset SPMSM. The evaluated rotors are shown in Fig. 1-18. They concluded that the inset SPMSM saliency improves with increasing the q-axis current due to saturating the motor iron. The author did not evaluate the performance during the heavy load condition and during dynamic speed variation.

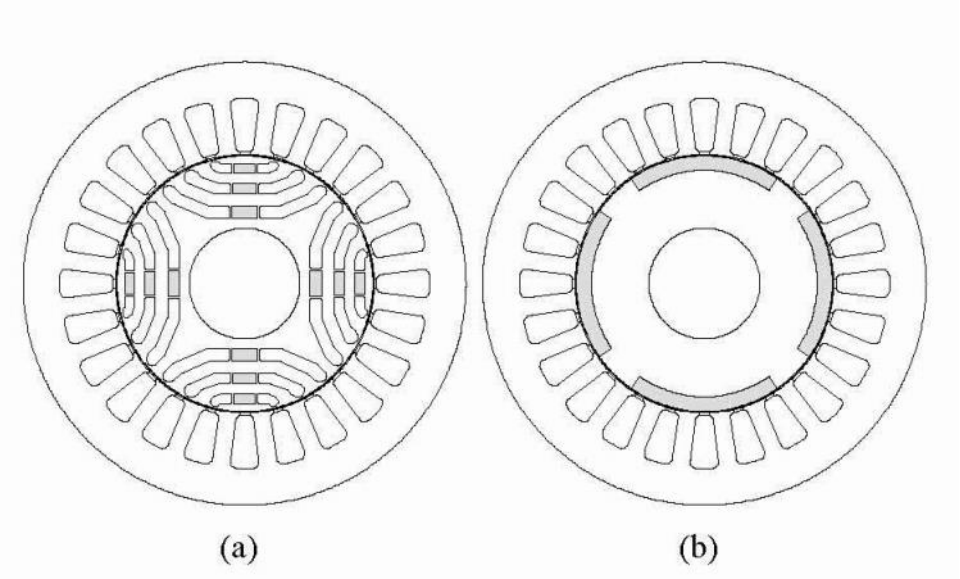

Fig. 1-18 Different rotor structure comparisons (a) IPM machine and (b) Inset PM machine [50]

In [51]-[53], the authors proposed using a simple short-circuit copper ring as in Fig. 1-19. This added an additional mutual inductance between the d-axis winding and the copper ring, which improves the performance of saliency-tracking.

Fig. 1-19 SPMSM rotor design with short-circuited copper ring [51]

In[54], a d-axis damper winding is added to the SPMSM rotor. The interaction between the damper winding and the armature flux introduces an inductance variation. However, this might affect the power conversion performance due to the influence of the damper winding.

In [8] , the author proposes using a narrow teeth tip, claiming that could introduce a small saliency in the SPMSM through utilizing the zig-zag leakage. Fig. 1-20 shows the flux level

when the d,q axis aligned with the stator tooth. The manufacturing process for a very narrow tooth structure might not be trivial.

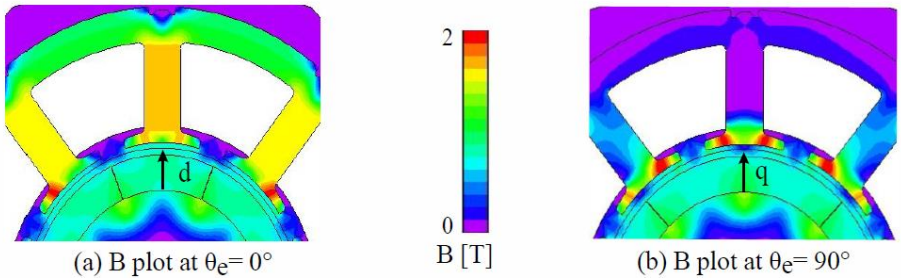

Fig. 1-20 Magnetic flux density plot from FEA at two rotor positions (stator bridge height = 0.4mm and no current excitation) [8]

In summary, prior spatial saliency design techniques are all based on either the rotor or stator design approach to achieve sufficient saliency for self-sensing control. Thus, the proposed SPMSM designs utilized ringed-shaped magnet with trapezoidal back-EMF, these designs didn't achieve the desired cogging and ripple torque for servo applications. At this time, there is still no appropriate saliency design proposed for SPMSM self-sensing control for servo applications that requires sufficient saliency even during the overload operation (200% rated torque is applied during acceleration periods) while producing smooth torque with very low ripple and cogging torque.

1.3 Control of Conventional PMSMs

Relevant control topics for PMSMs are reviewed in this section. First, the PMSM model is reviewed. Afterward different control techniques are reviewed briefly.

1.3.1 Permanent magnet synchronous machine (PMSM) model

Permanent magnet motors have different types as discussed early in this chapter. For example, in SPMSMs, the magnet is placed on the rotor surface; these have no saliency (Ld =

Lq). For IPMSMs, the magnet is buried inside the rotor that leads to different inductance in the d-axis and q-axis, which causes saliency in the machine. In inset PM machines, the magnet is placed on the surface of the rotor, but the gap between the magnets is filled with iron, causing different inductances in the d, and q axes. Forming a salient machine. Fig. 1-21 shows the different rotor structure for the different PM machine types.

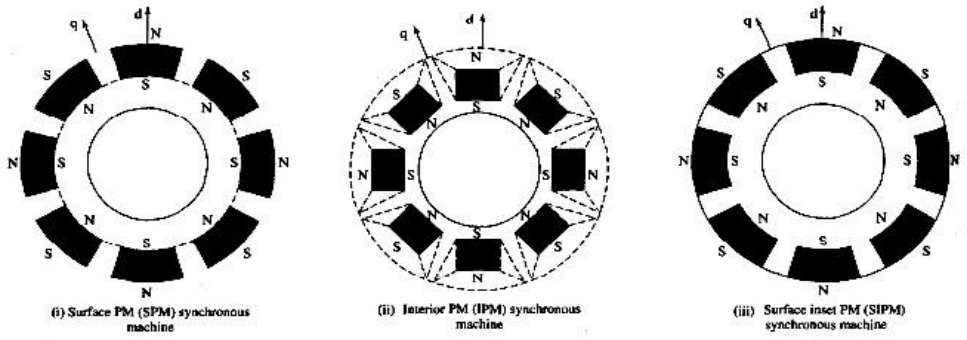

Fig. 1-21 (i) Surface mount PM machine (ii) interior PM machine (iii) inset PM machine [55]

Fig. 1-22 shows both the stationary and rotor reference frame; from this figure, it is easy to find the transformation matrix from abc frame to rotor reference frame as in (1-8)[56].

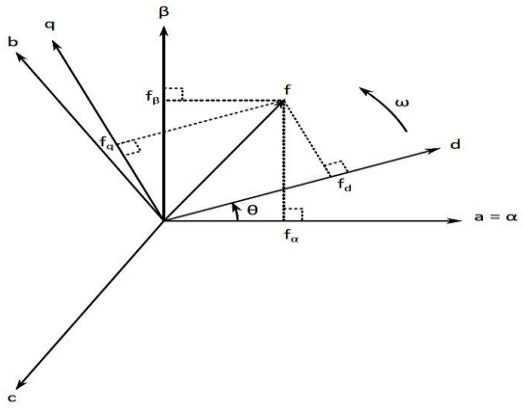

Fig. 1-22 αβ stationary reference frame and dq rotor reference frame for PM machine

$$\begin{bmatrix} f_d^r \\ f_q^r \\ f_0^r \end{bmatrix} = \begin{bmatrix} \cos(\theta) & \cos(\theta - \frac{2\pi}{3}) & \cos(\theta + \frac{2\pi}{3}) \\ -\sin(\theta) & -\sin(\theta - \frac{2\pi}{3}) & -\sin(\theta + \frac{2\pi}{3}) \\ \frac{1}{2} & \frac{1}{2} & \frac{1}{2} \end{bmatrix} \begin{bmatrix} f_a \\ f_b \\ f_c \end{bmatrix} \quad (1\text{-}8)$$

The state equations for PMSM are shown in equations (1-9) and (1-10) [57]. These equations are general for all PM machines. In the case of SPMSM, L_d is equal to L_q. These equations can also be written in terms of flux linkage as in (1-11) and (1-12).

$$V_{ds}^r = r_s\, i_{ds}^r + L_d \frac{d}{dt} i_{ds}^r - \omega_r L_q\, i_{qs}^r \quad (1\text{-}9)$$

$$V_{qs}^r = r_s\, i_{qs}^r + L_q \frac{d}{dt} i_{qs}^r + \omega_r L_d\, i_{ds}^r + \omega_r \lambda_{pm} \quad (1\text{-}10)$$

$$V_{ds}^r = r_s\, i_{ds}^r + \frac{d}{dt} \lambda_{ds}^r - \omega_r \lambda_{qs}^r \quad (1\text{-}11)$$

$$V_{qs}^r = r_s\, i_{qs}^r + \frac{d}{dt} \lambda_{qs}^r + \omega_r \lambda_{ds}^r \quad (1\text{-}12)$$

where: $\lambda_{ds}^r = L_d\, i_{ds}^r + \lambda_{pm}$ and $\lambda_{qs}^r = L_q\, i_{qs}^r$

The PMSM torque is given by (1-13) [57].

$$T_{em} = \frac{3}{4} p \left[\lambda_{pm}\, i_{qs}^r + (L_d - L_q)\, i_{ds}^r\, i_{qs}^r \right] \quad (1\text{-}13)$$

FW-IPMSM has a negative saliency ($L_d < L_q$), so a negative d axis current is required to weaken the flux during the high-speed, low load conditions. While FI-IPMSM has a positive saliency ($L_d > L_q$).

The authors in [37] -[39] , demonstrate that FI-IPMSM can be used in automotive applications to minimize the drive losses along the driving cycle. During the constant power region, there is no need to inject a large negative d-axis current to weaken the flux, copper losses can be minimized, and thermal limits of the machine is improved.

Fig. 1-23 shows the vector diagram for both FW-IPMSM and FI-IPMSM. From this diagram, it is shown that a significant reduction in the d axis current in constant power region (high speed and low torque) can be achieved, thus reducing the machine losses during the high-speed operation.

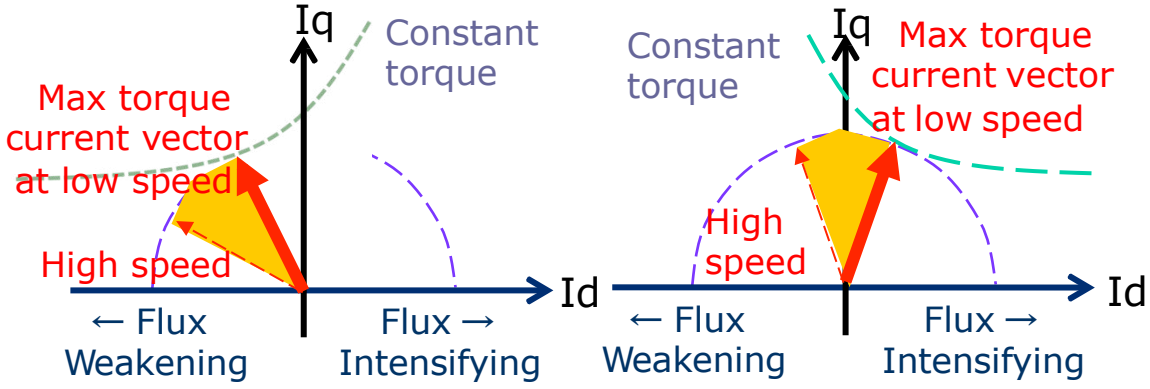

(a) FW-IPMSM (b) FI-IPM

Fig. 1-23 Vector diagram for: (a) FW-IPMSM, (b) FI-IPM [37]

The motor airgap torque and flux linkage can be controlled using several techniques. The main method is through controlling the motor currents in the synchrouns reference frame.

1.3.2 Current vector control

Current vector control (CVC) is commonly used for control of electrical machines. Stator terminal voltage is manipulated by adjusting the duty ratios of switches of a voltage source PWM inverter to achieve closed-loop control of current in the rotor reference frame by using measured phase current for feedback. The current vector is chosen to achieve the desired performance (torque and flux).

PI current regulators are commonly used for CVC. The current vectors can be represented by a complex number ($i_d^r + j\, i_q^r$), and the relation between the d-axis and q-axis voltages is cross-coupled as seen in (1-9) and (1-10). The complex vector current regulator (CVCR) was

developed in [58]. The CVCR (block diagram is shown in Fig.1-24) was shown to have better performance than classical PI regulators, with relatively low parameter sensitivity and requiring minimal additional computation. This is achieved by using a complex zero to cancel the motor complex pole. It has thus become an industry standard for servo drives.

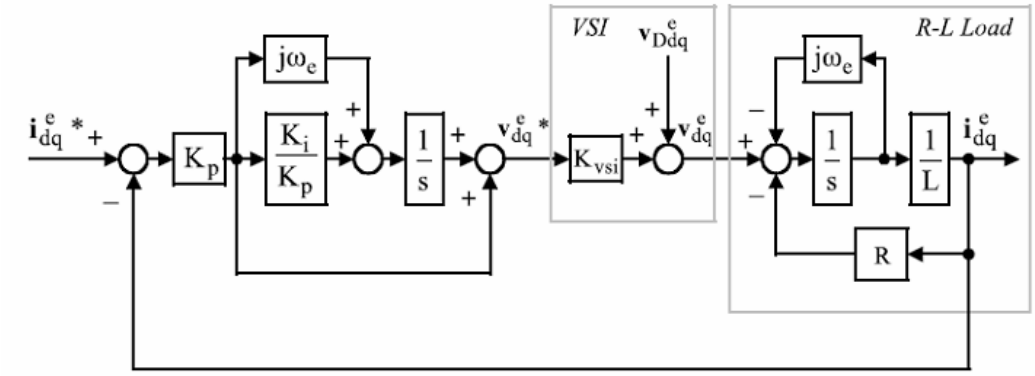

Fig.1-24 Complex vector current regulator assuming decoupled back-EMF [58]

This CVCR can also be implemented in the discrete time domain. However, this requires a high ratio of fundamental-to-sampling frequencies, otherwise, a direct conversion of the above CVCR algorithm in discrete time tends to become highly oscillatory or unstable. In [59], a discrete time current regulator design (direct-design CR) is proposed which accounts for the delays in the system between the sampling of the feedback signals and the application of the PWM command. This allows using CVCR for low switching frequency applications (low ratio of fundamental-to-sampling frequencies). The block diagram for this method is shown in Fig.1-25. In [59], the direct design CR showed excellent performance during a speed sweep, as well as step and sawtooth current command trajectories.

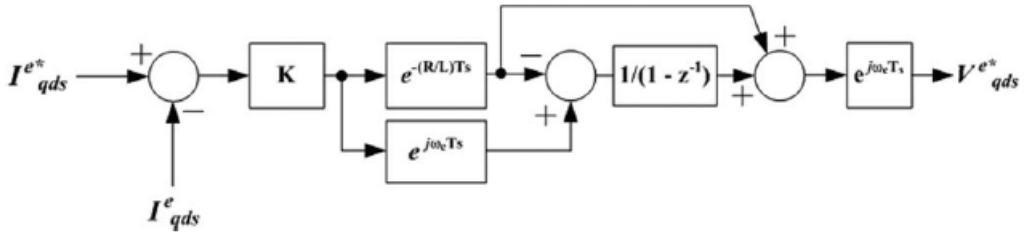

Fig.1-25 Complex vector current regulator assuming decoupled back-EMF [59]

The CVCR is a good technique to control the motor current and to indirectly control the motor airgap torque and stator flux linkage using (1-13), which makes the torque control accuracy using this controller sensitive to the estimated motor parameters. The dynamic performance of this controller depends on the tuned current regulator bandwidth which limits the dynamic performance of the servo motor. The torque and flux in this controller are cross-coupled, manipulating the motor flux dynamically will affect the torque dynamics of the motor. This limit using loss minimization techniques that are based on manipulating the flux linkage to minimize the motor for servo applications.

1.3.3 Deadbeat-direct torque and flux control (DB-DTFC)

Deadbeat control is a discrete time control method in which the inverse plant model is solved to achieve the desired output in one switching period, i.e. "Dead in one beat". Fig.1-26 shows the block diagram for Deadbeat control.

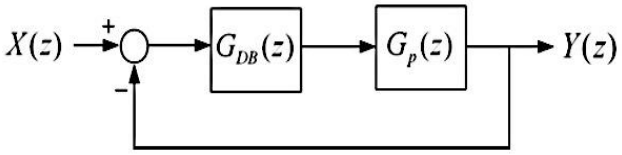

Fig.1-26 Deadbeat control block diagram

$$\frac{Y(z)}{X(z)} = \frac{G_p(z)^* G_{BB}(z)}{1 + G_p(z)^* G_{BB}(z)} = z^{-1} \quad (1\text{-}14)$$

Deadbeat-direct torque and flux control (DB-DTFC), as developed and evaluated in [60][67], is a control strategy in which the machine torque and flux are control state variables and the inverter applied volt-second vector is the manipulated input. The controller is derived from the inverse system model. The DB-DTFC law for the PMSMs, under the high switching frequency approximation, is shown in (1-15) through (1-18). The block diagram for DB-DTFC for PMSMs is shown in Fig.1-28, where the current and flux observers are key components required for proper implementation of DB-DTFC since it requires one-step advanced information to take into account the PWM delay. Discrete-time domain flux and current observers are shown in Fig.1-27.

$$\Delta T_{em}[k] = T_{em}[k+1] - T_{em}[k] \quad (1\text{-}15)$$

$$v_{qs}^{r} T_s = M\, v_{ds}^{r} T_s + B \quad (1\text{-}16)$$

$$M = \left(\frac{(L_q - L_d)\, \lambda_{qs}^{r}[k]}{(L_q - L_d)\, \lambda_{ds}^{r}[k] + L_q\, \lambda_{pm}} \right) \quad (1\text{-}17)$$

$$B = \left(\frac{L_d L_q}{(L_q - L_d)\, \lambda_{ds}^{r}[k] + L_q\, \lambda_{pm}} \right) x$$

$$\left[\left(\frac{4\,\Delta T_{em}}{3P} - \frac{\omega_r T_s}{L_d L_q} \left((L_q - L_d)\, (\lambda_{ds}^{r\,2} - \lambda_{ds}^{r\,2}) - L_q\, \lambda_{ds}^{r}\, \lambda_{pm} \right) - \right. \quad (1\text{-}18)$$

$$\left. \frac{r_s T_d\, \lambda_{qs}^{r}[k]}{L_d^2 L_q^2} \left((L_d^2 - L_q^2)\, \lambda_{ds}^{r} - L_q^2\, \lambda_{pm} \right) \right]$$

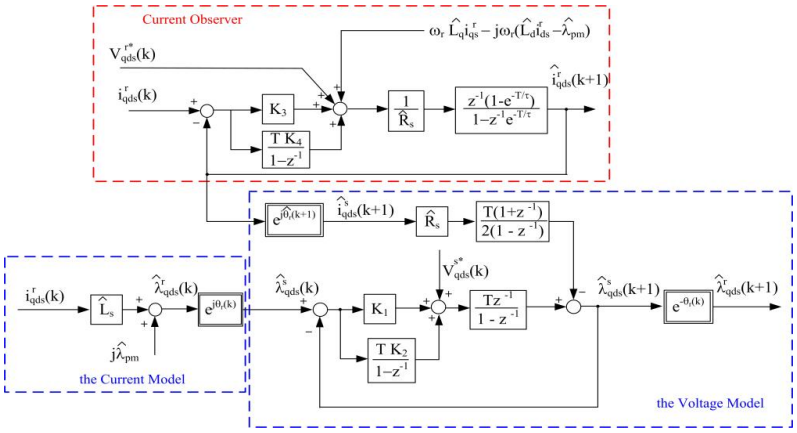

Fig.1-27 State block diagrams of discrete time current and flux observers systems for PMSMs [68]

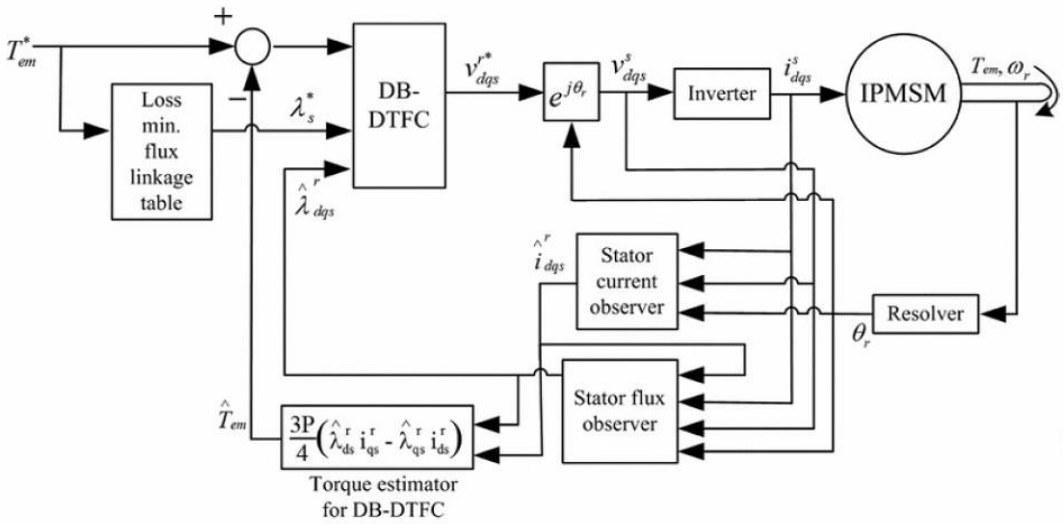

Fig.1-28 Block diagram of DB-DTFC control for IPMSMs [67]

DB-DTFC has significant advantages because it is an inverse model solution as listed below:

- This control law has the best dynamic performance in which the command tracking, and disturbance rejection can be achieved in one sample period and not limited by the current loop bandwidth like in CVCR. This dynamic response is very useful with servo drive that requires a high dynamic performance.

- A single control law works seamlessly across the complete torque-speed operation range of the electrical machine and utilizes the entire inverter capability.
- DB-DTFC provides direct and independent control of torque and stator flux linkage. Thus, while the required torque can be achieved, the stator flux linkage provides a controlled degree of freedom to manipulate the losses in the machine as well as the inverter. For example, in Fig.1-29, all the blue vectors represent the volt-sec solutions that will deliver the required torque. However, each of the voltage vectors will induce a different stator flux linkage. The stator flux linkage can be then chosen to suitably manipulate the losses.

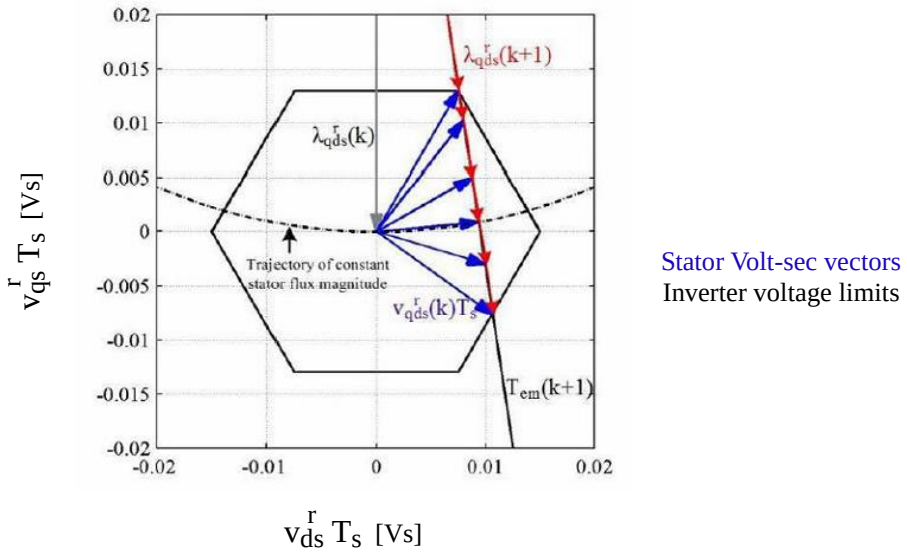

Fig.1-29 Graphical representation of DB-DTFC voltage solution for IPMSMs[67]

- A high-frequency flux linkage can be injected into the motor with zero torque ripple without affecting the dynamic performance of the drive. This allows using this feature for parameter estimation as in [69] or for injection based self-sensing control as in [70] and [71] .

1.3.4 Control techniques for loss minimization

This section will briefly review the main loss minimizing techniques for PMSMs found in the literature. First, the PMSMs losses will be investigated, then the main loss minimizing techniques will be discussed, limitations of these techniques when they used in servo applications will be highlighted.

1.3.4.1 Permanant magnet machine losses

Losses in PM machines can be classified into 2 main categories: copper loss, which occurs in the stator winding, and core loss which occur in the core. The following subsections will provide a brief introduction to these losses.

Copper losses in the stator winding

When the current is flowing in the stator conductors with finite resistance, it will dissipate power, which increases the temperature of the winding. (1-19) shows the relationship between the losses with the stator current.

$$P_{cu\text{-}loss} = R\, i(t)^2 \qquad (1\text{-}19)$$

Copper losses are normally called winding losses. Additional considerations must be considered to calculate the winding losses in the machine such as resistance temperature dependency, skin effect, and proximity effect.

The winding resistance is variable with temperature; (1-20) can be used to estimate the resistance at different temperatures.

$$R(T) = R(T_o)\,[\,1+\alpha_o\,(T-T_o)\,] \qquad (1\text{-}20)$$

where T is the temperature, T_o is the temperature at 20^oC, α_o is the linear temperature coefficient. From this equation, increasing the temperature will increase the copper resistance and more losses will appear in the machine.

Skin effect also increases the AC resistance of the stator winding, in which the AC current doesn't homogeneously distribute in the stator coils, and the current density near the conductor surface is higher than at the center of the conductor. Increasing the frequency of the current reduces the penetration depth of the current in the conductor and the effective resistance increases.

Proximity effect occurs due to the interaction between the induced magnetic field in each conductor with the rest of the conductors, which will cause a non-homogeneous distribution of the current in the stator coils. This phenomenon depends on the frequency of the current, in which the resistance will increase with increasing frequency.

Calculating the exact current distribution requires detailed information about the conductor geometry, insulation thickness, and position of serial and parallel conductors as well as the phase shift between them.

Core losses (iron loss)

Core losses in the PM machine occur in steel laminations and permanent magnets. These losses can be divided into two main groups, Hysteresis and eddy current losses.

Hysteresis Loss:

The magnetic core of the machine is made of ferromagnetic material like steel, or composite material. Ferromagnetic materials are used to enhance the magnetic flux in the airgap by providing a low reluctance path to the field in the working airgap.

From the microscopic perspective, the magnetic material consists of a huge number of small regions (magnetic domain), which are intrinsically magnetized, and each region stores a specific amount of energy. Without applying any external field, the magnetization direction is randomly distributed, which results in zero magnetized material. Adding external field realigns the domains to have magnetized material. This process is shown in Fig.1-30.

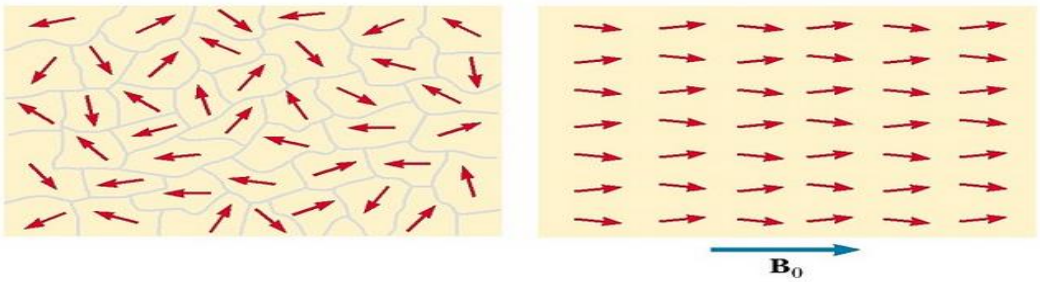

(a) no field – unmagnetized material (b) with applying field – magnetized material

Fig.1-30 Magnetic domain in ferromagnetic material [72]

Higher magnetizing field aligns more domains. The permeability of the material will reach the value of air when the entire domains are aligned (reach the saturation). Even after removing the external field, most of the domains keep their orientation and the resulting flux density is called remanence, (Br). Opposing external field strength has to be used in order to demagnetize the material. This field is called coercive field strength (Hc). Fig.1-31 shows the characteristic hysteresis loop of flux density versus magnetic field strength for a full cycle of sinusoidal excitation and maximum flux density Bm [72] .

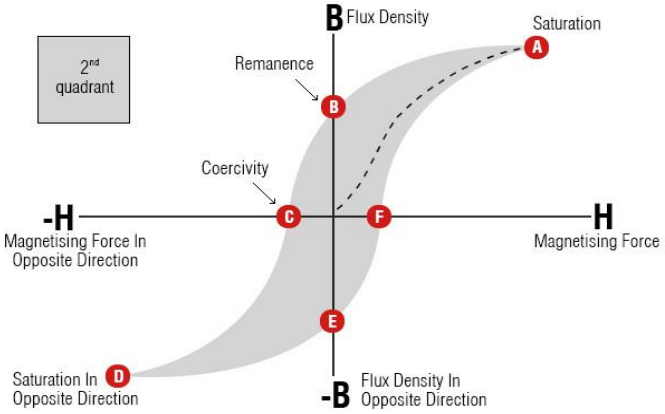

Fig.1-31 Hysteresis loop for soft magmatic material [72]

Hysteresis losses are defined by the energy lost due to the movement of magnetic domains during the magnetization/demagnetization process and the area of the hysteresis loop determines the amount of energy lost during one cycle.

Eddy Current Losses:

Eddy current can be defined as the induced circulating current in the conductive material due to the variable magnetic field. These currents can cause significant thermal losses in electrical machines, especially for high frequency. This phenomenon occurs on steel and conductive permanent magnets.

Faraday's law of induction explains the origin of eddy currents. A positive time derivative in flux density causes a negative induced voltage in the material. The electrical conductivity of the material determines the magnitude of eddy currents and the resulting power loss. Eddy currents also affect the distribution of the magnetic field, especially at high frequency.

Eddy currents circulate in an orthogonal plane to the varying flux vector. Thin laminations for both the stator and rotor instead of solid material can minimize these currents

(minimizing circulating current path minimizing the eddy current losses). Fig.1-32 shows the effect of laminations.

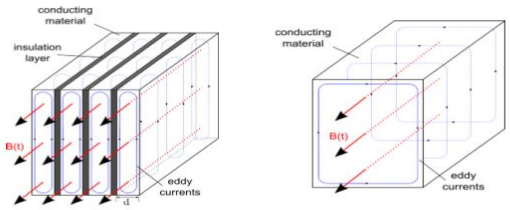

(a) laminated core (b) solid core

Fig.1-32 Eddy currents path in solid and laminated materials

1.3.4.2 Loss minimization techniques

Loss minimization techniques for electrical machines have been investigated for over 30 years. Fig.1-33 shows a diagram of different loss minimization techniques.

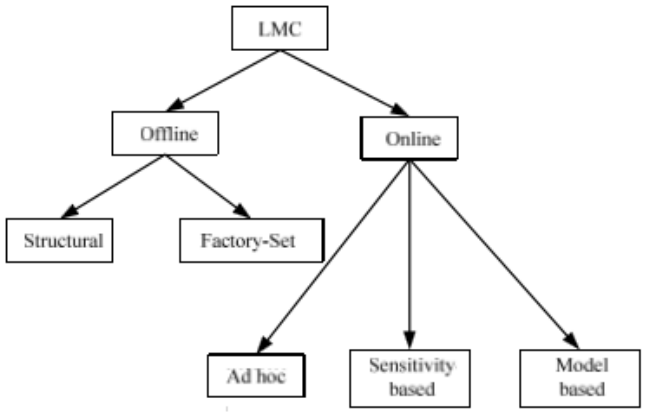

Fig.1-33 Categories of loss minimization techniques [73]

Offline techniques try to minimize losses by restricting the operating point of the machine to its optimum point based on pre-determined conditions [74]. Offline techniques cannot be used to minimize the loss dynamically (while the machine is running).

Online techniques are used to minimize the power loss while the motor is running. They usually utilize feedback information, motor parameters and models of losses, or both.

Online loss minimization methods can be divided into 3 main categories: ad hoc search methods, sensitivity function-based search methods, and model-based method. The appropriate method is selected based on the application in terms of the convergence speed, parameter sensitivity, and convergence error.

Ad-hoc Search Method

In Ad-hoc search methods, the controller is designed to minimize the input power to the system or to minimize the loss. This method does not depend on the motor model or parameter.

In [75] the author used this method to minimize the loss in an IPMSM, in which he perturbed the d axis current and used it as a control variable to minimize the DC input power to the system. The d axis is adaptively changed to minimize the dc input power; this method is called adaptive loss minimization control. Fig.1-33 shows the block diagram of this method.

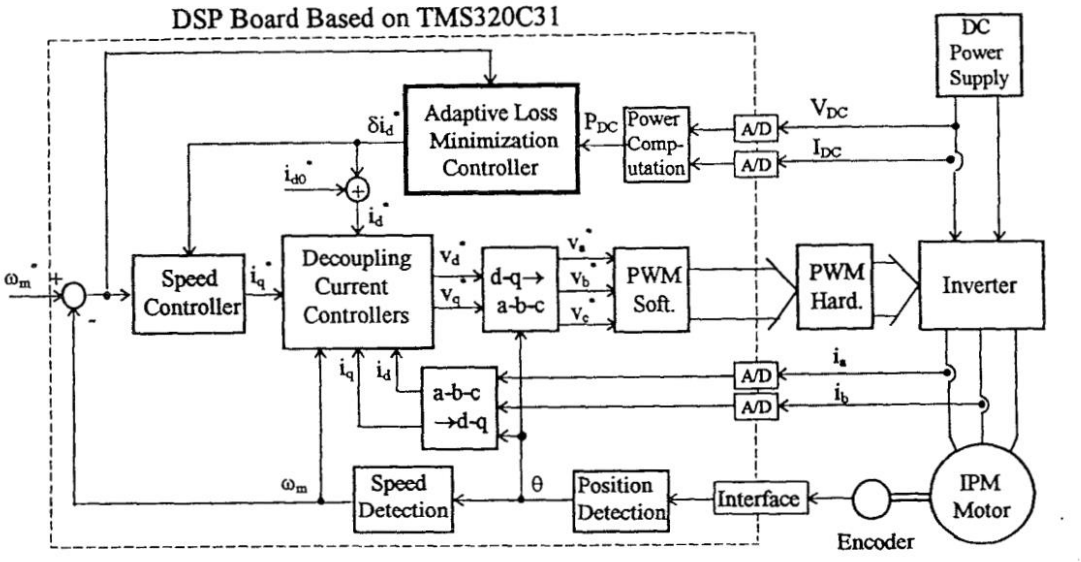

Fig.1-34 Adaptive loss minimization control for IPMSM [75]

The main advantage of the ad hoc search method is that it is independent of motor model or parameter, but it requires steady state loss or input power to evaluate and update the control.

Thus, this method has slow convergence speed and it is not suitable for servos that have fast dynamic torque commands.

Sensitivity Function based Search Methods

Sensitivity function-based search methods have features of both model-based and ad-hoc methods. This method is used in modern control techniques, like fuzzy logic and neural network-based loss minimization controllers. In [76], the author uses fuzzy logic control to set the optimum d-axis stator current, which in turn, minimizes the input power. Membership functions are built based on the estimate of the sensitivity function ($\Delta P_{in}/ \Delta i_{ds}$). This determines the relationship between varying the d-axis current (i_{ds}) and the resulting input power (P_{in}). The d-axis current command is selected based on this relationship to minimize the input power.

Model-based Method

The model-based method depends on the motor parameter and the specific power loss equation [74]. The dependency on the motor parameter leads to deviation from the optimal operating point under parameter variations. However, it is the best method among the three methods for dynamic loss minimization.

Typically, in CVC, the dq- current references are calculated based on a maximum torque per ampere (MTPA), maximum torque per volt (MTPV), or loss minimizing control (LMC) schemes in order to reduce steady-state losses. MTPA is commonly used for operation below base speed where the copper losses dominate the total motor loss and a sufficient voltage is available. MTPA minimizes copper losses. The MTPA trajectory may be calculated using the torque equation and minimizing the current for a fixed torque as shown in [78]. However, due to

the saturation characteristics, it may be necessary to use lookup tables (LUTs) or curve fitting based on experimentally obtained torque maps.

Beyond the base speed, it is not possible to operate along the MTPA trajectory because the required voltage for CVC exceeds the inverter voltage limits. In this operating region, the control scheme is switched to MTPV control to utilize the available voltage limit and source sufficient current to deliver the required torque. The MTPV trajectory minimizes the iron-losses. MTPV trajectory may be calculated analytically as discussed in [78]. However, it is sensitive to parameter estimation errors, and it may be necessary to use LUTs based on experimentally obtained torque maps. The MTPA and MTPV trajectories for an IPMSM are shown in Fig.1-35.

Since MTPA and MTPV may also require LUTs to account for parameter variations due to saturation, it is often better to obtain loss maps in the entire torque-speed operation conditions and prepare a loss-minimizing current command LUT. Such a control strategy is potentially more accurate and is expected to perform better in terms of steady-state loss-minimization over the entire operation capability of the machine drive system. However, the drawback of this method is the time required to experimentally obtain the loss maps required to form the LUT.

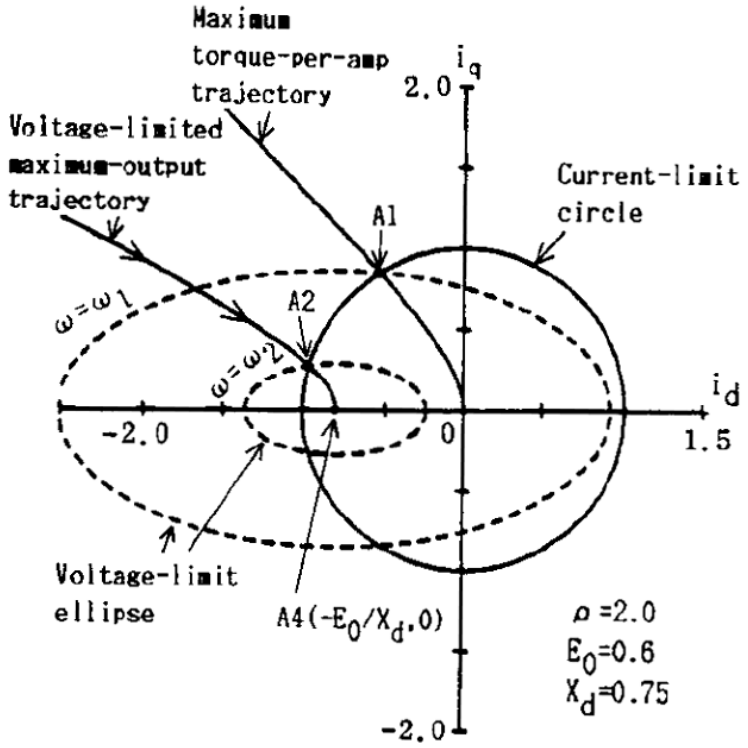

Fig.1-35 MTPA and MTPV trajectories for an IPMSM with theoretical infinite speed capability [78]

The authors of [75] proposed selecting the optimum operating point based on a loss model that models both copper and iron loss to minimize the total motor loss in the IPMSM. Only steady-state losses are considered.

Manipulating the dq current command dynamically using CVC will impact the torque dynamics of the drive due to the cross-coupling between torque and flux and due to the limited current requlator bandwidth. For this reason, this method is not commonly adopted with servo drives.

Flux linkage based dynamic loss mimizing DB-DTFC control for IPMSM

In [67], Wei Xu proposed a dynamic loss model for an IPMSM. The proposed loss model was used to estimate the total machine loss as a function of the inverter volt-sec vectors (flux linkage) at the switching period level, which is suitable for DB-DTFC controller. The proposed

loss model was derived through mapping magnetic B-H loss properties to the controllable state characteristics, λ-I, using FEA simulation. In the simulation, the eddy current loss related term (the square of the derivative of flux density) is integrated over the entire machine space. Then, this term is compared with square of the derivative of flux linkage in the stationary reference frame at time steps consistent with the inverter switching frequency. The B-H hysteresis term, i.e. the hysteresis loop area over one fundamental cycle, is compared with λ-I hysteresis loop area under constant torque and speed operation with and without high-frequency minor loops. The conducted FEA simulation results show that the λ-I relationship can be utilized in place of the magnetic B-H relationship to accurately represent the iron loss in the machine. For real-time control purposes, Xu used an approximate real-time model to calculate the hysteresis loop area (approximate the hysteresis loop by elliptic shape) using the Volt-sec vector at the switching period level.

Xu includes copper loss, hysteresis loss, and eddy current loss in the proposed dynamic loss model. He evaluated this dynamic loss model for dynamic loss minimization through adopting DB-DTFC. Online dynamic loss minimizing DB-DTFC was implemented and experimentally evaluated for 10 kHz switching frequency using a golden-section search algorithm. Fig.1-36 summarizes the process.

From the experimental results, Xu demonstrated the ability of his model to reduce losses in real-time. Fig.1-37 compares the amount of energy saving for sinusoidal load torque with different frequencies for different loss models. With that, Xu proves that dynamic loss minimization with DB-DTFC can save energy for high-frequency dynamic loads.

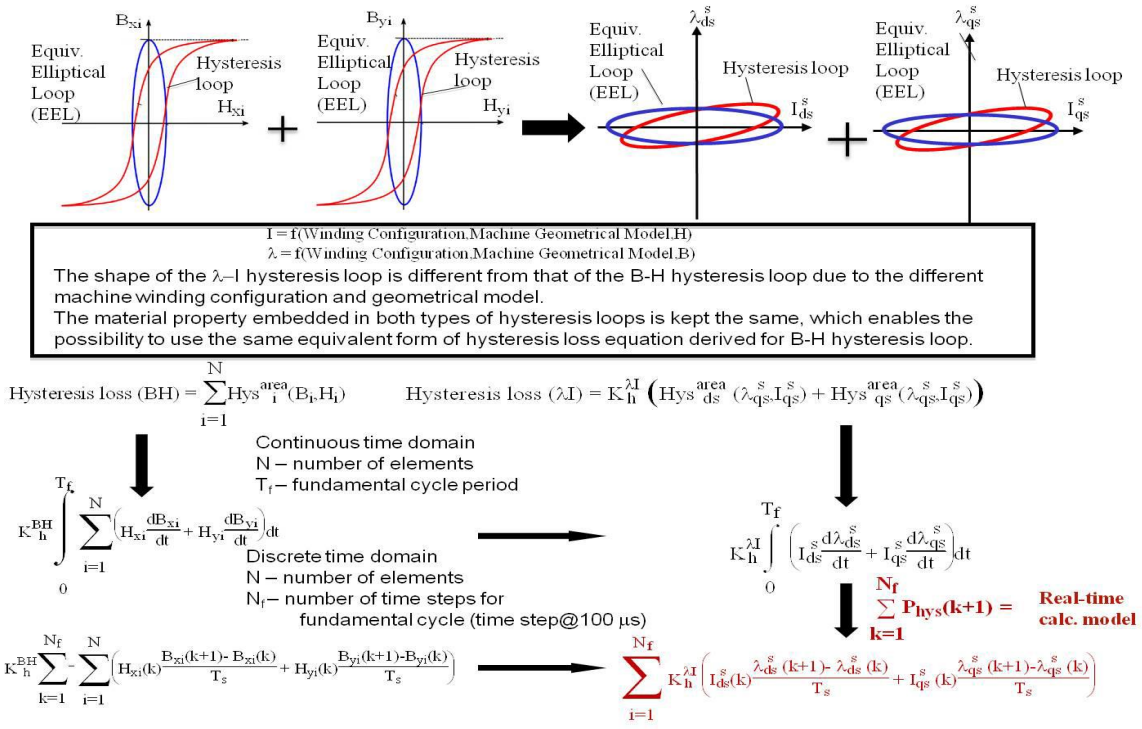

I = f(Winding Configuration,Machine Geometrical Model,H)
λ = f(Winding Configuration,Machine Geometrical Model,B)

The shape of the λ–I hysteresis loop is different from that of the B-H hysteresis loop due to the different machine winding configuration and geometrical model.
The material property embedded in both types of hysteresis loops is kept the same, which enables the possibility to use the same equivalent form of hysteresis loss equation derived for B-H hysteresis loop.

Fig.1-36 Dynamic loss model for IPMSM [67]

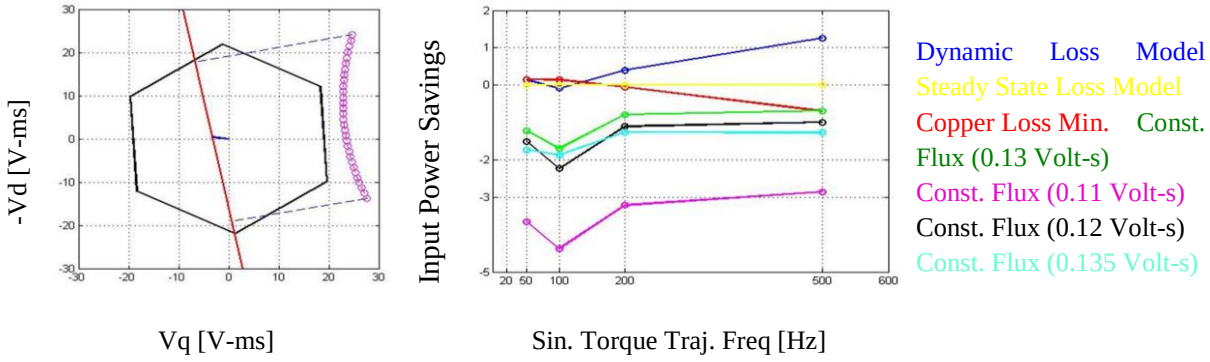

Fig.1-37 Energy saving using various loss minimization methods[67]

The proposed loss model requires an intensive computational effort inside the DSP. To overcome that, Xu activated the proposed algorithm when a step torque is commanded to the motor. The proposed solution was limited to the case of a motor running below the base speed, not at the voltage limit. In order to use this kind of algorithm with servo motors, a simpler loss

model is required, which allows running the algorithm every switching period, not only when a step torque is commanded. The algorithm needs to operate during the high-speed operation when the motor runs at the voltage limit during flux weakening operation.

Table 1-6 shows a comparison among physics-based method, model-based method, and the dynamic loss minimization control method, with respect to three different factors.

Table 1-6 Comparison among physics-based method, model-based method and dynamic loss minimization control method [67]

	Pre-calculation effort	Real time convergence	Loss minimization capability
Physics-based	Short	Long	Slow steady state
Model - based	Short	Short	Steady state solution
Dynamic loss	long	short	Dynamic &steady state solution

1.3.5 Self-sensing control techniques for PM motors

Self-sensing techniques provide a handy way to control the motor without any external position sensor by using the motor itself as a sensor. This will improve the reliability of the drive, decrease its cost and will decrease the physical size of the system. Self-sensing techniques are mainly divided into two categories, tracking the back-EMF voltage of the motor at medium and high speed, or injecting a high-frequency signal and tracking the motor saliency at zero and low speed.

1.3.5.1 Back EMF tracking

Back-EMF self-sensing technique can be used in any kind of electromagnetic machines. This method is based on estimating the rotor speed and position from the measured or estimated back-EMF voltage. This technique is suitable for medium and high-speed operations, but at zero and low-speed operation the back-EMF voltage becomes very small. This leads to a decrease in

the signal to noise ratio of the back-EMF signal which occurs due to inverter nonlinearities and dead-time effects [79].

The back-EMF signal can be estimated using a back-EMF state filter. This filter has a similar structure to a current observer in a stationary reference frame [80][81]. Fig.1-38 shows the block diagram of the back-EMF state filter for PM machines. This filter can estimate the back-EMF signal within its bandwidth.

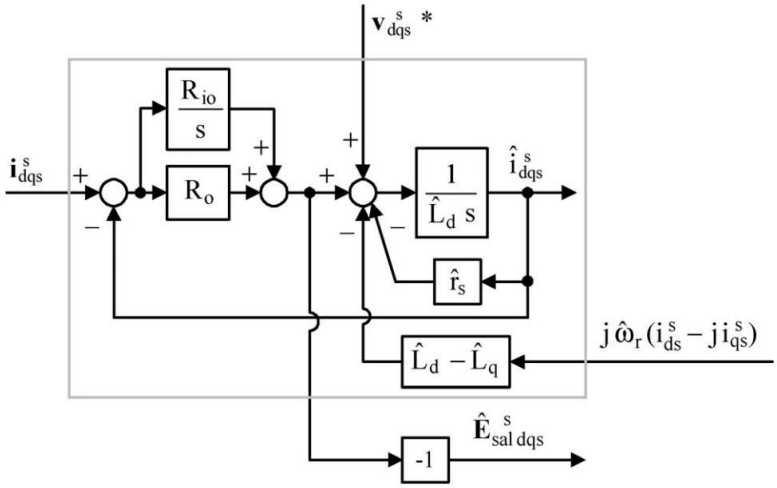

Fig.1-38 Back-EMF state filter for PM machines [81]

Different methods can be used to estimate the rotor position and speed from the back-EMF signal, like arctan method as in [82]. The estimated position and speed using this method will be noisy. The authors of [83] propose using a cascaded filter with the arctan method to filter out the noise. This will affect the dynamic performance of this method. A Luenberger style observer can be used to extract the position and speed from the estimated back EMF signal [81]. Fig.1-39 shows the block diagram of the position observer.

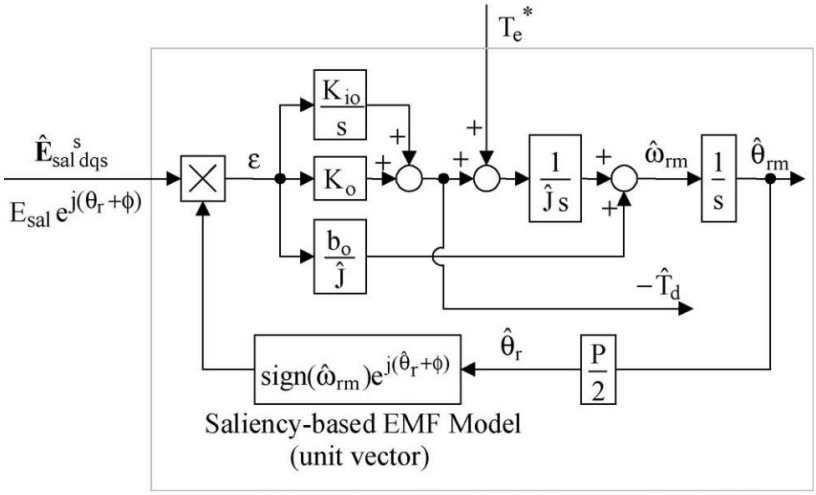

Fig.1-39 Luenberger style saliency-based EMF observer [81]

The back-EMF method is very effective for the medium and high-speed operation, but at low-speed operation, the signal-to-noise-ratio drops down due to the volt-sec error between the commanded and actual inverter volt-sec. In [84], a volt-sec sensor was used to measure the actual inverter output. This improves the back-EMF self-sensing performance in induction machine drives, allowing running the motor at very low speed.

1.3.5.2 Injection based self-sensing control

Back-EMF self-sensing cannot be used at zero and low speed. To be able to fully control the motor in the self-sensing mode without the need for a position sensor, injection-based techniques were developed. These techniques are based on tracking the motor saliency which varies as a function of the rotor position. This requires a salient motor like IPMSM or a special designed SPMSM.

To estimate the rotor position from the motor saliency, a high-frequency signal (voltage or current) is injected into the machine. From the measured signals (current or voltage) a position can be extracted using a Luenberger style saliency tracking observer, or a state filter.

Different injection techniques were reported in the literature. In this section, rotating vector injection method, pulsating vector injection method, and flux injection-based method will be discussed.

Rotating vector injection

Injecting a balanced rotating vector is one of the simplest ways to extract the rotor position. In this method AC signal is injected into the stationary reference frame, to form a rotating vector in the motor rotor reference frame. Either a voltage or current signal can be injected to estimate the position. It is common to inject a rotating voltage vector with voltage source inverters and estimate the rotor position and speed from the measured current. Voltage signal injection is used due to the availability of current sensors in industrial drives. Injecting a rotating vector is used to extract the motor saliency image. This type of injection will cause an extra torque ripple in the drive.

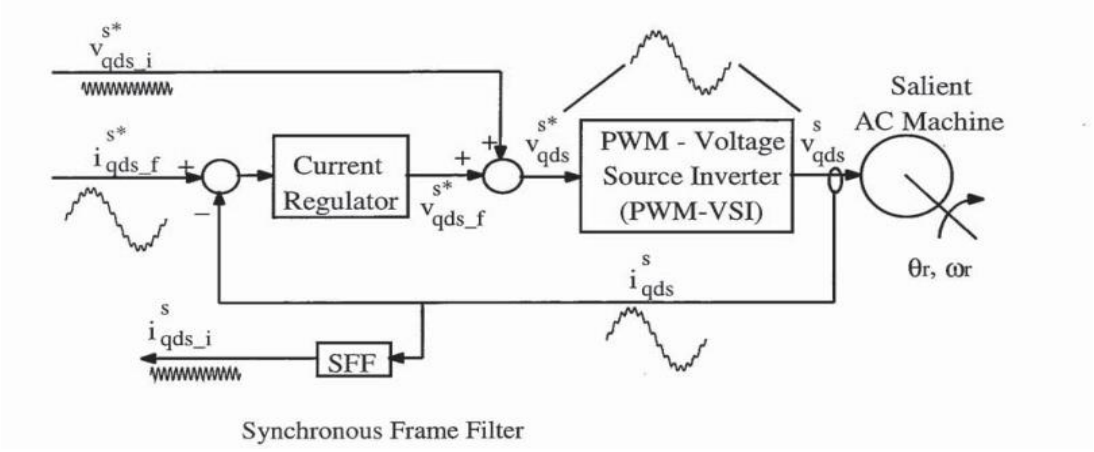

Fig.1-40 Rotating vector injection-based self-sensing [85]

The negative sequence component of the carrier current vector is modulated with the second harmonic of the rotor position. The position can be estimated from this current using:

direct calculation as in [87][88], magnitude peak detection as in [86], through using phase locked loop (PLL) state filter as in [88], or using tracking observers [89].

Pulsating vector injection

Another injection technique is injecting the high-frequency signal to the estimated synchronous frame typically to the d axis. This will cause lower ripple torque compared to the rotating vector case. The error between the estimated and actual reference frame can be extracted from the modulated high-frequency current. Fig.1-41 illustrates the injection process in the estimated d axis[90].

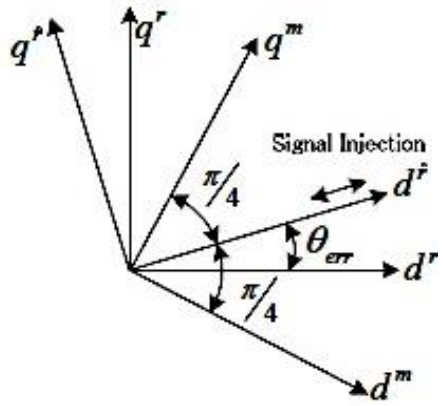

Fig.1-41 Pulsating vector injection into the estimates d axis [90]

The injected high-frequency voltage in the actual reference frame with ignoring the voltage drop across the winding resistance can be written as (1-21), the injected voltage in the estimated frame is given in (1-22). Using the transformation matrix to transform the injected voltage from the estimated frame to the actual reference frame to obtain (1-23).

$$\begin{bmatrix} V^{r}_{d\text{-}hf} \\ V^{r}_{q\text{-}hf} \end{bmatrix} = \begin{bmatrix} L_d & 0 \\ 0 & L_q \end{bmatrix} \frac{d}{dt} \begin{bmatrix} i^{r}_{d\text{-}hf} \\ i^{r}_{q\text{-}hf} \end{bmatrix} \quad (1\text{-}21)$$

$$\begin{bmatrix} \hat{V}^{r}_{d\text{-}hf} \\ \hat{V}^{r}_{q\text{-}hf} \end{bmatrix} = V_c \begin{bmatrix} \cos \omega_c t \\ 0 \end{bmatrix} \quad (1\text{-}22)$$

$$\begin{bmatrix} V^{r}_{d\text{-}hf} \\ V^{r}_{q\text{-}hf} \end{bmatrix} = T^{-1}_{\theta_r} \begin{bmatrix} \hat{V}^{r}_{d\text{-}hf} \\ \hat{V}^{r}_{q\text{-}hf} \end{bmatrix} = V_c * \begin{bmatrix} \cos \theta_{err} & \cos \omega_c t \\ -\sin \theta_{err} & \cos \omega_c t \end{bmatrix} \quad (1\text{-}23)$$

Comparing (1-21) and(1-23), the measured high-frequency current in the estimated rotor reference frame can be written as in (1-24).

$$\begin{bmatrix} \hat{i}^{r}_{d\text{-}hf} \\ \hat{i}^{r}_{q\text{-}hf} \end{bmatrix} = \frac{1}{2 L_d L_q} * \begin{bmatrix} \Sigma L + \Delta L \cos(2\theta_{err}) & -\Delta L \sin(2\theta_{err}) \\ -\Delta L \sin(2\theta_{err}) & \Sigma L - \Delta L \cos(2\theta_{err}) \end{bmatrix} * V_c \begin{bmatrix} \cos \omega_c t \\ 0 \end{bmatrix} \quad (1\text{-}24)$$

The high-frequency current component in the q-axis contains the spatial information (θ_{err}) as in **Error! Reference source not found.**. A heterodyning demodulation process can be used to estimate the rotor position. Figure 1.28 shows the block diagram of the demodulation process [27].

$$\hat{i}^{r}_{q\text{-}hf} = -V_c * \frac{\Delta L}{2 L_d L_q \omega_c} \cos(\omega_c t) \sin(2\theta_{err}) \quad (1\text{-}25)$$

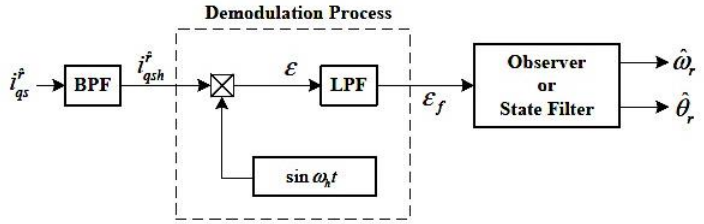

Fig.1-42 Demodulation process with d axis pulsating voltage injection [90]

Fig.1-43 shows the block diagram for self-sensing CVC for AC machines using pulsating injection method. Synchronous reference frame filter (SRFF) which is proposed in [89] is used with current observer is used to split the fundamental component current from the high-

frequency component without any phase distortion. SRFF is designed by rotating the signal to -ω_c and using high pass filter then rotate the signal again to $2\omega_c$ and use another high pass filter as shown in Fig.1-44. An enhanced Luenberger style tracking observer is used to estimate the rotor position and speed [8] .

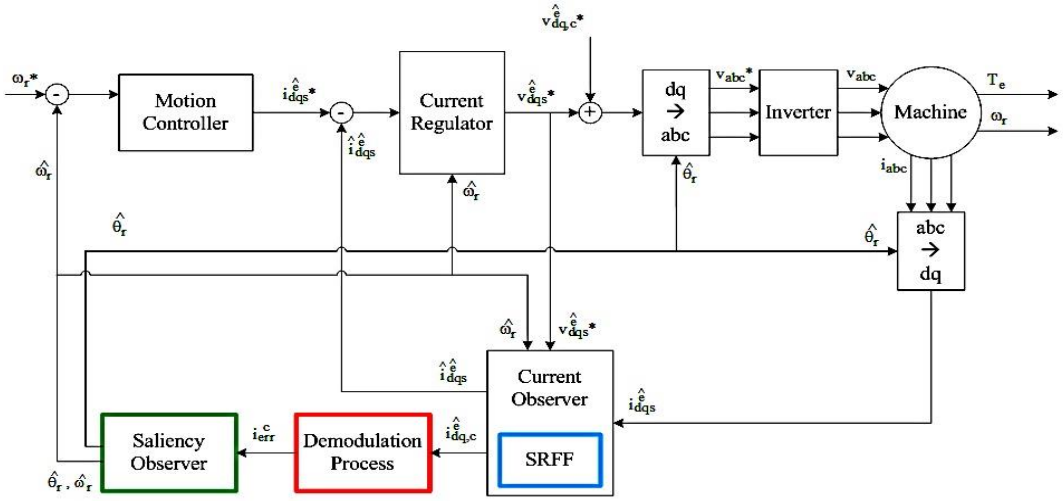

Fig.1-43 Block diagram of the close-loop self-sensing vector control for AC machine

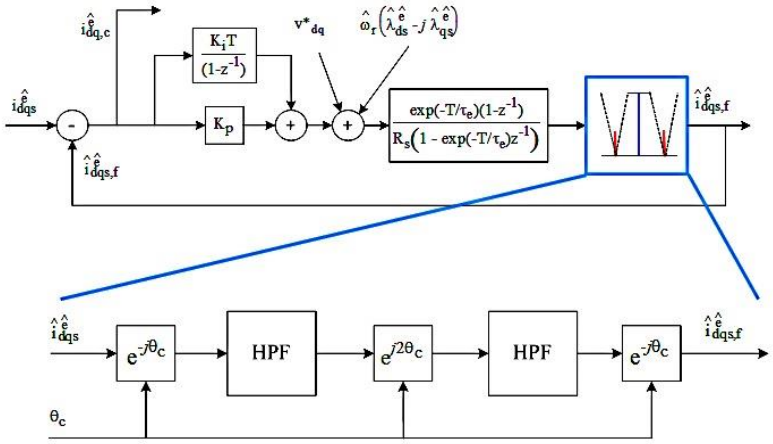

Fig.1-44 Current observer and SRFF to split the fundamental current component from the high frequency component

Many researchers implemented self-sensing through pulsating vector injection with CVCR. In [92] the authors implemented self-sensing through pulsating vector injection for

SPMSM and they proposed using a separate disturbance observer in order to improve the disturbance rejection performance. The block diagram of this observer is shown in figure 1.31.

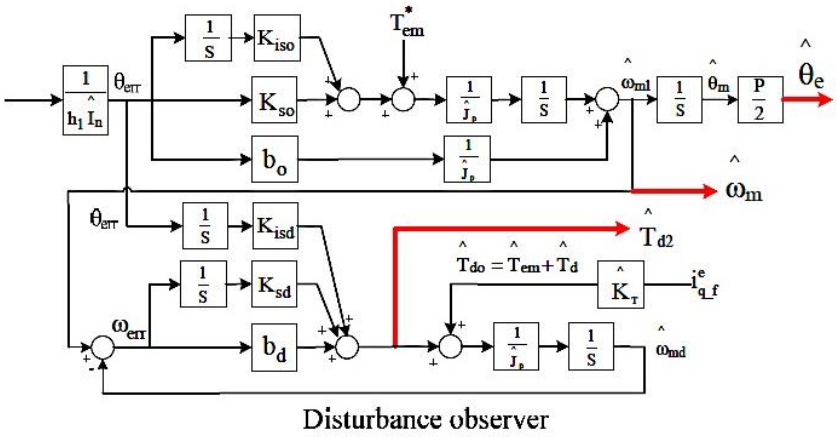

Fig.1-45 Block diagram of separate disturbance observer [92]

In [93] the authors discussed the effect of the injection axis, they proposed using d-axis injection at no load condition and control the d-axis current to be a non-zero value which will cause a slight torque ripple in the drive, under load conditions they proposed switching the injection to the q-axis and reducing the d-axis current back to zero which will reduce the effect of the inverter dead-time and will decrease the harmonics in the converter.

In [94] the authors proposed injecting a square wave pulsating signal with a zero average to the estimated d-axis frame. And they show that the measured current in the estimated q –axis frame contains the rotor position information.

Square wave injection with half of the switching frequency was proposed in [95]. The authors proposed using high-frequency ripple regulators to reduce the impact of inverter dead-time. However, this technique requires dual current sampling for every PWM cycle and requires an advanced DSP.

Wide speed range self-sensing control

Wide speed range self-sensing control requires combining both back-EMF tracking and injection-based self-sensing techiques together. Direct switching between these two algorithms lead to spikes in the estimated position and speed at the moment of switching. Thus, a smooth transition without any significant error in the estimated motor speed or position.

In [122], the authors proposed combining both saliency-based and back-EMF tracking through weighting function (G_w) with using a single phase-locked loop (PLL) to estimate the motor position and speed as in Fig.1-46.

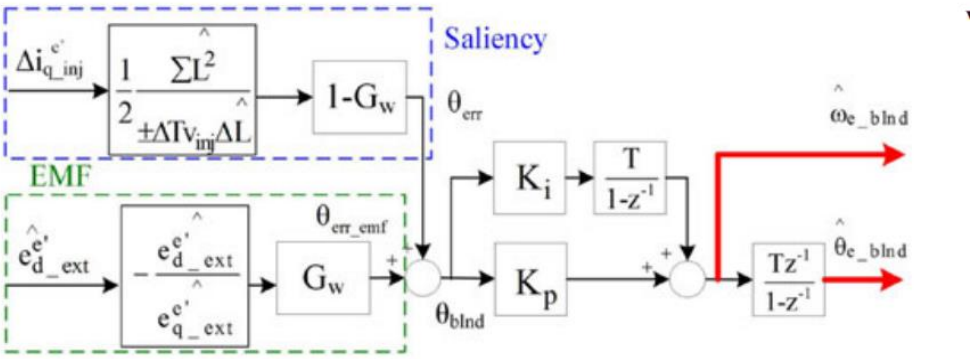

Fig.1-46 Single PLL combing the saliency-based and EMF-based position feedback signal[122]

The presented results in [122] show a smooth transition between the two self-sensing techniques with small position error when using an appropriate weighting function which depends on the speed trajectory. For servo applications, it is necessary to develop a similar technique that is not trajectory dependent. Forming a physics-based (model-based) solution would help in generalizing the method without the need to evaluate different weighting functions.

In summary, DB-DTFC has a superior dynamic performance compared to CVC, it is a great opportunity to evaluate using this controller in servo drives that require high dynamic performance. Dynamic loss minimization DB-DTFC algorithm demonstrated good performance, it is a great opportunity to adopt this technique to control servo motors with minimum losses without affecting the dynamic performance of the motor through selecting the optimum flux every switching period. The operation of this algorithm needs to be extended to operate at the voltage limit during flux weakening operation.

Injecting a rotating or pulsating signal will add some torque ripple to the drive. This limit using those algorithms in servo applications. The reported algorithms in the literature have a poor dynamic performance and work in steady -state speed or low acceleration rate condition. It is an opportunity to inject a high-frequency flux along the torque line with DB-DTFC. This allows extracting the spatial information from the measured current with zero torque ripple. The developed algorithm needs to have a sufficient estimation bandwidth, which allows using this algorithm in servo applications.

There is also an opportunity to develop a smooth transition technique to combine both injection-based and back-EMF techniques to run the motor completely using self-sensing control. This solution needs to be general and independent of the speed trajectory while achieving high dynamics performance.

1.4 Testing Dynomometers

Dynamometers are widely used in research labs to evaluate the torque, speed, and efficiency of electrical motors. A back-to-back configuration is one of the most commonly used dynamometer configurations. This configuration consists of two electric motors – one as a load

motor and the other as a tested motor – connected through shaft couplings and a torque sensor. Standard torque sensors measure the windup torque component. Those sensors do not correctly include the inertial torque component that exists during transient speed operation (this requires measuring the motor instantaneous acceleration and a pre-knowledge of the motor inertia). This limits the ability of the torque sensor to measure the dynamometer shaft torque during transient speed operation.

For certain classes of applications, such as servo motors, transient performance is a primary metric which is not easily measurable on traditional dynamometers. Furthermore, transient losses have a direct impact on their thermal limit. In all of these dynamometer setups, the inertia of the test and load motor is known or can be readily estimated.

To perform a direct measurement of dynamic torque during transient speed operation, the acceleration effect (inertial torque) needs to be considered [96]. Including the acceleration effect requires an angular acceleration sensor with adequate bandwidth, which is typically not used in dynamometers (the available angular acceleration sensors in the market have limited rotational angles and are typically not used with rotating shafts [97]). More details about the inertial torque that appears during the transient speed operation can be found in [99].

Many observers that model the dynamometer are found in the literature. In [99], the authors compared different techniques for controlling the resonant-load problem. One of these techniques was using a compliant body observer that models the tested motor load motor and the coupling between them. A similar observer was presented in [100] and [101]. Fig.1-47 shows the block diagram of compliantly coupled load [99], This model can be used to model the dynamometer test stand.

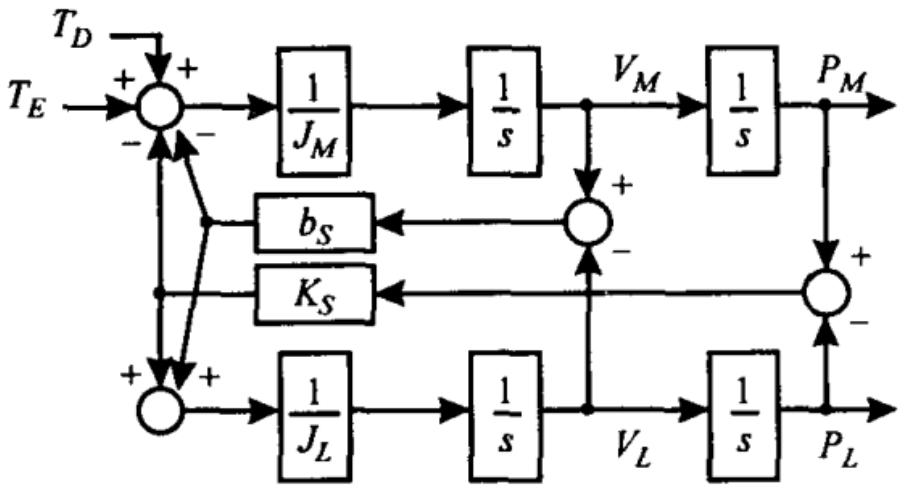

Fig.1-47 Block diagram of compliantly coupled load [99]

The authors of [102] also proposed similar observer that models the two motors and the coupling between them; this observer was used to estimate the speed of the load motor based on the tested motor. The authors of [103] proposed using a simplified inverse model for the two-mass system (or dynamometer) to suppress the residual vibration in the system.

In summary, many observers in the literature were used to resolve the resonant-load problem or to estimate the load motor position without using a position sensor on the load motor side. However, the opportunity of using a similar observer to estimate the dynamometer shaft torque accurately with high bandwidth during both steady state and transient speed operation including the acceleration effect, without using any extra sensor has not been reported. Developing this methodology will allow an accurate estimation of the servo cycle loss for the studied motors.

1.5 Research Opportunities Identified

The following research opportunities have been identified from the state-of-the-art:

- **Develop a Methodology to Design Servo Motors that are Suitable for Dynamic Loss Minimization**

  State-of-the-art servo motors are designed to achieve the desired cogging, peak, and ripple torque, without considering the dynamic loss behavior during servo applications. It is an opportunity to develop a methodology to design a servo motor that can combine the benefits of well-known servo motor types, has a better dynamic loss minimization performance for high-speed servo cycles, suitable for self-sensing control, and uses less active material (PM) while satisfying the servo requirements. This would improve the performance of the servo drive and reduce size and cost.

- **Develop a Methodology to Design a FW-SPMSM Servo Motor that is Suitable for Image Tracking Self-Sensing Control**

  FW-SPMSM servo motors achieve low copper loss by maximizing the airgap flux generated from the magnet achieving low losses for high-torque low-speed servo applications. State-of-the-art FW-SPMSM servo designs are not suitable for self-sensing control. These motors are typically designed to achieve a very low cogging and ripple torque without considering motor saliency. State-of-the-art techniques to improve the self-sensing performance of FW-SPMSM degrade the motor power conversion and cannot be used in servo applications. There is an opportunity to develop a methodology to design FW-SPMSMs for servo applications

with a non-degrading saliency enabling the motor to be controlled with saliency-based self-sensing technique even during overload operation and during motor acceleration, without sacrificing the peak torque capability of the motor, while achieving a very low cogging and ripple torque.

- **Develop a Methodology to Accurately Evaluate Motor Transient Loss**

Dynomometers are used to experimentally evaluate the performance of electrical motors. These dynamometers can be used to evaluate the steady-state loss and to measure the motor efficiency and loss maps but cannot be used to directly measure the motor transient losses. Dynamic performance is essential for servo motors. Measuring servo motor losses accurately during dynamic operation helps in understanding the thermal limits of the drive and would be helpful to fairly compare different servo motor designs. There is an opportunity to develop a methodology to use the same dynamometers and be able to evaluate the dynamic performance of the motor, including motor losses during duty cycle servo applications using only standard dynamometer sensors.

- **Develop a Methodology to Minimize the Total Motor Losses Dynamically without Affecting the Torque Dynamics of the Servo Drive**

The state-of-the-art loss minimization techniques with current regulation (CVCR) affects the torque dynamics of the drive. Since servo applications require high-dynamic performance, loss minimization algorithms are not typically used in servo drives. There is an opportunity to use the attractive feature of the independent control of the motor airgap torque and stator flux linkage of DB-DTFC to minimize the servo motor losses dynamically at the switching period level, without affecting the drive dynamics. This requires developing an algorithm that is suitable

for realtime application and can operate even at the voltage limit during flux weakening operation.

- **Develop a High-Dynamic Performance Self-Sensing Algorithm Applicable for Wide Speed Range Servo Applications**

The state-of-the-art injection-based self-sensing algorithms to control the motor at zero and low-speed operations are based on voltage and current injection. The high-frequency injection in these algorithms causes torque ripple in the drive, which limits using these algorithms in servo applications. The reported techniques have a good performance during steady-state or slow transients and cannot be used in high-performance servo drives. There is an opportunity to develop an injection-based self-sensing algorithm with zero torque ripple. This algorithm needs to achieve high dynamic performance to be used in some servo applications. Back-EMF self-sensing can be used at medium and high-speed operation. Controlling the servo motor using self-sensing techniques for a wide speed operation requires developing a methodology for a smooth transition between back-EMF tracking and saliency-based (injection-based) tracking self-sensing technique, allowing controlling the motor in wide speed operation without degrading the dynamic performance of the motor.

Chapter 2 PM Servo Motor Design Methodologies for Dynamic Loss Minimization

The main technical content of this chapter has been published in two technical papers in [123] and [124]. This chapter presents a fair comparison between the standard servo motor designs used in the literature, SPMSMs, and IPMSMs. A fair comparison is achieved by using the same stator, magnet, while achieving very low cogging and ripple torque, which is essential for servo motors. Followed by a new servo motor design is proposed, which is called FI-SPMSM. This design combines the benefits of the previous designs, uses less magnet material, and is suitable for self-sensing and dynamic loss minimization control by varying the motor stator flux linkage to minimize the total motor losses during dynamic cycle operations.

First, machine sizing equations which are based on Maxwell's equations were used to calculate the initial design dimensions for the SPMSM motor, then the final design dimensions were found by performing 2D-FEA using JMAG software. Then a flower shaped IPMSM motor is designed, this motor has same magnet and stator as the SPMSM. The IPMSM rotor is designed to achieve the servo motor requirements. Finally, a methodology to design FI-SPMSM motor is presented. The same stator is used as the SPMSM. This motor is designed using less magnetic materials.

Servo cycle methodology that can be used to systematically evaluate different servo motor designs for loss minimization capabilities presented. The dynamic loss minimization performance of the designed motors is expermently evaluated in this chapter including motor

loss portioning for several parts of the motor. Finally, the scalabilty analysis of the designed motors is presented.

2.1 Servo Applications, Requirments, and Structure

Servo motors require high dynamic performance. Different types of servo motors are able to serve this purpose. Permanent magnet synchronous motors (PMSMs) tend to have low inertia, high-power density, and efficiency, making them the most commonly used type of servo motors.

Different PMSM designs are used for servo applications, but the two main types are the surface PM (SPMSM) and the interior PM (IPMSM). Servo motor design is optimized to achieve very low levels of ripple and cogging torque. For these reasons, an IPMSM servo motor generally has low reluctance torque (low saliency ratio). The main advantage of an IPMSM configuration compared to an SPMSM is that there is no need to use a sleeve for high-speed operation.

To achieve the required servo performance, motor designers try to design servo motors with very low cogging and ripple torque. Ripple and cogging torque requirements for servo applications requirements were presented in the first chapter of this thesis, for convenience, it is repeated in Table 2-1. Due to the extra ripple and cogging torque that is caused by manufacturing process variations, the simulated ripple and cogging torque using FEA is set to be lower than the specified practical requirements in Table 2-1.

Table 2-1 Servo motor application requirements

Specifications	Practical requirement	FEA requirement
Cogging torque	< 1.5% rated torque	< 0.5% rated torque
Torque ripple	< 4% rated torque	< 2% rated torque

In general, servo applications can be categorized into two main groups: point-to-point servo cycles and continuous operational servo cycles. Example of those cycles is shown in Fig. 2-1. The difference between those two types of cycles was discussed in chapter 1. This thesis investigates the design methodologies for servo motors used in high-speed partial-torque continuous servo application with a 1-minute time span.

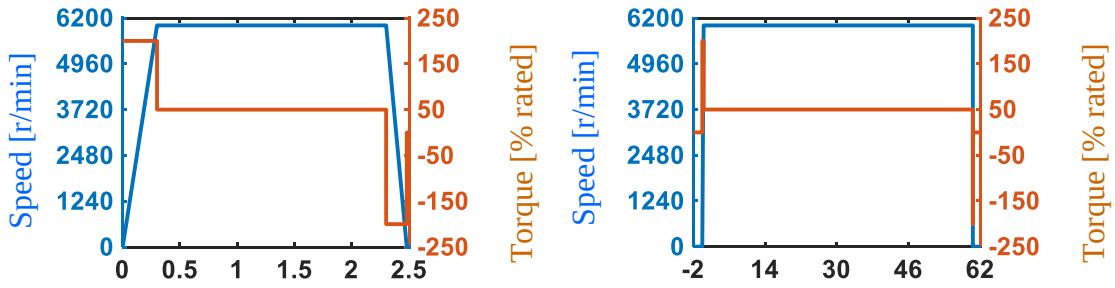

(a) point-to-point cycle (b) continuous operational cycle

Fig. 2-1 Examples of servo cycles: point-to-point cycle and continuous operational cycle

These cycles are generated so that the motor provides the rated mechanical power during the constant speed operation, while the acceleration rate is adjusted so that the motor torque during the acceleration/ deceleration period is limited to 2 pu rated torque.

2.2 Conventional Permanent Magnet Synchronous Servo Motor Design

2.2.1 SPMSM analytical design

In this section, machine sizing equations which are derived from Maxwell's equations are used to calculate the initial design dimensions for the SPMSM. These equations are found in

[104] and are briefly mentioned in this section. Fig. 2-2 shows a cross-sectional view of SPMSM motor with the main dimensions labeled.

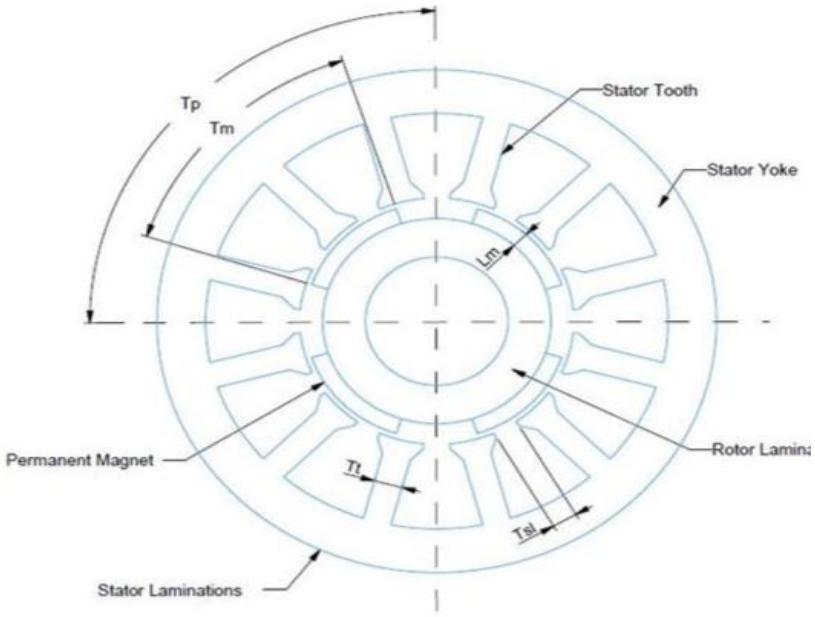

Fig. 2-2 Cross-sectional view that shows the main dimentions for SPM motor

SPMSM is size by the torque it has to develop and by its thermal capacity. Mechanical output power and torque are related as in (2-1).

$$P=T.\Omega \tag{2-1}$$

Maximum available electromagnetic power in the machine air-gap occurs when the phase current and the phase back EMF are in phase as in (2-2).

$$P = m.E.I \tag{2-2}$$

where: m = number of phases,
E = phase back EMF(V_{rms}),
I = phase current (A_{rms}),
T = airgap torque (Nm),
Ω = mechanical speed (rad/sec).

By assuming sinusoidal air-gap flux distribution, the induced back EMF voltage can be written as in equation (2-3).

$$E_{peak} = 2\,\pi f_e\, N_{ph}\, K_{w1}\, \phi_p \qquad (2\text{-}3)$$

Magnetic flux per pole can be found using equation (2-4).

$$\phi_p = \frac{2}{\pi} L\ B_g\, \tau_p \qquad (2\text{-}4)$$

where: f_e = fundamental frequency (Hz),
N_{ph} = effective number of turns in series,
K_{w1} = fundamental winding factor,
ϕ_p = magnetic flux per pole (Wb),
L = stack length (m),
B_g = peak flux density (tesla),
τ_p = pole pitch $=\pi \bullet D_i/p$ (m),
D_i = inner stator diameter (m),
p = number of poles,

The RMS value of the magnetic flux density ($B= \frac{B_g}{\sqrt{2}}$) is defined as the Magnetic Loading. Machine torque can be calculated by substituting the back-EMF voltage as in (2-3) into (2-1) to obtain (2-5).

$$T= \frac{P}{\Omega} = \frac{M\ p\ E\ I}{2\,\pi f_e} = m.\ K_{w1}.N_{ph}.B.\ D_i.L.I \qquad (2\text{-}5)$$

For surface magnets, the fundamental flux density in the air-gap can be calculated using the first harmonic approximation as in (2-6). Magnet length can then be calculated using (2-7).

$$B_g=\frac{4}{\pi} \bullet B_m \bullet \sin(\alpha) \qquad (2\text{-}6)$$

$$B_g = \frac{B_r}{1+\mu_r \frac{L_g}{L_m}} \qquad (2\text{-}7)$$

where: τ_m = the magnet pitch (m),

2α = magnet span (degree) corresponds to τ_m as shown in Fig. 2-3,

L_m/L_g = magnet / air-gap length (m)

μ_r = relative permeability of the magnet

B_r = remnant flux density (tesla)

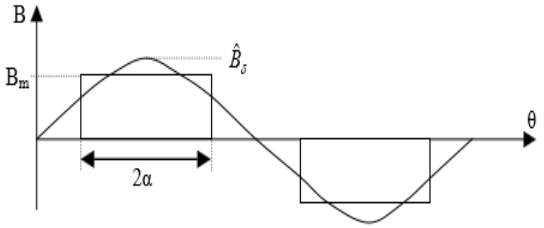

Fig. 2-3 Quasi-square wave and it is fundamental [104]

The above equations were used to obtain the initial design parameters for the baseline SPMSM motor. The airgap length is fixed to 0.4 mm (smallest feasible length). 12 slots and 10 poles configuration was selected to achieve high winding factor (0.966) and low cogging torque [105]. Bread-loaf magnet is used in this motor, this helps in achieving a very small cogging and ripple torque [106]. Table 2-2 summarizes the main characteristics and dimensions of the baseline motor.

Table 2-2 SPM baseline motor specifications

Spec.	Value	Spec.	Value
rated power	1HP	stator inner diameter	43 mm
rated Torque	2.387 N.m	airgap length	0.4 mm
rated speed	3000 RPM	stack length	45 mm
number of poles	10	Phase resistance	0.627 Ω
number of slots	12	calculated BEMF	108 V_{peak}
stator outer diameter	76.4 mm	rated current	3.29 A_{rms}

2.2.2 SPMSM design using 2D - FEA

Final design dimensions were calculated by performing FEA using JMAG 2D-FEA software. The design was optimized to fit the servo application requirements, which are shown in Table 2-1. Fig. 2-4 shows the cross-sectional view of this motor. Fig. 2-5-a shows the calculated back-EMF voltage for this machine using 2D-FEA. Fig. 2-5-b shows the cogging torque for this

machine which is calculated by spinning the motor at the rated speed without exciting the stator using 2D-FEA. The cogging torque is around 0.25% the rated torque. This low cogging torque is achieved by optimizing the magnet shape, reducing the back-EMF harmonics.

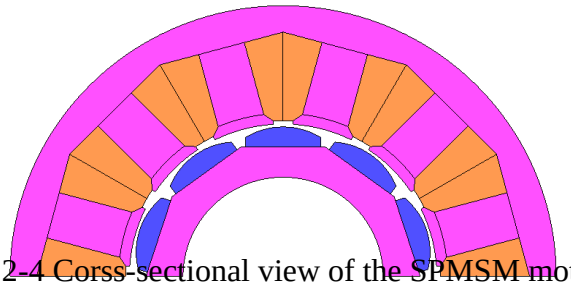

Fig. 2-4 Corss-sectional view of the SPMSM motor

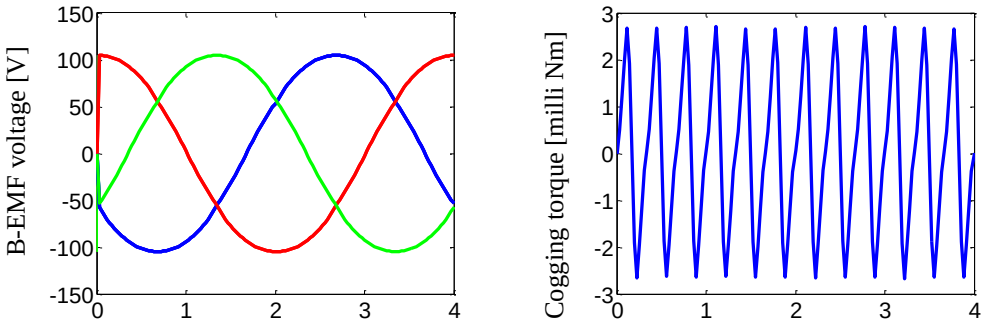

(a) back-EMF voltage (b) cogging torque

Fig. 2-5 SPMSM perfomance calculated using 2D-FEA

The rated torque is calculated using 2D-FEA. The motor FEA model is excited with a sinusoidal current which is aligned with the back EMF. Fig. 2-6-a shows the rated torque (Torque at the rated current) for this machine. It is clear from Fig. 2-6-b that the torque ripple is around 0.03 Nm (1.25% rated torque).

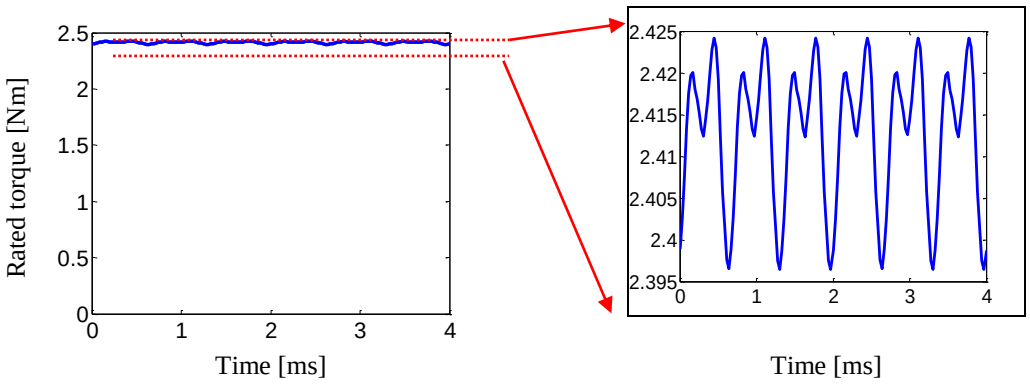

(a) rated torque (b) zoomed image

Fig. 2-6 Calculated torque using 2D-FEA for the SPMSM

Fig. 2-7 shows the magnetic flux density distribution at no load condition. From this figure, the leakage flux between the magnet is small (due to the SPMSM structure with air between the adjacent magnets). The stator winding is selected to be concentrated windings, which is easier to manufacture and will minimize the effect of the end winding, which means lower copper loss in the machine.

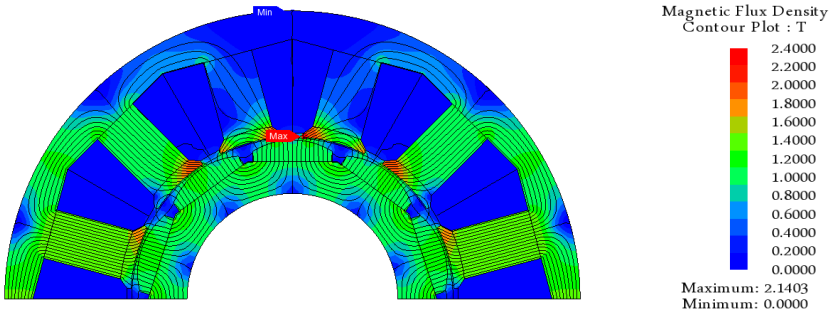

Fig. 2-7 SPMSM flux density distribution at no load condition

Fig. 2-8 shows the dq inductances variation with the load condition. From this figure, this machine is not suitable for high-frequency injection (HFI) self-sensing techniques which are used to estimate rotor position and speed during zero and low-speed operation without using any position sensor.

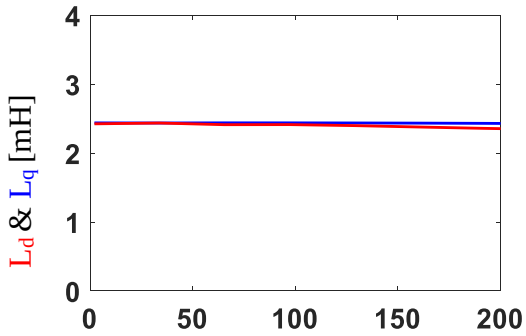

Fig. 2-8 SPMSM inductance for different load conditions

2.2.3 IPMSM servo motor design

IPMSM servo motor design needs to achieve the servo application requirements. This motor needs to have a very low cogging and ripple torque. For this reason, this kind of motor is designed with low saliency and reluctance torque.

An IPMSM rotor was designed using the same magnet as the SPMSM rotor to reduce the manufacturing cost of this prototype rotor. To achieve low cogging and ripple torque performance, a flower shape IPMSM rotor configuration is used. In this configuration, 0.4 mm of iron was added around the magnet. Fig. 2-9 shows a cross-sectional view of this rotor. Adding this thin layer of iron on top of the magnet reduces the airgap flux density by 10%. This can be seen from Fig. 2-20-a and Fig. 2-20-b; the peak torque in the IPMSM is 10% lower than the SPMSM. This happens due to the airgap flux reduction in this motor.

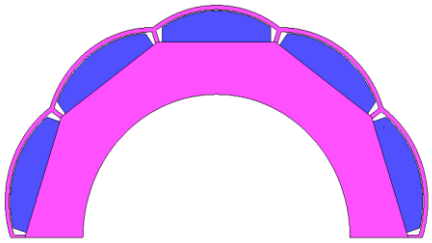

Fig. 2-9 IPMSM rotor

To explore the effectiveness of the proposed flower shape IPMSM rotor, this rotor is compared with circular shape IPMSM rotor as in Fig. 2-10. The flower shape rotor has lower back-EMF harmonics as shown in Fig. 2-11-d, and larger fundamental back-EMF (lower rated current) as in Fig. 2-11-c. This motor achieves significantly lower cogging torque compared to the circular shape rotor IPMSM as in Fig. 2-11-b.

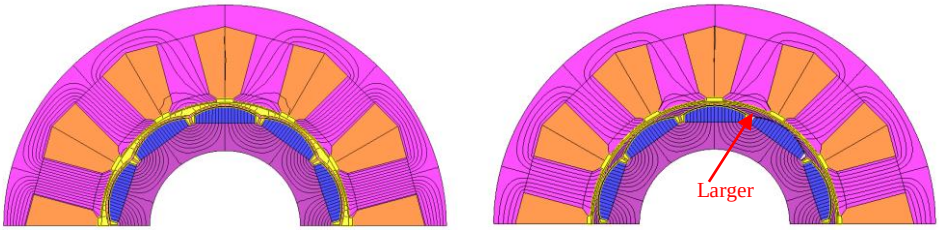

(a) flower-shape rotor IPMSM (b) circular-shape rotor IPMSM

Fig. 2-10 Cross-sectional view and flux lines for IPMSM using flower and circular shape rotors

Fig. 2-12-a shows the calculated back-EMF voltage for the IPMSM designed with flower shapred rotor (this design will be called IPMSM) using 2D-FEA. Fig. 2-12-b shows the cogging torque for this machine which is calculated by spinning the motor at the rated condition without exciting the stator with current using 2D-FEA. It is around 0.025% the rated torque.

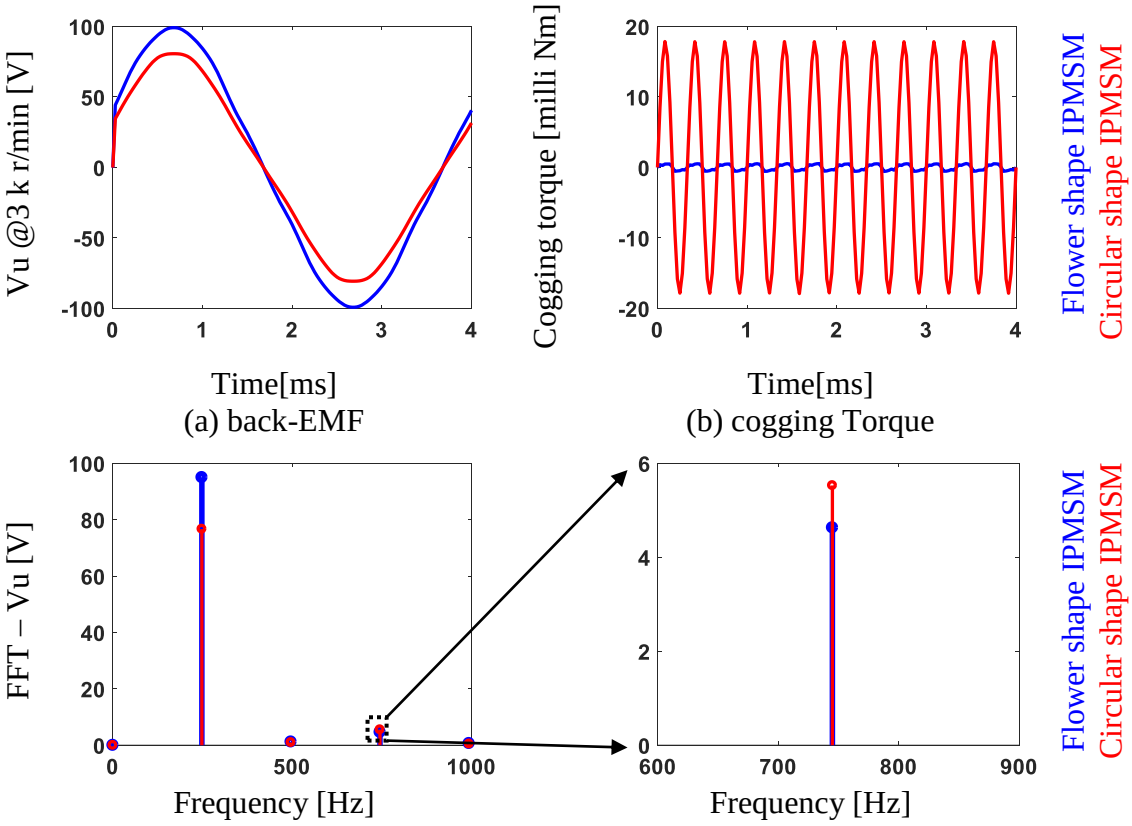

(a) back-EMF (b) cogging Torque

(c) FFT-Back-EMF (d) zoomed on (c)

Fig. 2-11 Performance comparison between flower-shape rotor IPMSM and circular-shape rotor IPMSM

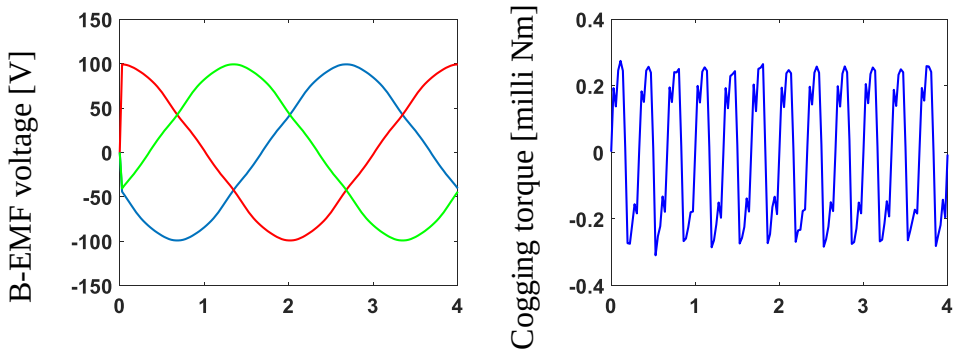

(a) back-EMF voltage (b) cogging torque

Fig. 2-12 IPMSM perfomance calculated using 2D-FEA

The torque of this motor is then evaluated at 4.7 A_{peak} (rated current for the SPMSM) using 2D-FEA, the motor FEA model is excited with a sinusoidal current which is aligned with the back EMF. Fig. 2-13-a shows the torque at the rated current for the SPMSM. The IPMSM achieves 2.14 Nm (89% of SPMSM torque) for this machine. The torque ripple for this motor can be seen in Fig. 2-13-b which is around 0.05166 Nm (2.17% rated torque).

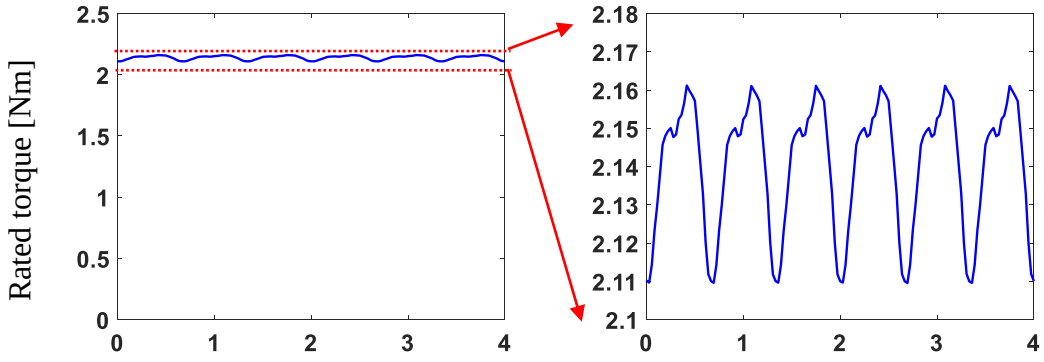

(a) rated torque (b) zoomed image

Fig. 2-13 Calculated torque using 2D-FEA for the IPMSM

Fig. 2-14 shows the magnetic flux density distribution at no load condition. The leakage flux in the iron bridge on top of the magnet is high, this reduces the airgap flux (flux linkage), and lead to increase the rated current compared to the SPMSM. Using this kind of rotor requires laminating the stator iron, to reduce the rotor eddy current losses. However, the rotor losses in the SPMSM are very small, thus a solid rotor is used.

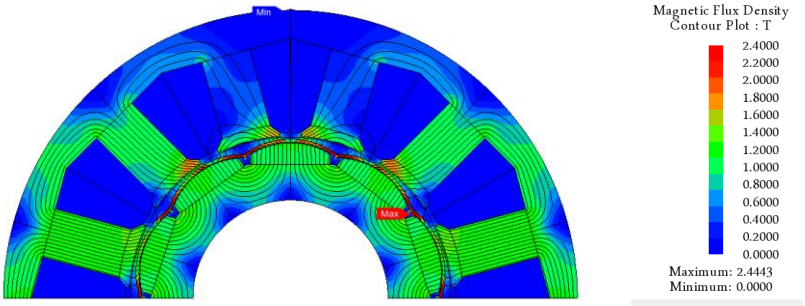

Fig. 2-14 IPMSM flux density distribution at no load condition

Fig. 2-15 shows the dq axis inductance variations with the load condition for the IPMSM. From this figure, the IPMSM has enough saliency (around 11%) to be used with HFI self-sensing control.

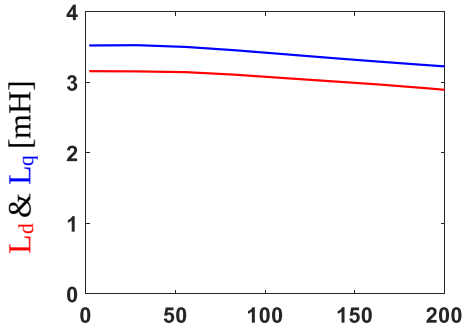

Fig. 2-15 IPMSM inductance for different load conditions

2.2.4 Performance comparison between the SPMSM and IPMSM for servo applications

In this section, the results of a fair performance comparison between SPMSM and IPMSM is presented. Both motors use same stator, same magnet, and same airgap length. First, the back-EMF signal is compared for the two motors as in Fig. 2-16.

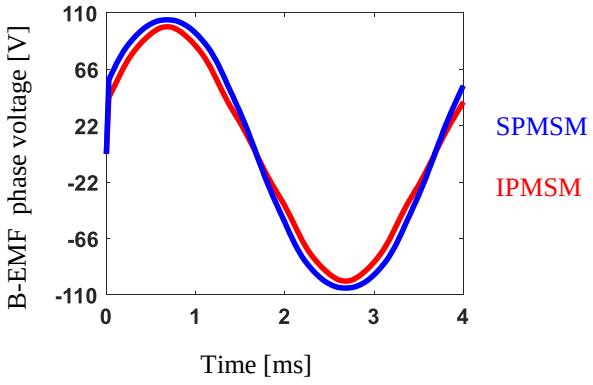

Fig. 2-16 Back-EMF comparison between SPMSM and IPMSM calculated using 2D-FEA

SPMSM achieves higher back-EMF, because this motor has lower leakage flux as shown in Fig. 2-17, in which six leakage flux lines appear in case of IPMSM, while in case of SPMSM there are only 5 flux lines.

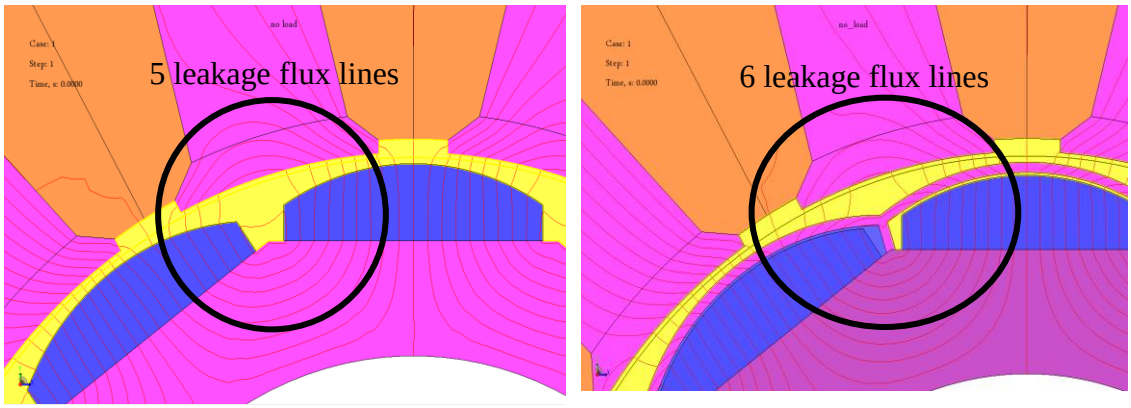

SPMSM IPMSM

Fig. 2-17 Comparison of the leagake flux for the SPMSM and IPMSM

There is also a small MMF drop occurring in the iron bridge on top of the magnet, which can be seen from the magnetic circuit shown in Fig. 2-18.

The inductances for the two motors are compared in Fig. 2-19. IPMSM has higher inductances than the SPMSM. This because the SPMSM flux encounters larger effective airgap (magnet has a similar permeability to air). The SPMSM motor has a negligible saliency as in Fig. 2-8, thus this motor is not suitable for injection based self-sensing control. On the other hand, the IPMSM motor has a small saliency ratio (around 11%) as in Fig. 2-15, which makes this motor suitable for injection based self-sensing control.

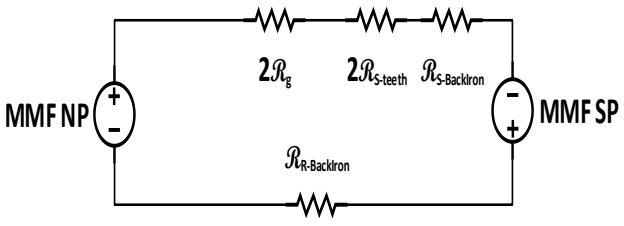

SPMSM

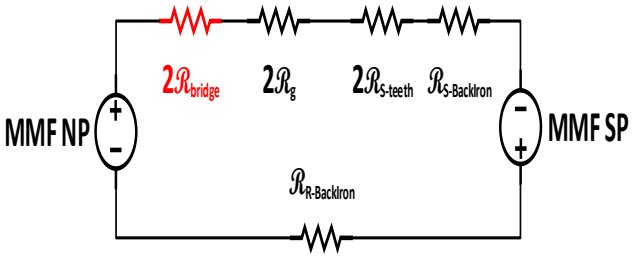

IPMSM

MMF NP: north pole magnet MMF
MMF SP: south pole magnet MMF
$\mathcal{R}_g$: airgap reluctance
$\mathcal{R}_{S\text{-}teeth}$: stator teeth reluctance
$\mathcal{R}_{S\text{-}BackIron}$: stator back iron reluctance
$\mathcal{R}_{R\text{-}BackIron}$: rotor back iron reluctance
$\mathcal{R}_{bridge}$: iron bridge on top of the magnet reluctance

Fig. 2-18 Direct axis magnetic circuit for IPMSM and SPMSM

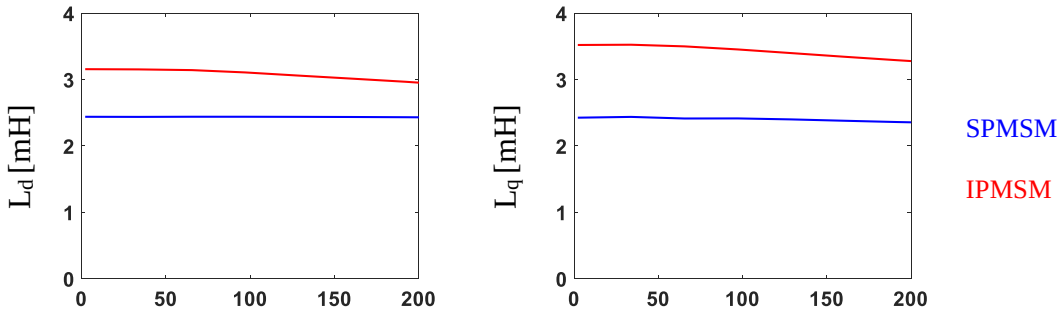

(a) d-axis inductance

(b) q-axis inductance

Fig. 2-19 Comparison of the estimated inductance variation with load condition for SPMSM and IPMSM

The efficiency maps for the two motors were generated using JMAG-RT software and using a set of correction factors. These correction factors were obtained from designing similar motor and through comparing 2D with 3D-FEA simulations. These factors are summarized in

Table 2-3. These factors were used to consider the effect of end winding, and leakage flux reducing the simulation time (without using 3D FEA).

Table 2-3 Correction factors used with 2D-FEA

Quantity	Correction factor
airgap flux density	0.9
inductance	1.3
iron loss	2

Airgap flux density correction factor is obtained by comparing the calculated back-EMF from 2D-FEA with 3D-FEA simulations with modeling the end winding. Inductance correction factor is used to add the leakage inductance to the 2D calculated inductance. This factor is calculated by comparing 2D-FEA and 3D-FEA simulations. Iron loss correction factor was found by measuring iron loss for similar motor with the same materials (at a different speed and torque conditions) and comparing it with the estimated loss from the 2D-FEA.

JMAG software uses the above correction factors to adjust the current phase and amplitude, then the corresponding loss for that current is obtained from the loss lookup tables that are generated based on FEA. Iron loss correction factor is used to adjust the iron loss coefficients that are already programmed in JMAG. These correction factors will be verified later though comparing the calculated corrected back-EMF and inductance values with the measured values.

Fig. 2-20 compares the efficiency and iron loss maps for both motors. SPMSM achieves 10% higher peak torque, this is because this motor has higher airgap flux and higher back-EMF. However, IPMSM has lower iron loss compared to SPMSM, this because this motor has lower

airgap flux. SPMSM has a wider high-efficiency region (sweet spot) than the IPMSM. Both motors in this analysis use same magnet volume.

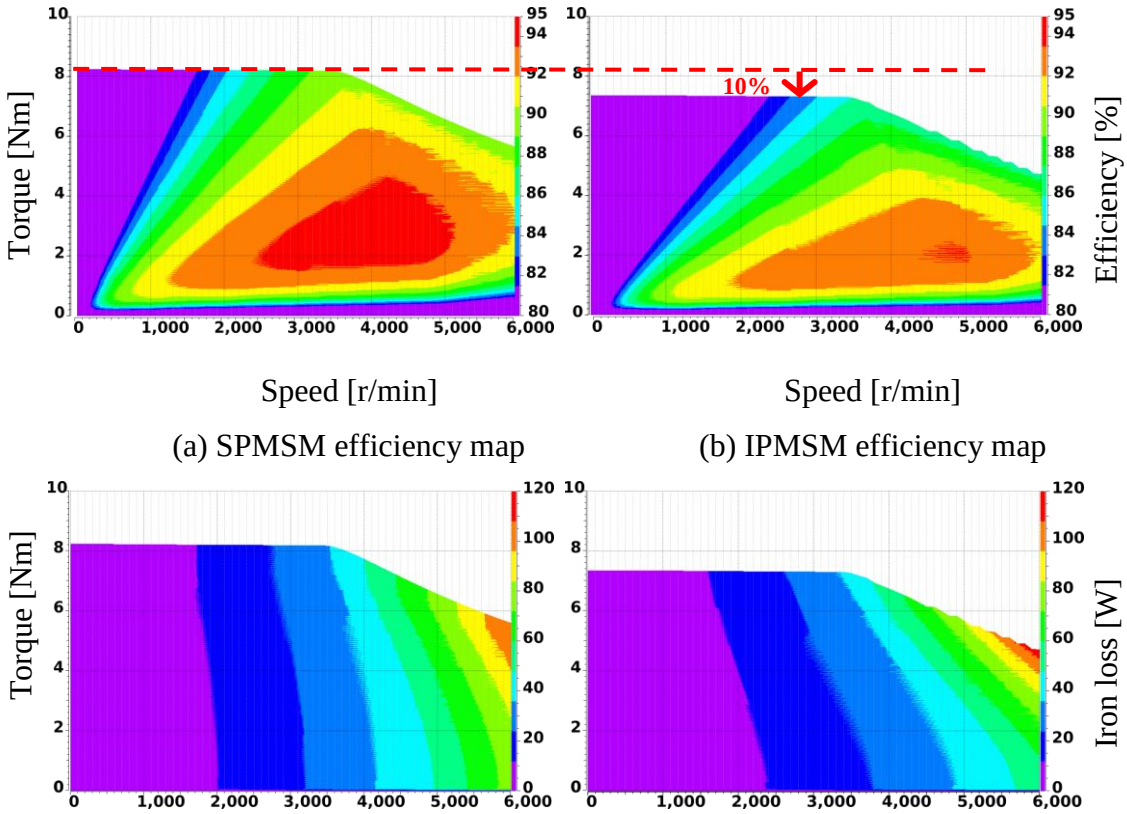

(a) SPMSM efficiency map (b) IPMSM efficiency map

(c) SPMSM iron loss map (d) IPMSM iron loss map

Fig. 2-20 Efficiency and iron loss maps for SPMSM, IPMSM

From the above analysis, SPMSM maximizes the airgap flux per magnet volume compared to IPMSM. However, IPMSM has a detectable saliency which can be used in injection-based self-sensing control. This conclusion is valid for servo motors, in which the reluctance torque component is small (to achieve very low cogging and ripple torque).

2.3 Flux Intensifing Surface Mounted Permanent Magnet Motor (FI-SPMSM) Design

In the previous section, the performance of both SPMSM and IPMSM motors was compared. SPMSM achieves higher airgap flux density per magnet volume compared to the IPMSM. However, IPMSM has lower airgap flux and lower iron loss with a detectable saliency, which make this motor suitable for injection based self-sensing.

In this section, a new servo motor design methodology is proposed, called FI-SPMSM. The designed motor using the proposed design methodology combines the benefits of both SPMSM and IPMSM. This design maximizes the airgap flux per magnet volume like an SPMSM and has a detectable saliency like the IPMSM. This motor uses lower magnetic material and has significantly lower iron loss compared to previous motors.

The FI-SPMSM design methodology is similar to the FI-IPMSM design methodology as in [37] , in which the airgap flux is reduced. With that, a lower iron loss is achieved during high-speed operation, and a lower negative d-axis current is required to weaken the flux when the motor operates at the inverter voltage limit during the high-speed operation. An inverted saliency (Ld > Lq) is introduced to the motor by adding q-axis flux barriers. This saliency is helpful for both self-sensing purpose and for boosting the airgap flux during peak torque operation.

Analytical equations for designing SPMSM are still valid for the case of the FI-SPMSM. In this thesis, the fundamental airgap flux density of the SPMSM was reduced by decreasing the magnet span from 162° to 110° electrical degree using (2-6). This is done to reduce the flux weakening current during the high-speed operation (6000 r/min) to zero, which improves high-speed efficiency. This was done using the first harmonic assumption; Fig. 2-21 shows the

reduction of the fundamental airgap flux density by reducing the magnet span. This will reduce the motor back-EMF at 6000 r/min from 190 $V_{\Phi-peak}$ to 165 $V_{\Phi-peak}$. The maximum voltage provided by the inverter is 170V (limited by the inverter DC link voltage).

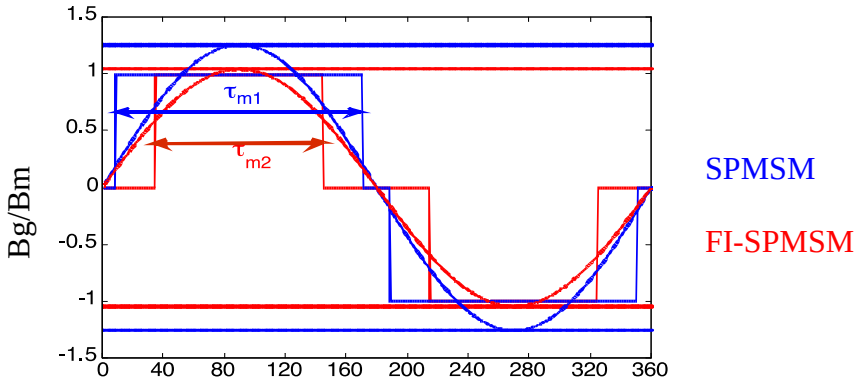

Fig. 2-21 Magnet span reduction to reduce the fundamental air-gap flux

After reducing the fundamental air-gap flux (through reducing the magnet span), a sufficient inverted saliency ratio ($L_d > L_q$) is added to the motor. This is done by optimizing the q-axis flux barriers and by shaping the magnet to reduce the airgap harmonics (decrease the ripple and cogging torque).

Multi-objective optimization using genetic algorithm is done using Matlab™ optimization engine with JMAG™ Designer software. 30 generations with 10 population size are used. The optimization engine ran 273 cases to find the optimum solution, for every case the current was set to zero to measure the cogging torque and to the rated current to measure the average torque, while the motor is spinning at 3000 r/min.

The optimization objectives were set to maximize the saliency ratio (Ld / Lq), maximize the average torque, limiting the cogging torque to be less than 0.55%, and limiting the torque

ripple to be less than 3%. Fig. 2-22 indicates the parameters varied during the optimization process, the varied range is shown in Table 2-4.

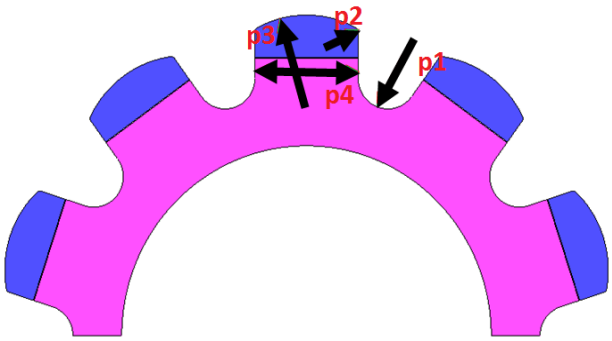

Fig. 2-22 Varied geometry during optimization process for FI-SPMSM rotor

Table 2-4 Varied parameters during the optimization process

Parameter	Range
Q-axis flux barrier radius (p1)	1 - 2.2 mm
Magnet fillet radius (p2)	0.25-1.5 mm
Magnet outer radius (p3)	5 - 15 mm
Magnet span (p4)	5-8 mm

Fig. 2-23 shows the optimization process results. Case number 253 is selected, marked in red, since it optimizes the average torque production while achieving the desired saliency and meeting the torque ripple and cogging requirements.

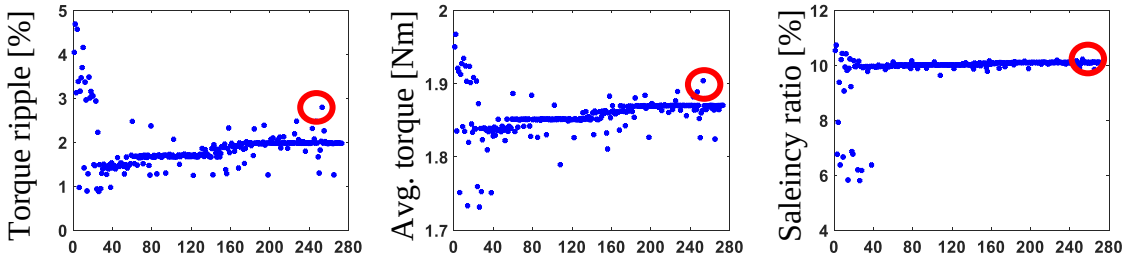

(a) torque ripple (b) average torque (c) saliency ratio

Fig. 2-23 Ooptimization process results for FI-SPMSM rotor

Fig. 2-24 compares the back-EMF voltage calculated at 3000 r/min for the SPMSM, IPMSM, and FI-SPMSM. These results were obtained using JMAG 2D, FEA. FI-SPM has lower back-EMF compared to both SPMSM, and IPMSM, thus allows running the motor at high-speed operation with lower flux-weakening current, which achieves lower high-speed copper loss. The FI-SPMSM has lower airgap flux density, thus this motor can achieve lower iron loss compared to both SPMSM and IPMSM.

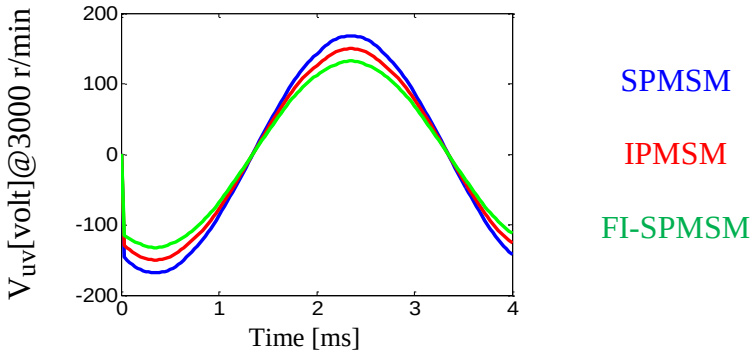

Fig. 2-24 Back EMF voltage for SPMSM, IPMSM & FI-SPMSM calculated using 2D-FEA

Fig. 2-25 shows the variation of the dq axis's inductances with increasing the applied load on the motor. The proposed FI-SPMSM has a positive trackable saliency ($L_d > L_q$), making it suitable for injection-based self-sensing techniques.

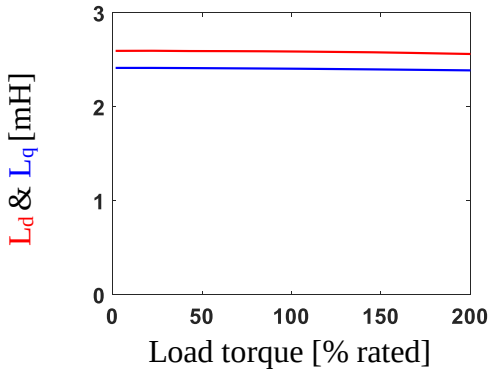

Fig. 2-25 FI-SPMSM inductance at different load conditions evaluated using 2D FEA

Moreover, FI-SPMSM motor has a lower magnet leakage flux in the axial direction compared to both IPMSM and SPMSM rotors. This is due to using a shorter magnet span in the FI-SPMSM motor (larger gap between the magnets with larger reluctance). In the previous analysis, both SPMSM and IPMSM rotors have approximately a 10% total leakage flux. However, FI-SPMSM motor has only 3.5% total leakage-flux. This leads to a different correction factor for this motor as in Table 2-5. These correction factors will be validated later with the experimental evaluation.

Table 2-5 Correction factors used with 2D-FEA for FI-SPMSM

Specification	Correction factor
airgap flux density	0.965
inductance	1.2
iron loss	2

Fig. 2-26 shows the reluctance path for the axial leakage flux from the magnet for both SPMSM and FI-SPMSM. The air reluctance in the axial direction for the SPMSM is smaller (magnet span is short), while in the case of the FI-SPMSM, the air reluctance in the axial direction is larger (larger distance between the magnets). This leads to lower magnet leakage flux in the axial direction for the FI-SPMSM compared to the SPMSM.

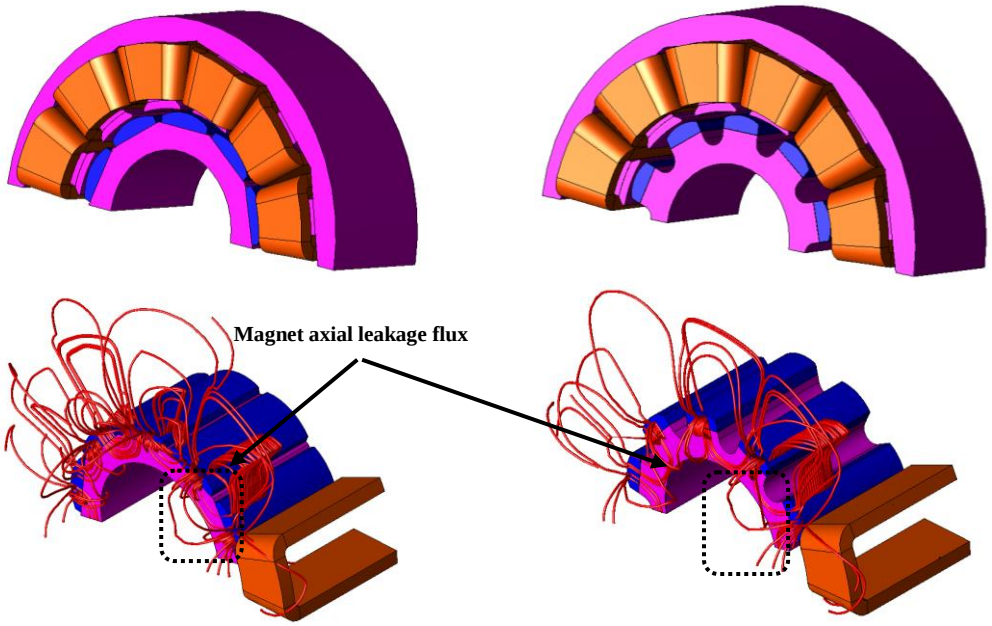

(a) SPMSM (b) FI-SPMSM

Fig. 2-26 3D model and axial magnet leakage flux for SPMSM and FI-SPMSM

To explore the benefits of the q-axis flux barriers in the proposed FI-SPMSM rotor, the flux barriers partially filled with iron (same rotor structure like the SPMSM rotor), and flux barriers completely filled with iron (inset SPMSM structure) are used as in Fig. 2-27 . Using the SPMSM rotor iron with the FI-SPMSM magnet achieves similar average torque. This motor has an inverted very small saliency (this motor has FI properties) while shaping the flux barriers in the FI-SPMSM rotor improves the saliency allowing usage for self-sensing purposes. Fig. 2-28 compares the saliency ratio for these two motors at different load conditions.

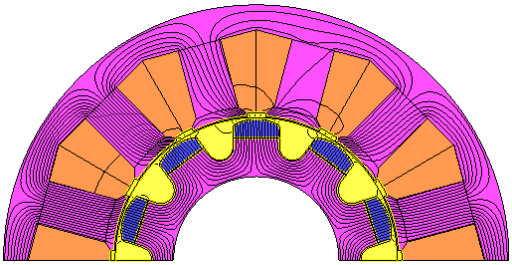

(a) FI-SPMSM

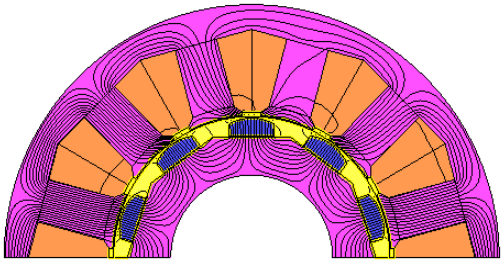

(b) SPMSM rotor iron with FI-SPMSM Magnet

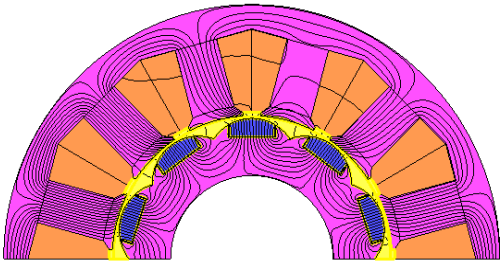

(c) Inset SPMSM

Fig. 2-27 Cross-sectional view of FI-SPMSM, SPMSM with a shorter magnet span and inset SPMSM

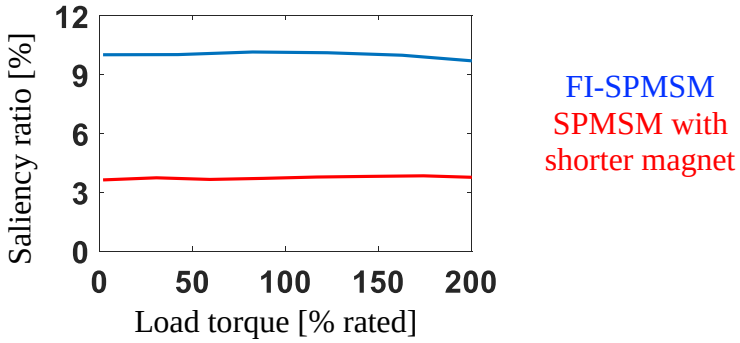

Fig. 2-28 Saliency ratio comparison between FI-SPMSM and SPMSM with shorter magnet span

FI-SPMSM rotor is then converted to an inset SPMSM rotor by adding iron between the magnets as in Fig. 2-27-c. The iron between the magnets provides a path for the flux to leak,

affecting the torque production of the motor and decreasing the average torque by 6.6%. Fig. 2-29 compares the average torque for the two motors using the same excitation current.

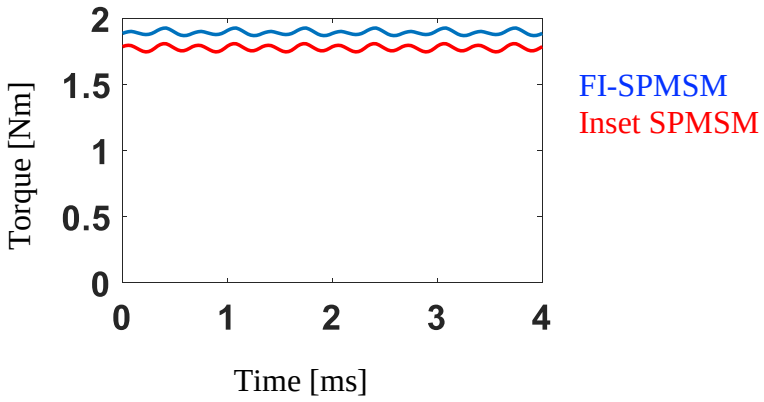

Fig. 2-29 Average torque comparison between FI-SPMSM and inset SPMSM at 4.7 A_{peak}

Self-Sensing Properties of the Designed FI-SPMSM

Self-sensing techniques are useful methods to control the motor without any physical position sensor, through using the motor itself as a sensor. This improves the reliability of the drive and decreases the drive physical size and cost. Two main self-sensing techniques are used in the literature; the first one is effective for medium and high-speed operation through tracking the motor back-EMF. This method works for all electromagnetic machine types [107].

The other self-sensing technique is used to control the motor during zero and low-speed operations. This is done by tracking the motor saliency, which can be tracked by injecting a high-frequency signal on top of the fundamental signal [108]. This method is effective in salient motors like IPMSM, however, applying these techniques to SPMSM requires designing the motor for that purpose.

FI-SPMSM is designed to have good self-sensing properties during zero and low-speed operation. The dq axis inductances are almost fixed with load condition. In this case, no massive

inductance lookup tables are required for self-sensing control. Also, the saliency image of this motor is fixed with load variations; this simplifies the image template for image tracking self-sensing control [109]. Fig. 2-30 shows the FI-SPMSM saliency image at different load conditions. This image was obtained through exciting the FEA motor model with a high frequency rotating current vector, then observing the high-frequency stator flux linkage.

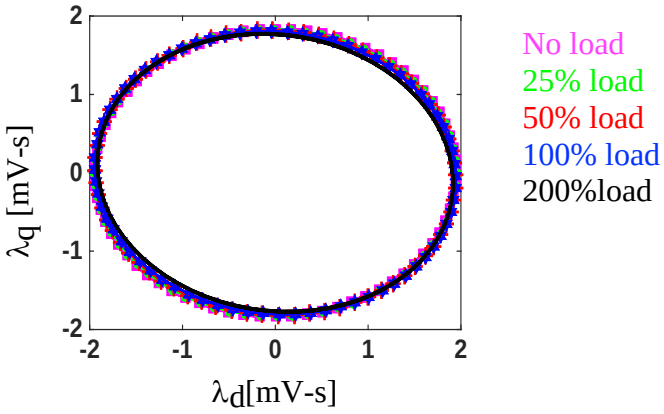

Fig. 2-30 Saliency image of FI-SPMSM at different load conditions

The accuracy of the injection based self-sensing technique also depends on the angular offset of the saliency image at different load conditions [110], due to cross-saturation effect between the d and q axis. The angular offset of the designed FI-SPMSM motor is less than 2 electrical degrees at 200% load, which can be ignored in many applications without the need for compensation lookup table to decouple its effect. Fig. 2-31 shows the angular offset at different load conditions). Results of self-sensing control for the FI-SPMSM motor will be discussed later in this thesis.

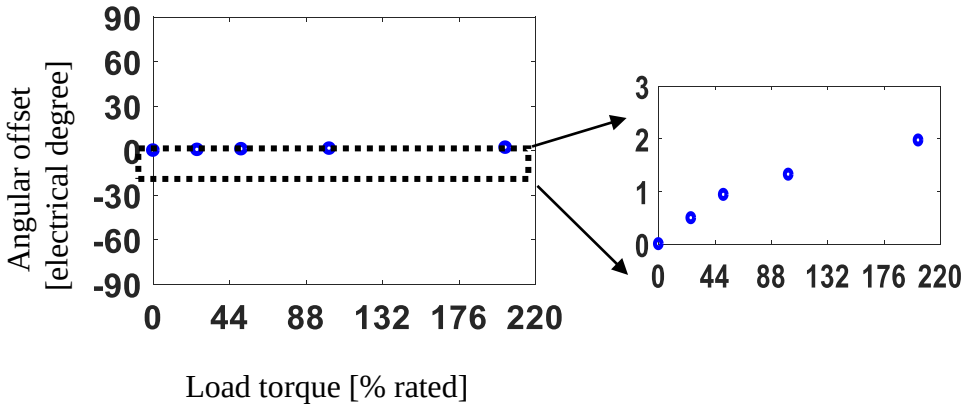

Fig. 2-31 Angular offset of FI-SPMSM saliency image at different load conditions

2.4 Performance Evaluation of the Designed Motors

In this section, the performance of the designed motors will be evaluated using both FEA simulation and experimental results. Cycle loss is experimentally evaluated in this section. First, the testeting dynamometer is investigated, including system identification and deadtime compensation.

2.4.1 Dynomometer test setup

In this project, a back-to-back, dual servo motor dynamometer test stand is used. Fig. 2-32 shows the block diagram of the test bench. The rectifiers in the power converters were not used. A DC power supply is connected directly to the DC link which is shared between the two inverters, enabling energy circulation between the tested and load motors. 2 capacitors with 3000 μF will be used for the DC link capacitor. Also, a big heat sink with fans is used to cool these converters.

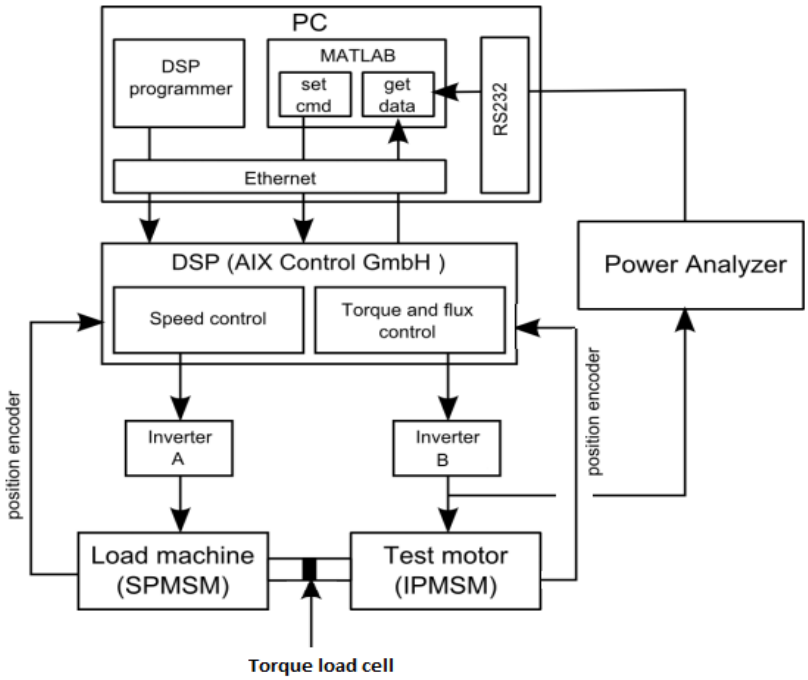

Fig. 2-32 Block diagram of the test stand

A motor drive analyzer (MDA810) from Teledyne LeCroy was used to calculate input and output power. MDA is a high sampling rate tool allows measuring motor power and losses even during transient conditions. Current sensor gains were calibrated using an external current probe. The offset in the current sensors is set to zero every time the system is run.

An AIX control system is used to control both inverters. This controller is programmed using DSP++ software using C code environment. Fig. 2-33 shows the constructed power rack, while Fig. 2-34 shows the tested dynamometer.

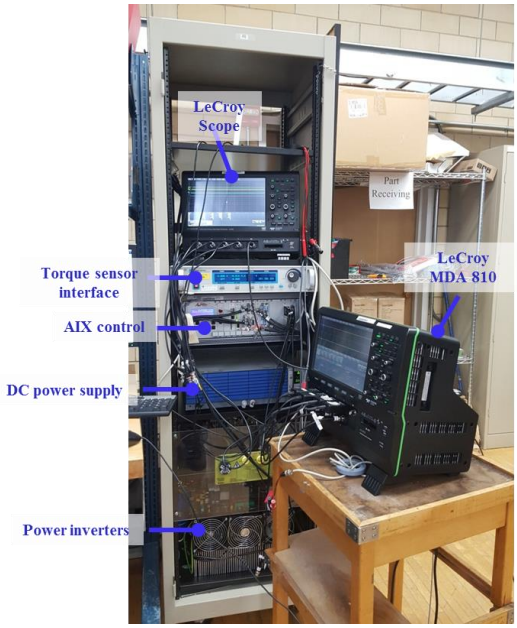

Fig. 2-33 The constructed power rack

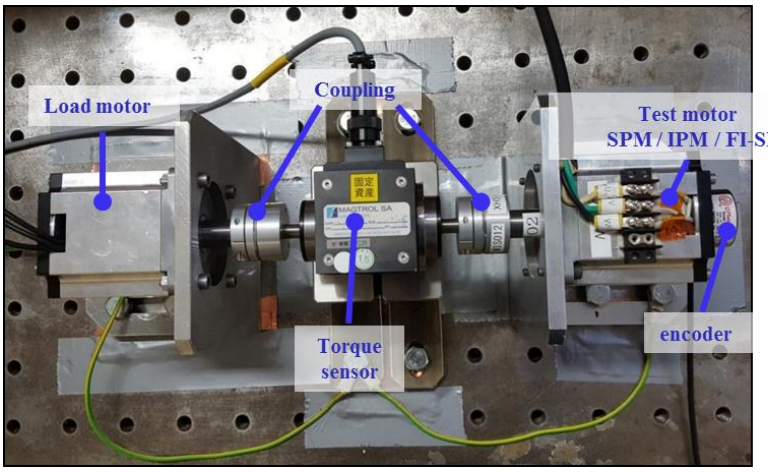

Fig. 2-34 The test dynamometer

Inverter non-lineraty compensation:

Inverter non-linearities such as dead-time, current clamping, turn on and turn off time of switching devices, and resistive voltage drops keep the actual inverter output voltage from matching the commanded voltage. Inverter nonlinearity compensation must be implemented for these two to match.

The compensation method used in this thesis was described in [111]. In this method, two phases of the motor are connected to the inverter and the motor rotor is locked as shown in Fig. 2-35. The phase current was controlled to be a sine wave with low frequency (this to minimize the effect of the motor inductance). Actual voltage was estimated from the measured current and from the motor resistance as in (2-8).

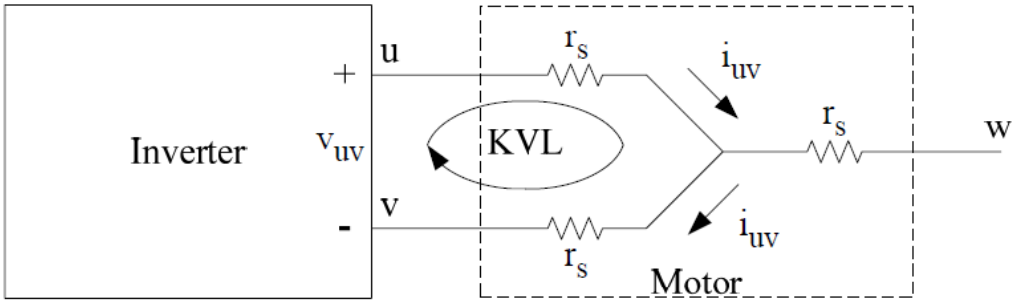

Fig. 2-35 Motor and inverter with phase disconnected and neglected inductance

$$V_{uv}(t)=2i_{uv}(t)r_s \quad (2\text{-}8)$$

Inverter nonlinearity compensation can be calculated as in (2-9). This compensation is for one phase, that's why the 0.5 factor appears in the equation.

$$V_{comp}(t) = 0.5*\{V_{uv}^*(t)- V_{uv}(t)\} \quad (2\text{-}9)$$

To find the duty cycle compensation, (2-9) was divided by the DC link voltage as in (2-10). d_{comp} as a function of current is shown in Fig. 2-36. A quadratic model for the measured d_{comp} was used, this will simplify the implementation of the compensation algorithm in the DSP without the need for a lookup table. The quadrature compensation equation is shown in (2-11).

$$d_{comp}(t)= V_{comp}(t)/V_{dc}(t) \quad (2\text{-}10)$$

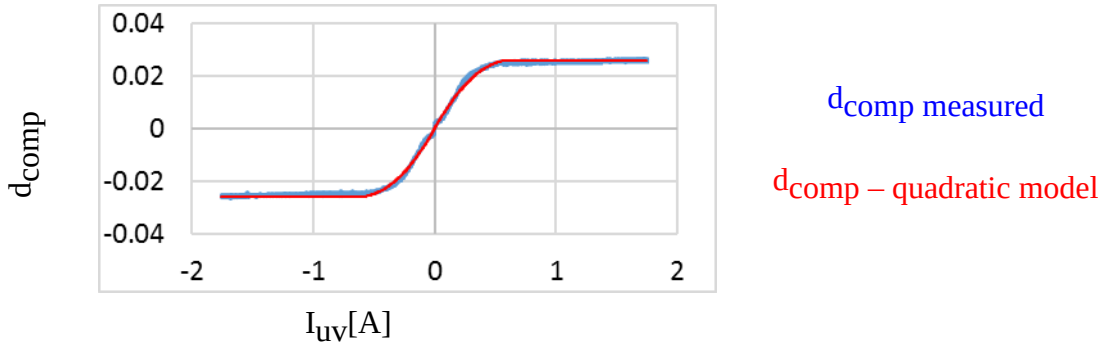

Fig. 2-36 Motor and inverter with phase disconnected and neglected inductance

$$d_{comp} = 0.06551 * (i + .63)^2 - 0.026 \quad \text{when } (i<0)$$
$$d_{comp} = -0.06551 * (i - .63)^2 + 0.026 \quad \text{when } (i>0) \qquad (2\text{-}11)$$

Motor alignment and Position observer:

In this thesis, single encoder with 5000 lines was attached to the load motor side. This encoder was used to measure position and speed for both motors. The alignment sequence is shown in Fig. 2-37. In this thesis, a dc d-axis current method is used to align both motors. In this method, a dc d-axis current is commanded from the motor in the stationary reference frame. This will align the rotor reference frame axis of the motor with the stationary reference frame (in this case with phase u). Before the alignment procedure, the encoder zero pulse was detected by rotating one of the motors at very low speed using open loop control.

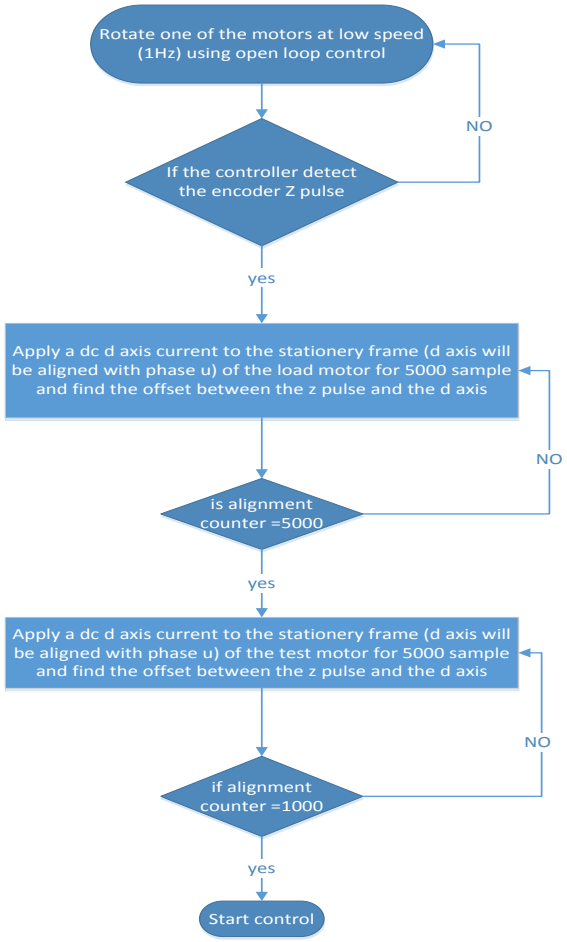

Fig. 2-37 Alignment of both load and tested motor

Average velocity can be calculated from the measured shaft position using the encoder. Using this signal as a feedback signal will degrade the performance of the motor, especially at low speed when the encoder quantization is significant. To overcome that, a position observer is used to estimate the instantaneous velocity, this will improve the response of the motor by resolving the delay property that is associated with the average velocity [112].

In this thesis, the motion observer was tuned to achieve the same bandwidth as the motion controller which is 50Hz. Fig. 2-38 shows the discrete time domain block diagram of the used motion observer.

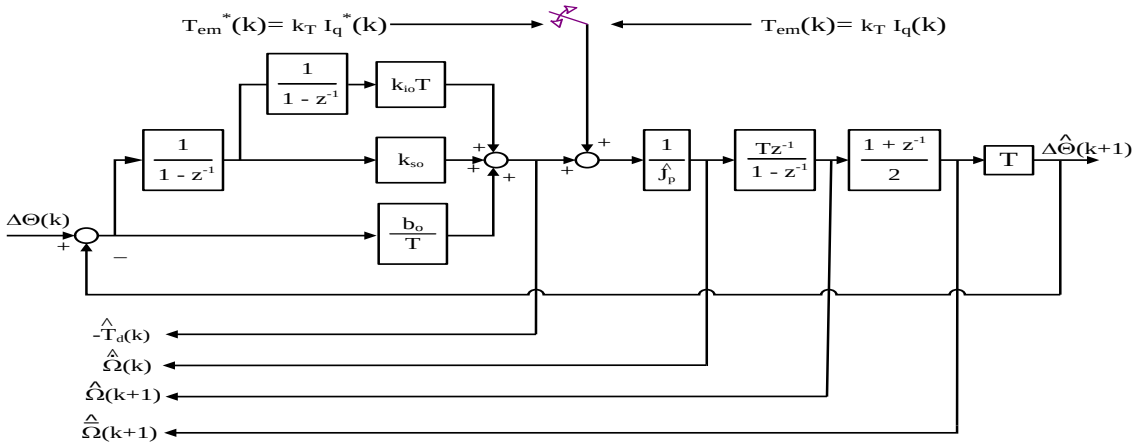

Fig. 2-38 Digital implementation of a reduced-order Luenberger style, discrete time motion observer [112]

Motor parameter estimation:

In this section, motor parameters are estimated. First, CVCR was implemented on the tested motor. Estimated parameters from FEA were used at this point. Permanent magnet flux was estimated by spinning the load motor at different speeds and commanding zero current in both d and q axis frames from the tested motor. In this case, back-EMF voltage will appear in the q-axis voltage, and zero voltage will appear in the d-axis voltage. Plotting the q-axis voltage versus the measured speed, and by finding the slope of this line, the estimated magnet flux was obtained. Fig. 2-39 shows the estimated magnet flux for the three motors.

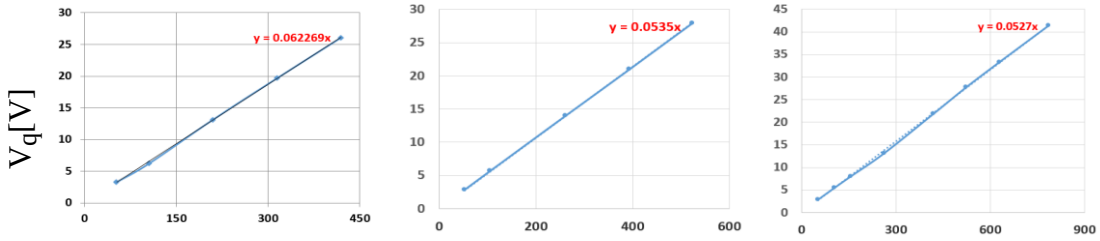

(a) SPMSM (b) IPMSM (c) FI-SPMSM

Fig. 2-39 Permanent magnet flux estimation for the three motors

Motor resistance was measured using a multimeter. This value is fixed for the three motors because same stator is used in evaluating the three motors performance. Motor inductances were estimated from the estimated stator flux linkage and the measured dq axis current. This method will be explained in detail later in this thesis. Table 2-6 summarizes the measured electrical parameters.

Table 2-6 Summary of the measured parameters for the tested rotors

	R	L_d	L_q	λ_{pm}
SPMSM	0.75 Ω	2.88mH	2.95mH	0.06227Wb
IPMSM	0.75 Ω	4.11mH	4.35mH	0.0535Wb
FI-SPMSM	0.75 Ω	3.3mH	2.925mH	0.0527Wb

Dynamometer mechanical parameters were estimated using flag test. In this test, a triangular speed is commanded, and both measured speed and airgap torque are monitored and plotted using xy mode to form the flag as in Fig. 2-40; satisfying (2-12).

$$T=J_p\frac{d\,\omega}{dt}+b_p\,\omega+T_\mu \qquad (2\text{-}12)$$

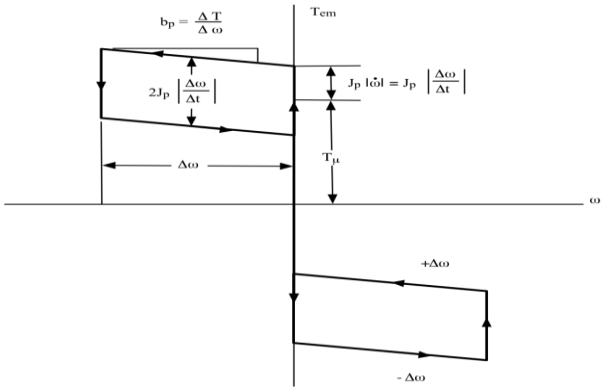

Fig. 2-40 Flag test example

A 2000 r/min triangular wave with 1Hz speed was commanded from the load motor, which is in speed control using CVCR with 1kHz bandwidth. Fig. 2-41 shows the measured speed, and the commanded airgap torque; while Fig. 2-42 shows the obtained flag.

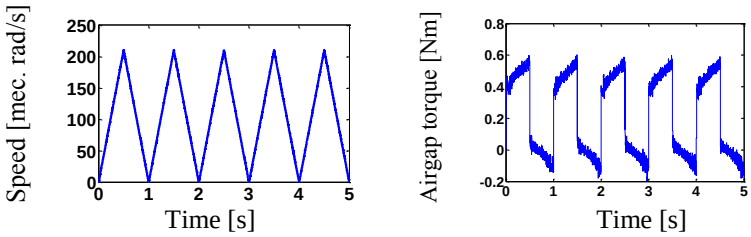

(a) measured speed (b) airgap torque

Fig. 2-41 Flag test experimental results

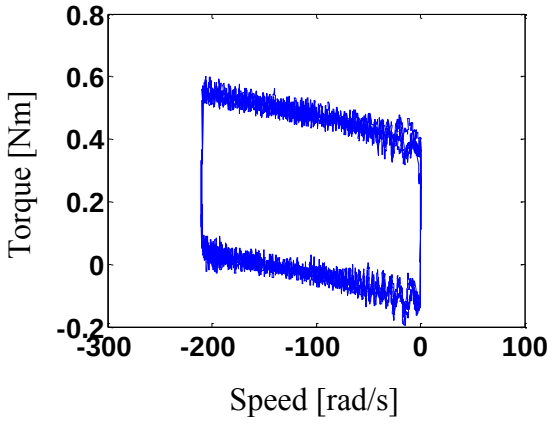

Fig. 2-42 Measured flag

By comparing Fig. 2-42 with Fig. 2-40, the mechanical parameters including motor inerta (J_p), dynamic friction (b_p) and coulomb friction (T_μ) are estimated. Table 2-7 summarizes the estimated parameters.

Table 2-7 Summary of the measured mechanical parameters for the tested dynamometer

J_p=590 [μkgm^2]	T_μ = 0.156 [N.m]	b_p =87.5 [μN.m.s/rad]

2.4.2 Performance evaluation comparison for the designed motors

In this section, the performance of the three motors is compared. The Back-EMF signal is measured and compared with the FEA, helping in verifying the correction factors that are used to consider the effect of end-winding. Then the inductance variation at different load conditions is

evaluated and compared with the estimated values from FEA. Finally, the efficiency and iron loss maps for the three motors are compared.

Back-EMF voltage for the three motors was measured using differential voltage probes. The load motor was controlled to spin the dynamometer at 3000 r/min and the line-line voltage was measured. Fig. 2-43 compares between the measured back-EMF voltage and with the simulated 2D-FEA and corrected 2D-FEA results for the three motors, this verifies the used flux correction factors. Fig. 2-44 compares the measured back EMF for the three motors.

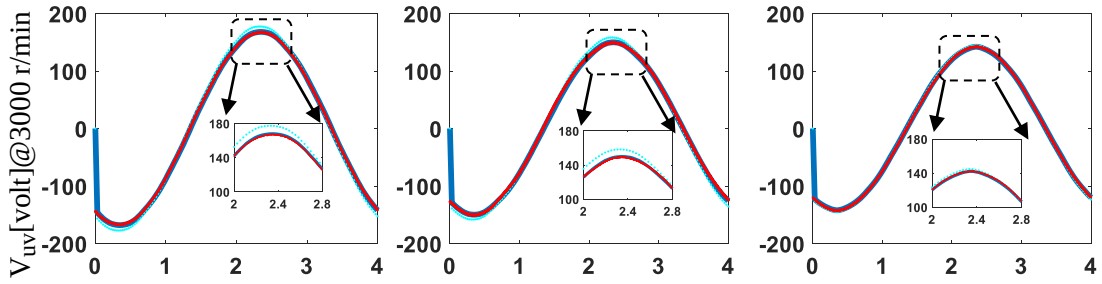

(a) SPMSM (b) IPMSM (c) FI-SPMSM

Legend: 2D-FEA & Corrected 2D-FEA & measured

Fig. 2-43 Simulated and measured back EMF voltage for SPMSM, IPMSM, and FI-SPMSM

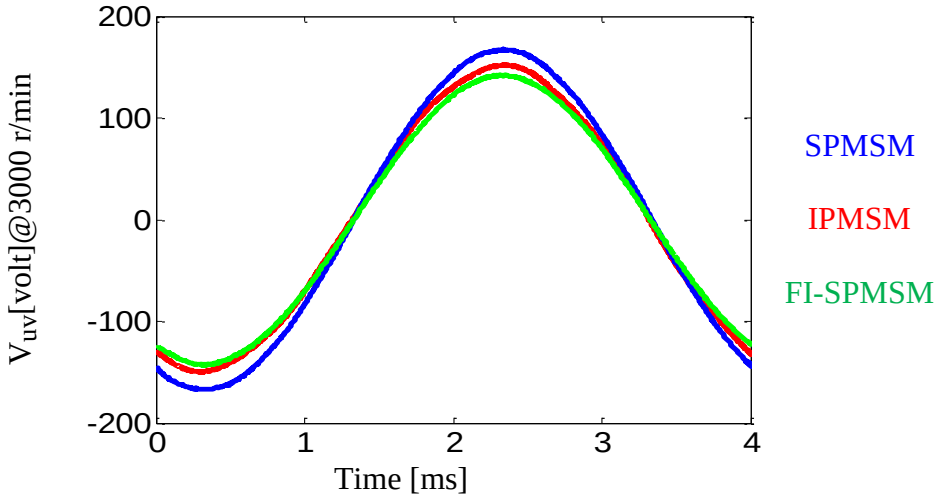

Fig. 2-44 Measured back EMF voltage for SPMSM, IPMSM, and FI-SPMSM

Then the dq axis inductances are measured and compared with the estimated values from the corrected 2D-FEA. Fig. 2-45 shows the results. These results verify the inductance correction factors used with FEA. As discussed previously, SPMSM and FI-SPM have a lower inductance compared to the IPMSM because the effective airgap in these motors is larger than the IPMSM case.

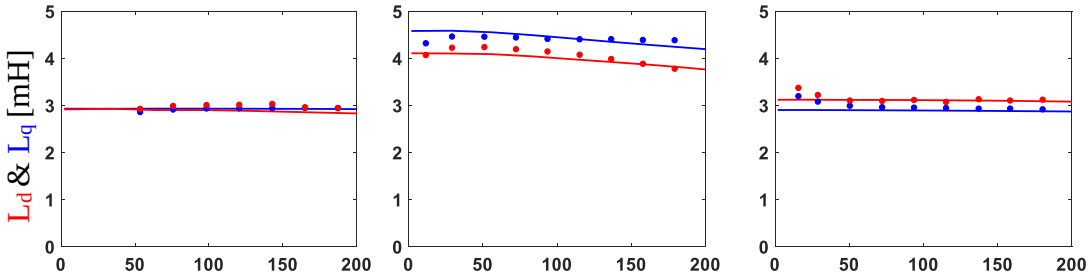

(a) SPMSM (b) IPMSM (c) FI-SPMSM

Legend : Solid line (-) FEA & Dot (·) measured

Fig. 2-45 Measured and simulated inductance variation with load condition for SPMSM, IPMSM, and FI-SPMSM

The efficiency and iron loss maps then compared for the three motors, obtained using JMAG-RT software with considering the correction factors that were discussed in the previous section. Fig. 2-46 shows the efficiency maps for the three motors. IPMSM has 10% lower peak torque compared to the SPMSM motor. However, this motor has lower high-speed low torque iron loss compared to the SPMSM. FI-SPMSM has 5% lower peak torque compared to the IPMSM, this motor has significantly lower iron loss compared to both SPMSM and IPMSM, which makes this motor very efficiency for high-speed servo applications. This motor uses only 64% magnet volume used in SPMSM and IPMSM. This will decrease the motor cost of this motor from 7-10 % (magnet cost for this size of motors is around 20-30% the total cost).

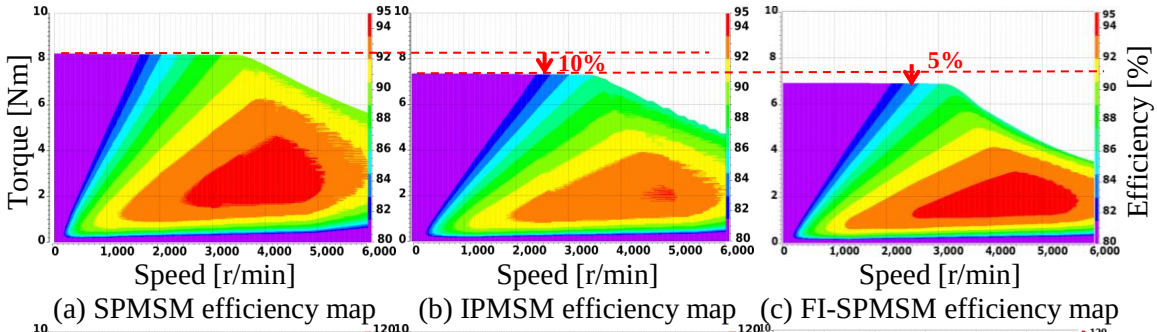

(a) SPMSM efficiency map (b) IPMSM efficiency map (c) FI-SPMSM efficiency map

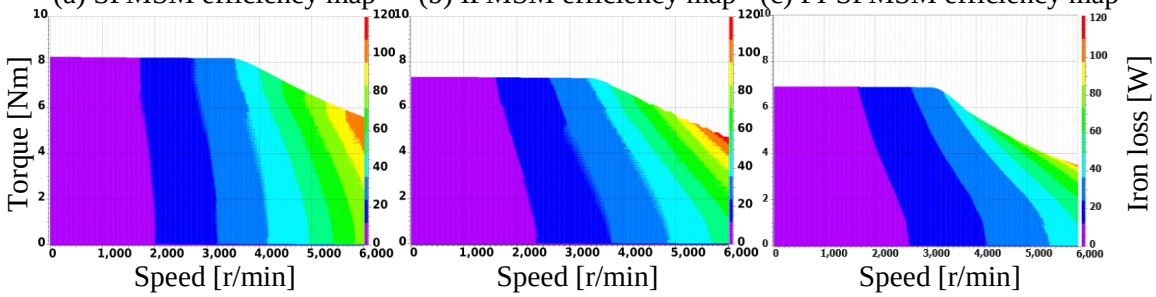

(d) SPMSM iron loss map (e) IPMSM iron loss map (f) FI-SPMSM iron loss map

Fig. 2-46 Efficiency and iron loss maps for SPMSM, IPMSM, and FI-SPMSM

Table 2-8 summarizes the main differences between the three motors. While Fig. 2-47 shows the fabricated rotors.

Table 2-8 Comparisons between the three designed motors

Specification	SPMSM	IPMSM	FI-SPMSM
back-EMF voltage @3000r/m (peak phase)	95V	86.5V	82.2V
PM flux (measured)	0.0623 Wb	0.0556 Wb	0.0529 Wb
rated current (measured)	3.63 A_{rms}	3.99 A_{rms}	4.19 A_{rms}
rated torque	2.38 N.m	2.38 N.m	2.38 N.m
magnet volume	100%	100%	64%
torque ripple (FEA)	1.1%	2.5%	2.8%
cogging torque (FEA)	0.3 %	0.35%	0.51%

Fig. 2-47 The fabricated rotors
(left) SPMSM (center) IPMSM (right)FI-SPMSM

Servo cycle loss evaluation

The energy loss in different servo cycles for the three fabricated rotors was evaluated experimentally. In order to do so, the tested motor is connected to a commercial 3 HP servo motor through a torque sensor. Fig. 2-48 shows the used dynamometer. A motor drive analyzer (MDA 810 from Teledyne LeCroy) is used to measure the tested motor loss.

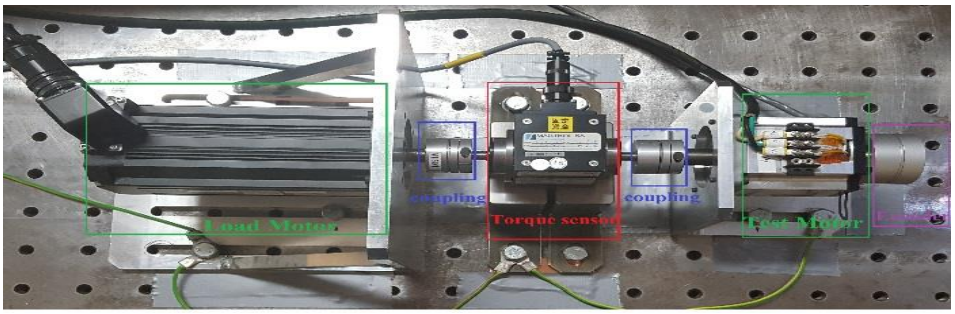

Fig. 2-48 The dynamometer test setup

The load motor was controlled using a field-oriented controller (FOC), while the tested motor was in motion control using loss minimizing control in deadbeat-direct torque and flux control (LMC-DB-DTFC). This controller controls the motor to operate at the optimum operating condition. More details about this controller are presented later in chapter 5. To evaluate the energy loss during acceleration and deceleration, the dynamic shaft torque signal is used to measure the mechanical motor power. This signal is obtained from a dynamic shaft torque observer, more details about this observer will be presented later in chapter 4.

The majority of servo motors used in automation run in a duty cycle operation, in which the motor is accelerated quickly by applying 2-3 times the rated torque for a short period of time then the motor run at high-speed with partial torque for few seconds.

To evaluate the dynamic loss minimization performance of the deigned FI-SPMSM motor using the developed design methodology, the motor is run in different continuous operational servo cycles. Energy lost is measured and compared with the designed SPMSM and IPMSM servo motors.

In the first evaluated cycle, the tested motors were accelerated from 0 to 4000 r/min in 200 ms, then these motors ran at 4000 r/min for 60 seconds. During this cycle, 1.8 Nm (74% rated torque) load torque was applied using the load motor. 200% of the rated torque was applied to the tested motor during the acceleration period. The copper loss for FI-SPMSM is higher than the SPMSM. This is because FI-SPMSM has lower magnet flux, so more current is required to produce the required torque. However, the iron loss is significantly lower in the FI-SPMSM compared to both the SPMSM and IPMSM. For this cycle, the FI-SPMSM has 32% lower

energy loss compared to the SPMSM, and 16.5% lower energy loss compared to the IPMSM; the results of this experiment are shown in Fig. 2-49.

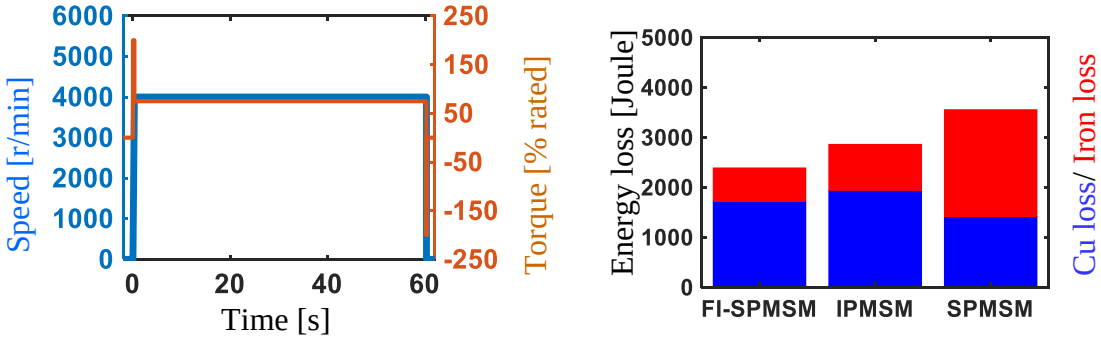

(a) 4000 r/min continuous servo cycle (b) measured cycle energy loss

Fig. 2-49 Measured Energy loss for the three rotors for 4000 r/min continuous servo cycle

Fig. 2-50 shows the results of the second evaluated cycle. In this cycle, the tested motors were accelerated from 0 to 4500 r/min in 225 ms, then these motors ran at 4500 r/min for 60 seconds. During this cycle, 1.6 Nm (66% rated torque) load torque was applied using the load motor. 200% of the rated torque was applied to the tested motor during the acceleration period. Like the previous cycle, FI-SPMSM has 40% lower energy loss compared to the SPMSM, and 20% lower energy loss compared to the IPMSM.

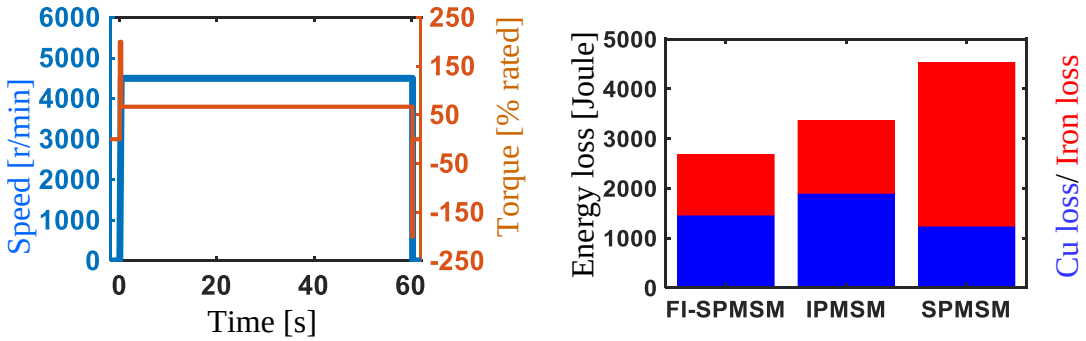

(a) 4500 r/min continuous servo cycle (b) measured cycle energy loss

Fig. 2-50 Measured Energy loss for the three rotors for 4500 r/min continuous servo cycle

In the previous cycles, the three motors were not operating at the voltage limit. It is expected to save more energy for higher speed cycles that operate at the voltage limit because a lower negative d-axis current is required to weaken the flux during the high-speed operation using FI-SPMSM compared to the SPMSM. The 6000 r/min servo cycle (the desired cycle) was not evaluated due to encoder speed limitations (maximum speed of the encoder was 4500 r/min).

The designed FI-SPMSM has better dynamic loss minimization performance compared to the SPMSM and IPMSM for high-speed duty cycle servo applications like robots or printers. However, there are few servo applications require the servo motor to run at low-speed with full load torque like the motor used to hold the robot arm. In this kind of application, the copper loss dominates the total motor loss. For this kind of applications FW-SPMSM will achieve the lowest losses due to maximizing the airgap-flux from the magnet leading to lower stator current. To see the performance of the designed motor in servo applications that run at low-speed full torque operation, another continuous operational servo cycle was evaluated. In this cycle, the tested motors were accelerated from 0 to 3000 r/min in 150 ms, then the motor ran at 3000 r/min for 60 seconds. During this cycle, the rated torque (2.4 Nm) was applied using the load motor. 200% of the rated torque was applied to the tested motor during the acceleration period. Loss comparison for this cycle is shown in Fig. 2-51. For this cycle, the copper loss dominates the cycle loss. In this case, FI-SPMSM has 28% higher losses than SPMSM and 5% lower than IPMSM.

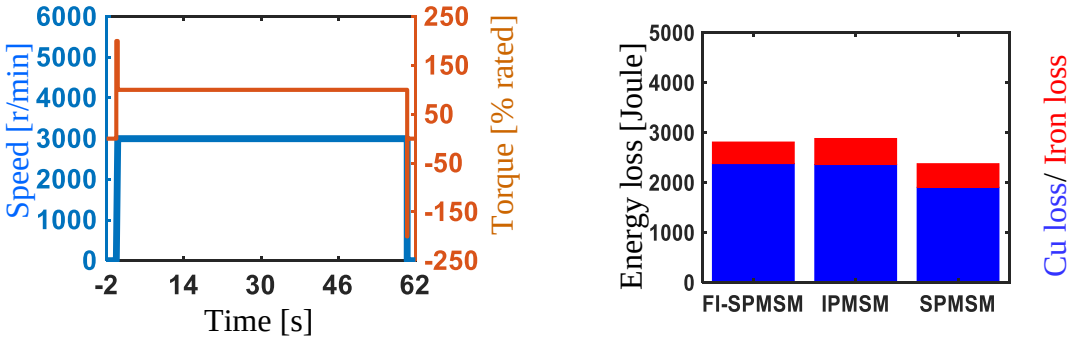

(a) 3000 r/min continuous servo cycle (b) measured cycle energy loss

Fig. 2-51 Measured Energy loss for the three rotors for 3000 r/min continuous servo cycle

FW-SPMSMs (usually called SPMSMs) achieve low copper loss compared to the FI-SPMSMs and IPMSMs, due to maximizing the airgap flux from the magnet achieving low energy lost in low-speed high-torque servo applications. This kind of motors is not suitable for injection-based self-sensing control like FI-SPMSMs and IPMSMs. Next chapter will present a methodology to design FW-SPMSM with enhanced self-sensing features, reducing the motor cost by removing the position sensor and the required long cable. This will improve the reliability of the servo drive while achieving a low copper loss with low energy loss.

Further investigation of the power loss which occurred in the designed motors will be investigated in the following subsection. The power loss will be partitioned among the motor parts and will be compared for the three motors.

2.4.3 Power loss partioining for the designed motors

In the previous section, the energy lost in the designed three motors were evaluated for several servo cycles. For high-speed partial-torque cycles as in the evaluated servo cycle in Fig. 2-50, FI-SPMSM achieved 40% lower energy loss compared to the SPMSM and 20% lower energy loss compared to the IPMSM. In this section, FEA simulations for the three motors were conducted when they ran at 4500 r/min and 1.6 Nm (66% rated torque) load torque. Fig. 2-52

shows the simulated power loss using FEA for the three motors, the FI-SPMSM achieves significantly lower stator iron loss leading to significantly achieving lower motor loss compared to the IPMSM and SPMSM.

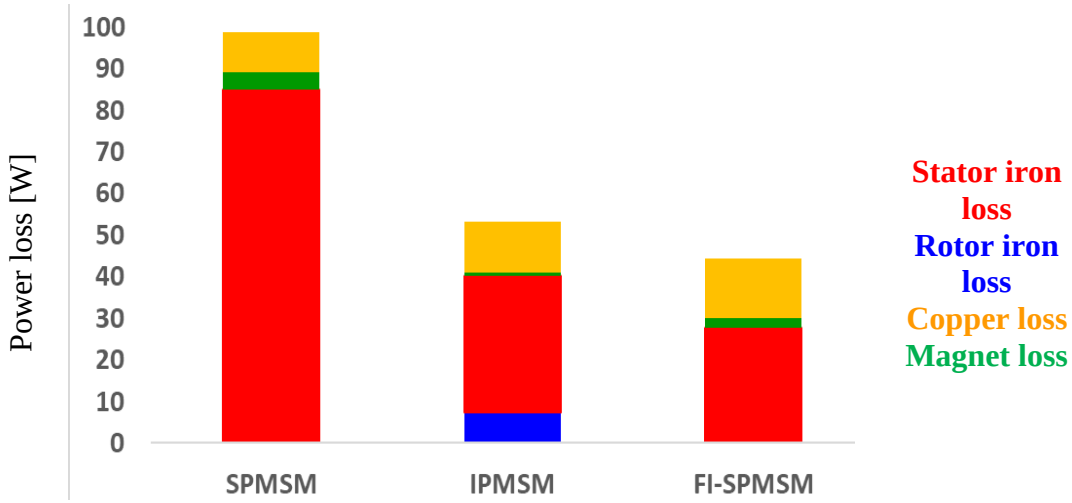

Fig. 2-52 Simulated power loss for the designed motors at 4500 r/min and 1.6 Nm

Fig. 2-53 shows the partitioned power loss for the three motors. The FI-SPMSM achieves the lowest stator iron loss compared to the IPMSM and SPMSM as in Fig. 2-53-a. However, this motor has the highest copper loss as in Fig. 2-53-c. This is because the FI-SPMSM has the lowest airgap flux linkage, leading to increasing the copper loss due to the extra current required to generate the same torque. The lowest flux linkage leads to significantly lower stator iron loss.

Both SPMSM and FI-SPMSM achieves a negligible rotor iron loss compared to the IPMSM as in Fig. 2-53-b. This due to the low leakage flux between the adjacent magnets in the rotor. However, the iron layer on top of the magnet of the IPMSM rotor provides a path for the flux to leak leading to more iron losses in the rotor and lowering the rotor flux linkage. On the other hand, this iron layer acts as a shield for magnets in the IPMSM rotor leading to achieve the lowest magnet eddy current loss as in Fig. 2-53-d. The FI-SPMSM achieves lower magnet eddy

current loss compared to the SPMSM due to using smaller magnets. Fig. 2-53-e shows the total rotor loss combining magnet and iron loss. The FI-SPMSM achieves the lowest rotor losses.

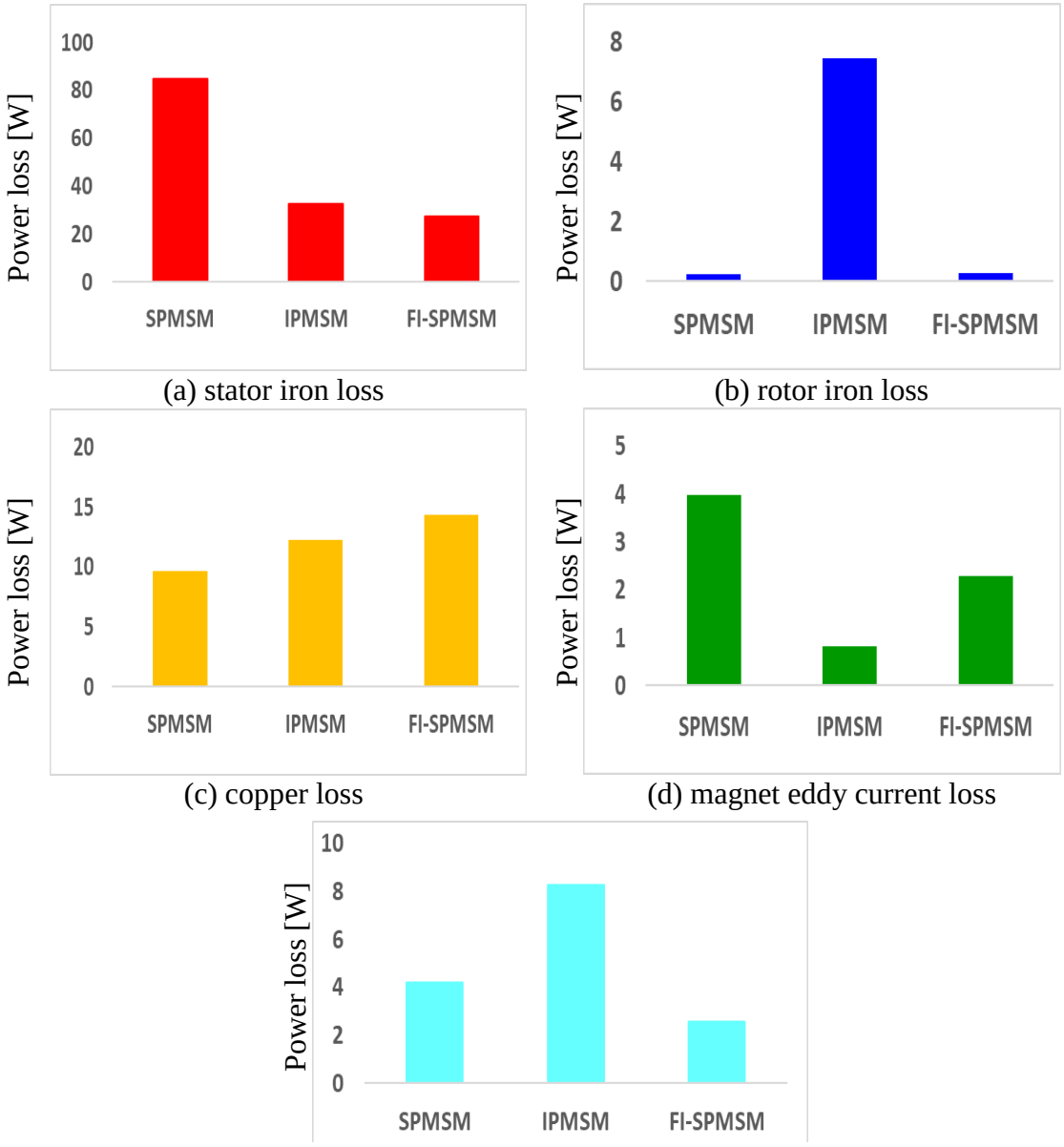

(a) stator iron loss

(b) rotor iron loss

(c) copper loss

(d) magnet eddy current loss

(e) rotor loss including magnet loss

Fig. 2-53 Simulated portioned power loss for the designed motors at 4500 r/min and 1.6 Nm

Fig. 2-54 shows the iron loss distribution for the three motors when they run at 4500 r/min and 1.6 Nm. The FI-SPMSM stator has the lowest iron loss in the stator back iron. While

the IPMSM rotor has a high iron loss in the iron layer on top of the magnet, this layer provides a path for the flux to leak.

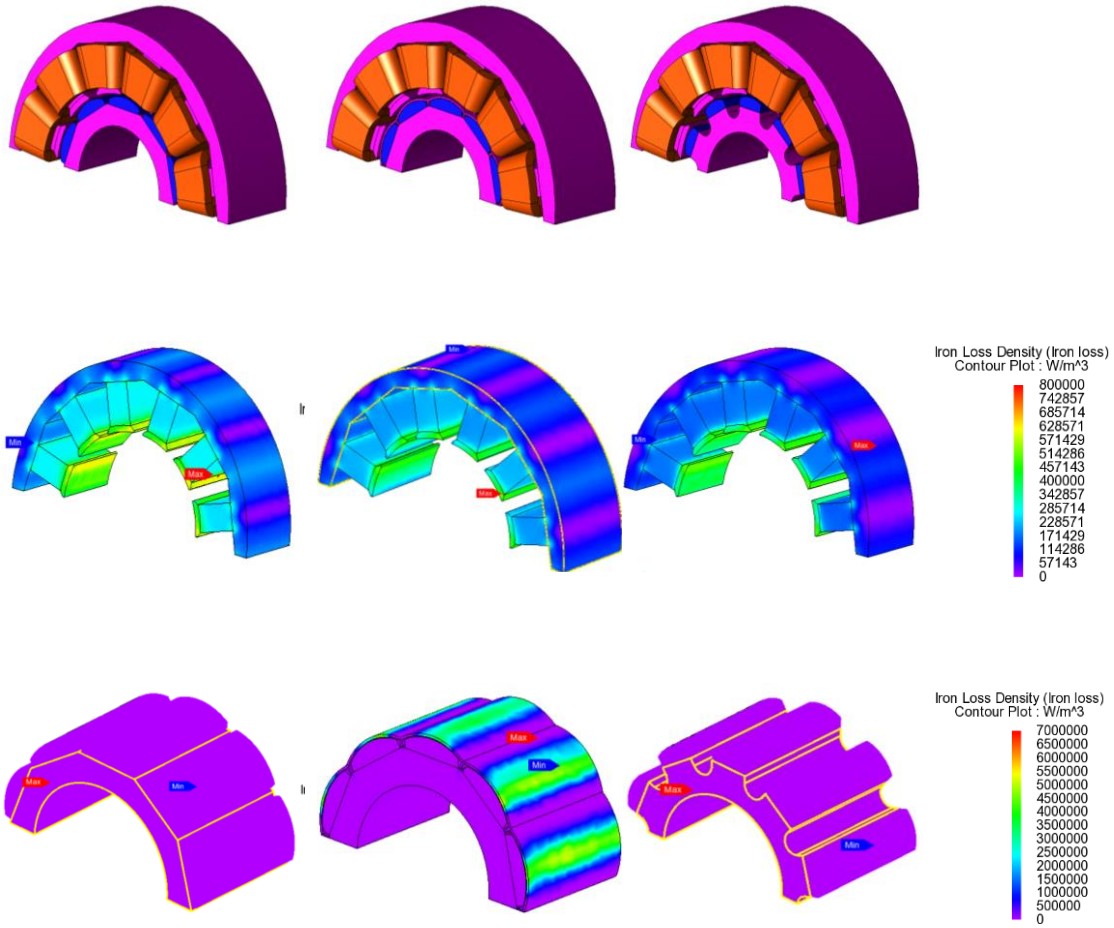

SPMSM IPMSM FI-SPMSM

Fig. 2-54 Iron loss distribution for the designed motors at 4500 r/min and 1.6 Nm

The magnet loss can be further reduced by segmenting the magnets. Fig. 2-55 shows the magnet eggy current loss for the designed motors, this figure also shows the losses for the FI-SPMSM rotor using 3 and 5 magnet segments. Using 5 magnet segments reduces the magnet loss to 1.7 W from 2.2 W for the 1 segment case. However, using 5 magnet segments increases the

manufacturing complexity of the motor and is not necessary for this negligible improvement in the magnet loss which is very small compared to the stator iron loss.

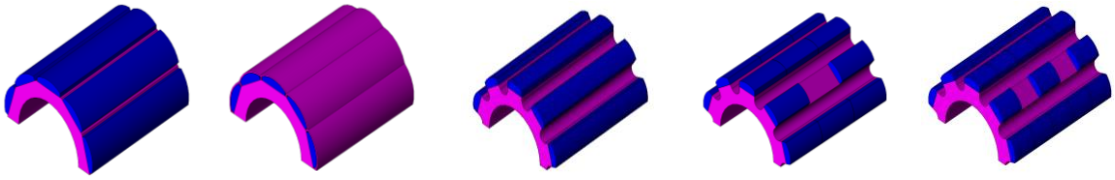

SPMSM – 1 seg. | IPMSM – 1 seg. | FI-SPMSM – 1 seg. | FI-SPMSM – 3 seg's | FI-SPMSM – 5 seg's

(a) evaluated rotors

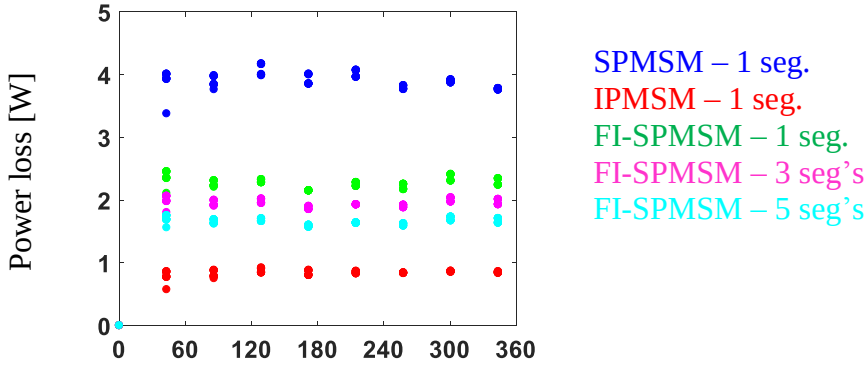

(b) magnet eddy current loss for the evaluated

Fig. 2-55 Simulated magnet eddy current loss for the designed motors at 4500 r/min and 1.6 Nm

The above analysis shows the benefits of the proposed FI-SPMSM design for servo applications. The previous analysis was performed on 1 HP size motors. Next section will evaluate the performance of the proposed FI-SPMSM design for different motor sizes.

2.5 Scalablility Analysis for the Designed FI-SPMSM Motor

In this section, scalability analysis for the designed motors is performed. The three motors are scaled down to 100 W and scaled up to 5 kW. Efficiency maps, iron loss maps, and energy lost in continuous operational servo cycles were evaluated using 2D-FEA.

2.5.1 Scaling down the designed motors to 100 W

The designed motors were scaled down to 100 W. For this small size motor, the airgap length is reduced to 0.3 mm and a 100 V DC link is used for this small size motor. Table 2-9 summarizes the main dimensions of the evaluated 100 W motors.

Table 2-9 Main dimensions of the designed 100 W motors

	Stator outer diameter	Rotor outer diameter	Airgap	Stack length	Resistance	Rated current	Rated torque	Number of turns	Magnet volume
SPMSM	39 mm	21.35 mm	0.3 mm	30 mm	7.54 Ω	0.65 Arms	0.32	90	100%
IPMSM	39 mm	21.35 mm	0.3 mm	30 mm	7.54 Ω	0.76 Arms	0.32	90	100%
FI-SPMSM	39 mm	21.35 mm	0.3 mm	30 mm	7.54 Ω	0.81 Arms	0.32	90	64%

Motors performance was evaluated using 2D-FEA. Efficiency and iron loss maps are generated and compared for the three motors as in Fig. 2-56. The SPMSM motor achieves 15% higher peak torque compared to the IPMSM motor, the difference is larger than the 1 Hp case due to using fixed airgap 0.3 mm which is not scaled by the same ratio that the rotor and stator are scaled. In this case, the leakage flux portion becomes larger compared to flux linkage leading to lower peak torque. The FI-SPMSM achieves 5% lower peak torque compared to the IPMSM. Hence the FI-SPMSM has the lowest airgap flux, this motor achieves the lowest iron loss as in Fig. 2-56-f.

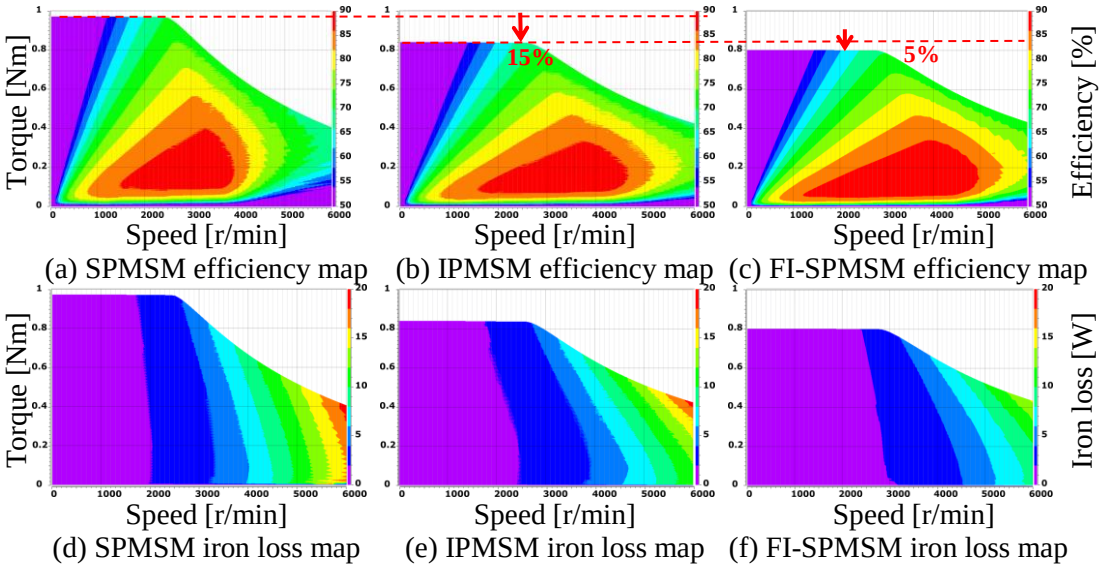

(a) SPMSM efficiency map (b) IPMSM efficiency map (c) FI-SPMSM efficiency map

(d) SPMSM iron loss map (e) IPMSM iron loss map (f) FI-SPMSM iron loss map

Fig. 2-56 Efficiency and iron loss maps for 100 W SPMSM, IPMSM, and FI-SPMSM

Motor inductance variation with load is then evaluated for the scaled down motors as in Fig. 2-57. The IPMSM motor has higher inductance compared to both SPMSM and FI-SPMSM due to the smaller effective airgap, this motor has 12% trackable saliency that can be used for injection-based self-sensing control. The FI-SPMSM has smaller inverted saliency about 5%, this small saliency ratio might be hard to track, this would make self-sensing control for the FI-SPMSM harder due to tracking smaller saliency ratio.

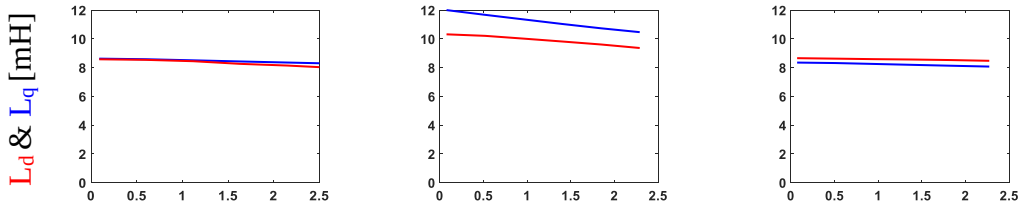

(a) SPMSM (b) IPMSM (c) FI-SPMSM

Fig. 2-57 Simulated inductance variation with load condition for the 100 W SPMSM, IPMSM, and FI-SPMSM

The performance of the 100 W scaled down motors during continuous operational servo cycles is then simulated. Fig. 2-58 shows the energy loss for the 4000 r/min, and 75% rated

torque cycle. The FI-SPMSM and IPMSM achieved lower energy loss compared to the SPMSM due to the lower negative d-axis flux weakening current that is required to run the motor at this speed, leading to a lower copper loss in addition to lower iron loss. As the speed increased, the iron loss becomes more significant leading to the FI-SPMSM to achieve lower energy loss compared to both IPMSM and SPMSM as in Fig. 2-59 for the 4500 r/min 67% torque cycle.

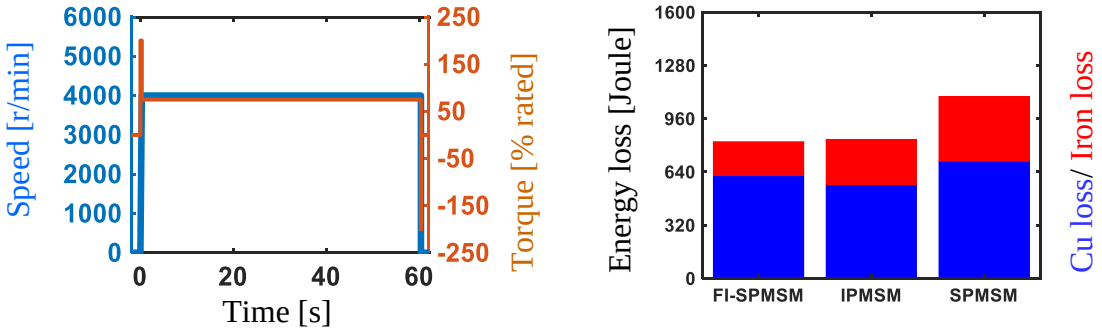

(a) 4000 r/min continuous servo cycle (b) measured cycle energy loss

Fig. 2-58 Simulated energy loss for the 100W motors ran at 4000 r/min continuous servo cycle

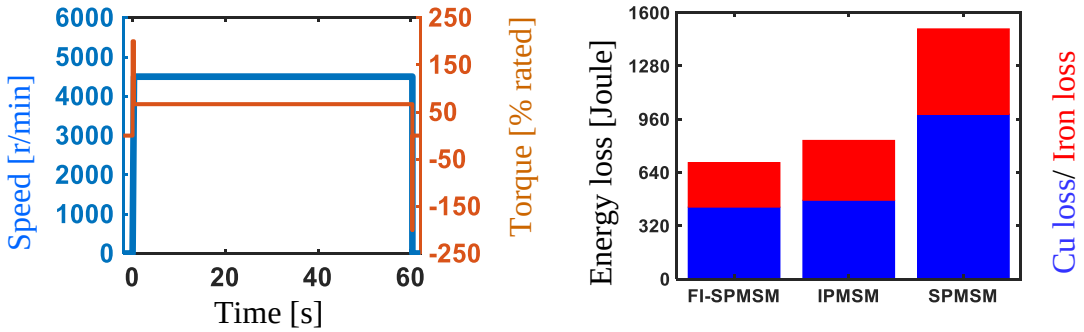

(a) 4500 r/min continuous servo cycle (b) measured cycle energy loss

Fig. 2-59 Simulated energy loss for the 100W motors ran at 4500 r/min continuous servo cycle

Copper loss dominates the motor loss for the small size motors due to the high number of turns and high resistance value. The key advantage of the IPMSM and FI-SPMSM for small size motor is that they require lower negative d-axis current to weaken the flux, leading to lower

copper losses in addition to the lower iron loss which is achieved due to lower airgap flux linkage.

For the low-speed high torque cycle, the SPMSM would provide the lowest cycle loss due to utilizing the magnet flux to minimize the motor current and copper losses which dominate the cycle loss. This is clear from the simulated results in Fig. 2-60, in which the motors run at low speed without weakening the flux while 100% torque is applied to the motors.

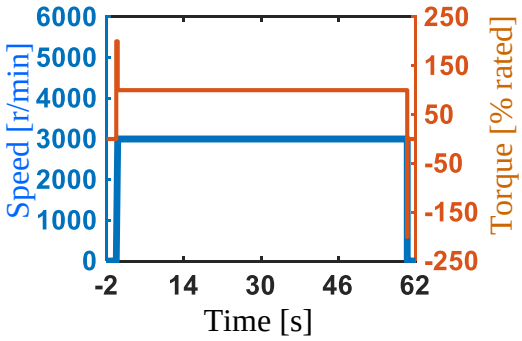

(a) 3000 r/min continuous servo cycle

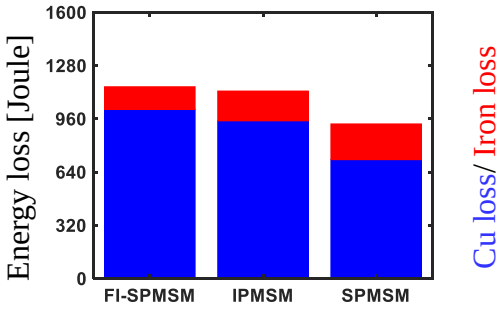

(b) measured cycle energy loss

Fig. 2-60 Simulated energy loss for the 100W motors ran at 3000 r/min continuous servo cycle

2.5.2 Scaling up the designed motors to 5 kW

The designed motors are scaled up to 5 kW. For this large size servo motor, the airgap length is set to 0.75 mm for the IPMSM and 1mm for both FI-SPMSM and SPMSM to include the impact of the retaining sleeve, which is required to protect the magnet when the motor during the high-speed operation. 270 V DC link is used to evaluate the dynamic loss minimization performance of the scaled motors. Table 2-10 summarizes the main dimensions of the evaluated 5 kW motors.

Table 2-10 Main dimensions of the designed 5 kW motors

	Stator outer diameter	Rotor outer diameter	Airgap	Stack length	Resistance	Rated current	Rated torque	Number of turns	Magnet volume
SPMSM	121 mm	66.65 mm	1 mm	100	0.035 Ω	15.6	15.9	18	100%
IPMSM	121 mm	66.9 mm	0.75	100	0.035 Ω	18.4	15.9	18	100%
FI-SPMSM	121 mm	66.65 mm	1 mm	100	0.035 Ω	19.8	15.9	18	64%

Motors performance was evaluated using 2D-FEA. Efficiency and iron loss maps are generated and compared for the 5 kW motors as in Fig. 2-61. The SPMSM motor achieves 7% higher peak torque compared to the IPMSM motor, the difference is smaller than the 1 Hp case due to using smaller airgap length for the IPMSM. The FI-SPMSM achieves 10% lower peak torque compared to the IPMSM. Hence the FI-SPMSM has the lowest airgap flux, this motor achieves the lowest iron loss as in Fig. 2-61-f.

Large motors have lower resistance due to using a lower number of turns, leading to achieving a lower copper loss. For this reason, the FI-SPMSM has a wide high-efficiency region due to achieving very low iron loss compared to the IPMSM and the SPMSM motors.

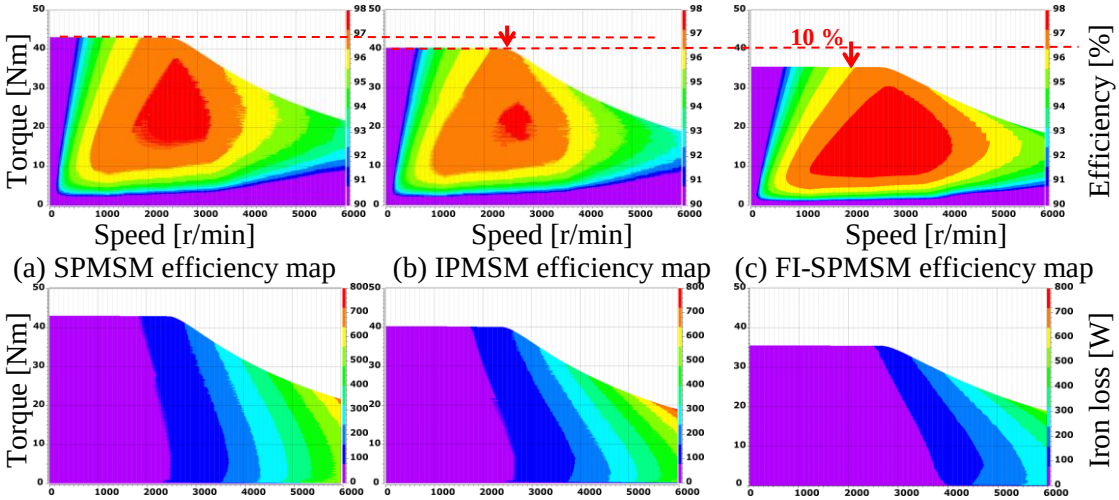

(a) SPMSM efficiency map (b) IPMSM efficiency map (c) FI-SPMSM efficiency map

(d) SPMSM iron loss map (e) IPMSM iron loss map (f) FI-SPMSM iron loss map

Fig. 2-61 Efficiency and iron loss maps for 5 kW SPMSM, IPMSM, and FI-SPMSM

Motor inductance variation with load is then evaluated for the scaled-up motors as in Fig. 2-62. The FI-SPMSM still achieve a small inverted saliency that can be used for self-sensing purposes.

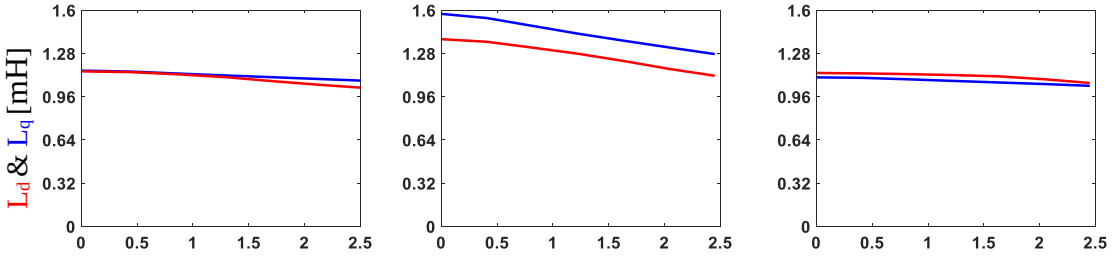

(a) SPMSM (b) IPMSM (c) FI-SPMSM

Fig. 2-62 Simulated inductance variation with load condition for the 5 kW SPMSM, IPMSM, and FI-SPMSM

The performance of the 5kW scaled up motors during continuous operational servo cycles is then simulated. Fig. 2-63 shows the energy loss for the 4000 r/min, and 75% rated torque cycle. The FI-SPMSM achieved lower energy loss compared to the SPMSM and IPMSM due to the significantly lower iron loss which dominates the large size motors loss. Similar results are shown in Fig. 2-64 for the 4500 r/min 67% torque cycle.

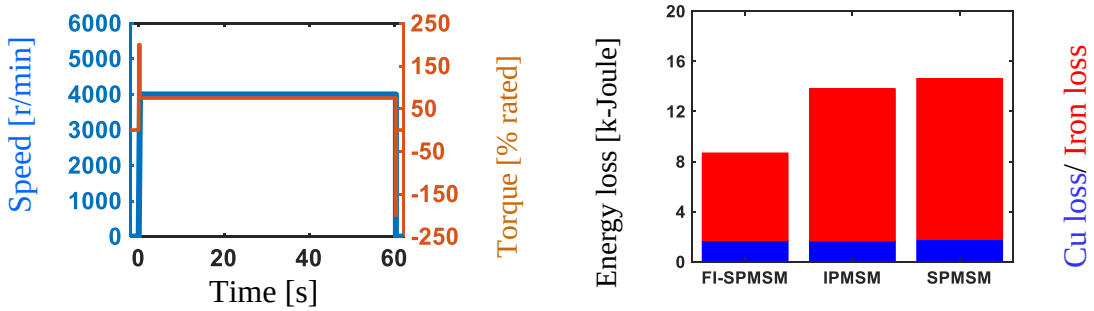

(a) 4000 r/min continuous servo cycle (b) measured cycle energy loss

Fig. 2-63 Simulated energy loss for the 5 kW motors ran at 4000 r/min continuous servo cycle

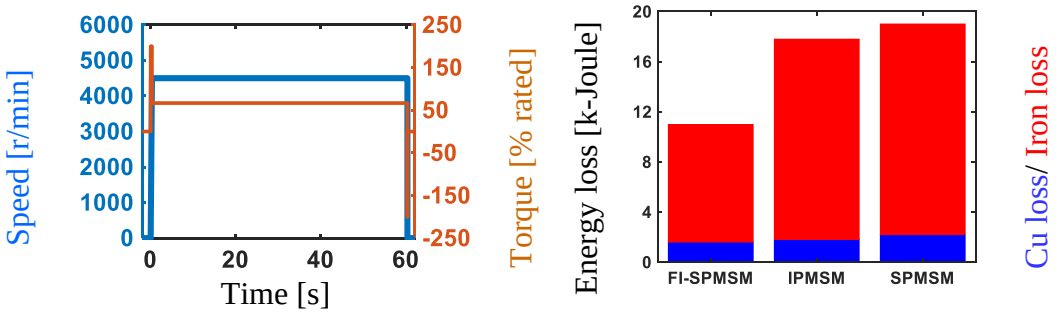

(a) 4500 r/min continuous servo cycle (b) measured cycle energy loss

Fig. 2-64 Simulated energy loss for the 5kW motors ran at 4500 r/min continuous servo cycle

Iron loss is a significant portion of the motor loss in large motors. These motors typically achieve higher efficiency compared to the smaller size motor due to the lower copper loss which occurred due to the small resistance value which results of using a lower number of turns with larger wire diameter for the stator winding. To evaluate the performance of the proposed 5 kW FI-SPMSM, the energy lost in the 3000 r/min, full torque cycle is evaluated for the three motors as in Fig. 2-65. The FI-SPMSM has a larger copper loss compared to both motors. However, this motor achieves lower cycle energy loss compared to both SPMSM and IPMSM, due to the significantly lower iron loss.

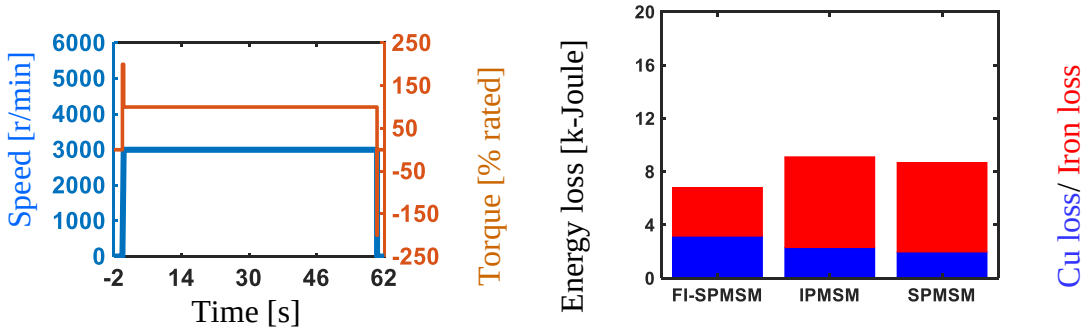

(a) 3000 r/min continuous servo cycle (b) measured cycle energy loss

Fig. 2-65 Simulated energy loss for the 5 kW motors ran at 3000 r/min continuous servo cycle

2.6 Summary

This chapter presents a fair comparison between the two common PM servo motor types found in the literature, SPMSM and IPMSM, followed by a methodology to design a new servo motor with less magnet material compared to the standard designs. The proposed design is called the FI-SPMSM, which has a significantly lower loss for high-speed servo cycles. The key observations and conclusions from this chapter are summarized as follows.

- SPMSM maximizes the airgap flux density per magnet volume. While IPMSM has lower airgap flux compared to the SPMSM, this motor achieves lower iron loss during high-speed operation and has trackable saliency that can be used for self-sensing control.
- The proposed FI-SPMSM combines the benefits of both SPMSM and IPMSM configurations. It maximizes the airgap flux density per magnet volume like an SPMSM, and it has a low iron loss and detectable saliency like an IPMSM.
- The proposed FI-SPMSM uses only 64% of the magnet volume in the SPMSM, which significantly reduces the manufacturing cost of this motor.
- Copper loss dominates the cycle loss for low-speed high torque cycles. In these kinds of cycles, the SPMSM motor will have the lowest cycle loss.
- Iron loss becomes significant for high speed, low torque cycles. In this case, FI-SPMSM will have the lowest losses compared to both SPMSM and IPMSM.
- A significant amount of energy could be saved during high-speed continuous operational servo cycles if the proposed FI-SPMSM is adopted. The proposed rotor structure could save more energy for higher speed cycles when the motor is running at the voltage limit.

- The decreased thermal loading (lower cycle energy loss) could be used to enable faster acceleration or to downsize the machine, both of which are very useful outcomes for servo motor applications.
- The q-axis flux barriers in the FI-SPMSM motor improves the motor self-sensing performance through improving the motor saliency, these barriers also improve the motor torque production though reducing the magnet leakage flux.
- The proposed FI-SPMSM design can save a significant amount of energy when it is used in large size servo motors, due to the significantly lower iron loss, which dominates the large size motor losses.
- The IPMSM motor achieves a low eddy current magnet loss, however, the iron loss in this motor is significant.
- The proposed FI-SPMSM design achieve lower magnet eddy current loss and rotor iron loss compared to the standard FW-SPMSM design.

Chapter 3 FW-SPMSM Servo Motor Design with Enhanced Self-Sensing Properties

In the previous chapter, the FI-SPMSM design was proposed. This design has good dynamic performance and could save a significant amount of energy for high-speed partial-torque servo cycles. This design also has good self-sensing properties which will be discussed later in chapter 6 of this thesis. However, FI-SPMSM achieves lower peak torque and higher losses compared to FW-SPMSM for servo applications that run at low-speed and high torque, due to the higher copper loss.

In this chapter, a methodology to design an FW-SPMSM for servo applications with enhanced self-sensing properties, enabling accurate and high dynamic performance self-sensing, without sacrificing the peak torque capability of standard FW-SPMSM design is presented. This requires an FW-SPMSM servo motor with detectable saliency that doesn't degrade with increasing the load condition. The designed FW-SPMSM using the proposed design methodology achieves low energy loss for servo applications that run at low-speed high torque. This design can be controlled using saliency-based self-sensing techniques even during overload conditions.

First, an FW-SPMSM servo motor with asymmetrical rotor structure using shifted PM's is evaluated and used as a baseline motor. Then a methodology to design symmetrical rotor structue FW-SPMSM that can achieve attractive self-sensing properties without affecting the power conversion performance of the motor is presented. Then, an optimization process to design a 3.7 kW FW-SPMSM motor using the developed design methodology is presented. The

performance of the proposed design is compared with the baseline motor experimentally and using FEA simulations. Finally, scalability analysis for the design motor is conducted.

3.1 FW-SPMSM Servo Motor Design Requirements and Goals

FW-SPMSMs have lower losses compared to FI-SPMSMs during low-speed high-torque operation. These motors use more magnetic materials compared to FI-SPMSMs and require lower current to achieve the desired torque compared to FI-SPMSMs (FW-SPMSMs have larger airgap flux).

Typical FW-SPMSMs have a small saliency, which makes these type of motors not suitable for injection-based self-sensing control. Many researchers have proposed modifying machine geometry to create a small saliency. However, the proposed designs might degrade the power conversion capability of the motor including losses, average torque, ripple torque, and cogging torque. These motors were proposed for general applications. However, high-performance FW-SPMSM design for servo applications, i.e.motors with very low ripple and cogging torque, are not reported in the literature.

Servo motors are designed to achieve very low ripple and cogging torque, which helps by improving the speed regulation of this kind of motors allowing accurate position, speed, and acceleration control. In this chapter, a 3.7 kW FW-SPMSM servo is designed. The cogging and ripple torque requirements for servo applications were discussed in chapter 1 and repeated in Table 3-1 for convenience.

Table 3-1 The 3.7 kW FW-SPMSM servo motor cogging and ripple torque requirments

Specification	Value
Cogging torque	< 0.5 % rated torque
Ripple torque	< 2 % rated torque

The selected baseline motor in this research has 24 slots double-layer full pitch distributed winding stator. Table 3-2 summarizes the key features of the baseline motor. Fig. 3-1 shows a cross-sectional view of the baseline motor. This design has asymmetrical rotor structure using shifted ring-shaped magnets.

Table 3-2 The FW-SPMSM baseline motor specifications

Specification	Value	Specification	Value
Rated power	3.7 kW	Rated frequency	133.33 Hz
Rated speed	2000 r/min	Rated current	6.8 A_{rms}
Max speed	4000 r/min	Rated torque	17 Nm
Number of poles	8	Peak torque	43 Nm

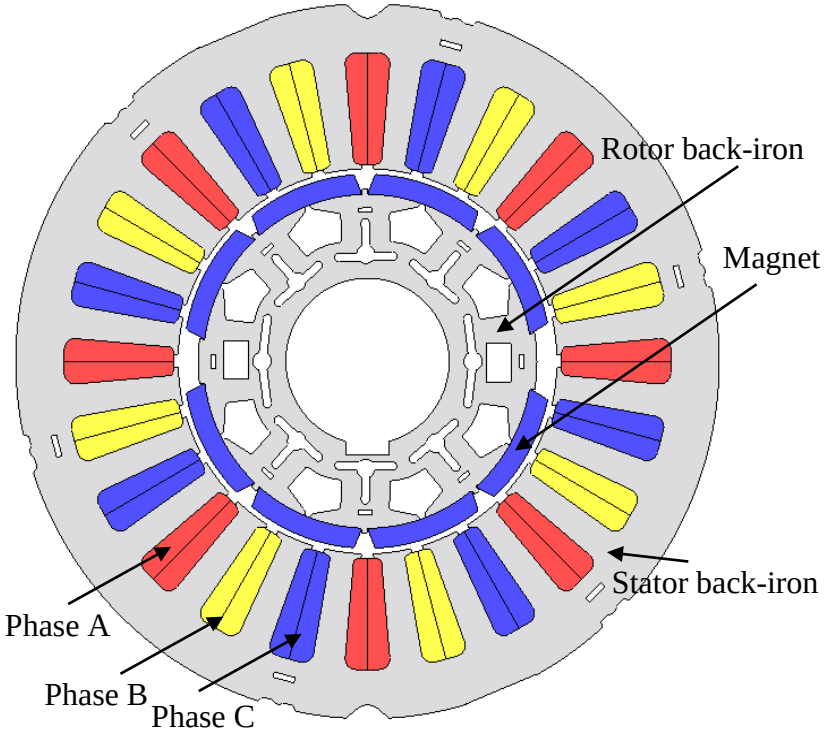

Fig. 3-1 The 3.7 kW FW-SPMSM baseline motor (asymmetrical rotor)

To achieve the desired cogging and ripple torque requirements using ring magnets, an asymmetrical rotor design is used in the baseline motor. To evaluate this methodology, 2D-FEA simulation was performed using symmetrical rotor design with ring magnets, then using asymmetrical rotor design with shifted ring magnets. To simplify the simulation, a solid rotor without any flux barriers or rotor holes was used as in Fig. 3-2.

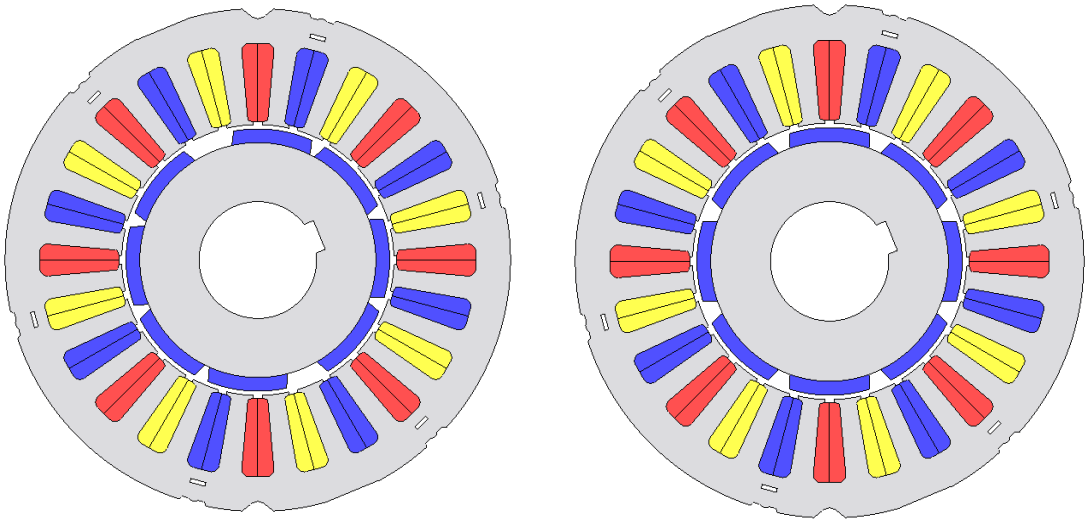

(a) asymmetrical rotor design (b) symmetrical rotor design

Fig. 3-2 Cross-sectional view of the symmetrical and asymmetrical rotor designs using ring magnets witout flux barriers

Fig. 3-3-a compares the back-EMF waveform calculated at 2000 r/min for both designs. Fig. 3-3-b compares the cogging torque for both designs. Fig. 3-4 compares the back-EMF for both designs spectrally. The symmetrical rotor design using ring magnets has higher fundamental component compared to the asymmetrical rotor design with shifted magnets, however, the back-EMF harmonics (mainly 5^{th},7^{th}, and 11^{th}) are significantly higher in the symmetrical rotor design, this leads to significantly higher cogging torque. For this reason, ring magnets with symmetrical rotor design are not suitable for servo applications.

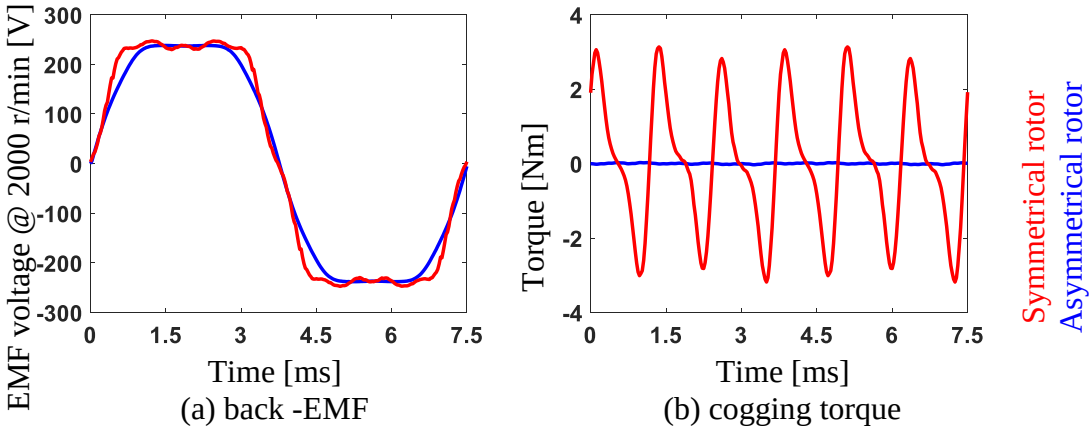

(a) back -EMF (b) cogging torque

Fig. 3-3 Back-EMF and cogging torque comparison between symmetrical and asymmetrical rotor designs using ring magnets

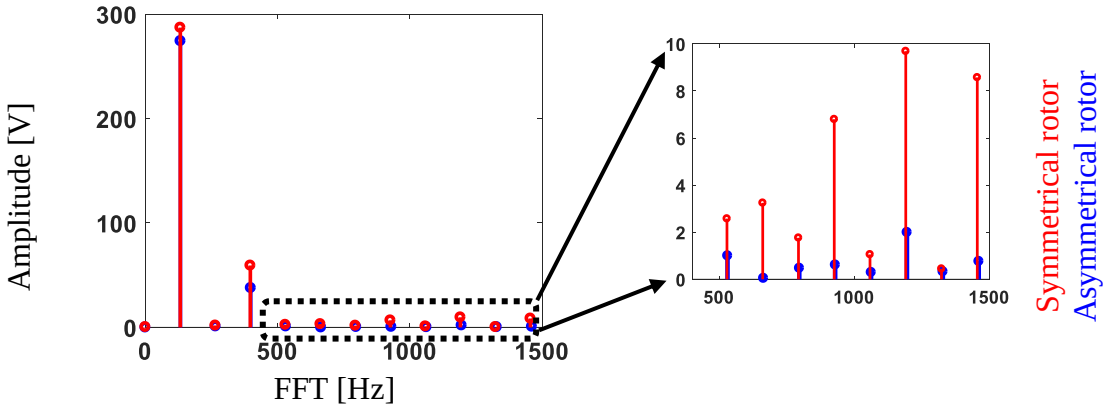

Fig. 3-4 Back-EMF FFT comparison between symmetrical and asymmetrical rotor designs using ring magnets

In the asymmetrical rotor design, 4 pieces of magnets are placed close to each other for each half, then the angle between the two half's is adjusted to cancel the airgap flux and back-EMF harmonics achieving significantly low cogging torque. To discuss this concept in more detail, the airgap flux for phase A is calculated using FEAby summing the flux for each coil in that phase. This is done for both symmetrical and asymmetrical rotor designs using ring magnets.

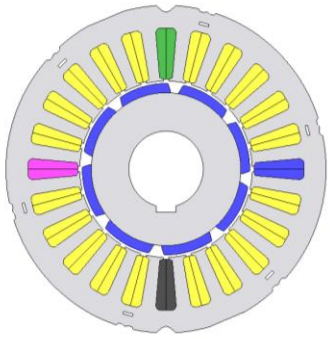

(a) positive coils for phase A

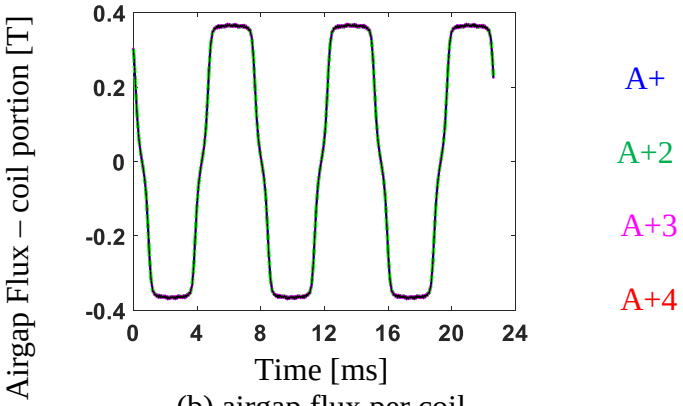

(b) airgap flux per coil

Fig. 3-5 Airgap flux linkage per coil for the symmetrical rotor design using ring magnets

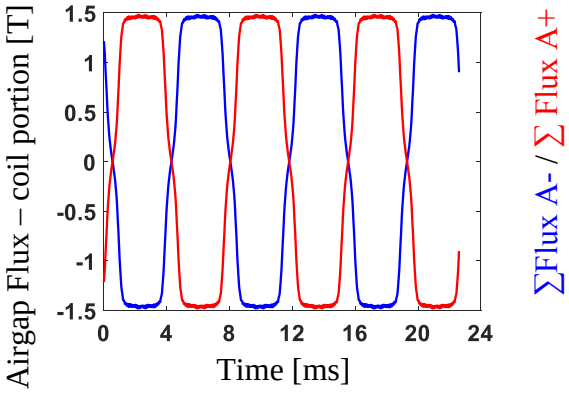

(a) positive and negative coils flux linkage for phase A

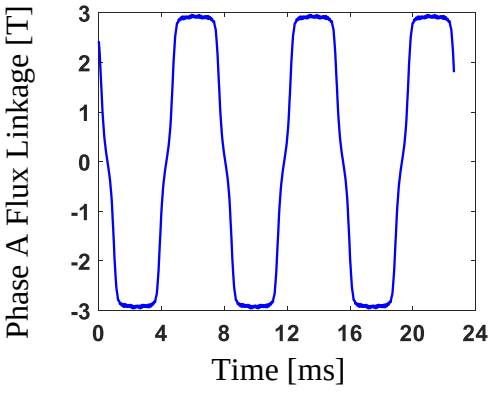

(b) phase A flux linkage

Fig. 3-6 Airgap flux linkage for phase A using the symmetrical rotor design using ring magnets

Fig. 3-5 shows the airgap flux linkage for each conductor in one direction (current going into the page). Because the magnet is uniformly distributed along the rotor, and full pitch winding is used, the airgap flux per conductor is identical for the 4 conductors of phase A. To calculate the total airgap flux linkage for phase A, the flux for each coil is added together. This is done for both positive and negative coils (current going into the page and returning out of the page). Fig. 3-6 shows the total airgap flux for phase A.

To verify the previous results, Phase A back-EMF is calculated as in (3-1) And compared with the calculated back-EMF from the FEA as in Fig. 3-7. This result verifies the used methodology.

$$EMF_{phase\ A} = \text{Flux linkage A} * \omega_r * \mu_{iron} \quad (3\text{-}1)$$

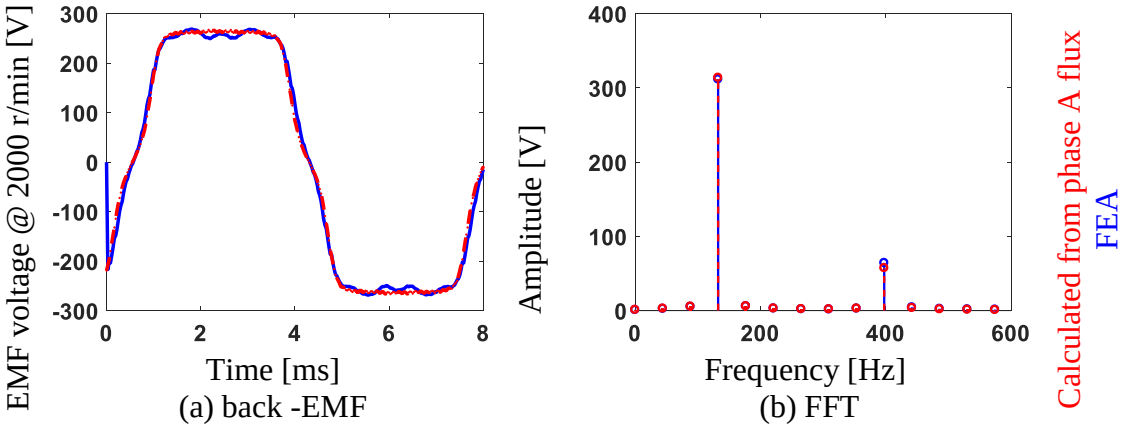

Fig. 3-7 Symmetrical rotor design using ring mangets back-EMF calculated using FEA and using (3-1)

The same methodology is used to calculate the airgap flux linkage per conductor for phase A for the asymmetrical rotor design. The results are shown in Fig. 3-8. The airgap flux per coil is not identical for each coil as in the symmetrical rotor design. This happens because the magnet is distributed non-uniformly around the rotor. The airgap flux per coil is not purely periodic as shown in Fig. 3-8-b. However, phase A flux which is obtained by adding the airgap flux from each coil is periodic and smooth as in Fig. 3-9-b.

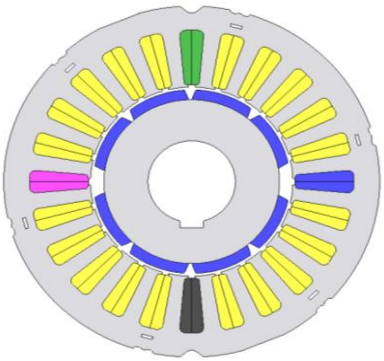

(a) positive coils for phase A

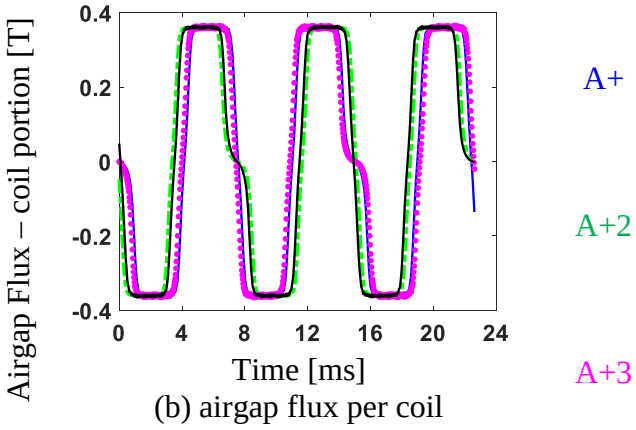

(b) airgap flux per coil

Fig. 3-8 Airgap flux linkage per coil for the asymmetrical rotor design

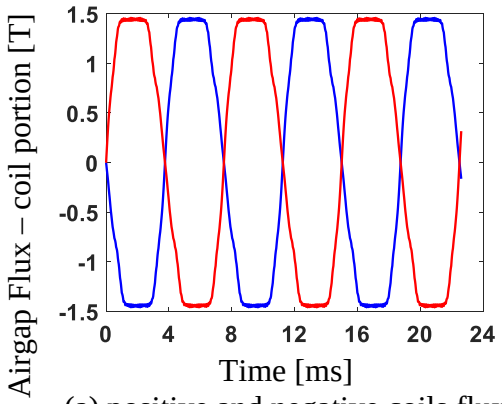

(a) positive and negative coils flux linkage for phase A

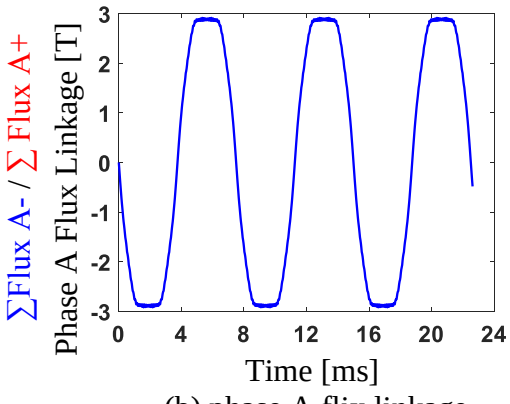

(b) phase A flix linkage

Fig. 3-9 Airgap flux linkage for phase A using the asymmetrical rotor design

Then the back-EMF was calculated using (3-1) and compared with the calculated back-EMF from the FEA as in Fig. 3-10, this verifies the previous analysis.

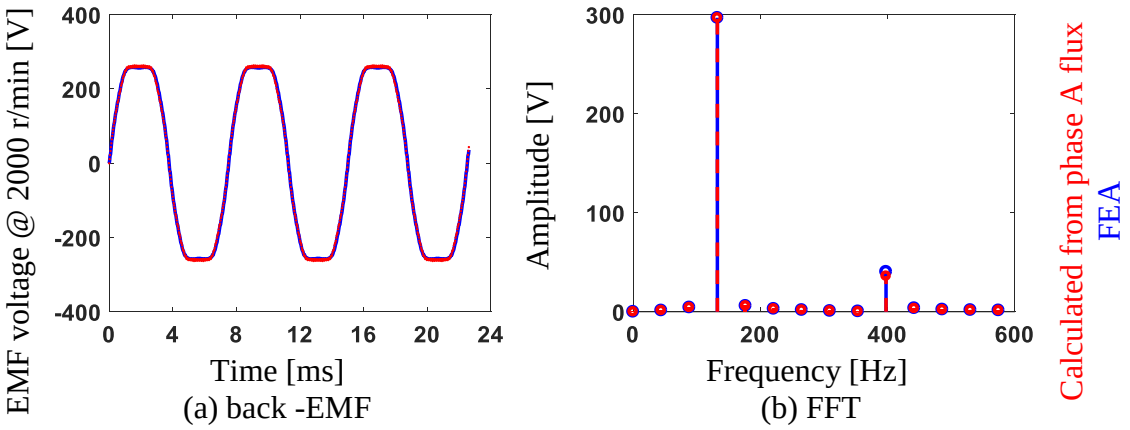

Fig. 3-10 Asymmetrical rotor design back-EMF calculated using FEA and using (3-1)

From the previous analysis the asymmetrical rotor design can achieve very low ripple and cogging torque. The asymmetry is designed to achieve the desired flux per coil, then the sum of the coil fluxes will achieve low harmonics and low cogging and ripple torque. Fig. 3-11 shows the impact of magnet asymmetry (the gap between adjacent magnets) on the airgap flux for a certain coil.

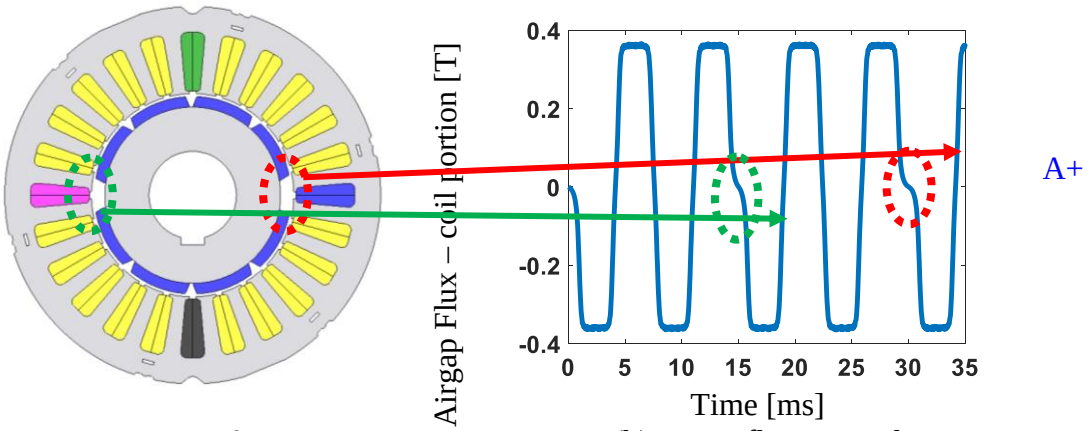

Fig. 3-11 Impact of magnet asymmetricity on the airgap flux per coil

Fig. 3-12 compares the flux per coil for the symmetrical and asymmetrical rotor designs using ring magnets. The phase flux linkage for both designs is periodic. The asymmetric design

has lower 3rd harmonic compared to the symmetric design (the flux shape is closer to a sinewave shape).

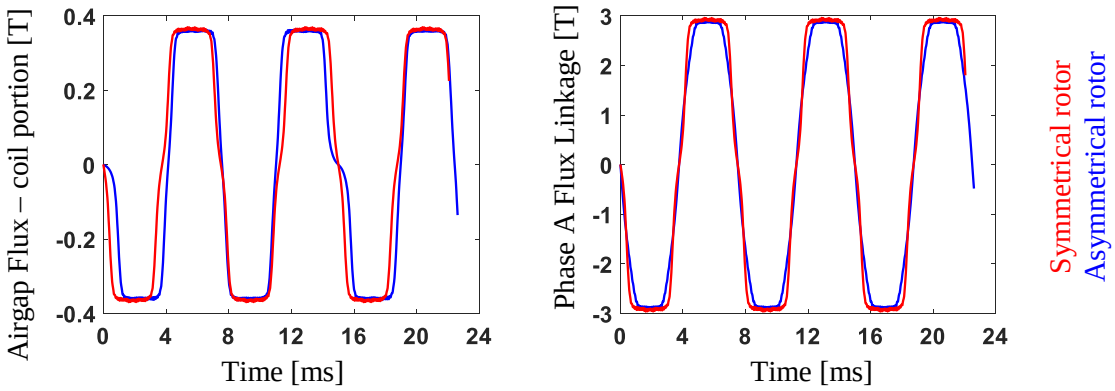

(a) positive and negative coils flux linkage for phase A

(b) phase A flux linkage

Fig. 3-12 Airgap flux per coil and phase flux comparison between symmetrical and asymmetrical rotor designs using ring magnets

The asymmetrical rotor design is very effective at canceling the airgap flux and back-EMF harmonics achieving very low cogging and ripple torque. However, the center of mass in this design will be different than the center of rotation (center of the rotor), this would cause significant vibration and mechanical issues. To overcome that, asymmetric rotor holes and flux barriers were designed to move the center of mass back to the center of rotation.

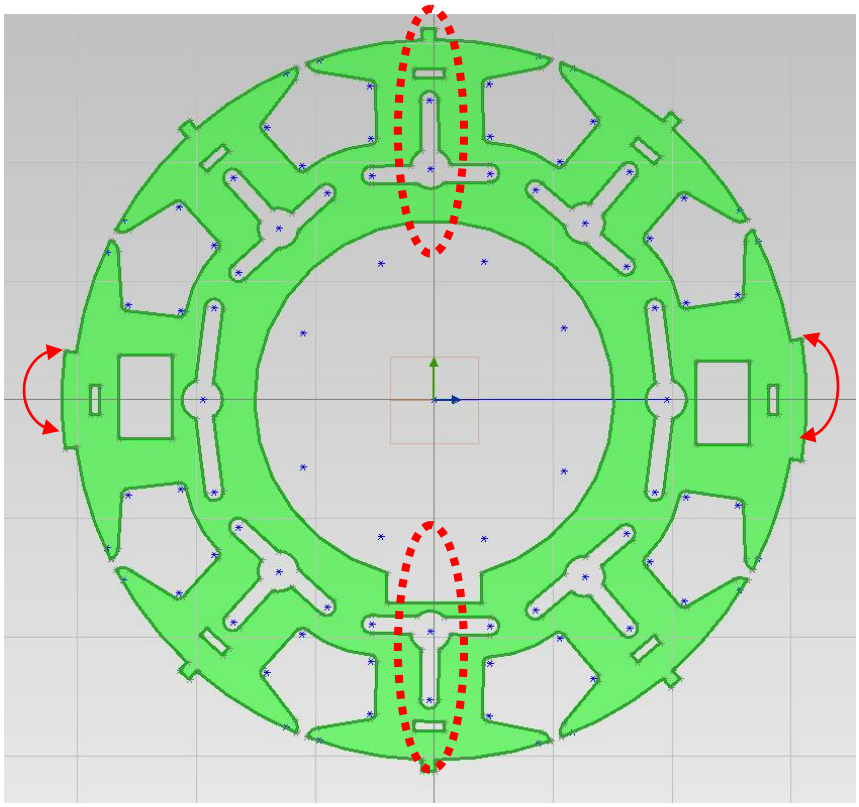

Fig. 3-13 Asymmetrical flux barriers and rotor holes to move the center of mass to the center of rotaion for the aysmetric design

The rotor holes are very effective at moving the center of mass to match the center of rotation, these holes force the magnet flux to flow in a smaller iron path, leading to a saturating the rotor flux path leading to a decrease in the d-axis inductance and creating a small saliency for this motor. This also affects the torque production of the motor, in which the d-axis flux will be lower and lower back EMF would be achieved. Fig. 3-14 compares the magnetic flux density for the asymmetric rotor design with and without the rotor holes. Adding the rotor holes increases the magnetic flux in the rotor iron and saturates the rotor iron as in Fig. 3-14-a.

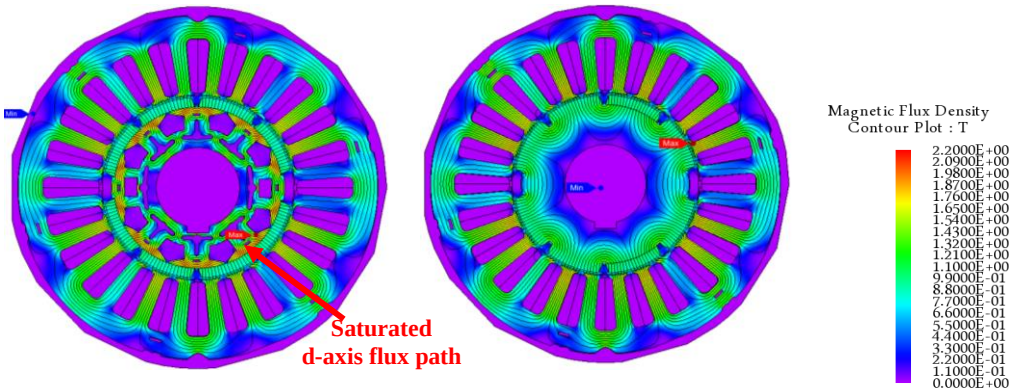

(a) asymmetrical rotor design with flux barriers (b) asymmetrical rotor design without flux barriers

Fig. 3-14 No load flux density and flux line comparison between the asymmetric rotor design with and without flux barriers

Fig. 3-15-b shows the cogging torque for the asymmetrical rotor design with and without the rotor holes. In both cases, very low cogging torque that meets the servo application requirements is achieved. This is because the rotor holes have a small impact on the motor cogging torque due to not deeply saturating the rotor iron with the rotor holes. Fig. 3-15-a shows the back-EMF with and without using the flux barriers for the asymmetrical rotor design. Adding the flux barriers saturates the d axis flux path in the rotor, and slightly reduces the back-EMF voltage by 6%.

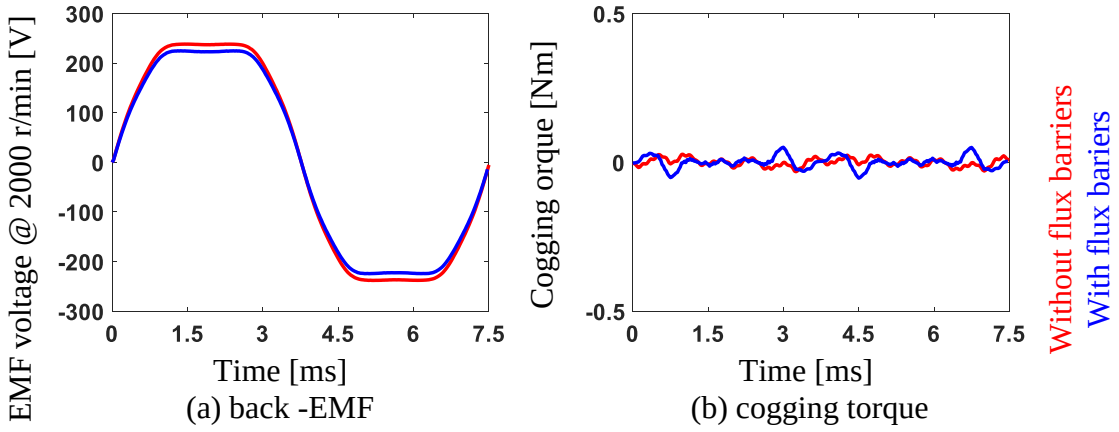

(a) back -EMF (b) cogging torque

Fig. 3-15 Back-EMF and cogging torque comparison between asymmetrical rotor design with and without flux barriers

Achieving lower back-EMF by adding the flux barriers leads to lower torque for the same excitation current by the same percentage (6% lower torque at the same current) as in Fig. 3-16-a, both designs achieve very low ripple torque. Fig. 3-16-b compares the saliency ratio with and without the rotor holes for the asymmetrical rotor design. Adding the rotor holes decreases the d-axis inductance and improves the saliency ratio. However, both motors achieve similar saliency at 200% load when the winding current saturates the d-axis inductance. The rotor holes are effective to move the center of mass back to the center of rotation. They also improve the self-sensing performance of the motor but will slightly decrease the back-EMF and torque production of the motor.

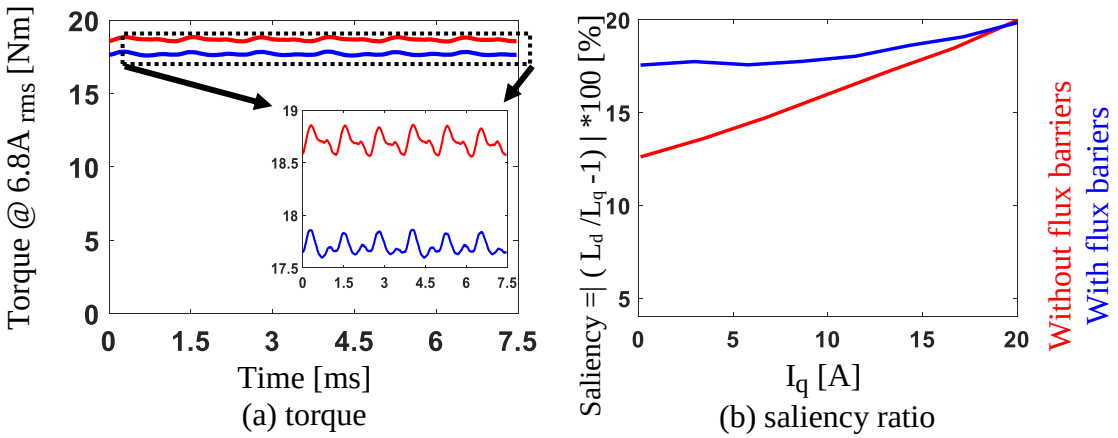

Fig. 3-16 Torque and saliency ratio comparison between asymmetrical rotor design with and without flux barriers

Fig. 3-17 shows the dq axis inductance variation with increasing the load torque (q-axis current). Adding the rotor holes decreases the d-axis inductance which improves the self-sensing performance.

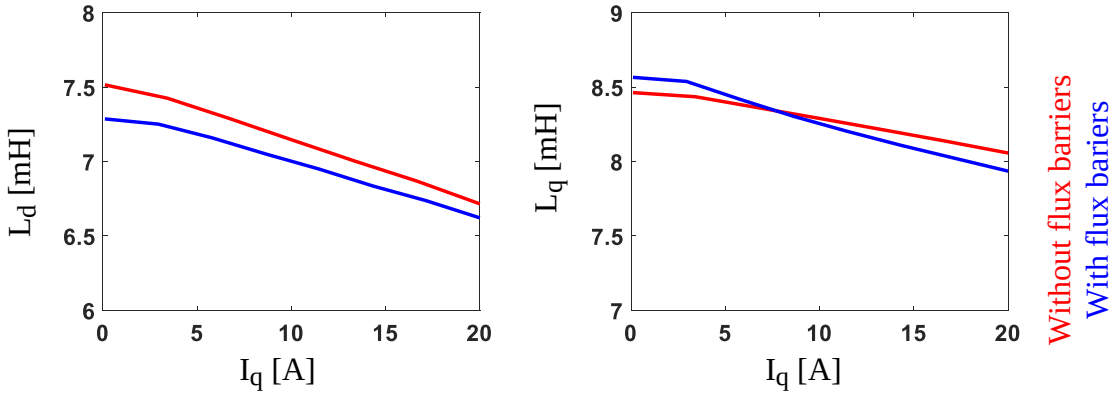

(a) d-axis inductance (b) q-axis inductance

Fig. 3-17 Dq-axis inductance comparison between asymmetrical rotor design with and without flux barriers

The d and q axis inductance in the asymmetrical design are cross-coupled in which both L_d, L_q decreases with increasing the load. This design is sensitive to the tolerance of placing the magnets on the rotor. A small error will lead to an increase in the cogging and ripple torque (harmonic cancellation will not be fully achieved).

3.2 Design Methodolgy for Symmetrical rotor FW-SPMSM Servo Motor with Enhanced Self-Sensing Properties

In this section, a methodology to design a FW-SPMSM with symmetrical rotor structure with enhanced self-sensing properties is presented. The methodology starts with identifying the key design variables that impact the self-sensing properties of the FW-SPMSM designed for servo applications. Then these parameters will be optimized to achieve the desired motor power conversion and self-sensing performance. The tradeoff between self-sensing and power conversion performance are investigated using 2D FEA using JMAG™ Designer software. These key design variables are discussed below.

- ***Magnet shape***

To achieve very low cogging and ripple torque, the magnet needs to be shaped to achieve sinusoidal back-EMF with low harmonics. Bread-loaf or arc shape magnets can be used. To realize the impact of magnet shape on the motor self-sensing properties, three rotors were designed using arc, bread loaf, and thick bread loaf magnets. Fig. 3-18 shows the designed rotors.

Fig. 3-19 shows the inductance and saliency ratio variation with motor current. The designed rotor with bread loaf magnet has similar q-axis inductance to the one with arc magnets. Bread loaf magnets are thicker in the center where the d-axis flux path pass leading to lower d-axis inductance with increasing the saliency ratio by a factor of two. Further increase in the bread-loaf magnet thickness leads to lower d-axis inductance, however, the q-axis inductance will also slightly decrease due increasing the magnet edge thickness where the q-axis flux path pass leading to small enhancement in the motor saliency as can be seen in Fig. 3-19-c.

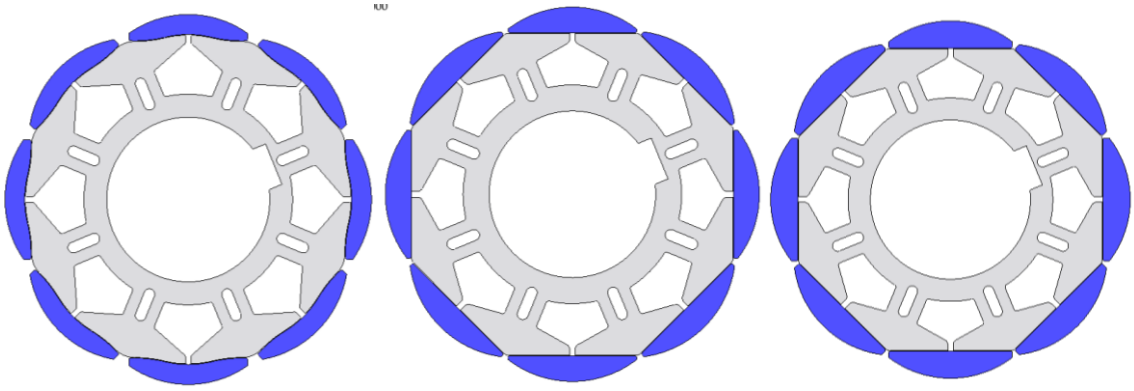

(a) designed rotor using arc shape magnet

(b) designed rotor using bread loaf magnet

(c) designed rotor using thick bread loaf magnet

Fig. 3-18 The designed rotors using different magnet shapes

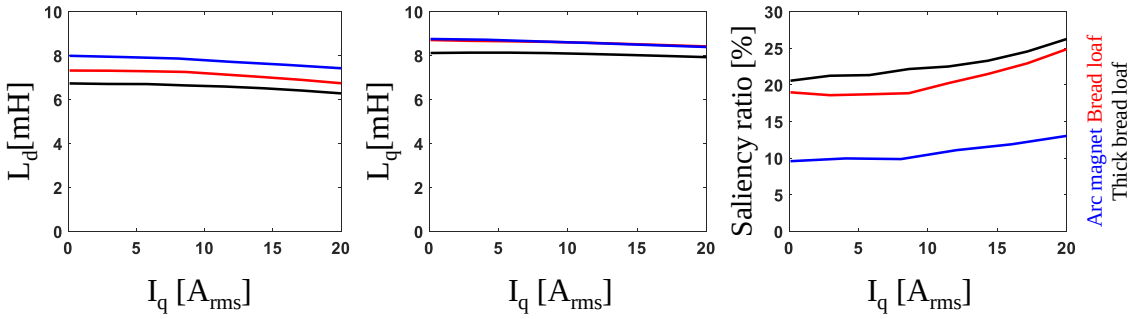

(a) d-axis inductance (b) q-axis inductance (c) saliency ratio

Fig. 3-19 Motor inductance and saliency ratio Vs load using different magnet shapes

In general, bread-loaf magnets are easier to manufacture, the thickness of magnet typically is selected to avoid magnet demagnetization at the worst operating condition.

- ***Iron notches***

Adding small iron notches between adjacent magnets leads to increase in the leakage flux as in Fig. 3-21, reducing the motor airgap flux linkage and average torque. However, these iron notches will decrease the reluctance in the q-axis flux path, increasing the q-axis inductance without affecting the d-axis inductance, which enhances the motor saliency ratio. Fig. 3-20 shows the designed rotors with and without iron notches. The rotor without the notches produces 17.78 Nm torque while the torque after the iron notches slightly decreased to 17.737 Nm. However, the motor saliency ratio improved by 80% as can be seen in Fig. 3-22-c.

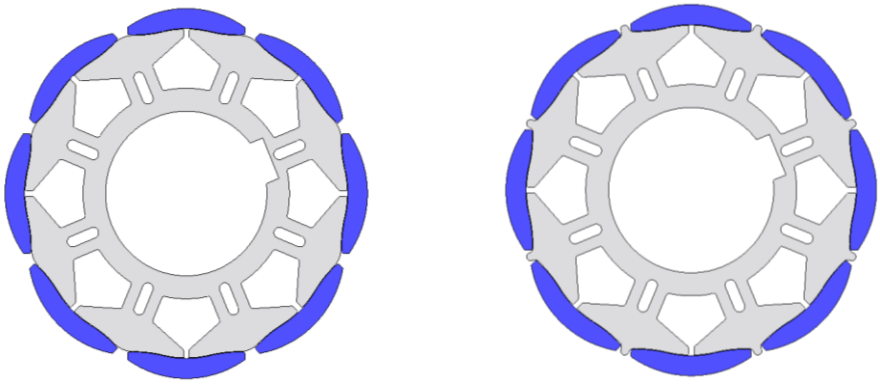

(a) rotor without iron notch (b) rotor with iron notch

Fig. 3-20 The designed rotors with and without iron notches

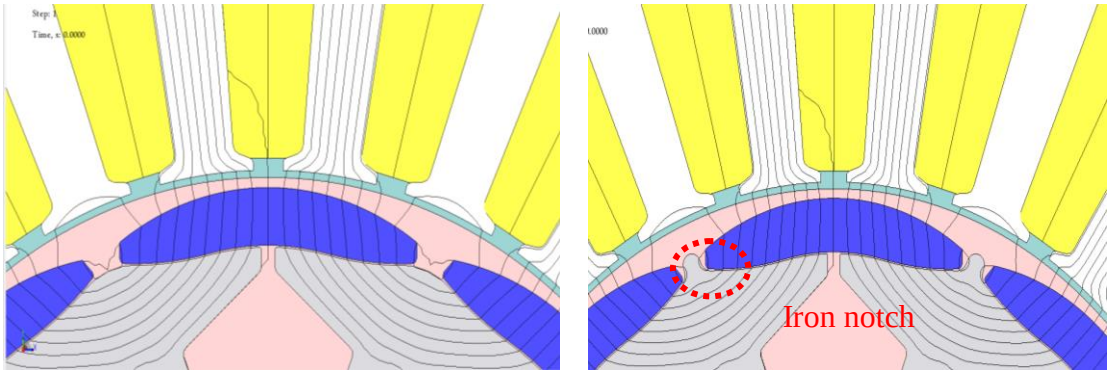

(a) leakge flux for rotor without iron notches (b) leakge flux for rotor with iron notches

Fig. 3-21 Lekage flux for rotors with and without iron notches

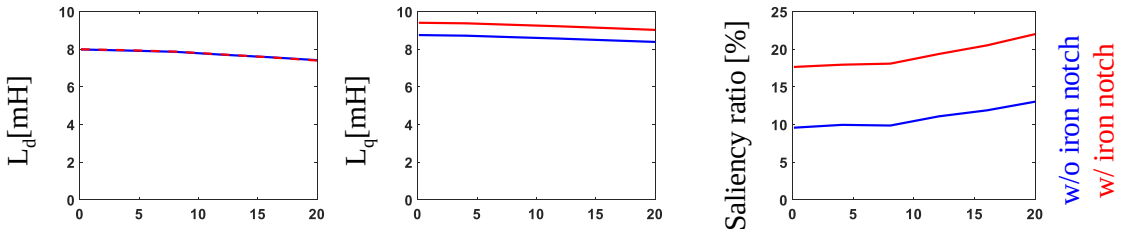

(a) d-axis inductance (b) q-axis inductance (c) saliency ratio

Fig. 3-22 Motor inductance and saliency ratio Vs load using different magnet shapes

- ***D-axis flux barriers***

The q-axis flux barriers were proposed with FI-SPMSM in the previous chapter of this thesis, these barriers used to decrease the q-axis inductance and were effective with flux intensifying motors. However, this kind of barrier is not effective with FW-SPMSM due to using longer magnet span. In this thesis, d-axis flux barriers are proposed. These barriers can be used to shape the flux path in the d-axis. The d-axis inductance can be decreased by slightly saturating the d-axis flux path in the rotor enhancing the motor saliency, however, this might slightly decrease the motor torque production due to slightly reducing the motor airgap flux linkage.

The impact of the flux barriers size on the motor saliency ratio and power conversion is evaluated using 2D-FEA. The flux barrier size is varied through varying the flux barrier angle as in Fig. 3-23. Selecting small flux barrier angle leads to small size barrier, with minimum impact on the motor saliency ratio, however, increasing the flux barrier angle leads to increase the barrier size, saturating the d-axis flux path in the rotor decreasing the d-axis inductance which enhances the motor saliency ratio. However, this will impact the motor average torque, as can be seen from Fig. 3-24.

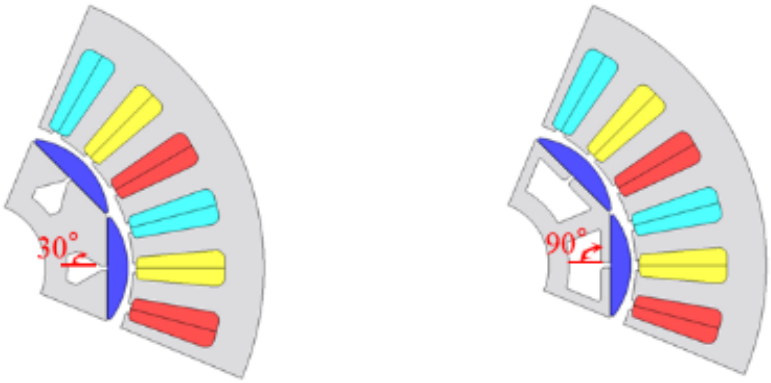

(a) rotor with small d-axis flux barriers

(b) rotor with large d-axis flux barriers

Fig. 3-23 The designed rotors using different flux barrier size

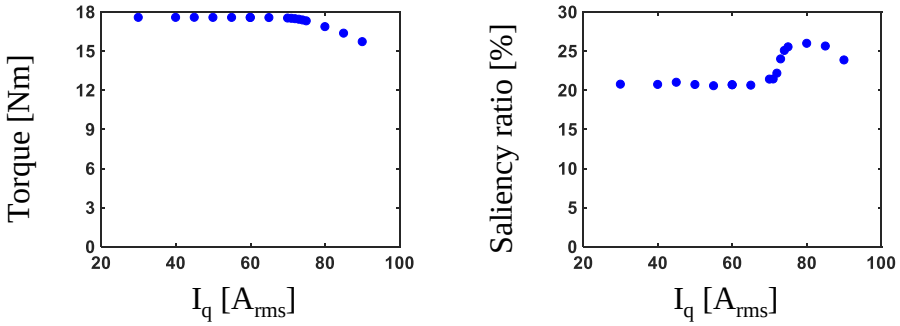

(a) torque (b) saleincy ratio

Fig. 3-24 Impact of the d-axis flux barriers on the motor power conversion and self-sensing performance

- ***Motor stack length***

The motor torque is linearly proportional to the stack length. Increasing the stack length will lead to increase the motor torque and size. This parameter can be adjusted to get the desired output torque from the designed motor. For example, decreasing the motor stack length will decrease the inductance in both d,q axes.This happens because the motor inductance is proportional to the effective stack length of the motor (l_e), as can be seen from the analytical expression for the motor inductance which is found in [104] and shown in (3-2), leading to a fixed motor saliency ratio as in Fig. 3-25-a. However, the extracted spatial information through injecting the high-frequency signal which can be calculated using (3-3) will be improved achieving a better signal-to-noise ratio through a larger ($\Delta L/(L_d*L_q)$) ratio as shown in Fig. 3-25-b.

$$L_{df} = \frac{12}{\pi^2} \bullet \frac{K_1 N_s N_f}{P} \bullet \frac{\mu_o l_e \tau_p}{g'_e} = \text{Constant} \bullet l_e \tag{3-2}$$

$$\varepsilon_f \approx \frac{-V_{inj}}{2\omega_c} \bullet \frac{\Delta L}{L_d L_q} \theta_{err} \tag{3-3}$$

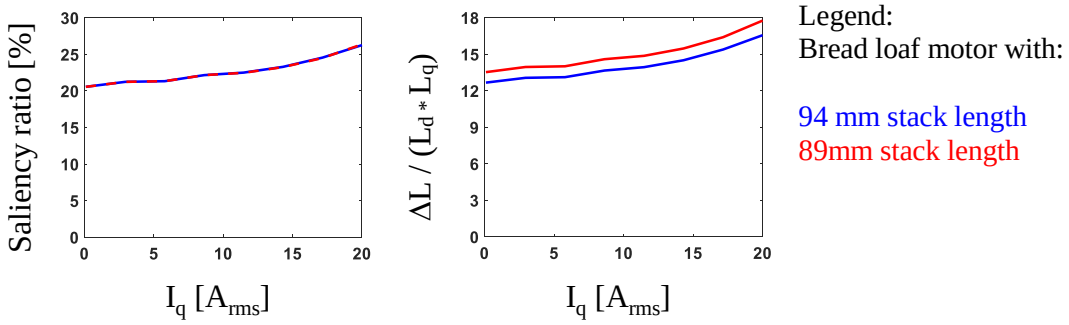

(a) saleincy ratio (b) spatial information

Fig. 3-25 Impact of motor stack length on the motor self-sensing properties

These key design variables need to be optimized simultaneously to obtain a good FW-SPMSM design with enhanced self-sensing features without affecting the power conversion of the motor. Next section will present a case study for the developed design methodology, in which a 3.7 kW FW-SPMSM for servo applications is designed. The performance of the designed motor will be compared with the baseline motor (with the asymmetrical rotor) performance.

3.3 Case Study – Design A 3.7 kW FW-SPMSM for Servo Applications with Enhanced Self-Sensing Properties

In the previous section, a methodology to design FW-SPMSM for servo applications using a symmetrical rotor structure with enhanced self-sensing properties was presented. This methodology is based on optimizing the key design variables that impact the motor self-sensing properties and were identified in the previous section.

In this section, a case study based on the developed design methodology is created. A 3.7 kW FW-SPMSM for servo applications using bread-loaf magnets is designed to achieve enhanced self-sensing properties, without affecting the power conversion performance of the

motor. Bread-loaf magnets are selected because they are easier to manufacture compared to arc-shaped magnets.

The identified key design variables were optimized through conducting a multi-objective optimization using JMAG 2D-FEA, the motor airgap is fixed, then the rotor geometry and magnet shape are varied as shown in Fig. 3-26. The range of the varied parameters is shown in Table 3-3.

Table 3-3 Range of the varied parameters during optimizing the symmetric FW-SPMSM rotor design

Parameter	Range
Magnet span – P1 (mm)	21-23
Magnet radius– P2 (mm)	18-22
Flux path thickness –rotor – P3 (mm)	0.6-1.4
Flux barrier angle– P4 (degree)	60-85

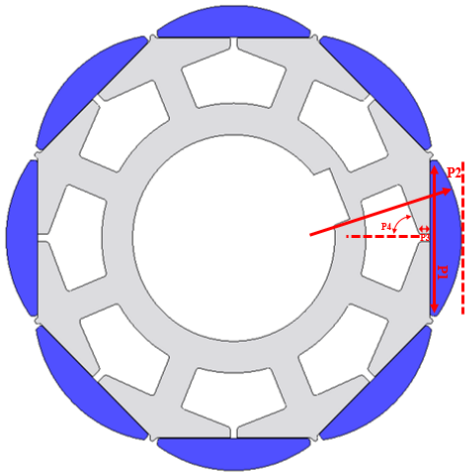

Fig. 3-26 Varied rotor geometry duirng the optimization process

The optimization objectives are summarized in Table 3-4. These objective functions were evaluated by running one study at no load condition at 2000 r/min speed. The average torque of the motor is indirectly optimized in this study, through maximizing the rms back-EMF voltage of

the motor. This corresponds to maximizing the permanent magnet flux of the motor and the magnet torque, which is dominant in SPMSMs.

Table 3-4 Objective functions and the corresponding weighting value

Objective function	weighting
Maximize the saliency ratio at no load	5
Limit the cogging torque to be less than 0.08 Nm-$_{pk-pk}$	10
Maximize the RMS voltage	10
Minimize the magnet area	1

Ten generations with 7 population size are set for the multi-objective optimization using a genetic algorithm. This algorithm ran 204 cases to achieve the desired objective functions. Fig. 3-27 shows the calculated objective functions for the evaluated cases.

The motor torque ripple is then evaluated for these cases. Finally, motor stack length is adjusted so that the motor torque will be similar to the motor with asymmetrical rotor design (baseline motor) torque. Initially same stack length like the baseline motor is used, then this length is decreased. Table 3-5 shows the selected rotor parameters for the optimum case. Fig. 3-28 shows a cross-sectional view of the optimized motor design.

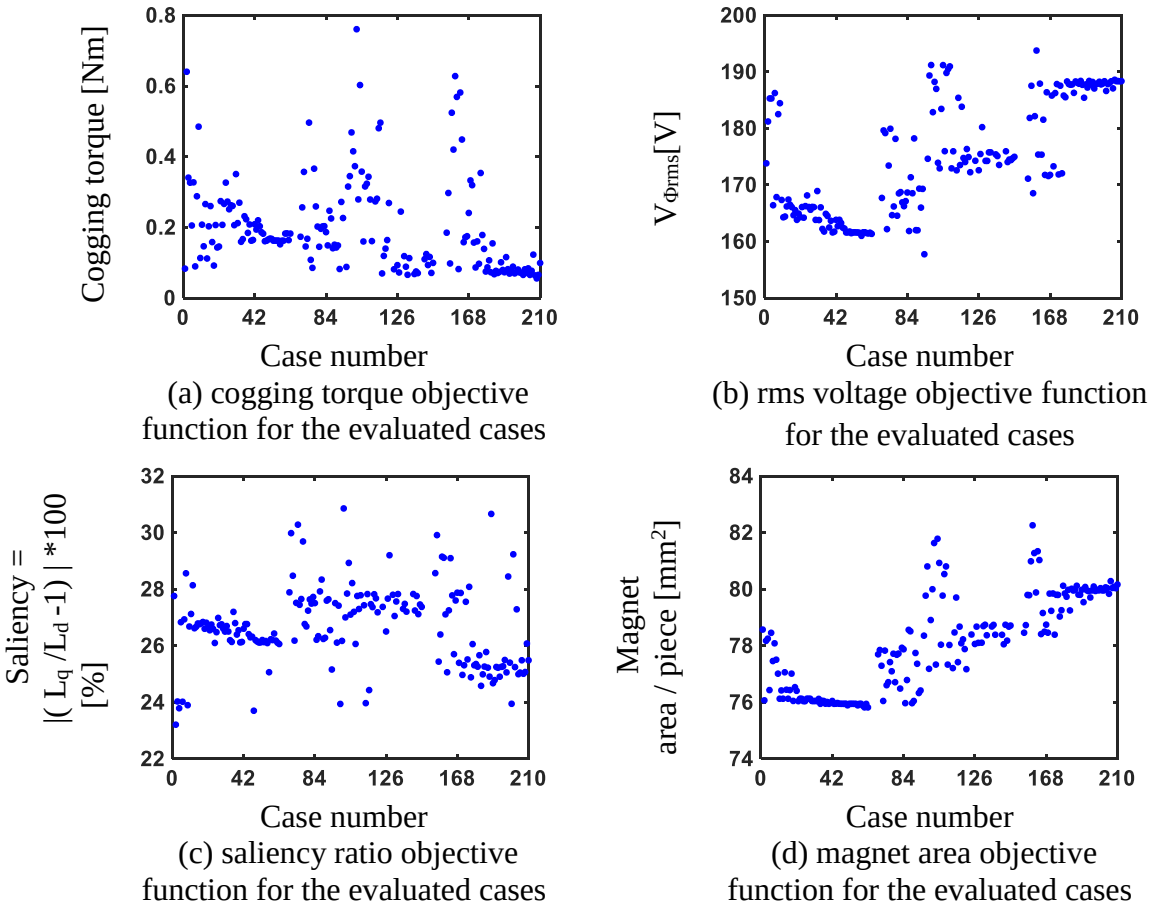

(a) cogging torque objective function for the evaluated cases

(b) rms voltage objective function for the evaluated cases

(c) saliency ratio objective function for the evaluated cases

(d) magnet area objective function for the evaluated cases

Fig. 3-27 Objective function values calculated during the rotor optimization for the bread-loaf FW-SPMSM design

Table 3-5 Rotor parameters for the optimum symmetric FW-SPMSM design

Parameter	Value
Magnet span – P1 [mm]	22.8
Magnet radius– P2 [mm]	19.6
Flux path thickness –rotor – P3 [mm]	1.2
Flux barrier angle– P4 [degree]	69
Stack length [mm]	94

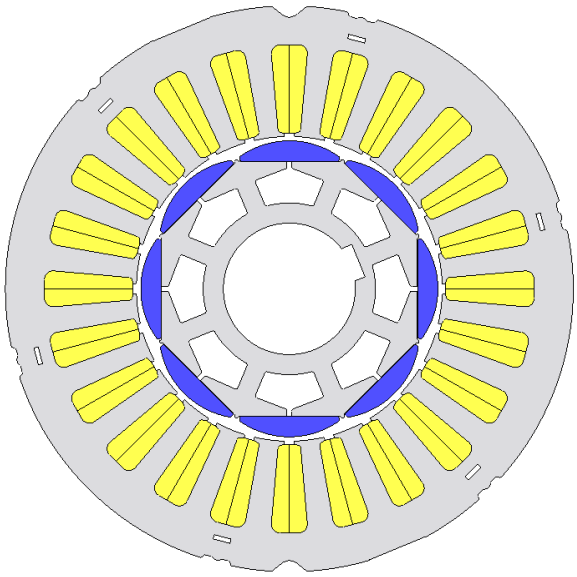

Fig. 3-28 The optimized motor cross-sectional view

The objective functions values for the optimum case are summarized in Table 3-6. This design achieves the desired cogging and ripple torque requirements for servo applications. This design achieves a 5.5% higher average torque compared to the baseline motor. This design uses 5.7% more magnet compared to the baseline motor.

Table 3-6 Objective functions value for the optimum symmetric FW-SPMSM design

Objective function	Value
$V_{\Phi rms}$[V]	187.2
Magnet area / piece [mm^2]	79.79 (105.72%)
Cogging torque [Nm]	0.0671 (**0.378%)**
Saliency ratio [%]	27
Ripple Torque [Nm]	0.339(**1.906%)**
Average Torque @ 6.8 A_{rms}	18.74 (105.496%)
Stack length [mm]	94

In order to achieve similar average torque with the designed motor compared to the asymmetrical rotor (baseline motor) while using similar magnetic material, the motor stack

length is reduced by 5.3%. In this case lower magnet volume is required, and lower and iron is needed in the motor total cost. Table 3-7 summarizes the main performance properties for this design.

Table 3-7 The optimized design performance when using a shorter stack length

Motor property	Value
Magnet volume %	100.1%
Cogging torque [Nm]	0.0636(0.36%)
Saliency ratio [%]	27
Ripple Torque [Nm]	0.3205(1.8%)
Average Torque @ 6.8 A_{rms}	17.7422 (99.88%)
Stack length [mm]	89

Fig. 3-29 compares the back-emf and torque harmonics of the designed motor using shorter stack length (this design will be called later the symmetrical rotor design) with the baseline motor (this design will be called the asymmetrical rotor design). This symmetrical rotor design has a similar power conversion with shorter stack length (smaller motor) compared to the asymmetric rotor motor design.

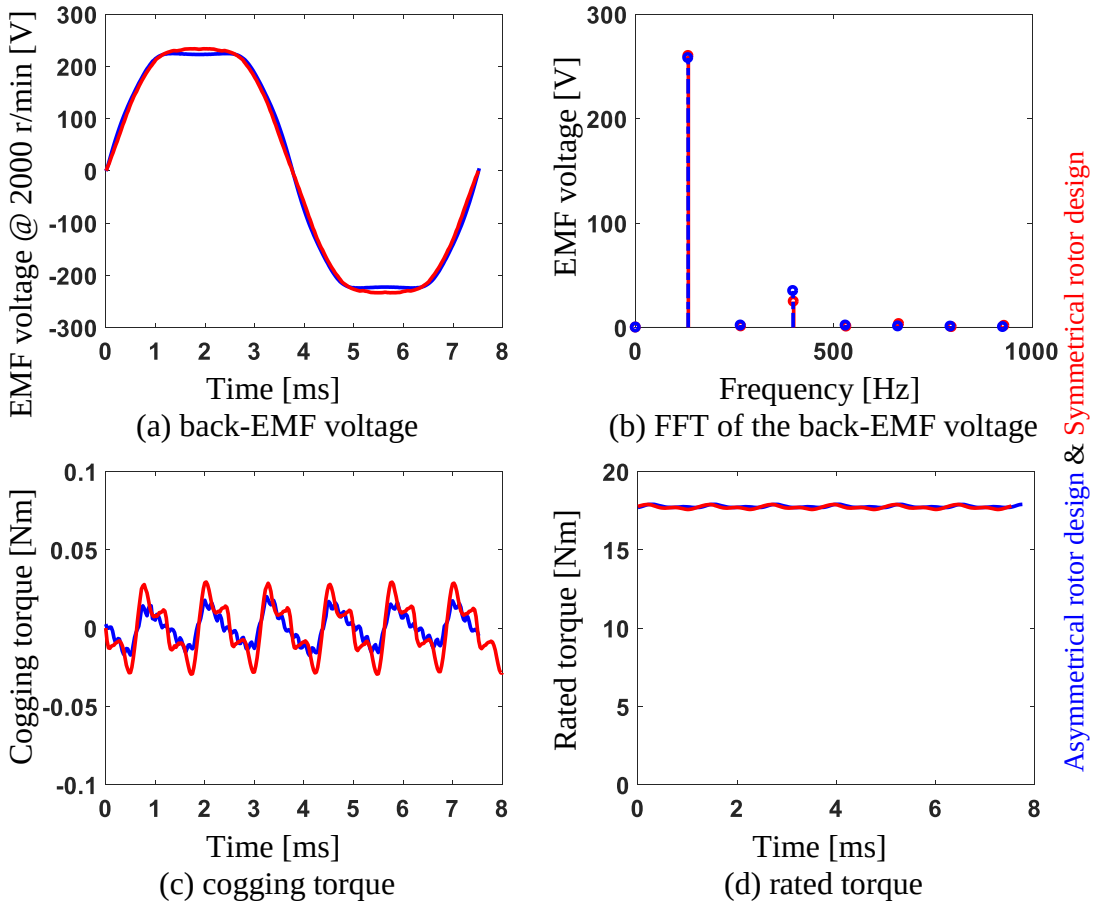

Fig. 3-29 Power conversion performance comparison between the symmetrical rotor motor and the asymmetrical rotor motor (baseline)

The torque linearity for the designed motor with symmetrical rotor structure is then evaluated using 2D-FEA and compared with the baseline motor which designed using asymmetrical rotor structure. The motors run at 2000 r/min, the d-axis current is set to zero, and torque is calculated for different q-axis current values (q-axis current is the same as the motor current). Both motors achieve similar torque per current as in Fig. 3-30-a.

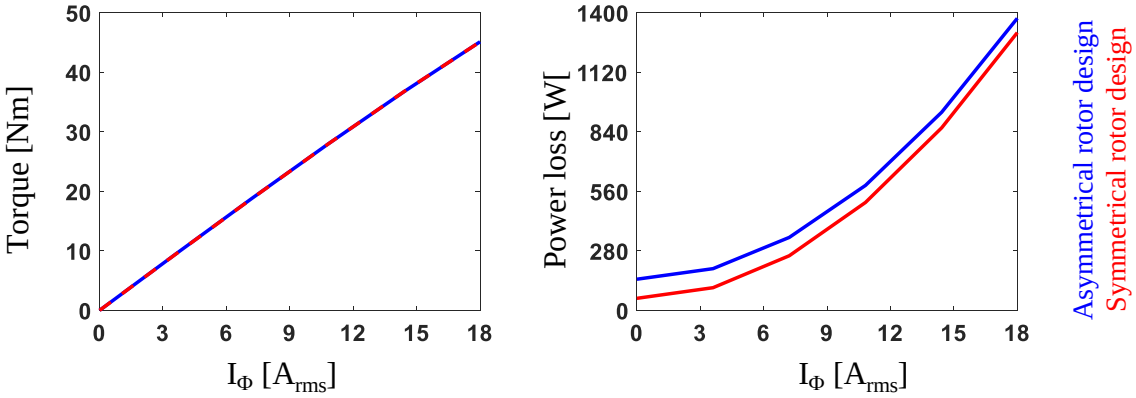

(a) torque linerity (b) simulated power loss at 2000 r/min

Fig. 3-30 Simulated torque linearity and loss comparison for SPMSM servo motor designed with symmetrical (proposed) and asymmetrical (baseline) rotors

The designed motor with the symmetrical rotor using bread-loaf magnets has lower losses compared to the designed motor with the asymmetrical rotor (baseline) rotor as shown in Fig. 3-30-b. This happens due to lower iron loss in the designed rotor with the symmetric. Lower iron loss are achieved in the symmetrical rotor design due to a shorter motor stack length (lower iron) and due to lower magnet flux passing the stator compared to the designed motor with the asymmetrical rotor, in which extra flux pass through the stator to cancel the airgap flux harmonics.

Self-sensing properties of the symmetrical rotor design are then evaluated and compared with the asymmetrical rotor design (baseline). The symmetrical rotor design achieves 47% more saliency ratio than the designed motor with asymmetrical rotor at no load condition. This number increases to 64% at twice the rated torque. The saliency ratio variation with increased motor load for the asymmetrical rotor design is almost fixed, however, it increases with increased motor load for the designed motor with the symmetrical rotor.

To visualize the attractive self-sensing properties of the designed motor with the symmetrical rotor, the motor d,q inductances are calculated using 2D-FEA at different q-axis

currents while setting the d-axis current to 0 (MTPA solution). Fig. 3-31-a compares the d-axis inductance for the asymmetrical rotor and the symmetrical rotor designs. The designed motor with symmetrical rotor has lower d-axis inductance.

The q-axis inductance in the designed motor with the symmetrical rotor does not decrease with increasing the q-axis current, as can be seen from Fig. 3-31-b, because the d-axis flux barriers lead to force the d-axis flux to slightly saturate the q-axis flux path. This is an attractive feature in the designed motor with the symmetrical rotor, in which the motor saliency will improve with increasing the motor load, due to stabilizing the q-axis inductance with load variations, while the d-axis inductance slightly decreases due to saturating the stator iron. This will improve the self-sensing performance for the FW-SPMSM. Decreasing the motor stack length leads to a decrease in the d and q inductances, while maintaining the same saliency ratio.

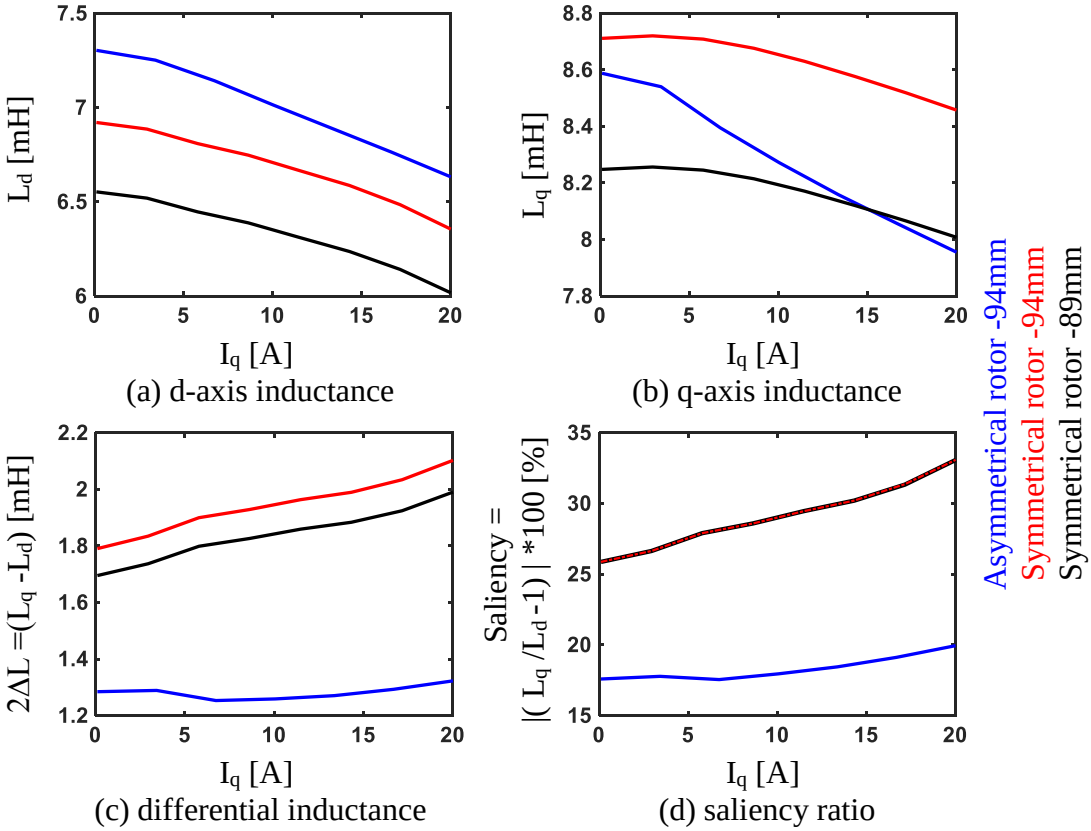

Fig. 3-31 Saliency ratio and inductance variation with motor load comparison between the symmetrical and asymetrical rotors

Fig. 3-32 shows the spatial information that can be extracted using either rotating or pulsating high-frequency injection. Reducing the stack length leads to improve the spatial information that can be extracted from the motor, which improves the self-sensing performance. The designed motor with the symmetrical rotor with shorter stack length improves the spatial information that can be extracted from the motor by 60% compared to the baseline motor with the asymmetrical rotor.

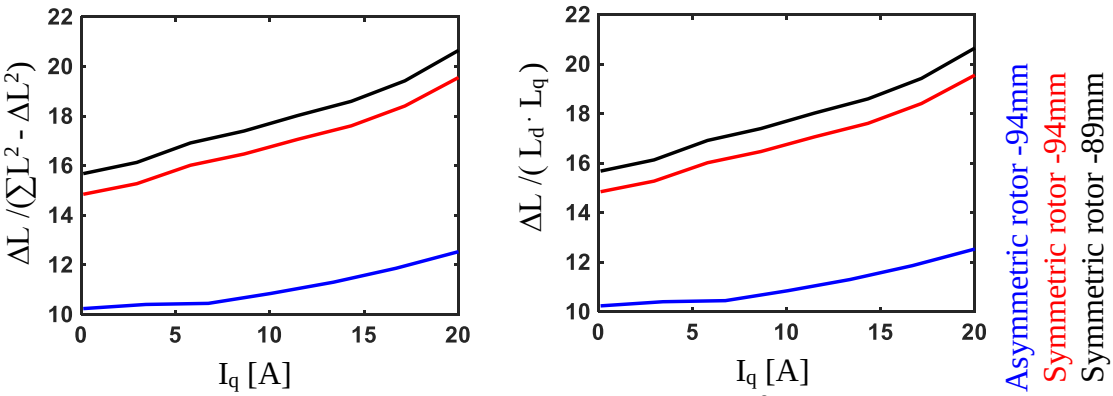

(a) spatial information using rotating HFI

(b) spatial information using pulsating HFI

Fig. 3-32 Self-sensing properties comparison between the designed motor with symmetrical and asymmetrical rotors

Finally, the demagnetization risk of the permanent magnet for the designed motor with the symmetrical rotor is evaluated at different temperatures and through injecting three times the rated current to the designed motor. The maximum temperature for the magnet is considered to be 120° C. Increasing the motor temperature from 20° C to 120° C leads to decrease the remnant flux of the magnet by 12%, leading to decrease the magnet flux and torque by the same percentage. Fig. 3-33 shows the BH curve for the used magnet (N38UH) at different temperatures.

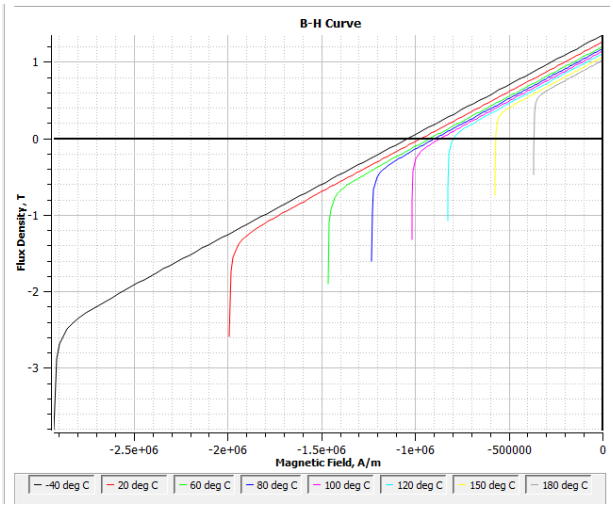

Fig. 3-33 BH curve for the used permanent magnet (N38UH)

The magnet demagnetization is evaluated by calculating the magnetization state of the magnet (J), which is calculated based on the estimated magnetic flux density (B) and magnetic flux strength (H) of the magnet using FEA. The relationship between the magnetic flux density (B), magnetization (M) and magnet flux strength (H) is shown in (3-4). The magnetization state (J) can be calculated from the magnetization (M) using (3-5).

$$B = \mu_o \mu_r (M+H) \tag{3-4}$$

$$M = \frac{J}{\mu_o \mu_r} \tag{3-5}$$

Substituting (3-5) into (3-4), the magnetization state (J) can then be calculated from the magnetic flux density and strength as in (3-6). The magnetization state is constant in the magnet when there is no demagnetization.

$$J = B - \mu_o \mu_r H \tag{3-6}$$

Fig. 3-34 shows the calculated magnetic flux density and strength when exciting the motor with 3 pu current in the negative d-axis current at 120° C. This flux weakening current significantly decreases the magnet flux linkage to the stator.

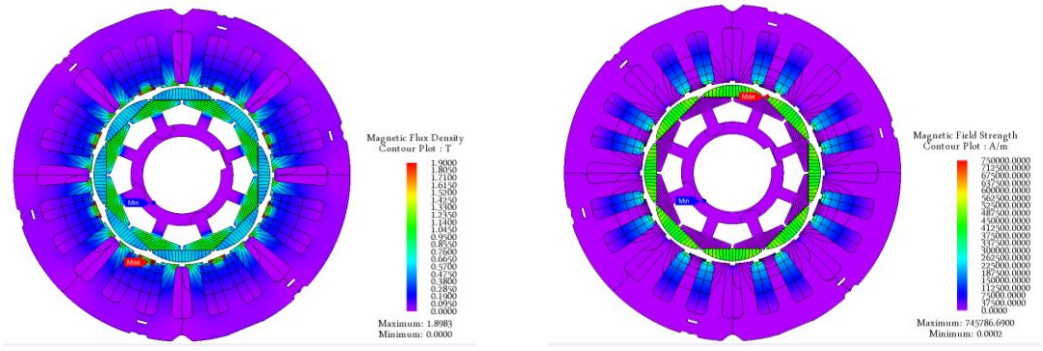

(a) Magnetic flux density (b) Magnetic flux strength

Fig. 3-34 Magnetic flux density and intensity when the motor is excited by 3 pu negative d-axis current at 120° C

The magnetization state of the magnet is then calculated using (3-6) and shown in Fig. 3-35, this calculation was repeated at different magnet temperatures. The magnet is not suffering any demagnetization, because the d-axis current is applied to the middle of the magnet (d-axis), which is thick in case of bread-loaf magnets.

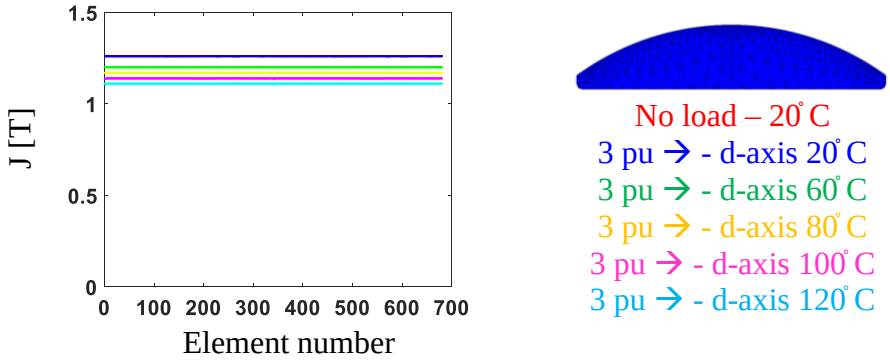

Fig. 3-35 Magnet magnatization state when the motor is excited by 3 pu negative d-axis current at different tempratures

Since bread-loaf magnets are thin in the edges, it is important to evaluate the demagnetization risk when applying q-axis current. This is done through injecting 3pu current in the q-axis (3 pu torque) direction at different magnet temperatures.

Fig. 3-36 shows the calculated magnetic flux density and strength when exciting the motor with 3 pu current in the q-axis current at 120° C. This magnetic flux density at the edge of the magnet is lower than the center of magnets due to the q-axis current.

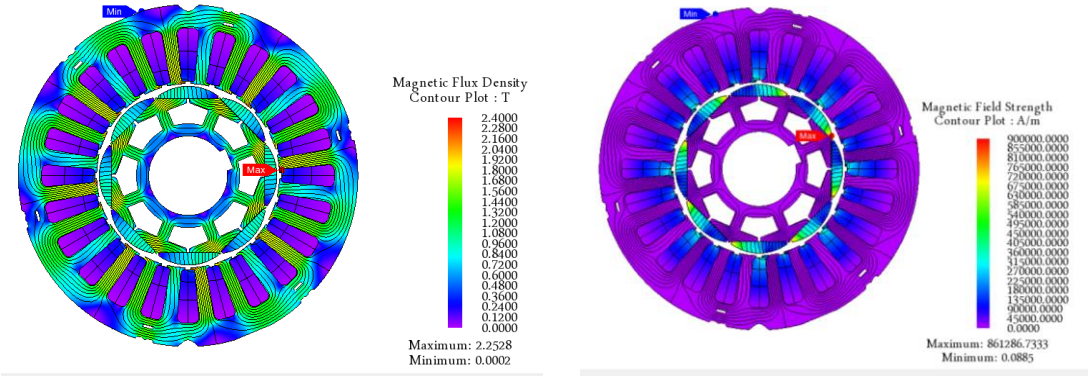

(a) Magnetic flux density (b) Magnetic flux strength

Fig. 3-36 Magnetic flux density and intensity when the motor is excited by 3 pu q-axis current at 120˚C

Fig. 3-37 shows the magnet magnetization state when exciting the designed motor with 3 pu q-axis current. At 120˚C few mesh elements in the magnet suffer partial demagnetization.

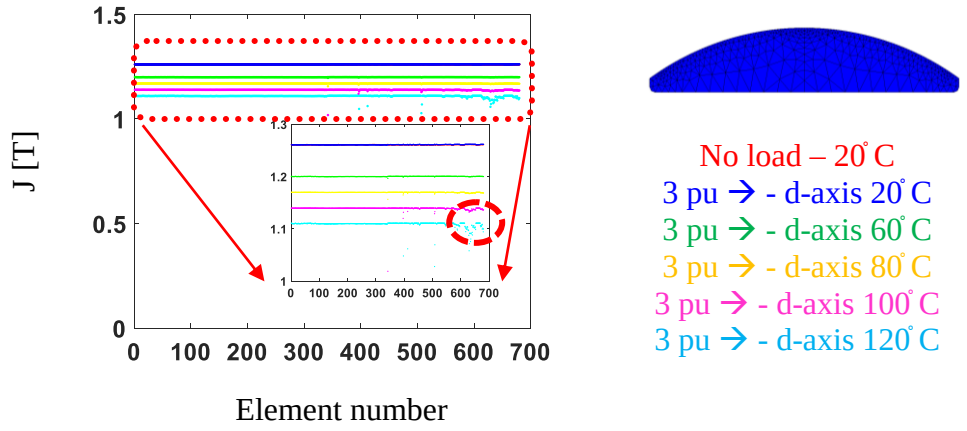

Element number

Fig. 3-37 Magnet magnatization state when the motor is excited by 3 pu q-axis current at different tempratures

Fig. 3-38 shows the area in the magnet that suffers partial demagnetization when running the motor at 120˚C with 3 pu q-axis current. The demagnetized area is very small. The impact of partial demagnetization is then evaluated using reuse demagnetization function in JMAG. In this function, the operating point in the magnet when the magnet suffers partial demagnetization is saved and used to evaluate the rated and cogging torque at 20˚C.

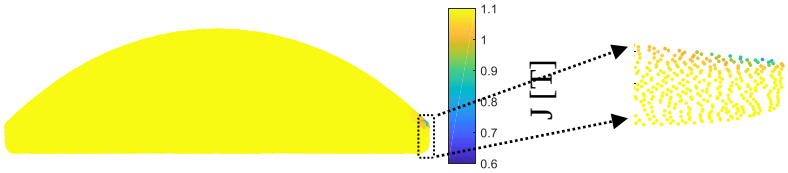

Fig. 3-38 Magnet magnatization state when the motor is excited by 3 pu q-axis current at 120° C

Reuse demagnetization function in JMAG doesn't support Arnold magnets (which is the used magnet in this motor). To overcome this issue, the BH curve is constructed based on the actual data and used with JMAG. Fig. 3-39 compares the calculated torque using the actual BH curves with the calculated torque using the constructed curves. These results verify the accuracy of the constructed curves.

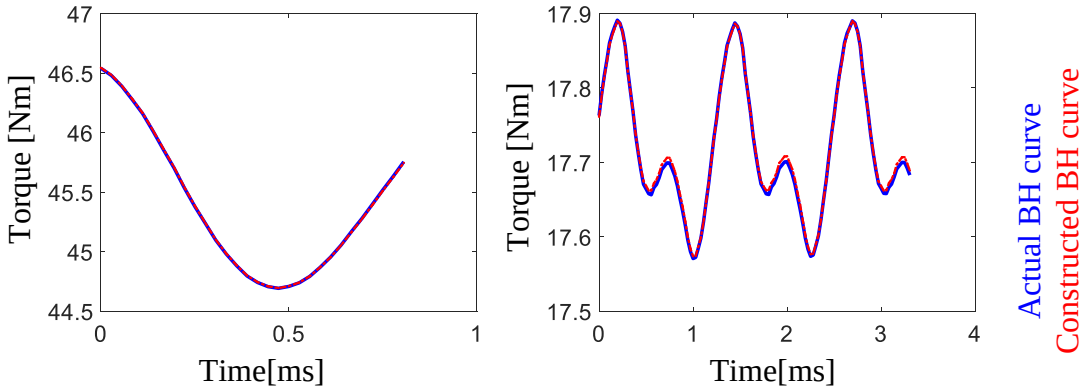

(a) 3 PU torque at 120° C (b) rated torque at 20° C

Fig. 3-39 Calculated torque using FEA with using the actual and constructed magnet BH curves

Finally, the constructed BH curves are used to evaluate the impact of magnet partial demagnetization on motor performance. At 2000 r/min with 3 pu current in the q-axis direction (3 times the rated torque), the magnet temperature is set to 120° C. The operating points in the magnet are then saved and used to run separate study at 20° C to calculate the rated and cogging torque of the motor after the partial demagnetization happened. Fig. 3-40 shows the result of this

test. The rated torque after partial demagnetization is decreased by 0.01%. This impact is small enough that there is no need to increase the magnet thickness. The cogging and ripple torque for the designed motor after the partial demagnetization are 0.415% and 1.8% respectively. These values still meet the desired performance

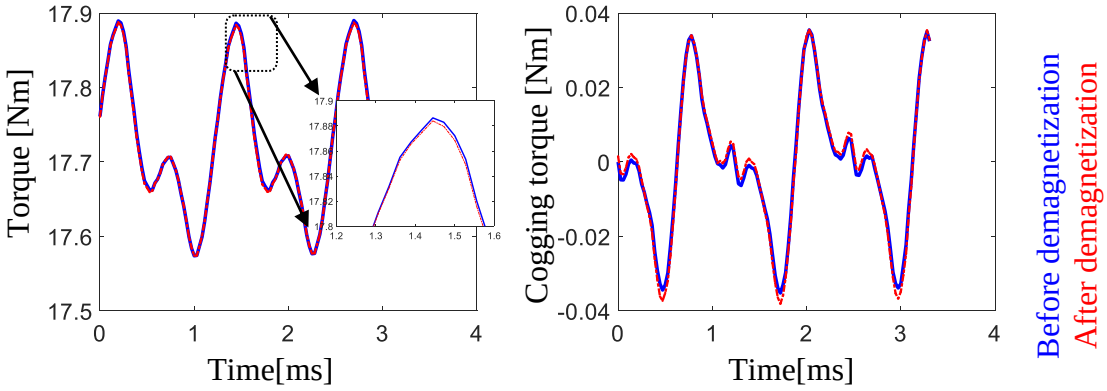

(a) rated torque at 20° C (b) cogging torque at 20° C

Fig. 3-40 Torque comparison before and after the partial demagnatization

3.4 Experimental Evaluation of the Design FW-SPMSMs

In this section, the performance of the designed FW-SPMSM with the symmetric rotor is experimentally evaluated and compared with the baseline motor (with the asymmetric rotor). These motors are connected to 7 kW servo motor and controlled using A quad B encoder with 1000 ppr. Fig. 3-41 shows the used dynamometer to evaluate the performance of the designed motors.

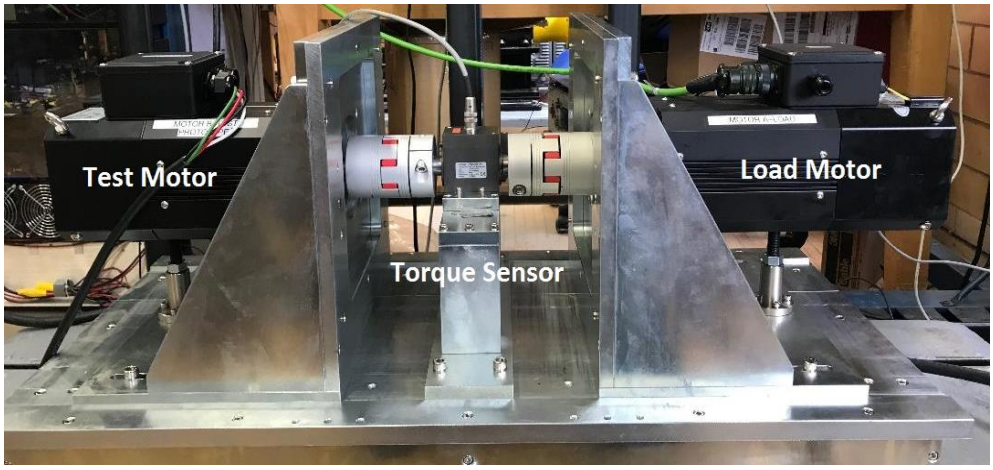

Fig. 3-41 The test dynomometer

Firstly, the FW-SPMSM designed with the asymmetrical rotor using shifted ring-shaped magnets (baseline motor) is connected to the dynamometer. The line-line back-EMF voltage of the motor at the rated speed is measured by spinning the dynamometer at 2000 r/min using differential voltage probes. Fig. 3-42 shows the measured line-line voltages, while Fig. 3-43 compared the measured line voltage with the expected one from 2D-FEA.

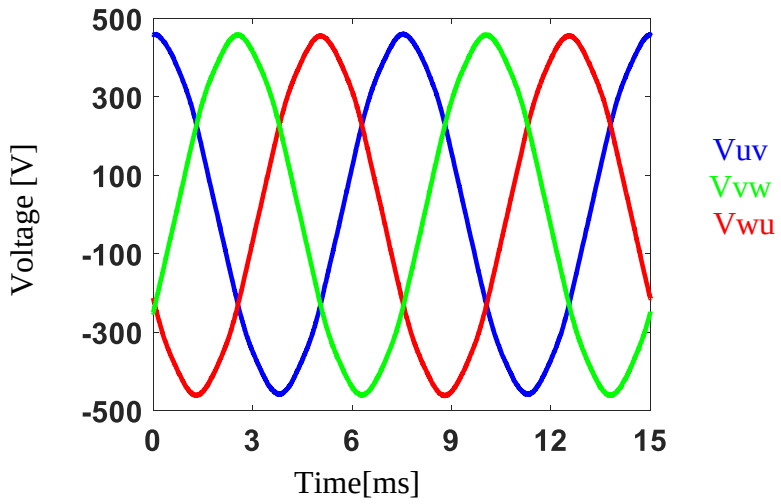

Fig. 3-42 Measured line-line back-EMF voltage at 2000 r/min
for the baseline motor with the asymmetrical rotor

Typically, the calculated back-EMF using 2D-FEA is lower than the measured value due to not modeling the end winding effect and leakage flux. However, the measured back-EMF for

the baseline motor with the asymmetrical rotor is higher than the calculated value using 2D-FEA. This is due to not perfectly canceling the back-EMF harmonics to achieve the desired low cogging and ripple torque, which reduces the fundamenta component as was discussed early in this chapter, this is clear from the FFT plot in Fig. 3-43-b.

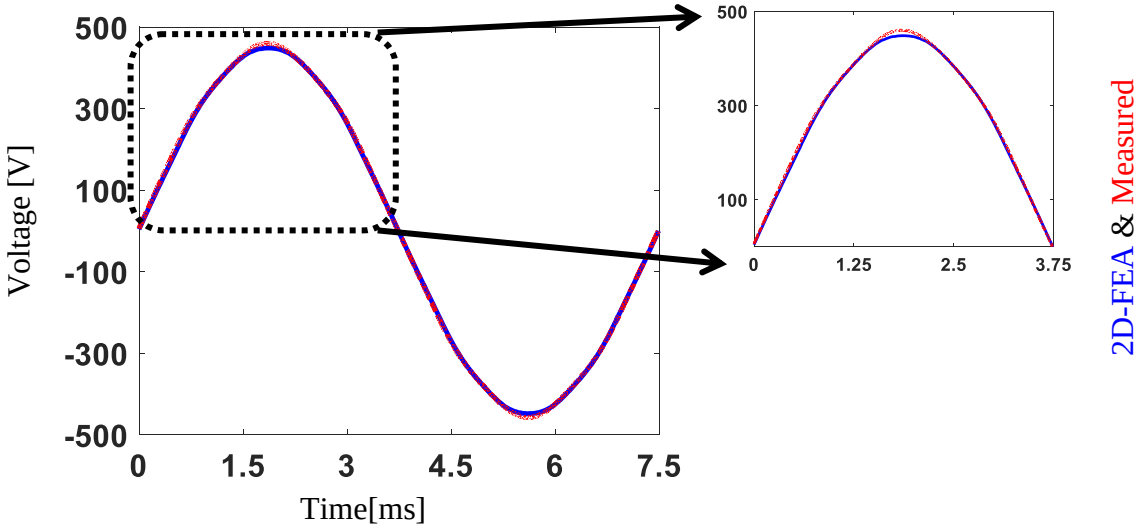

(a) Line back-EMF @ 2 k-r/min

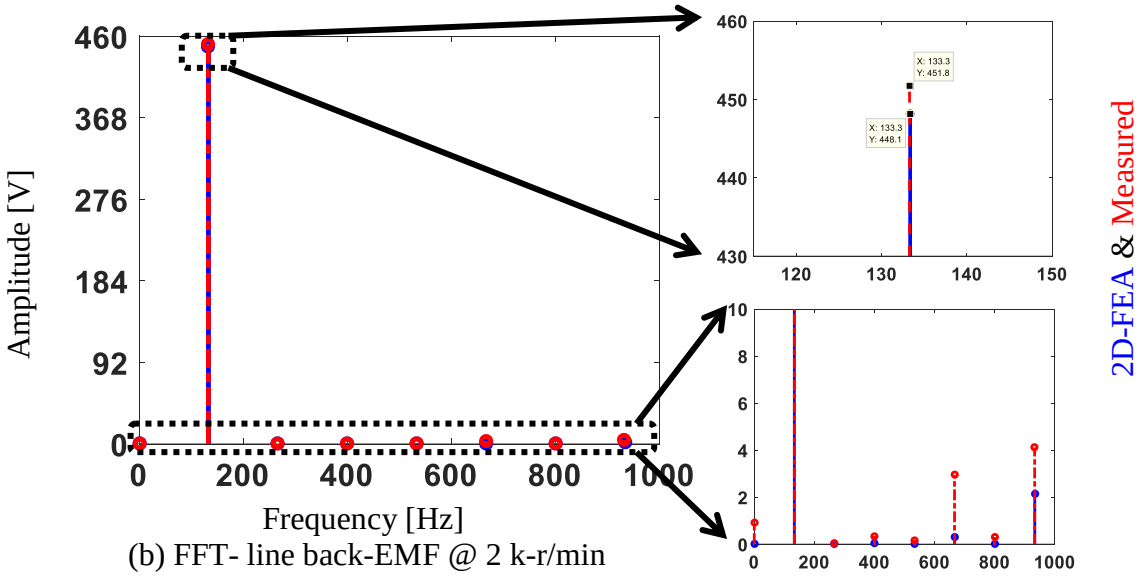

(b) FFT- line back-EMF @ 2 k-r/min

Fig. 3-43 Comparsion between the measured line back_emf and estimated using 2D-FEA at 2 k-r/min for the baseline motor with the asymmetrical rotor

The fundamental and secondary harmonics mainly 5th and 7th harmonics in the measured back-EMF are larger than the calculated values using 2D-FEA, which indicates larger ripple and cogging torque. Perfect harmonic cancellation is not achieved due to the manufacturing tolerance of the motor. Further investigation needs to be done in the future to quantify the impact of manufacturing tolerance on motor performance.

The motor magnet flux in then estimated through spinning the dynamometer at different speeds using the load motor. Zero d,q current is commanded to the test motor which is controlled using synchronous frame PI regulator, leading to the back-EMF voltage to show up on the commanded q-axis voltage for the tested motor as in Fig. 3-44. The slope of the back-EMF line at different speed represents the magnet flux value, for the baseline motor, this value is 0.309 Wb.

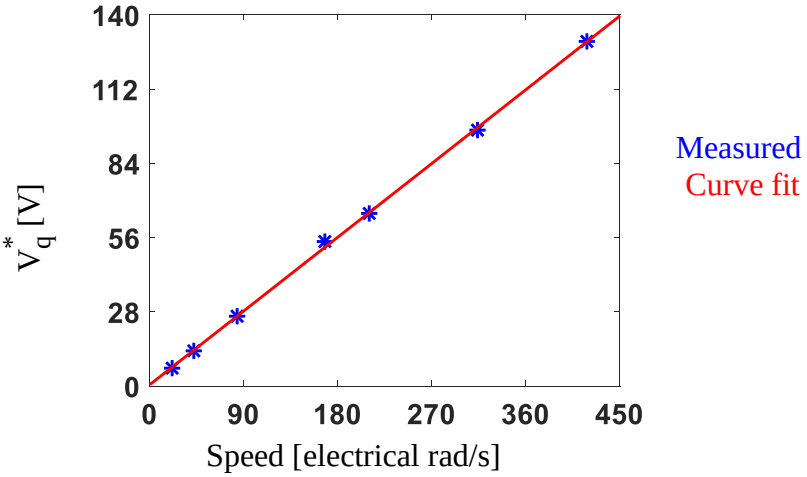

Fig. 3-44 Magnet flux estimation using synshonous frame PI regilatrs for the baseline motor with the asymmetrical rotor

The flag test method which was explained in section 2.4.1 was used to estimate the dynamometer inertia, static, and dynamic friction. The calculated values are summarized in

Table 3-5. Standard frequency response analysis was used to estimate the motor resistance and dq inductance values, the no-load values are also presorted in Table 3-5.

Table 3-8 Clculated electrical and mechincal parameters for the baseline motor using asymmetric rotor

Parameter	value	Parameter	value
T_{μ} [Nm]	0.7	L_d @ No load [mH]	10.5
B_p [mNm-s/rad]	4.56	L_q @ No load [mH]	12.12
J_p [kg-cm^2]	55.8	R[Ω]	1.45

The inductance variation with load current when commanding zero d-axis current is shown in Fig. 3-45, for the simulated values, 2.45 mH leakage inductance is added to both d,q alues to include the impact of leakage flux.

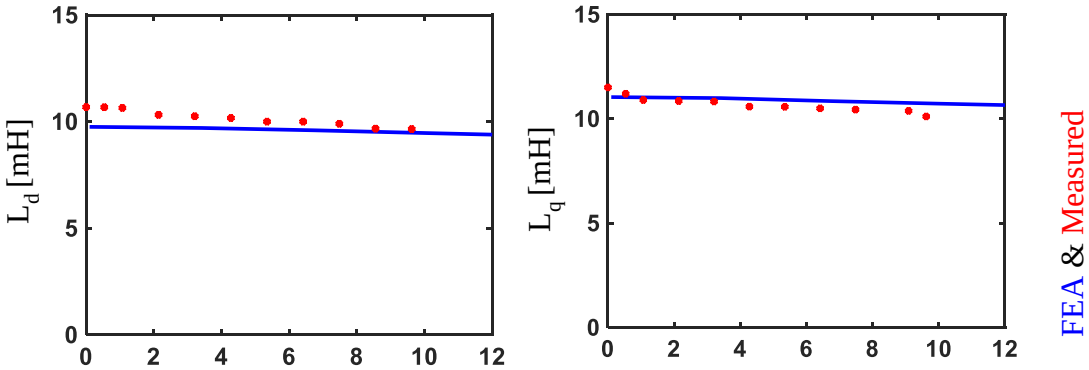

Fig. 3-45 Measured and simulated inductance variation with load current (I_d=0) for the baseline motor with the asymmetrical rotor

To evaluate the torque and losses of the machine, the baseline motor speed is controlled at 1000 r/min, and different torque values were commanded to the load motor. Motor losses, and torque linearity is then measured using torque transducer and motor drive analyzer. Fig. 3-46-a compares the measured torque linearity with the expected value from FEA, the measured value is slightly higher than expected due to higher back-EMF than the simulated one.

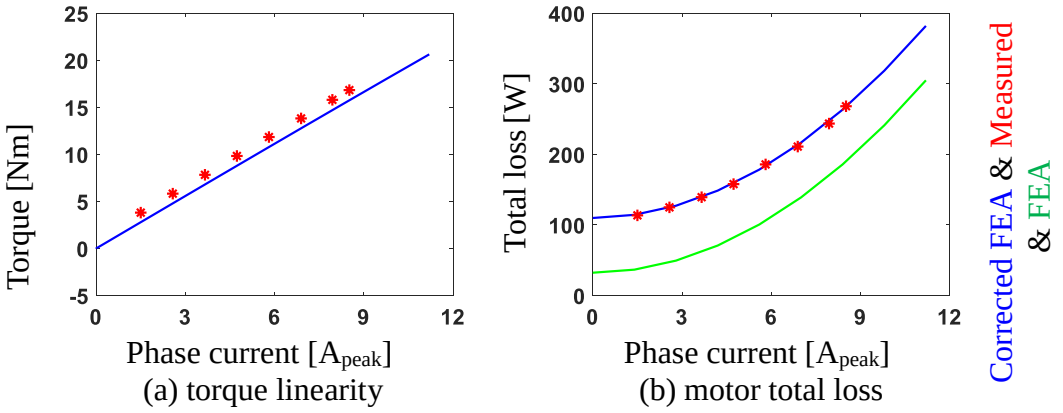

Fig. 3-46 Measured and simulated torque and power loss variation with load current (I_d=0) for the baseline motor with asymmetrical rotor

Fig. 3-46-b compares the measured motor losses with the expected value from 2D-FEA at different load current, while controlling the d-axis current to be zero. The measured value is higher than the expected from FEA, due to using pure sine wave excitation in the simulation. A correction factor is used to match the expected iron loss with the measured one, for this kind of material the correction factor is found to be 3.5. after correcting the iron loss, the corrected FEA results agrees with the measured value.

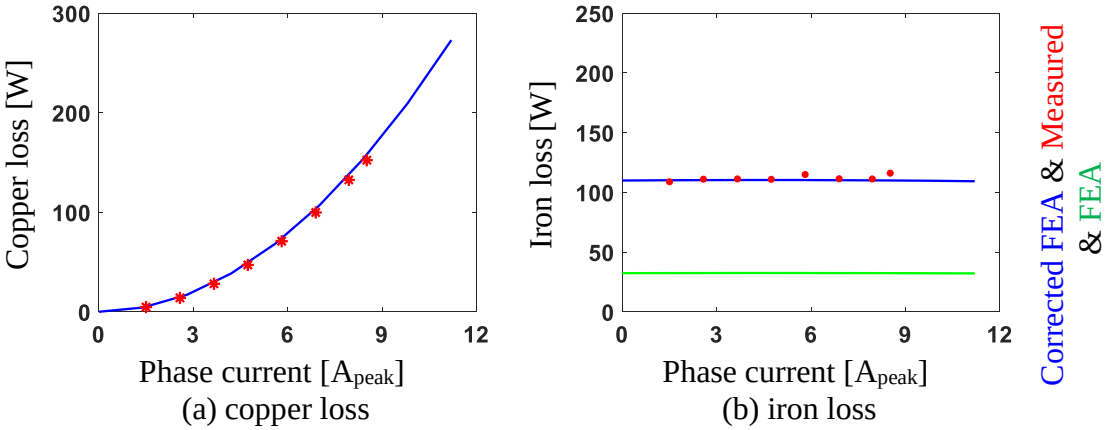

Fig. 3-47 Measured and simulated copper and iron loss variation with load current (I_d=0) for the baseline motor with the asymmetrical rotor

The measured iron loss is then calculated by subtracting the copper loss from the motor total loss and compared with the FEA. The measured iron loss agrees with the corrected FEA results using the 3.5 factor as in Fig. 3-47-b.

Then, the manufactured FW-SPMSM design with the symmetrical rotor using bread-loaf magnets is connected to the dynamometer and tested experimentally. Fig. 3-48 shows the manufactured rotor, this motor has a shorter stack length compared to the baseline motor.

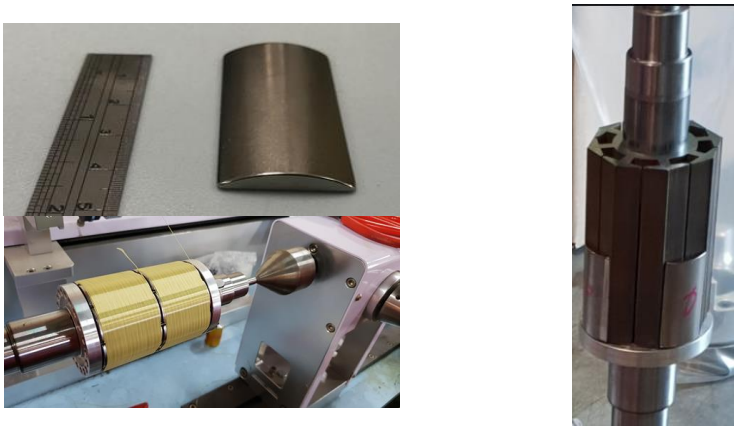

Fig. 3-48 Manufactured FW-SPMSM with the symmetrical rotor

The line-line back-EMF of the designed FW-SPMSM with the symmetrical rotor is measured using differential voltage probes and by spinning the dynamometer at 2000 r/min. Fig. 3-49 shows the measured result.

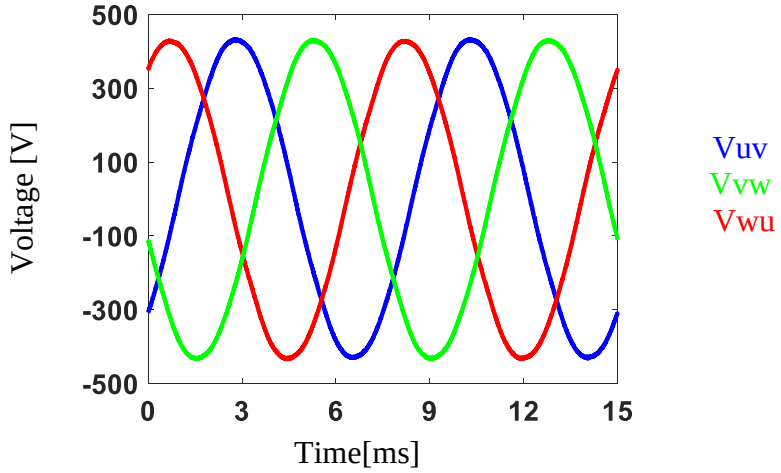

Fig. 3-49 Measured line-line back-EMF voltage at 2000 r/min
for the designed motor with the symmetrical rotor

The measured line-line back-EMF of the designed motor with the symmetrical rotor at 2000 r/min is compared with the calculated value using 2D-FEA as in Fig. 3-50-a. The measured value is 3.75% lower than the calculated one from 2D-FEA, due to not modeling the end winding effect and leakage flux. This motor achieves smaller secondary harmonicas in Fig. 3-50-b which indicates low cogging torque.

The magnet flux of this motor is then estimated and found to be 0.29614Wb, which is 4% lower than the fabricated motor using with the asymmetrical rotor as in Fig. 3-51. This difference happens due to not perfectly canceling the back-EMF harmonics for the motor with an asymmetrical rotor, leading to higher magnet flux and back-EMF than expected.

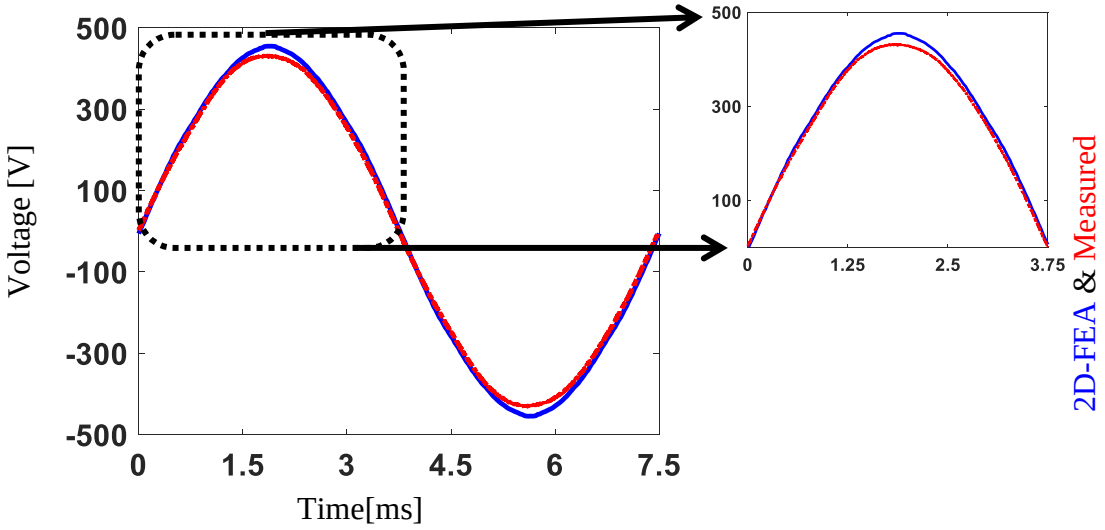

(a) Line back-EMF @ 2 k-r/min

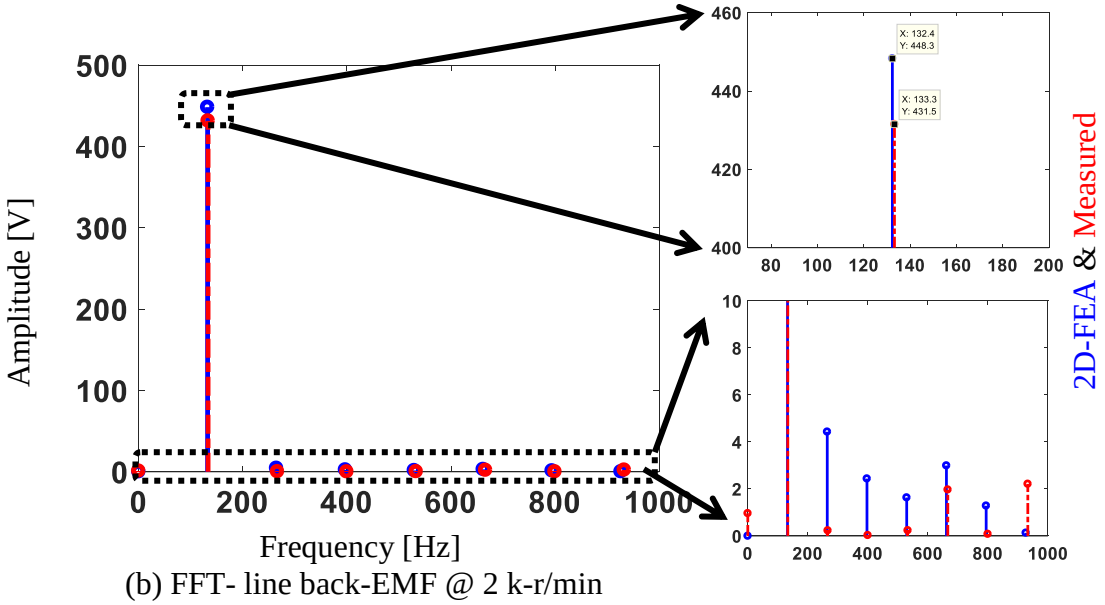

(b) FFT- line back-EMF @ 2 k-r/min

Fig. 3-50 Comparsion between the measured line back_emf and estimated using 2D-FEA at 2 k-r/min for the designed motor with the symmetrical rotor

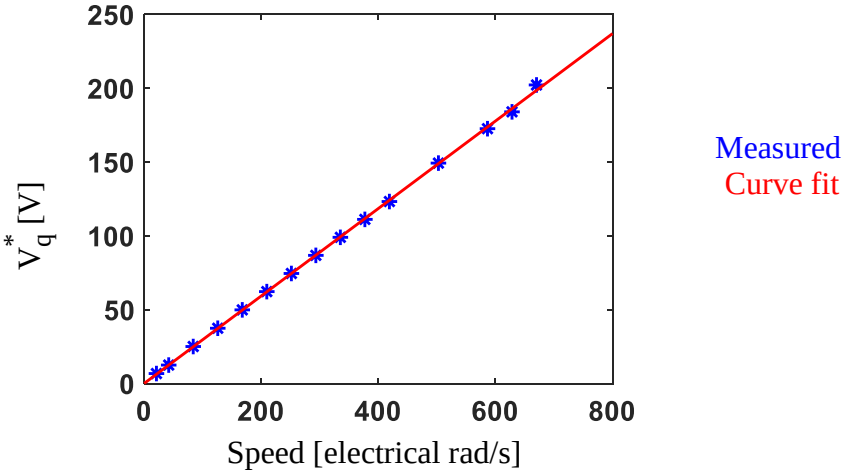

Fig. 3-51 Magnet flux estimation using synchronous frame PI regulators for the designed motor with symmetric rotor

The inductance variation with load current when commanding zero d-axis current for the designed motor the symmetrical roto is shown in Fig. 3-52. For the simulated value, 2.45 mH leakage inductance is added to both d,q values to include the impact of end-winding and leakage flux.

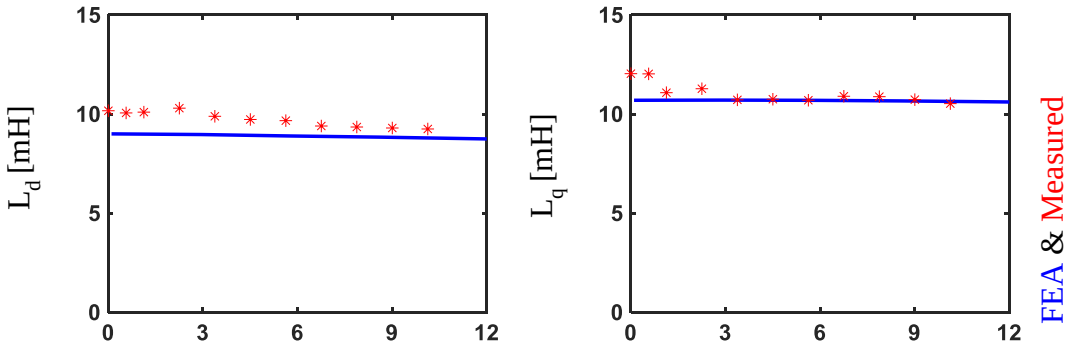

(a) d-axis inductance (b) q-axis inductance

Fig. 3-52 Measured and simulated inductance variation with load current (I_d=0) for the designed motor with the symmetrical rotor

The measured torque linearity with the expected value from FEA is compared in Fig. 3-53-a. While Fig. 3-53-b shows the measured motor losses with the expected value from 2D-FEA at a different load current, while controlling the d-axis current to be zero. The same correction factor used with this motor (3.5 factor), this factor is the same because the same stator is used in both designs, and stator iron loss dominates the motor iron loss, the corrected FEA results agree with the measured value.

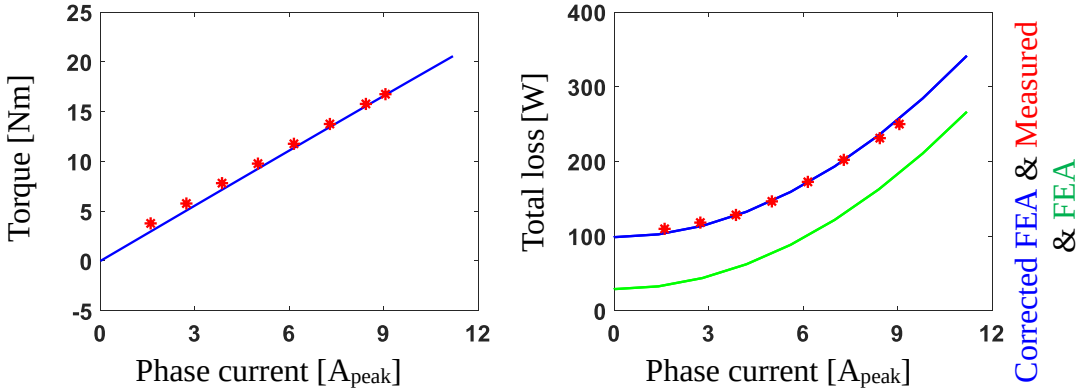

Fig. 3-53 Measured and simulated torque and power loss variation with load current (I_d=0) for the designed motor with the symmetrical rotor

The measured copper loss is then compared with the expected value as in Fig. 3-54-a. The measured iron loss is compared with the FEA and the corrected FEA results factor as in Fig. 3-54-b. The measured iron loss shows a good agreement with the corrected FEA results using the 3.5 factor.

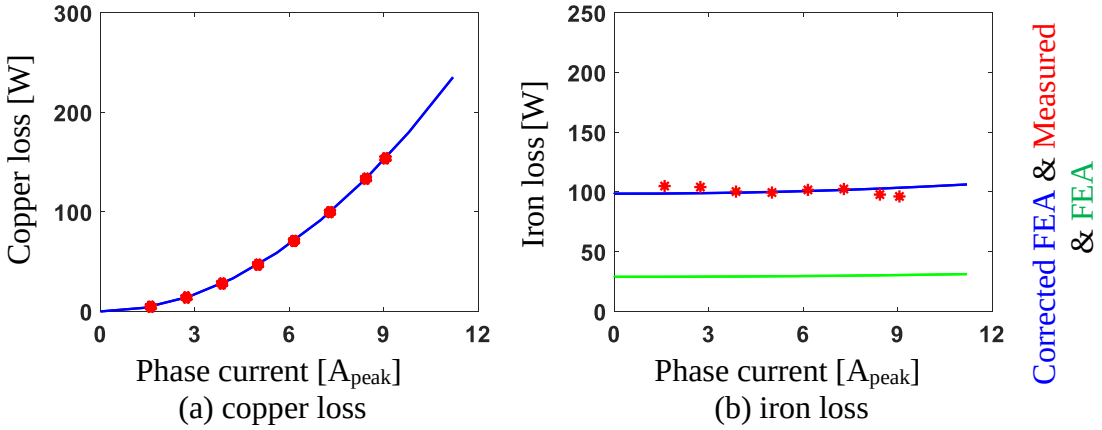

(a) copper loss (b) iron loss

Fig. 3-54 Measured and simulated copper and iron loss variation with load current (I_d=0) for the designed motor with the symmetrical rotor

The power conversion performance is then experimentally evaluated and compared for the baseline motor designed with the asymmetrical rotor and the designed motor using the symmetrical rotor. Fig. 3-55-a compares the torque linearity for the motors, the baseline motor with asymmetrical rotor achieves higher torque with current due to the higher magnet flux compared to the designed moot with the symmetrical rotor.

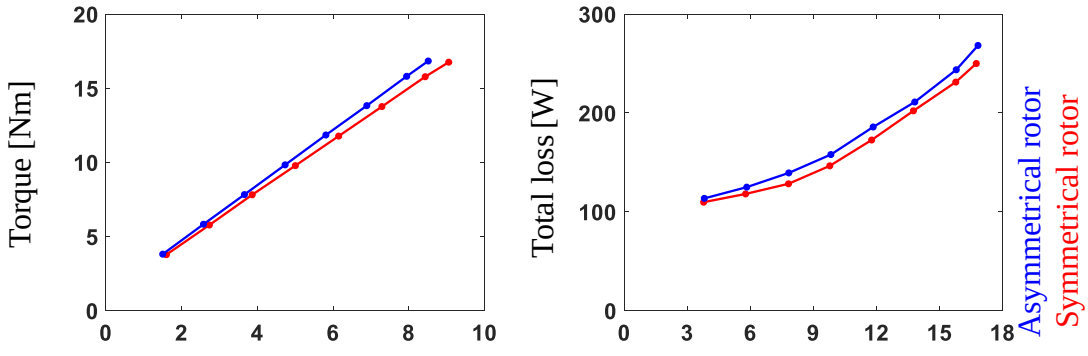

(a) torque linearity (b) motor total loss

Fig. 3-55 Comparison of the measured torque and power loss at 2000 r/min for the FW-SPMSM designed with the symmetrical and asymmetrical rotors

The designed motor with the symmetrical rotor achieves lower losses for the same torque level as in Fig. 3-55-b. Lower loss achieved with the designed motor with the symmetrical rotor due to the lower iron loss achieved in this design as in Fig. 3-56-b.

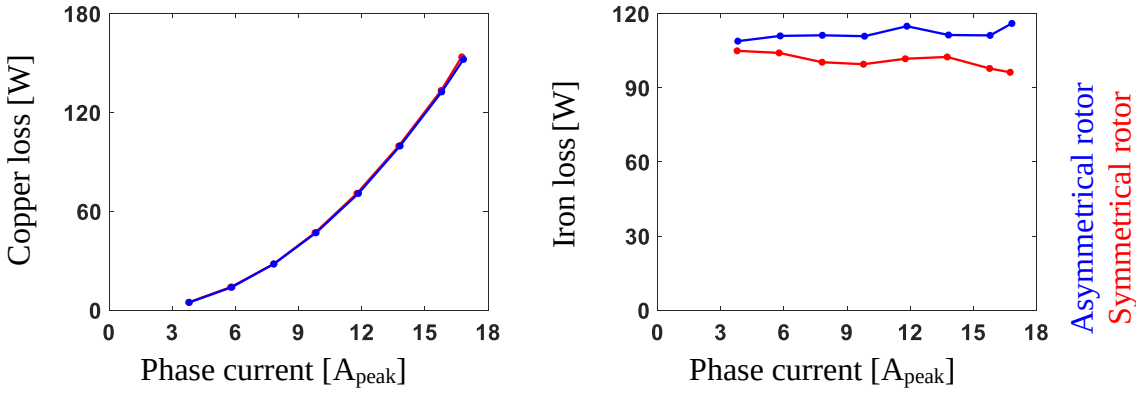

(a) copper loss (b) iron loss

Fig. 3-56 Comparison of the measured copper and iron loss at 2000 r/min for the FW-SPMSM designed with the symmetrical and asymmetrical rotors

The designed motor with the symmetrical rotor achieves slightly lower torque but lower losses compared with the asymmetrical rotor design. This motor has a lower stack length (89 mm compared to 94 mm with the asymmetric rotor). More torque can be obtained using the same stack length in both rotors.

The designed motor with the symmetrical rotor achieves lower loss, this motor has significantly better self-sensing properties. This motor is controlled using flux injection based self-sensing even at overload conditions. Chapter 6 of this thesis will present the experimental results performed on this motor.

3.5 Scalablility Analysis for the Designed FW-SPMSMs

This section will evaluate the performance of the design motors using symmetrical and asymmetrical rotors when they scaled down to 100 W and scaled up to 5 kW.

First, the designed motors are scaled down to 100 W. For this small size motor, the airgap length is reduced to 0.3 mm. The designed FW-SPMSMs with the symmetrical and asymmetrical rotors power conversion and self-sensing properties were compared using 2D-FEA. Table 3-9 summarizes the main dimensions of the evaluated 100 W FW-SPMSMs.

Table 3-9 Main dimensions of the designed 100 W FW-SPMSMs

	Stator outer diameter	Rotor outer diameter	Airgap	Stack length	Resistance	Rated current	Rated torque	Number of turns
Asymmetrical rotor	39 mm	20.4 mm	0.3 mm	**30 mm**	8.9 Ω	0.7 Arms	0.52 Nm	75
Symmetrical rotor	39 mm	20.4 mm	0.3 mm	**29.4 mm**	8.9 Ω	0.7 Arms	0.52 Nm	75

Fig. 3-57-a compares the back EMF of the 100 W scaled motors, while Fig. 3-57-b compares the torque linearity. The designed FW-SPMSM with the symmetrical rotor achieves higher torque at high current, while the asymmetrical rotor motor torque degrades at high current due to rotor saturation caused by the rotor holes. The designed 100 W FW-SPMSM with the symmetrical rotor has a shorter stack length compared to the asymmetrical rotor design while achieving the same rated torque at the rated condition.

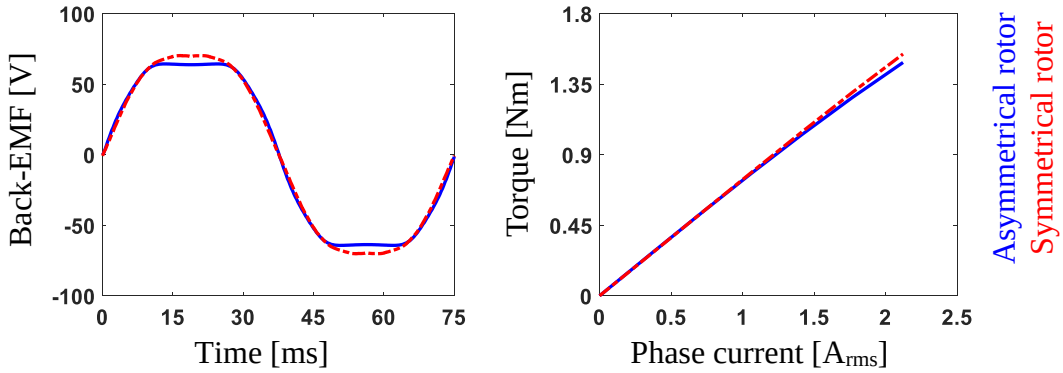

(a) back-EMF at 2000 r/min (b) torque linearity at 2000 r/min

Fig. 3-57 Comparison between the simulated back-EMF and torque linerity for the designed 100 W motors using symmetrical and asymmetrical rotors

Fig. 3-58-a compares the saliency ratio for the scaled down FW-SPMSM motors, the designed motor with the symmetrical rotor achieve significantly higher saliency ratio compared to the asymmetrical rotor design. This saliency ratio improves when loading the motor.

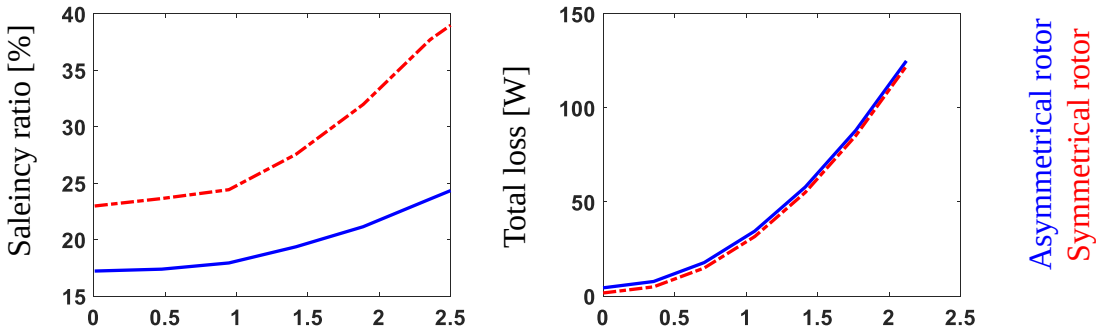

(a) saliency ratio (b) total motor loss at 2000 r/min

Fig. 3-58 Comparison between the simulated saliency ratio and motor loss for the designed 100W motors with symmetrical and asymmetrical rotors

Fig. 3-58-b compares the motor total loss for the scaled down FW-SPMSMs, the designed motor using the symmetrical rotor achieves slightly lower loss due to lower iron loss compared to the asymmetrical rotor design.

Then, the designed motors with symmetrical and asymmetrical rotors are scaled up to 5 kW. The FW-SPMSMs designed with symmetrical and asymmetrical rotors power conversion and self-sensing properties were compared using 2D-FEA. Table 2-10 summarizes the main dimensions of the evaluated 5 kW FW-SPMSMs.

Table 3-10 Main dimensions of the designed 5 kW FW-SPMSMs

	Stator outer diameter	Rotor outer diameter	Airgap	Stack length	Resistance	Rated current	Rated torque	Number of turns
Asymmetrical rotor	128 mm	64.15 mm	1 mm	**127 mm**	1.7 Ω	8.13 Arms	23.9 Nm	25
Symmetrical rotor	128 mm	64.15 mm	1 mm	**125 mm**	0.34 Ω	8.13 Arms	23.9 Nm	25

The calculated back-EMF using 2D-FEA for the 5 W scaled motors is shown in Fig. 3-59-a, while Fig. 3-59-b shows the torque linearity for both designs. Both designs achieve similar torque per current until twice the rated current, after that the asymmetric rotor start saturating leading to lower torque. The designed 5 kW FW-SPMSM with the symmetrical rotor has a shorter stack length compared to the asymmetric rotor design while achieving the same rated torque at the rated conditions.

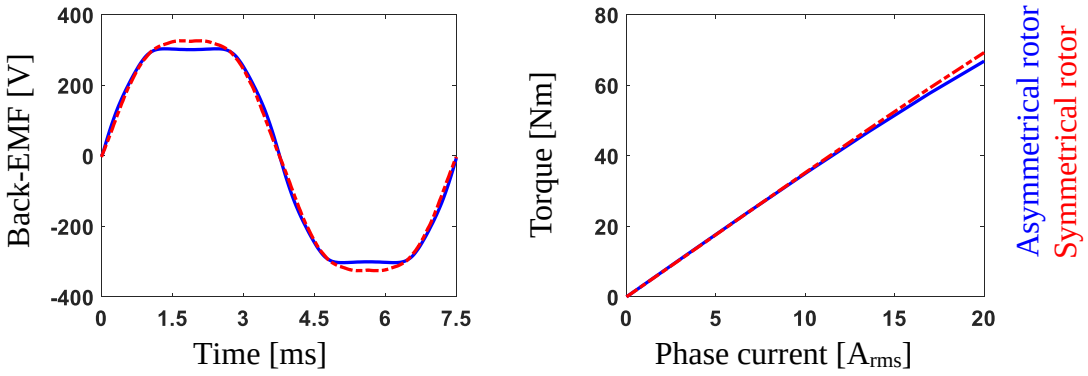

(a) back-EMF at 2000 r/min (b) torque linearity at 2000 r/min

Fig. 3-59 Comparison between the simulated back-EMF and torque linerity for the designed 5 kW motors with symmetrical and asymmetrical rotors

Fig. 3-60-a compares the saliency ratio for the scaled-up FW-SPMSM motors, the designed motor with the symmetrical rotor maintains the attractive saliency feature that improves with the load. The designed 5 kW FW-SPMSM using the proposed design methodology achieves lower losses as in Fig. 3-60-b due to the lower iron loss and achieves attractive self-sensing properties.

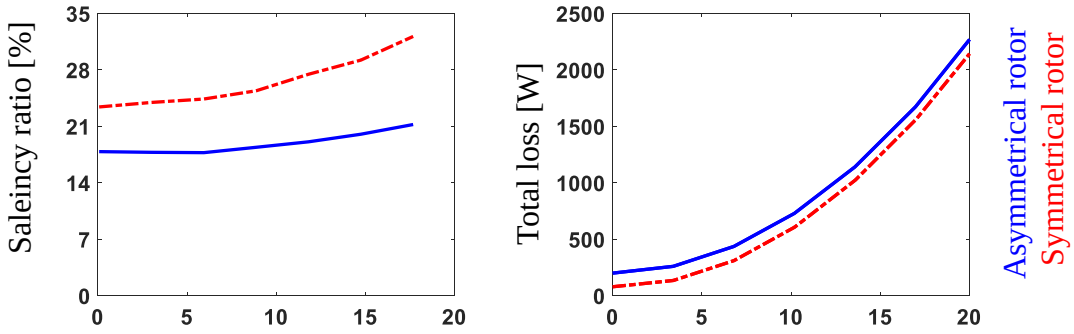

(a) saliency ratio (b) total motor loss at 2000 r/min

Fig. 3-60 Comparison between the simulated saliency ratio and motor loss for the designed 5 kW motors with symmetrical and asymmetrical rotors

The proposed FW-SPMSM with symmetrical rotor design achieves attractive power conversion and self-sensing features for small and larger size servo motors.

3.6 Summary

This chapter presents a methodology to design a FW-SPMSM for servo applications with attractive self-sensing properties. The key observations and conclusions from this chapter are summarized as follows.

- Designing FW-SPMSM motors for servo applications with very low cogging and ripple torque can be achieved by using ring magnets with shifted PM's, or by shaping the magnet to reduce the airgap flux harmonics, which can be done using bread-loaf or arc-shaped magnets.
- FW-SPMSM motors for servo applications with shifted ring PM's requires special mechanical design to move the rotor center of mass to the center of rotation, which can be done by using asymmetrical rotor holes.
- Using arc-shaped magnets helps to reduce the magnetic material that is required for bread-loaf magnets. However, the manufacturing cost of these magnets is higher.

- Adding small iron notches between adjacent magnets improves the self-sensing performance by increasing the q-axis inductance. However, they will slightly increase the leakage flux and will slightly affect the average torque of the motor.
- Adding d-axis flux barriers helps in saturating the d-axis flux path in the rotor which reduces the d-axis inductance, creating a detectable saliency.
- The d-axis flux barriers also help in stabilizing the q-axis inductance with load variation. This is achieved by using the d-axis flux to saturate the q-axis flux path. In this case, the self-sensing performance of the motor will not degrade with load variations like standard FW-PM motors. The d-axis flux barriers also help in reducing the rotor mass and inertia, which improves the dynamic performance of the motor.
- The demagnetization risk with bread-loaf magnets occurs when injecting q-axis current because this type of magnet is thin in the edges and thick in the middle.
- Experimental evaluation of the fabricated designs shows an improved self-sensing and power conversion performance for the designed motor using the developed design methodology.
- The proposed design methodology can be used for small, medium, and large size servo motor. Through this methodology motors with enhanced power conversion and self-sensing properties can be designed. This would reduce the cost of this motor by removing the position sensor.

Chapter 4 Dynamic Shaft Torque Observer Structure Enabling Accurate Dynamometer Transient Loss Measurements

The main technical content of this chapter has been published in two technical papers in [125] and [126]. This chapter presents a methodology to accurately estimate the dynamometer shaft torque components during both steady-state and transient using only standard drive sensors. Allowing the motor transient losses to be accurately measured using standard testing dynamometers.

Testing dynamometers are typically used for evaluating steady-state motor performance. These dynamometers use shaft windup torque sensors and power analyzers to measure the motor steady-state electrical and mechanical power. Then constructing motor efficiency and iron loss maps. However, evaluating the transient performance of the motor is not feasible using a dynamometer, this is due to the inertial torque component that appears during dynamic operation. This limit using the windup torque sensors to measure only steady-state losses.

In this chapter, the dynamic model of the dynamometer is constructed, then an observer that can estimate the shaft torque components is developed. The proposed observer is experimentally evaluated and used to measure motor transient loss. Finally, the parameter sensitivity of the proposed observer is conducted.

4.1 Dynamic Model of a Back-to-Back Dynamometer Configuration

Dynamometers are widely used in research labs to evaluate the torque, speed, and efficiency of electrical motors. A back-to-back configuration is one of the most commonly used dynamometer configurations. This configuration consists of two electric motors – one as a load motor and the other as a test motor – connected together through shaft couplings and a torque sensor. Standard torque cells measure the windup torque component.

Windup torque is then used to calculate the motor mechanical power during steady-state speed operation, while electrical power is calculated from the measured motor terminal voltage and current, this is typically done using power analyzers. Measuring these two quantities is used to generate the motor efficiency and loss maps.

Transient performance of servo motors is a primary metric which is not easily measurable on traditional dynamometers. This requires measuring the dynamometer dynamic shaft torque including the inertial torque component, which can be measured by measuring the angular acceleration. However, rotary angular accelerometers are not available in the market. In this section, the dynamic model for a dynamometer is constructed based on the mechanical model of the two motors and the mechanical connection between them, then a dynamic shaft torque observer is developed later in this chapter. This observer allows calculating the dynamometer shaft torque components including the inertial torque using standard dynamometer sensors allowing measuring the motor transient losses.

Fig. 4-1 shows the dynamometer. While Fig. 4-2-a shows the cross-sectional view of the used torque sensor, Fig. 4-2-b shows the mechanical model of the torque sensor. The

dynamometer model is shown in Fig. 4-3. From this figure, the resonant frequency of the system was calculated by finding the lowest natural frequency of a four lumped inertias system, as in (4-1).

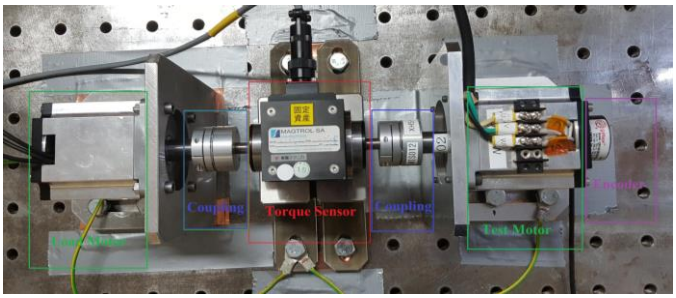

Fig. 4-1 Tested dynamometer

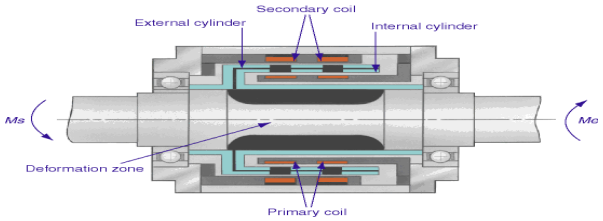

(a) cross-sectional view

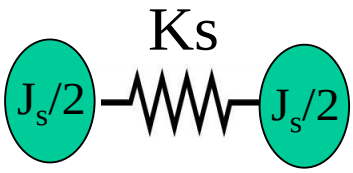

(b) mechanical model

Fig. 4-2 The used torque transducer

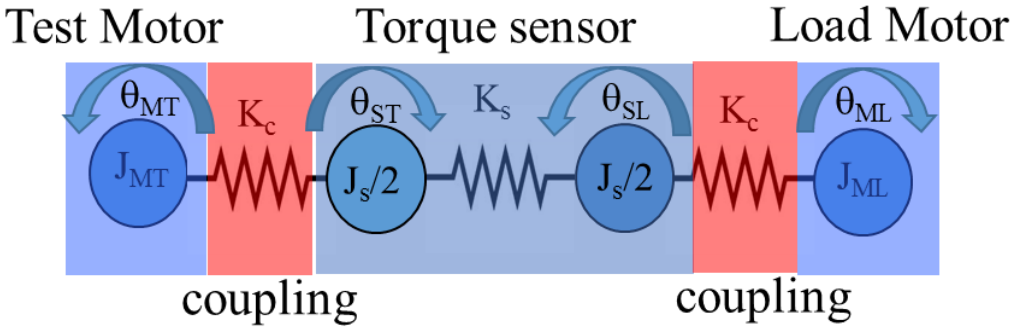

Fig. 4-3 Mechanical model of the tested dynamometer

$$\begin{bmatrix} J_{ML} & 0 & 0 & 0 \\ 0 & \frac{J_s}{2} & 0 & 0 \\ 0 & 0 & \frac{J_s}{2} & 0 \\ 0 & 0 & 0 & J_{MT} \end{bmatrix} * \begin{bmatrix} \ddot{\theta} \end{bmatrix} + \begin{bmatrix} K_c & -K_c & 0 & 0 \\ -K_c & K_c+K_s & -K_s & 0 \\ 0 & -K_s & K_c+K_s & -K_c \\ 0 & 0 & -K_c & K_c \end{bmatrix} * \begin{bmatrix} \theta \end{bmatrix} = \begin{bmatrix} 0 \end{bmatrix} \quad (4\text{-}1)$$

where $[\theta]`=[\theta_{MT}\ \theta_{ST}\ \theta_{SL}\ \theta_{ML}]$, θ_{MT} is the tested motor angular position, θ_{ML} is the load motor angular position, θ_{ST} is the angular position between the tested motor coupling and the torque sensor, θ_{SL} is the angular position between the load motor coupling and the torque sensor. J_{ML} is the load motor inertia, J_{MT} is the test motor inertia, J_s is the torque sensor inertia, K_c is the coupling stiffness, K_s is the torque sensor stiffness.

The resonant frequency is calculated solving (4-1) and found to be 520 Hz which is close to the measured frequency of 511 Hz. The resonant frequency is measured by measuring the system dynamic stiffness, which is measured through commanding a chirp torque (T_d) to the load motor and measuring the tested motor speed (Ω), while commanding a zero speed to the test motor ($\omega^* = 0$). Dynamic stiffness drops at the resonance to a low value as in Fig. 4-4. The measured resonant frequency can be used to calibrate the dynamometer model.

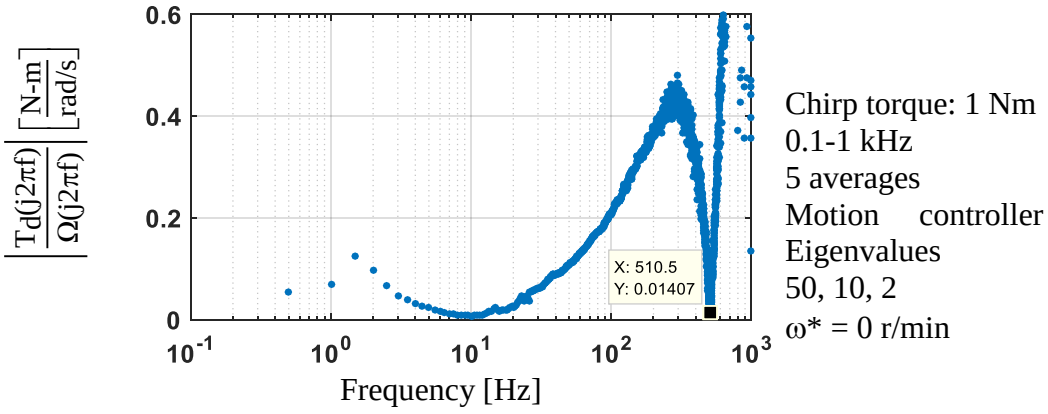

Fig. 4-4 Measured system dynamic stifness

The previous resonant frequency calculations verified the estimated inertia for both the

tested and the load motors. The stiffness of the shaft couplings and torque sensor are obtained from the datasheet. The above model is simplified by finding the equivalent stiffness between the tested and load motors. Half of the inertia of the torque sensor is added to both the tested and load motor inertias. Fig. 4-5 shows the simplified mechanical model for the dynamometer. Equivalent stiffness is calculated, as in (4-2).

$$\frac{1}{K_{eq}} = \frac{1}{K_c} + \frac{1}{K_s} + \frac{1}{K_c} \tag{4-2}$$

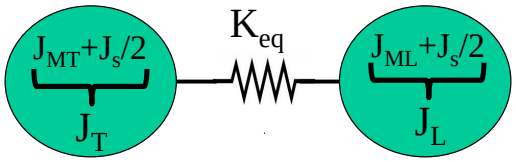

Fig. 4-5 Simplifed mechanical model of the tested dynamometer

The dynamic equation model for the simplified dynamometer model was found in [99] and expressed by (4-3) and (4-4).

$$T_{em\text{-}T} + T_{D\text{-}T} - K_{eq}(\theta_L - \theta_T) - b_p(\omega_L - \omega_T) = J_T \frac{d\omega_T}{dt} \tag{4-3}$$

$$T_{em\text{-}L} + T_{D\text{-}L} - K_{eq}(\theta_T - \theta_L) - b_p(\omega_T - \omega_L) = J_L \frac{d\omega_L}{dt} \tag{4-4}$$

where T_{em} is the airgap torque, T_D is the disturbance torque, θ and ω are the angular position and speed. J is the motor inertia, b_p is the damping coefficient. The subscript T means tested motor, while the subscript L indicates load motor.

The state block diagram of the dynamometer is constructed based on (4-3) and (4-4) and is shown in Fig. 4-6.

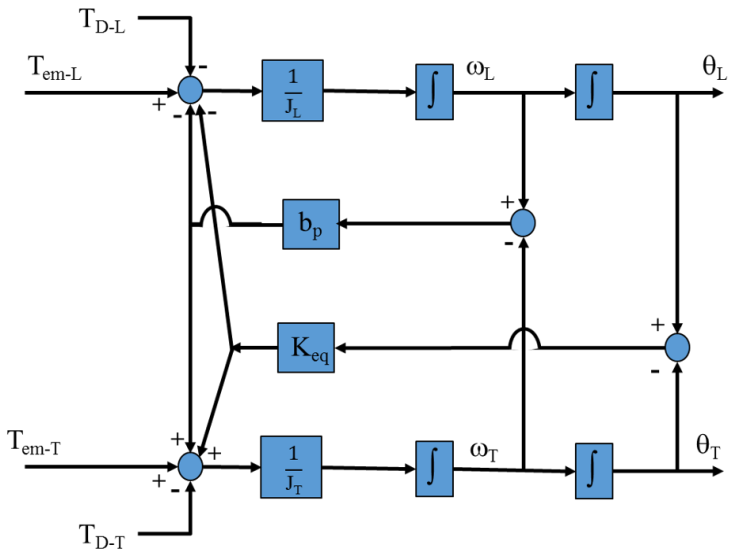

Fig. 4-6 State block diagram of the tested dynamometer[99]

4.2 Observer Structure for Shaft Torque Estimation

An observer structure for estimating the shaft torque is constructed based on the system model that was constructed in the previous section. Airgap torque for both tested and load motors, which are calculated based on the measured currents and estimated flux is used as a command feedforward signal for this observer structure. In this configuration, a single encoder is used and attached to the tested motor. This encoder will measure the angular position of the tested motor, while the angular position and speed of the load motor will be obtained from the constructed observer. The error between the measured and estimated position for the tested motor will be fed into the observer controller. This will force the shaft torque observer structure to track the actual system. Fig. 4-7 shows the system block diagram of the whole system with the observer structure.

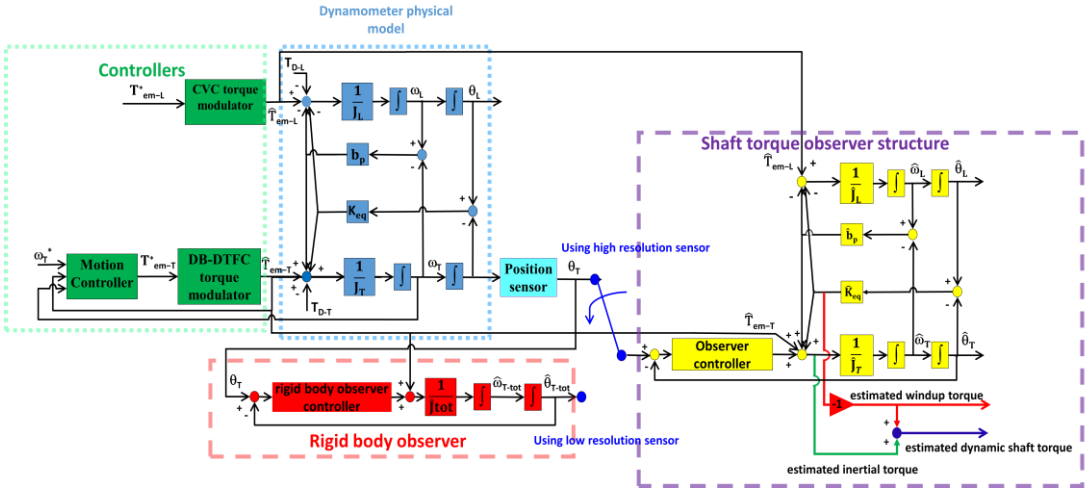

Fig. 4-7 System block diagram with shaft torque observer structure

Using the proposed shaft torque observer structure directly requires the use of a high-resolution position sensor (a sin-cos encoder or similar). This is necessary to minmize the quantization effect in the measured position. To overcome that and implement an observer structure for estimating shaft torque with a dynamometer that uses a conventional A quad B encoder, a Luenberger style rigid body position observer, as described in [112], is used in cascade with the proposed shaft torque observer structure as in Fig. 4-7. This mitigates the quantization problem.

The rigid body observer is typically used in standard motor control to estimate the instantaneous rotor speed with high fidelity and use it as a feedback signal, to improve the performance of the drive. This observer is usually tuned to have similar bandwidth to the motion controller. In this thesis, this observer is tuned for 50 Hz. This bandwidth can be increased by using a higher resolution encoder. The proposed torque observer structure can be tuned to achieve a high bandwidth depending on the application. In this thesis, it is tuned for 400Hz (the resonance dynamics is not the focus of this thesis). This observer can capture the system

dynamics even beyond its bandwidth, this is due to the command feedforward path.

Torque sensors measure the windup torque between the tested and load motor and generally have a negligible damping. The windup shaft torque can be calculated from the estimated positions of both load and tested motors, as in (4-5). This torque will match the measured torque from the torque sensor, and it only requires a few lines of code. During transient speed operation, the inertial torque term needs to be added to (4-5). With that, it is possible to estimate the dynamic shaft torque (torque during transient speed operation), as in (4-6).

$$T_{\text{shaft-windup}} = K_{eq} (\hat{\theta}_T - \hat{\theta}_L) \tag{4-5}$$

$$T_{\text{shaft-Dynamic}} = K_{eq} (\hat{\theta}_T - \hat{\theta}_L) + J_T \frac{d\, \hat{\omega}_T}{dt} \tag{4-6}$$

Measuring the shaft torque during transient speed operation is generally not feasible in standard torque sensors because torque sensors do not correctly consider the inertial torque term that exists during transient speed operation. So, if the torque sensor is used to measure the dynamic torque during transient speed operation, then the measured value will be lower than the actual torque of the system, which includes the inertial term. This will lead to overestimating the motor transient losses.

The effect of the motor inertia can't be neglected in dynamic loss evaluation for many applications. Typical motor-load inertia ratio was discussed in [113]. The authors recommended a small inertia ratio for a well-behaved servo-drive system. For example, a wafer-handling machine in an IC fabrication needs an inertia ratio close to 1:1. For applications with a high load inertia, a matching gear is typically used to achieve nearly unity inertia ratio, which improves the system performance.

4.3 Experimental Evaluation of the Observer Structure for Shaft Torque Estimation

In this thesis, a torque sensor (MAGTROL® TM300) that can measure the windup torque component with high bandwidth is connected to the system, and a torque sensor measurement is used as a baseline to validate the designed observer structure. The proposed observer would theoretically work even without having the torque sensor. In this case, different stiffness values need to be considered in the system model.

In order to validate the observer structure for estimating shaft torque, it was implemented on a test setup, as in Fig. 4-7. An interior permanent magnet synchronous motor (IPMSM) is coupled with a surface mounted PM motor (SPMSM) in a back-to-back configuration through a torque transducer. The angular position of the tested motor was measured using an incremental encoder that has 5,000 pulses/revolution. Table 4-1 summarizes the key parameters of the test setup. The tested motor is controlled via deadbeat-direct torque and flux control (DB-DTFC), while the load motor is controlled using current vector control (CVC). The proposed methodology would work with torque control techniques for any machine. It only requires estimating the motor airgap torque.

The dynamometer damping coefficient was measured by setting the damping coefficient (b_p) to zero in Fig. 4-7, then by commanding a low-frequency sine wave torque at different speeds. At higher speeds, the average estimated windup torque will have a small dc offset from the measured one, this is due to neglecting the dynamometer damping. Fig. 4-8 shows the torque offset due to damping at different speeds.

Table 4-1 Mechanical system parameters

Parameter	Value
Load / test motor inertia	$180.5e^{-6}/180.5e^{-6}$ kgm^2
Load / test motor magnet flux	0.0556 /0.0529 Wb
Load / test motor d axis inductance	4/3 mH
Load / test motor q axis inductance	4.7/3 mH
Torque cell inertia	$26.5e^{-6}$ kgm^2
Torque cell[14] / coupling stiffness	1450 / 6000 Nm/rad
Test motor rated torque / power	2.39 Nm / 750 W
Load motor rated torque / power	2.39 Nm / 750 W

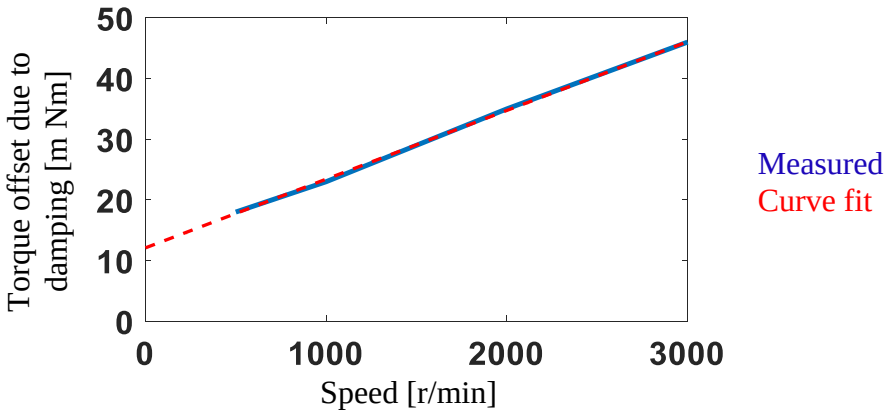

Fig. 4-8 Average torque offset due to dynamometer damping

The slope of the line in Fig. 4-8 represents the damping coefficient in the tested dynamometer.

Fig. 4-9-a shows the measured and estimated windup torque when neglecting the damping coefficient in the model. Fig. 4-9-b shows the same results when including the damping. From this figure, the motor's damping is small but needs to be considered in order to achieve accurate torque estimation.

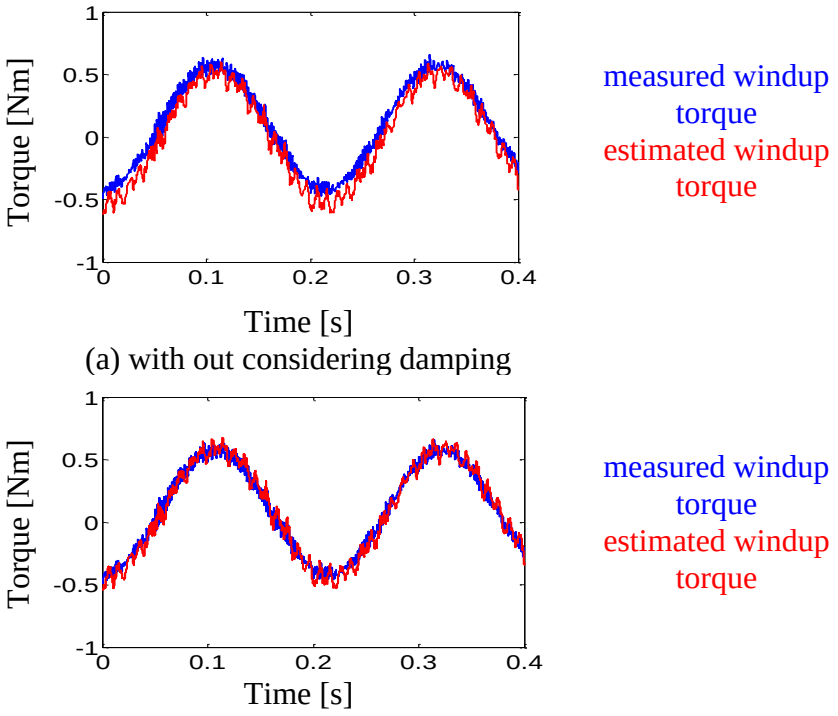

(a) with out considering damping

(b) with considering damping

Fig. 4-9 Estimated and measured windup torque at 3000 r/min with and without considering the damping

In order to evaluate the observer structure for estimating shaft torque, a 5 Hz sine wave torque is commanded from the load motor, and the tested motor is controlled to run at different speeds. The tested motor speed is controlled using a stiff velocity loop with a 50 Hz bandwidth (This bandwidth is limited by the used encoder. It can be further increased if a higher resolution position sensor is used). The velocity loop bandwidth is tuned to achieve a low RMS current for the same operation. Fig. 4-10 compares the measured q-axis current at different velocity loop bandwidth when the motor run at 100 r/min and 1Nm, through this test the motion controller bandwidth is selected.

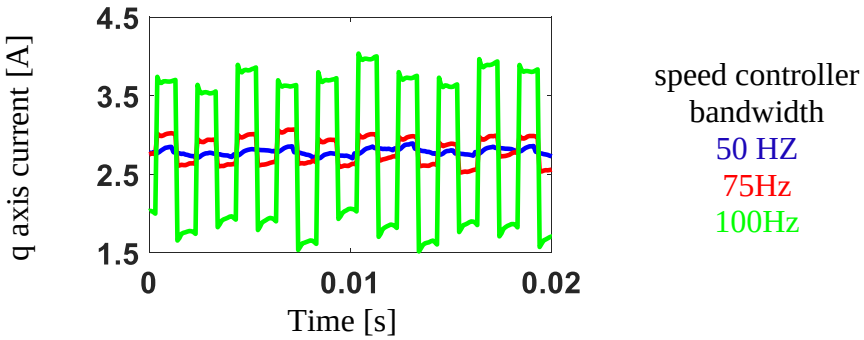

Fig. 4-10 Measured q-axis current when the motor runs at 100 r/min and 1Nm using different velocicty loop bandwidths

Having a stiff velocity loop compared to the commanded torque will force the inertial torque to be zero (treat the load torque as a disturbance and reject it to maintain steady-state speed operation). In this case, the windup torque will be very close to the dynamic shaft torque. Fig. 4-11 shows the measured windup torque, it also shows the estimated dynamic, windup, and inertial torque components from the proposed observer structure. The same experiment was repeated at different speeds. The observer is able to estimate the windup torque precisely.

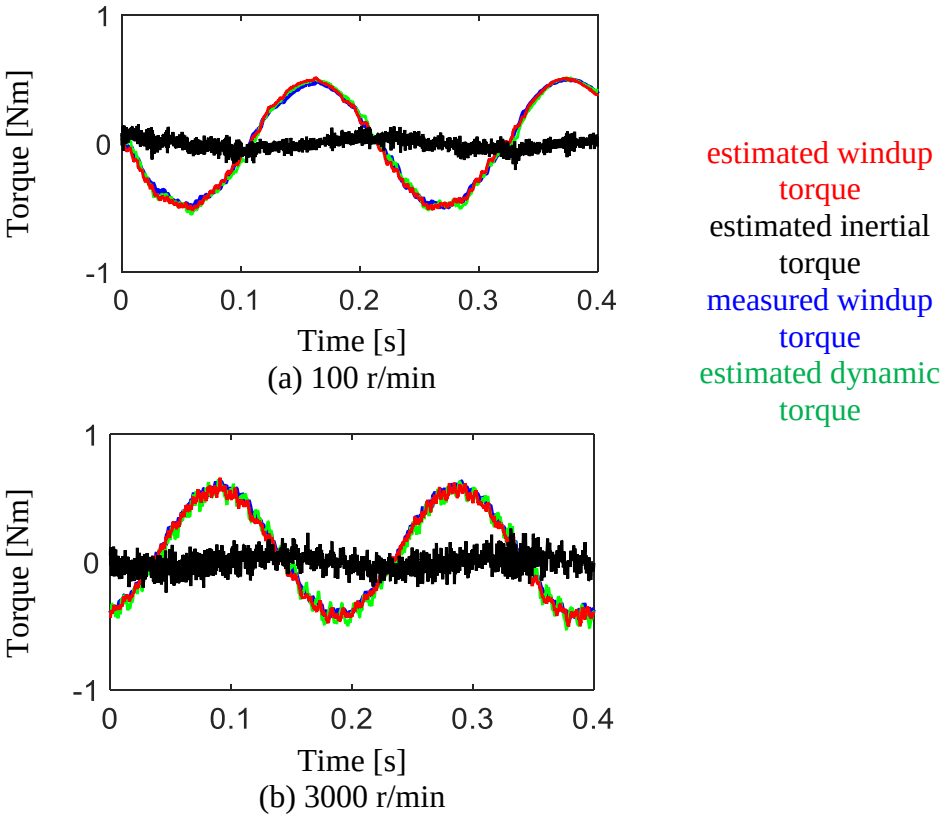

(a) 100 r/min

(b) 3000 r/min

Fig. 4-11 Estimated windup,dynamic,inertial and measured windup torque at two speeds

To make sure the observer structure for estimating shaft torque works correctly during dynamic speed transients, the tested motor was accelerated from 0 to 3000 r/min in 0.15 second. Fig. 4-12 shows the speed calculated from the encoder for this test.

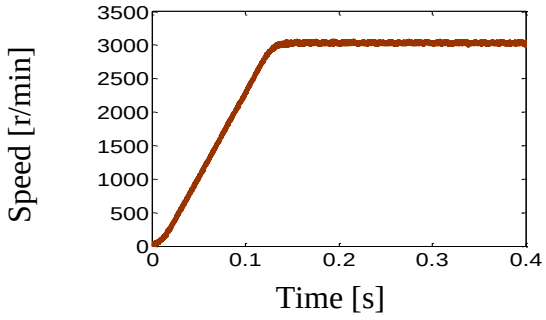

Fig. 4-12 Speed calculated from the encoder during accelration test

The estimated windup torque during the acceleration test was compared with the

measured windup torque from the torque sensor. The estimated windup torque matches the measured windup torque. Fig. 4-13 shows the results of this test. To observe the dynamic torque during the acceleration test, the inertial torque term is considered, as in Fig. 4-7. The estimated dynamic torque is overlaid with the measured windup torque as in Fig. 4-13. The inertial torque is also shown in the same figure.

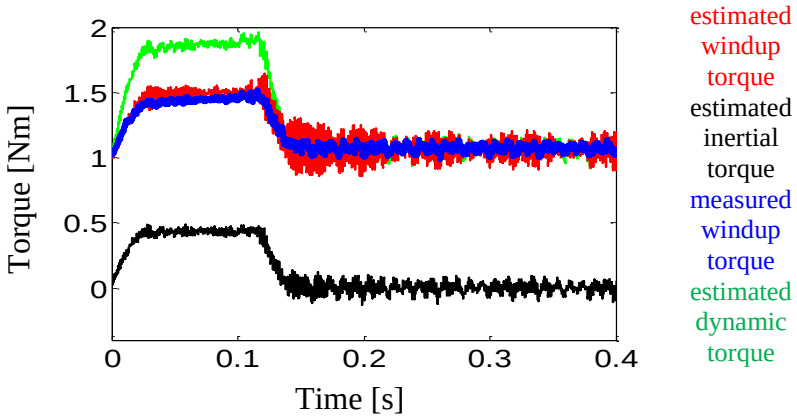

Fig. 4-13 Estimated windup, dynamic, inertial and measured windup torque at during a rapid acceleration test

Dynamic estimated torque combines both windup and inertial torque terms. As it is clear from Fig. 4-13 the dynamic torque is higher than the windup torque during the acceleration period, this due to the inertial torque component that appears during the transient speed operation. During steady-state speed, the inertial torque component becomes negligible, both dynamic and windup torque components become close to each other.

Similar results can be obtained if angular acceleration sensors with adequate bandwidth were available and used with the windup torque sensor. However, the proposed methodology doesn't require angular acceleration sensors.

Different techniques can be used to estimate the motor angular acceleration and then use it to calculate the inertial torque by multiplying the effective motor inertia ($J_T = J_{ML} + J_s/2$) with

the angular acceleration. Dynamic shaft torque is then calculated through adding the airgap torque to the inertial torque. The main techniques are:

Method 1:

Using a position sensor signal like an encoder to calculate the average angular acceleration ($\Delta\omega/\Delta t = \Delta[\Delta\theta/\Delta t]/\Delta t$), average inertial torque ($J_T*\Delta\omega/\Delta t$), and average dynamic shaft torque signals. The quantization effect will lead to very noisy signals, which are especially problematic for low-speed operation. The noise issue in addition to the associated delay with the average acceleration will significantly affect the accuracy of the dynamic loss measurements. The performance gets worse with using a lower resolution encoder.

Method 2:

Using a rigid body observer or a state filter to estimate the motor instantaneous acceleration, inertial torque, and dynamic shaft torque signals. In this case, the dynamometer parameters are lumped in a single inertia rotary system. This method is useful to reduce the quantization noise in the estimated acceleration and can achieve an acceptable performance during the high-speed operation. However, at low-speed operation, the signal will be noisy which degrade the accuracy of the transient loss measurements. The performance gets worse when using a lower resolution encoder.

Method 3:

Using the proposed dynamic shaft torque observer structure. This observer models the mechanical system for the dynamometer. This observer can accurately estimate the motor angular acceleration, inertial torque, and dynamic shaft torque signals with high-bandwidth with a very low noise level. This will lead to an accurate loss measurement during the steady-state and

dynamic speed operations. This observer can achieve a good performance even when using a low-resolution encoder.

To evaluate the previous techniques, the tested motor is controlled to run with a sine wave speed with 1 Nm load torque which is applied using the load motor. The estimated speed from the rigid body observer is used as a feedback signal. This improves the performance of the drive by reducing the impact of encoder quantization and runs the motor smoothly during the low-speed operation.

Fig. 4-14 shows the experimental results when the motor runs at sinewave speed profile with 100 r/min peak value. Estimating the dynamic torque signal using the calculated average angular acceleration from the encoder leads to a very noisy signal that cannot be used to calculate the dynamic shaft torque signal.

Estimating the dynamic torque signal using the rigid body observer has lower noise compared to the previous technique. However, this method is still significantly affected by quantization, this effect becomes worse in case of a lower-resolution encoder or at a lower speed.

The proposed observer structure is not affected by the quantization and can be used to evaluate the motor losses accurately even during low-speed operation, even when using a low-resolution encoder (800 pulses/revolution).

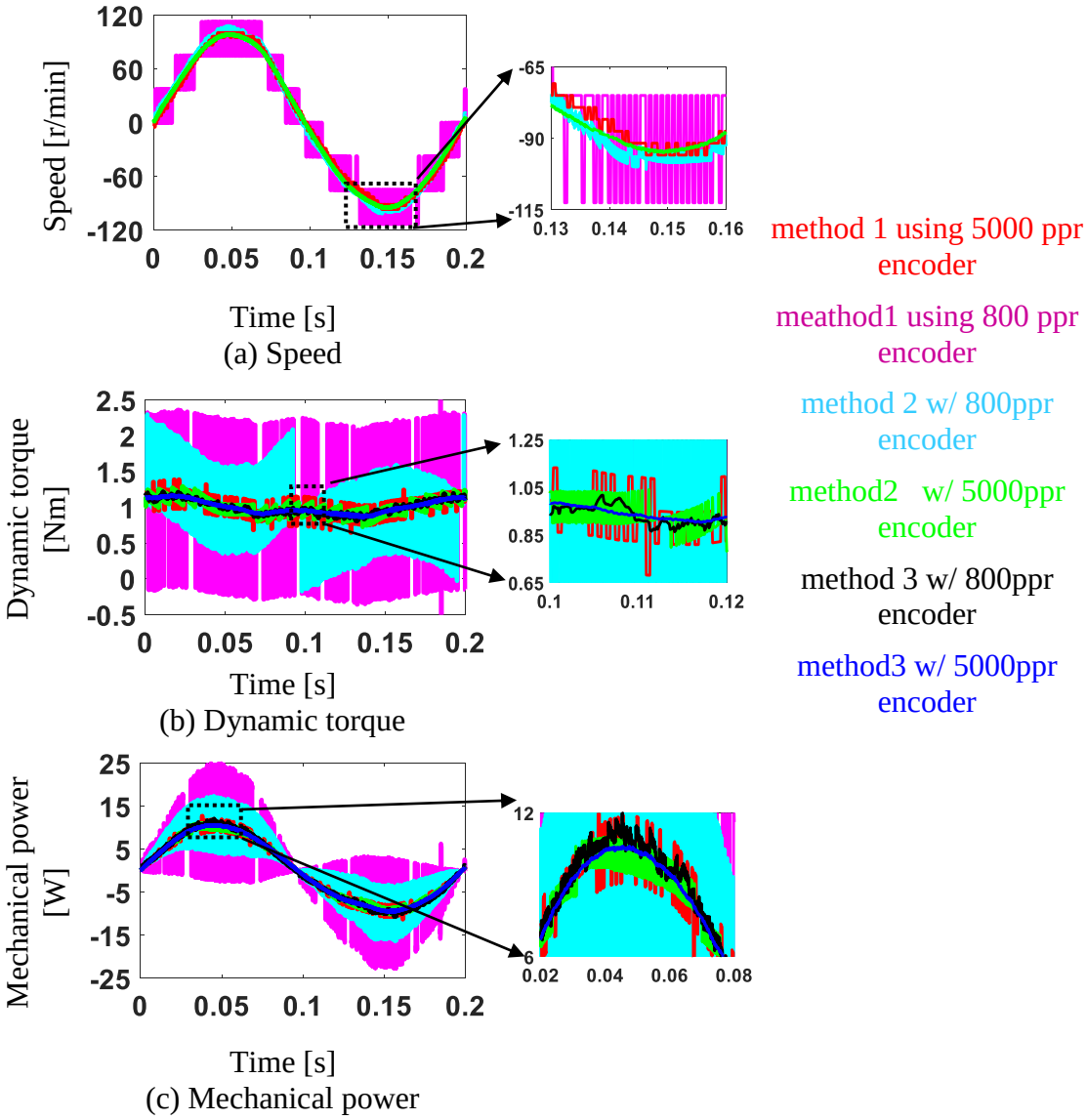

Fig. 4-14 Estimated dynamic torque and mechanical power using the torque observer, rigid body observer and encoder when the motor run at sinewave speed profile with 100 r/min peak

Fig. 4-15 shows the result when the motor runs at sinewave speed profile with 3000 r/min peak value. The encoder quantization effect becomes smaller with increasing the speed. During the high-speed operation, a rigid body observer (or state filter to estimate the acceleration) can be used to estimate the motor dynamic torque signal when using a good resolution encoder (5000 pulses/resolution). However, when using an 800 pulses/resolution encoder, the estimated

dynamic torque using the rigid body observer is still noisy even during the high-speed operation.

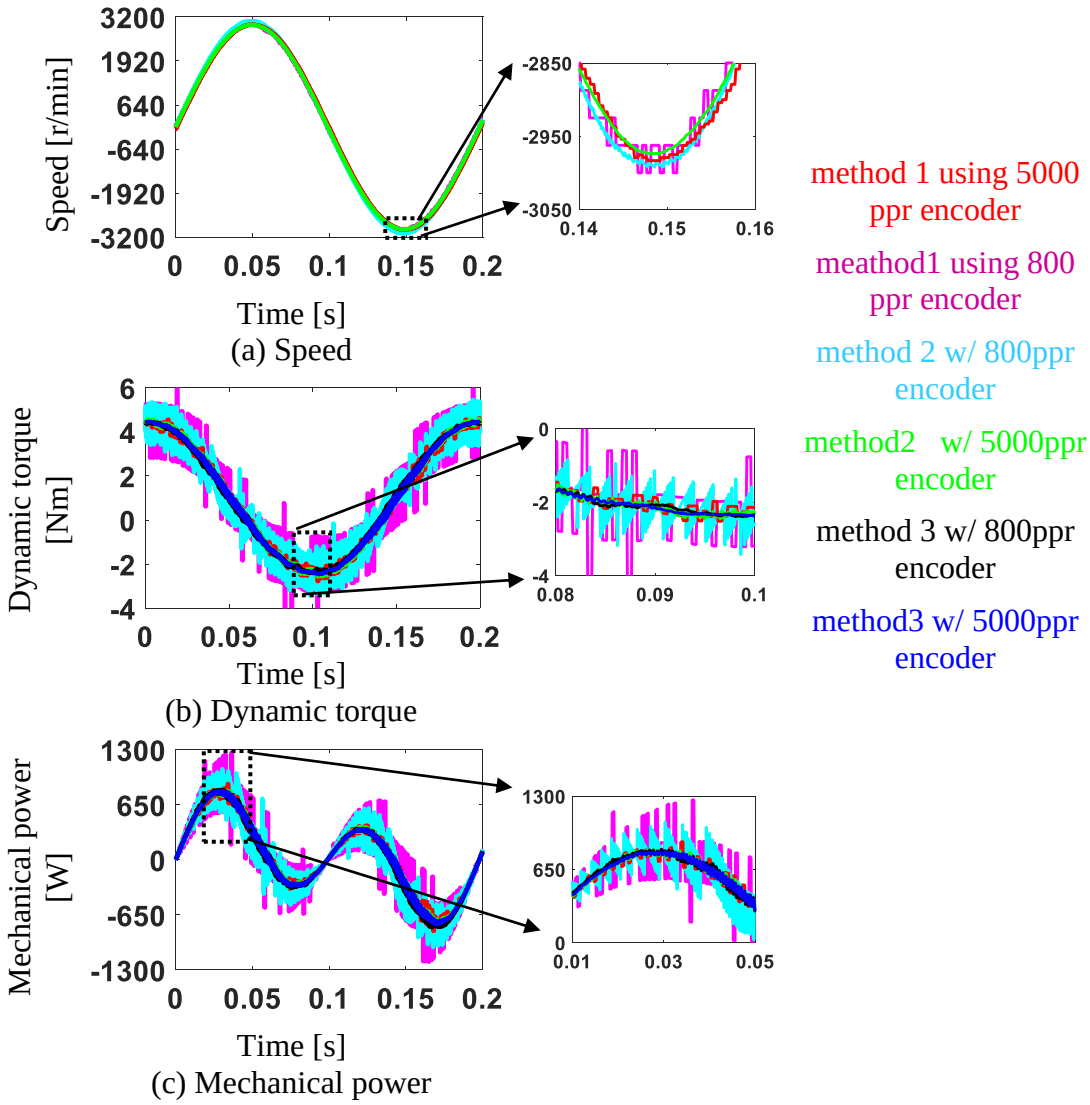

Fig. 4-15 Estimated dynamic torque and mechanical power using the torque observer, rigid body observer and encoder when the motor run at 3000 r/min sine wave speed profile

The proposed shaft torque observer structure exhibits good performance during both low and high-speed operation and using different A quad B encoder resolutions. This method is effective for laboratory testing since there is no need to use angular acceleration sensors and can

accurately operate using low-resolution encoders. This technique requires only 30 lines of code compared to 500 lines of code required for the control system.

4.4 Transient Loss Measurement During Acceleration of a Servo Motor

After successfully constructing and verifying the observer structure for estimating the shaft torque, the dynamic torque signal was used to measure the transient mechanical power. Instantaneous electrical power was calculated based on the measured voltages and currents of the tested motor. A high sampling rate motor drive analyzer (MDA 810 from Teledyne LeCroy) was used to measure both mechanical and electrical power. The measured transient loss was also compared with a loss model that is described in (4-7), More details about this loss model will be presented on chapter 5.

$$P_{loss} = \frac{3}{2} R \cdot (\hat{I}_{ds}^{r\,2} + \hat{I}_{qs}^{r\,2}) + K_h \cdot \omega_e \cdot (\hat{\lambda}_{ds}^{r\,2} + \hat{\lambda}_{qs}^{r\,2}) + K_e \cdot \omega_e^{\,2} \cdot (\hat{\lambda}_{ds}^{r\,2} + \hat{\lambda}_{qs}^{r\,2}) \qquad (4\text{-}7)$$

Fig. 4-16-a shows the measured electrical power during the acceleration test. Fig. 4-16-b compares the measured mechanical power calculated using the estimated dynamic torque with the mechanical power calculated from measured windup torque. From Fig. 4-16, the calculated mechanical power during the acceleration period using the measured windup torque from the torque sensor is lower than the measured mechanical power using the estimated dynamic torque, this due to neglecting the inertial torque component that appears during the transient speed operation. For steady state speed operation (when the motor ran at 3000 r/min), the mechanical power calculated using either the measured windup or estimated dynamic torque is identical.

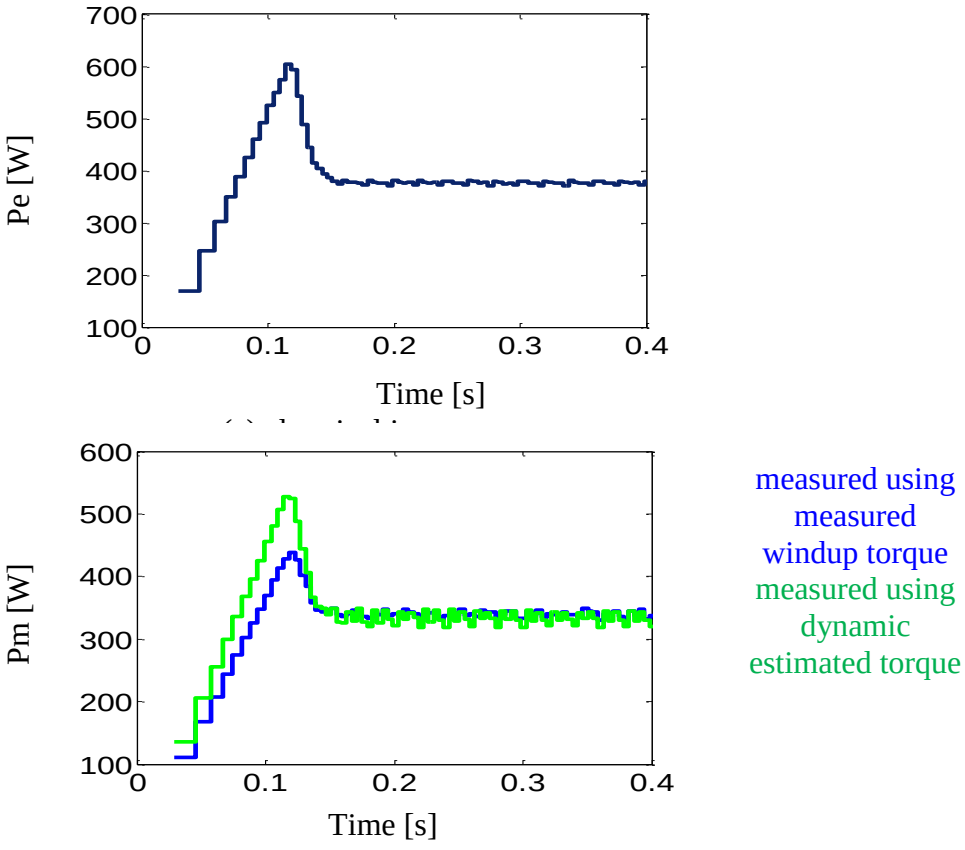

Fig. 4-16 Measured input and output power during acceleration test using both measured windup torque and dynamic estimated torque

Fig. 4-17 shows the measured motor loss using the dynamic estimated torque and the incorrectly measured loss using the measured windup torque. This figure also compares the losses with the expected losses from the constructed loss model in (4-7).

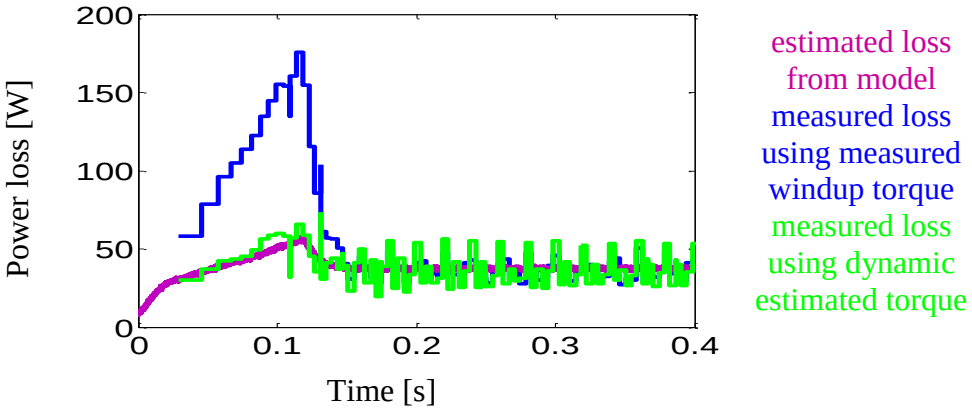

Fig. 4-17 Estimated loss from the loss model and measured loss using dynamic estimated torque, and measured windup torque

Fig. 4-17 indicates that the estimated loss during steady state speed operation is the same when using either estimated dynamic torque or measured windup torque. This is because the inertial torque is negligible. However, using the windup torque to estimate the motor losses during transients will lead to overestimating the motor losses.

To figure out the significance of the proposed method, a typical servo cycle loss is evaluated, the tested motor is accelerated from zero to 2850 r/min in 115 ms then decelerated again to zero, 2 Nm torque is applied using the load motor.

Fig. 4-18-a shows the calculated speed from the encoder during the evaluated cycle. While Fig. 4-18-b shows the shaft torque components during the studied cycle. The proposed observer structure estimates the windup torque component precisely. The inertial torque component appears during speed variations (acceleration, deceleration).

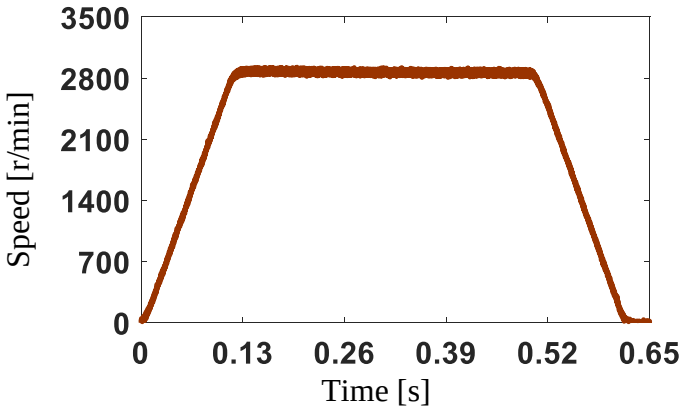

(a) speed calculated from the encoder

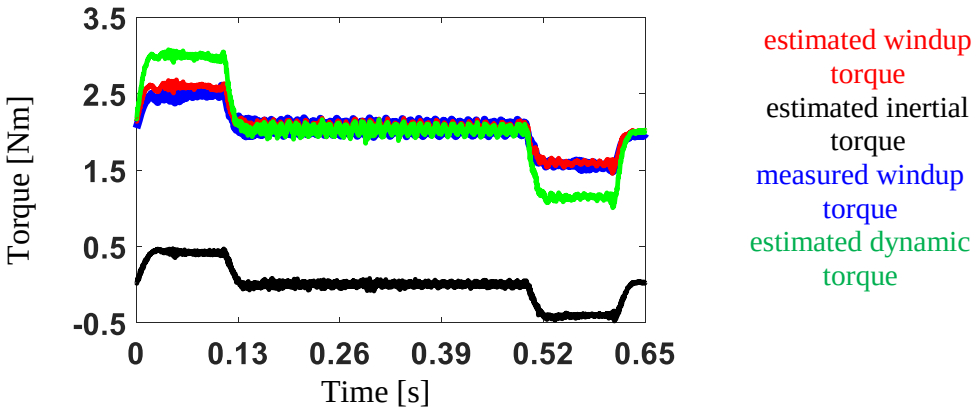

(b) shaft torque components

Fig. 4-18 Speed and shaft torque components for the evaluated cycle

Fig. 4-19-a shows the measured electrical power during this cycle, while Fig. 4-19-b compares between the mechanical power measured using the dynamic torque with the incorrectly measured mechanical power using the windup torque for the evaluated cycle.

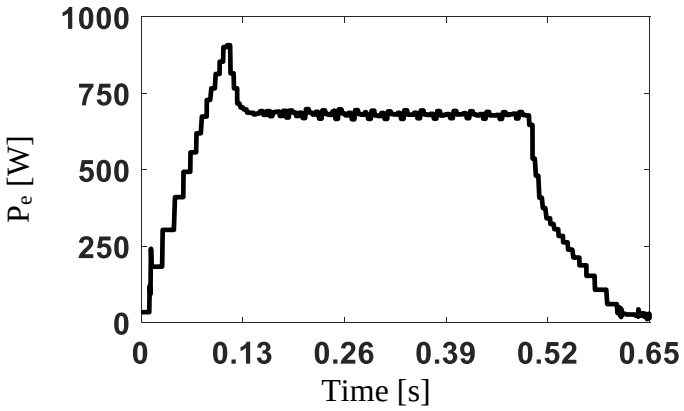

(a) speed calculated from the encoder

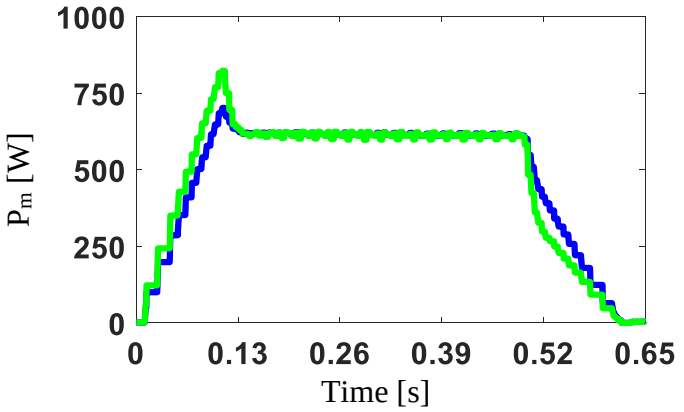

(b) shaft torque components

Fig. 4-19 Measured Input and output power during the evaluated cycle using both measured windup torque and dynamic estimated torque

Fig. 4-20-a shows the measured instantaneous losses (electrical power - mechanical power) using the dynamic torque signal. This result is consistent with the expected losses from the machine loss model, even though this model is not the focus of the paper. The key issue is that the calculated instantaneous power loss using the windup torque has significant error. Fig. 4-20-b shows the integrated power loss using the dynamic torque signal as well as the windup torque signal. In this case, both methods provide same energy loss at the end of the cycle, this because the motor acceleration rate is set to be the same as the deceleration rate (the overestimated transient loss during acceleration is recovered by the overestimated recovered

energy during deceleration).

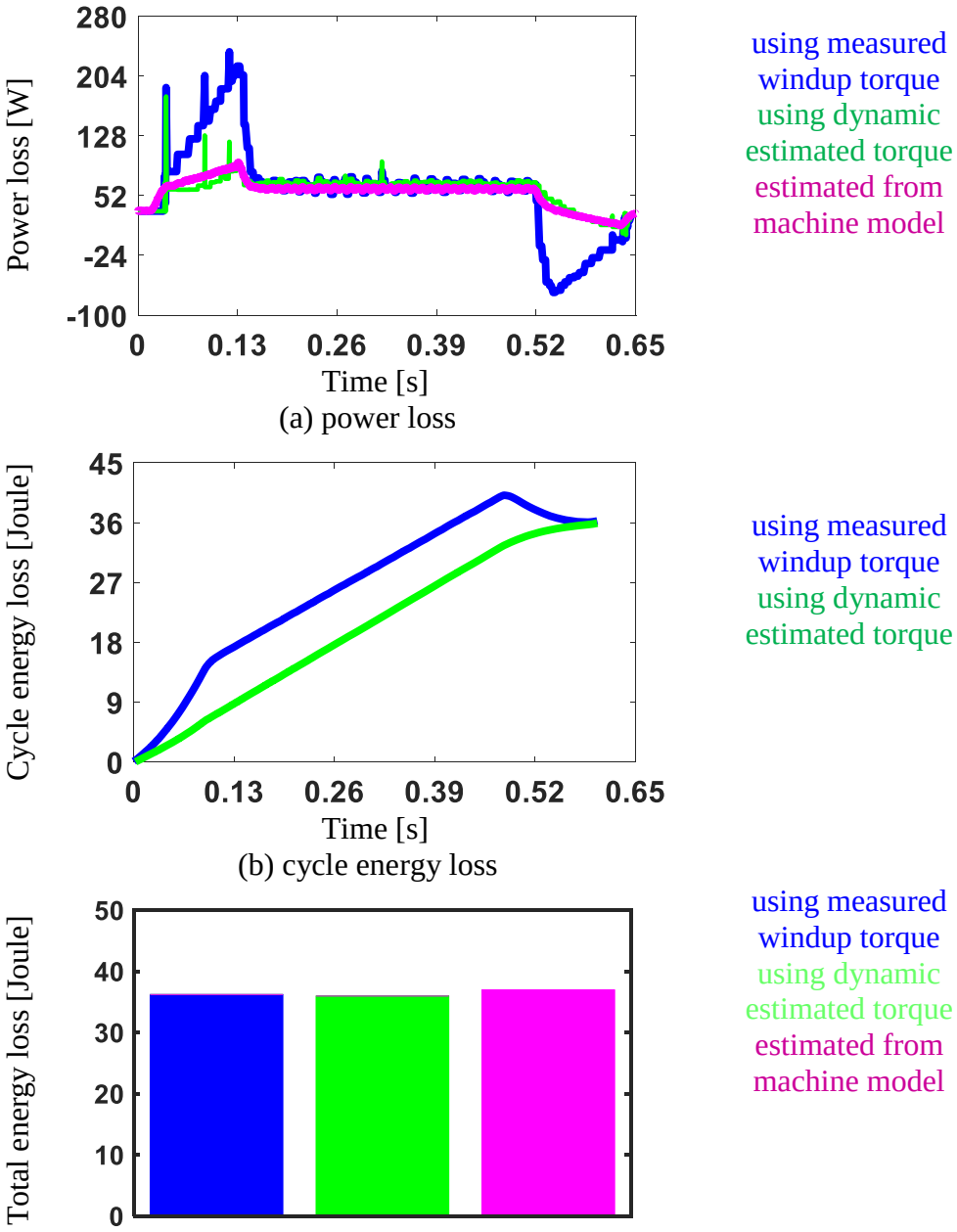

(a) power loss

(b) cycle energy loss

(c) total cycle energy loss

Fig. 4-20 Measured supply power and energy loss during the evaluated cycle using both measured windup and dynamic estimated torque

In practical cycles like automotive driving cycles and servo cycles, the acceleration rate

is different from the deceleration rate as can be seen from Fig. 4-21 for the California LA92 dynamometer driving cycle [127]. In this case, it is important to consider the inertial torque component to accurately estimate the supply energy loss.

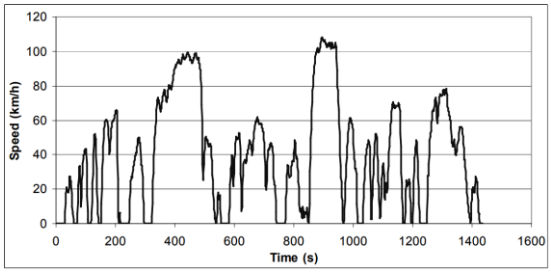

Fig. 4-21 California LA92 dynamometer driving cycle

To evaluate motor loss, which is the main goal of dynamometers, absolute power loss needs to be considered (losses during braking also need to be considered). Fig. 4-22-a shows absolute instantaneous power loss for the evaluated cycle, while Fig. 4-22-b shows integrated motor power loss. Ignoring the inertial torque component leads to overestimating the motor loss by 24% as can be seen from Fig. 4-22-c.

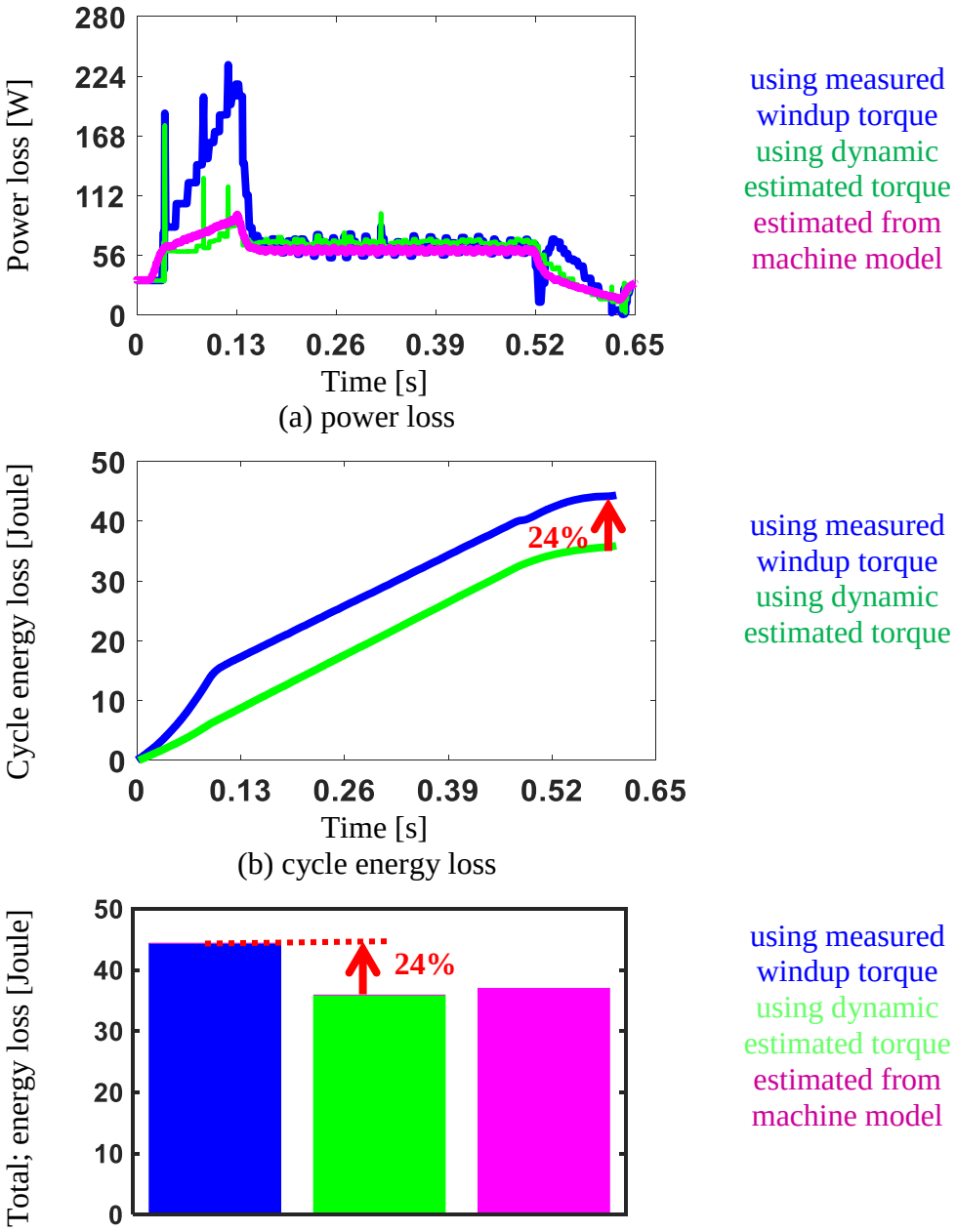

(a) power loss

(b) cycle energy loss

(c) total cycle energy loss

Fig. 4-22 Measured motor power and energy loss during the evaluated cycle using both measured windup and dynamic estimated torque

Evaluating the motor energy loss correctly helps in designing the motor (better understanding of its thermal limit). It also affects the power converter design, selecting the proper insulation materials and cooling system.

4.5 Parameter Sensitivity Analysis of the Proposed Shaft Torque Observer Structure

In this section, parameter sensitivity analysis of the proposed shaft torque observer structure is conducted. The proposed observer structure is not sensitive to the estimated equivalent stiffness within the observer bandwidth. The transfer function between the estimated windup torque to the actual windup torque for a system with known equal test-load motor inertias shown in (4-8)

$$\frac{\hat{T}_{WU}}{T_{WU}} = \frac{\hat{K}_{eq}}{K_{eq}} * \frac{J s^2 + 2b_p s + 2K_{eq}}{\hat{J}_s 2 + 2\hat{b}_p s + 2\hat{K}_{eq}} \qquad (4\text{-}8)$$

From (4-8), the proposed observer is not sensitive to the estimated equivalent stiffness. Fig. 4-23 shows the simulation results for a windup torque estimation accuracy for a different estimated stiffness factor value.

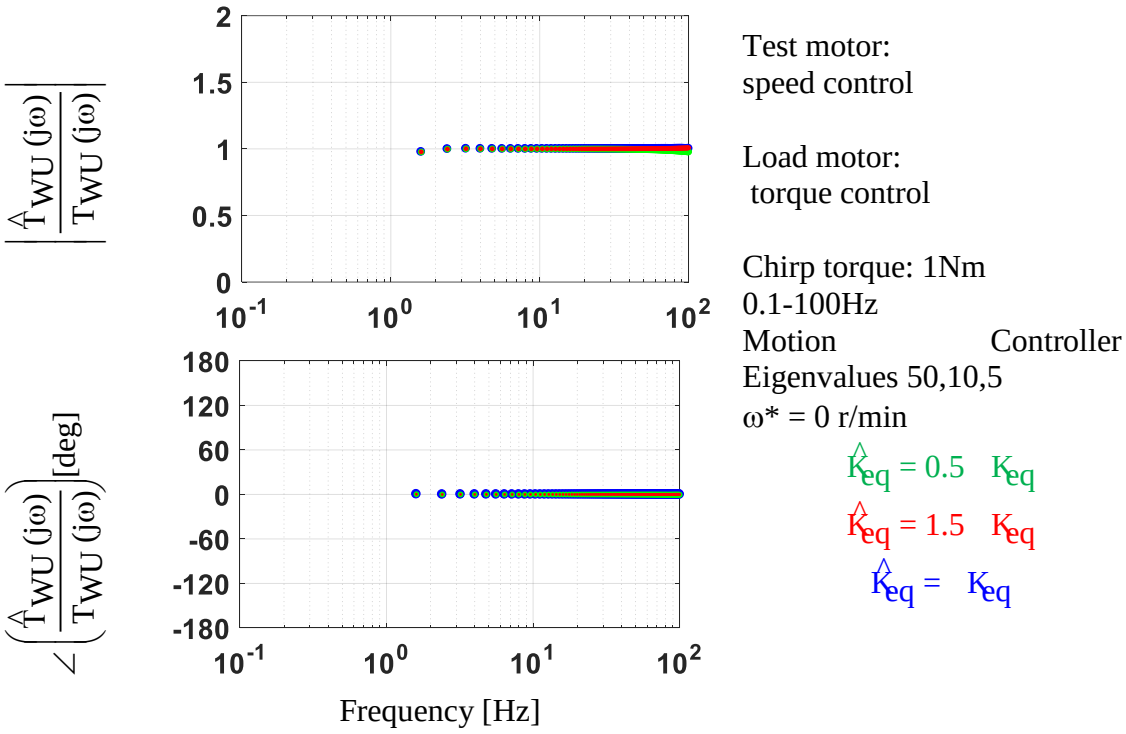

Fig. 4-23 Simulation results for windup torque estimation accuracy at different estimated stiffness factor values

Fig. 4-24 shows the experimental results for the windup torque estimation accuracy for different estimated stiffness values, these results agree with the simulation results in Fig. 4-23. The coherence plots document the quality of the experimental results.

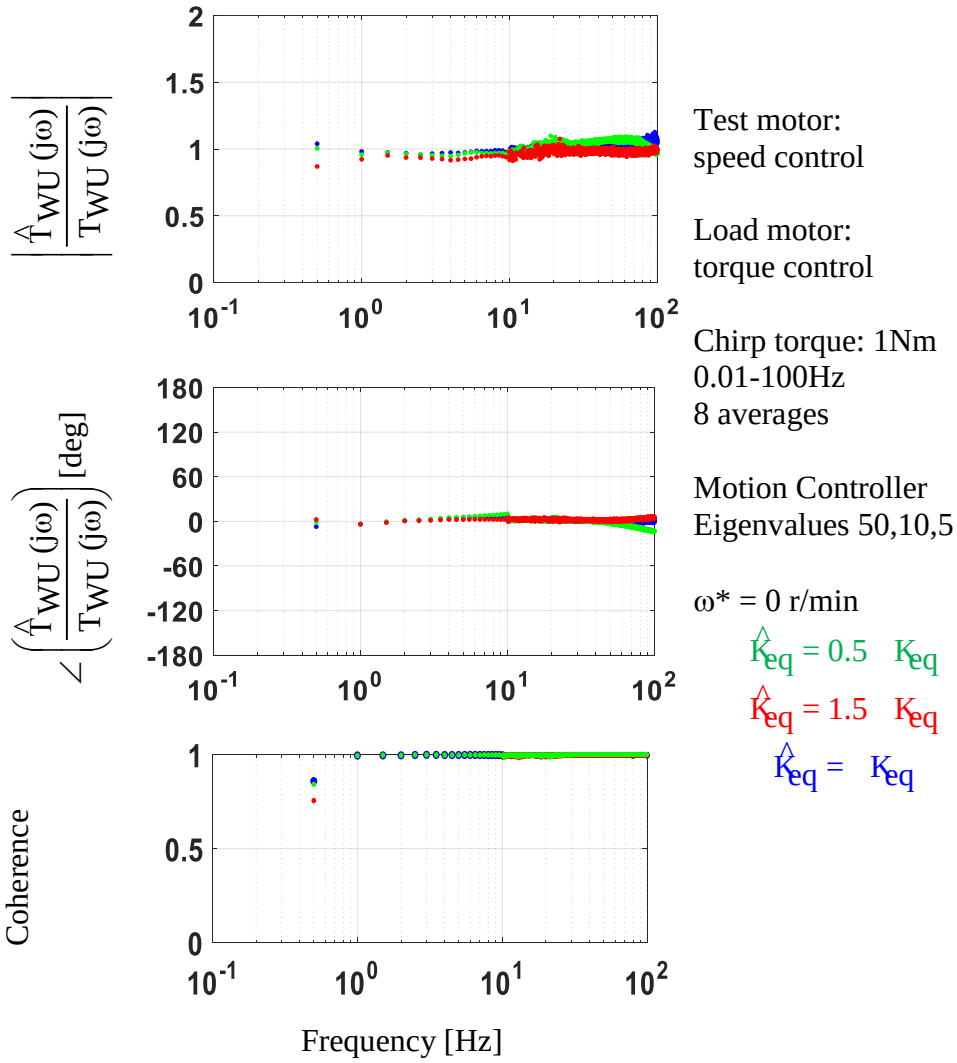

Fig. 4-24 Experimental results for windup torque estimation accuracy at different estimated stiffness factor values

It is also clear from (4-8) that the windup torque estimation accuracy is not sensitive to the estimated system damping factor for frequencies lower than the resonant frequency. The estimated damping factor becomes significant for frequencies close to the resonant frequency when the damping torque dominates the shaft torque.

Fig. 4-25 shows the simulation results for the windup torque estimation accuracy for a different estimated damping factor for frequencies lower than the resonant frequency. While the

experimental results for the same case are shown in Fig. 4-26.

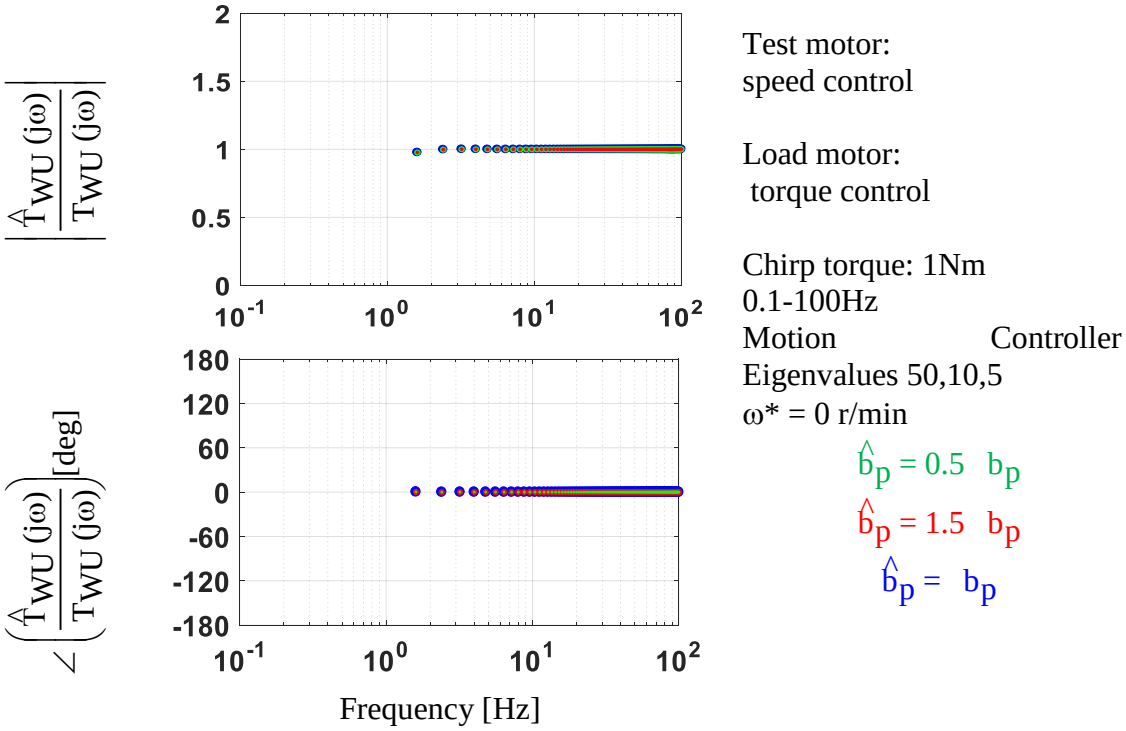

Fig. 4-25 Simulation results for windup torque estimation accuracy at different estimated damping factor values

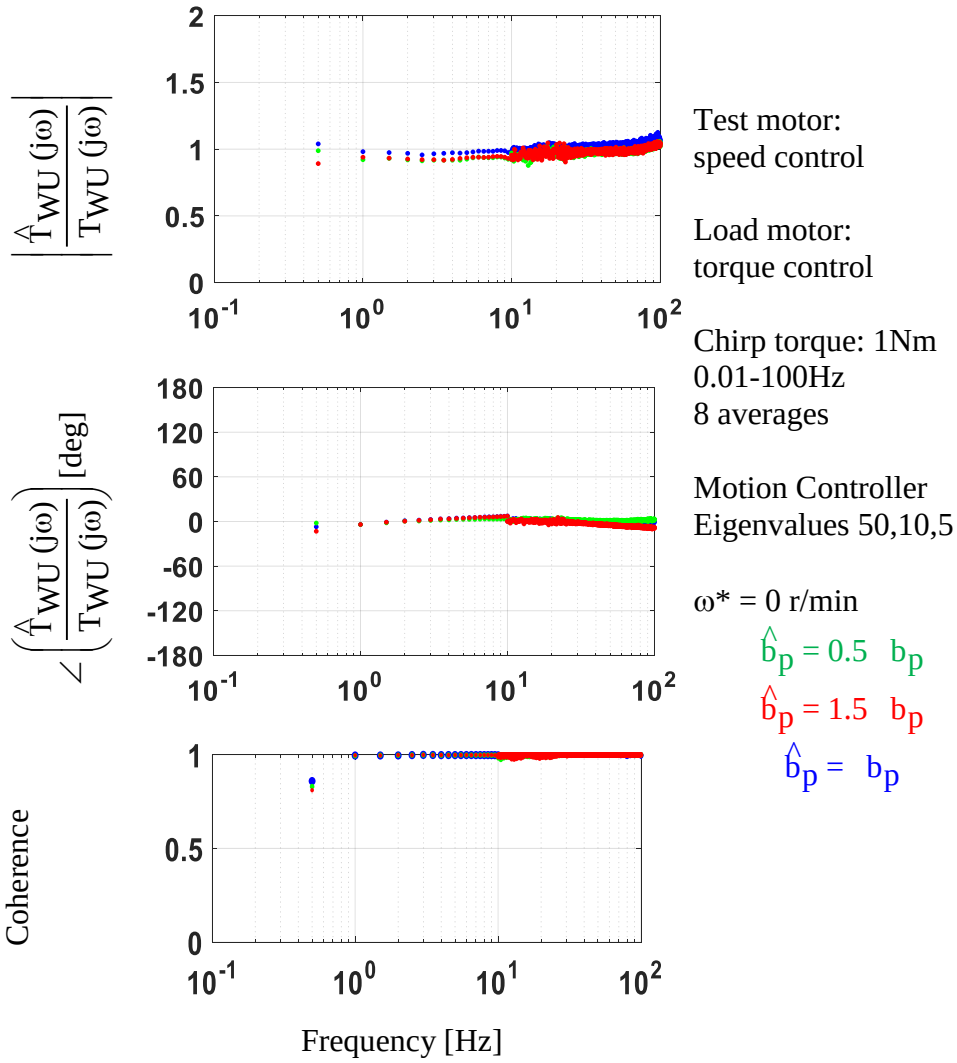

Fig. 4-26 Experimental results for windup torque estimation accuracy at different estimated damping factor values

Finally, the effect of the estimated load motor inertia on the windup torque estimation accuracy is evaluated. The torque estimation accuracy transfer function is shown in (4-9). From this equation, the windup torque estimation accuracy is proportional to the ratio $\{(J_T + J_L) / (\hat{J}_T + \hat{J}_L)\}$.

$$\frac{\hat{T}_{WU}}{T_{WU}} = \frac{\hat{K}_{eq}}{K_{eq}} * \frac{\left((J_T+J_L)\ s^2\right)\left[\left(\frac{J_T \cdot J_L}{J_T+J_L}\right)s^2\ b_p s+\ K_{eq}\right]}{\left((\hat{J}_T+\hat{J}_L)\ s^2\right)\left[\left(\frac{\hat{J}_T \cdot \hat{J}_L}{\hat{J}_T+\hat{J}_L}\right)s^2\ \hat{b}_p s+\ \hat{K}_{eq}\right]} * \frac{(\hat{b}_p\ s+\ \hat{K}_{eq})*[T^*_{em\text{-}L}-\ T^*_{em\text{-}T}] + s^2[\hat{L}_T\ T^*_{em\text{-}L}-\hat{J}_L\ T^*_{em\text{-}T}]}{(b_p s+\ K_{eq})*[T_{em\text{-}L}\ -\ T_{em\text{-}T}] + s^2[J_T\ T_{em\text{-}L}\ -\ J_L\ T_{em\text{-}T}]} \quad (4\text{-}9)$$

Fig. 4-28 shows the experimental results for the windup torque estimation accuracy for a different estimated motor inertia values, these results agree with the simulation results in Fig. 4-27.

The estimated windup torque is sensitive to the estimated load inertia. This happens due to using a single encoder in the tested motor side and estimating the load motor position and speed from the constructed observer. The estimated inertial torque will also be sensitive to the estimated tested motor inertia.

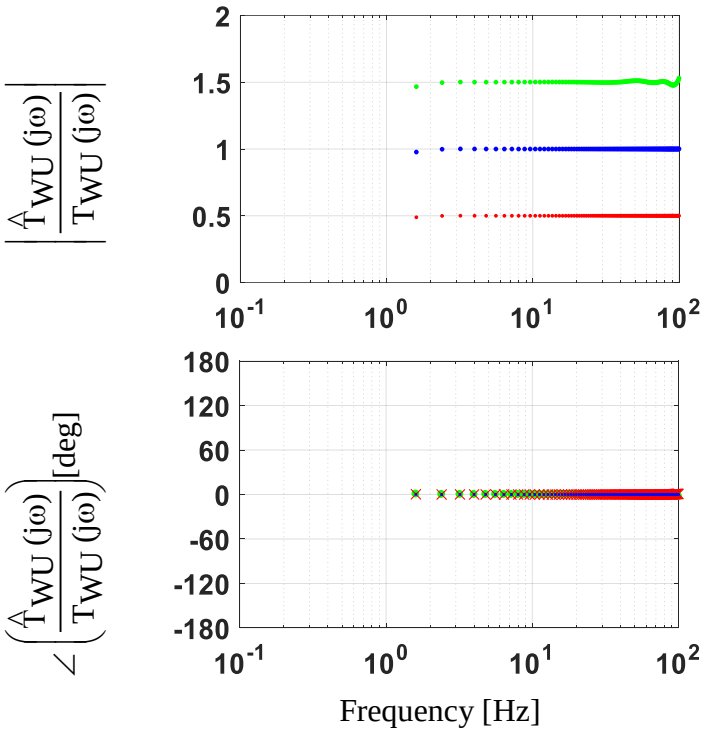

Test motor:
speed control

Load motor:
torque control

Chirp torque: 1Nm
0.1-100Hz
Motion Controller
Eigenvalues 50,10,5
ω* = 0 r/min

$\hat{J}_L = 0.5\ J_L$

$\hat{J}_L = 1.5\ J_L$

$\hat{J}_L = J_L$

Fig. 4-27 Simulation results for windup torque estimation accuracy at different estimated motor inertia values

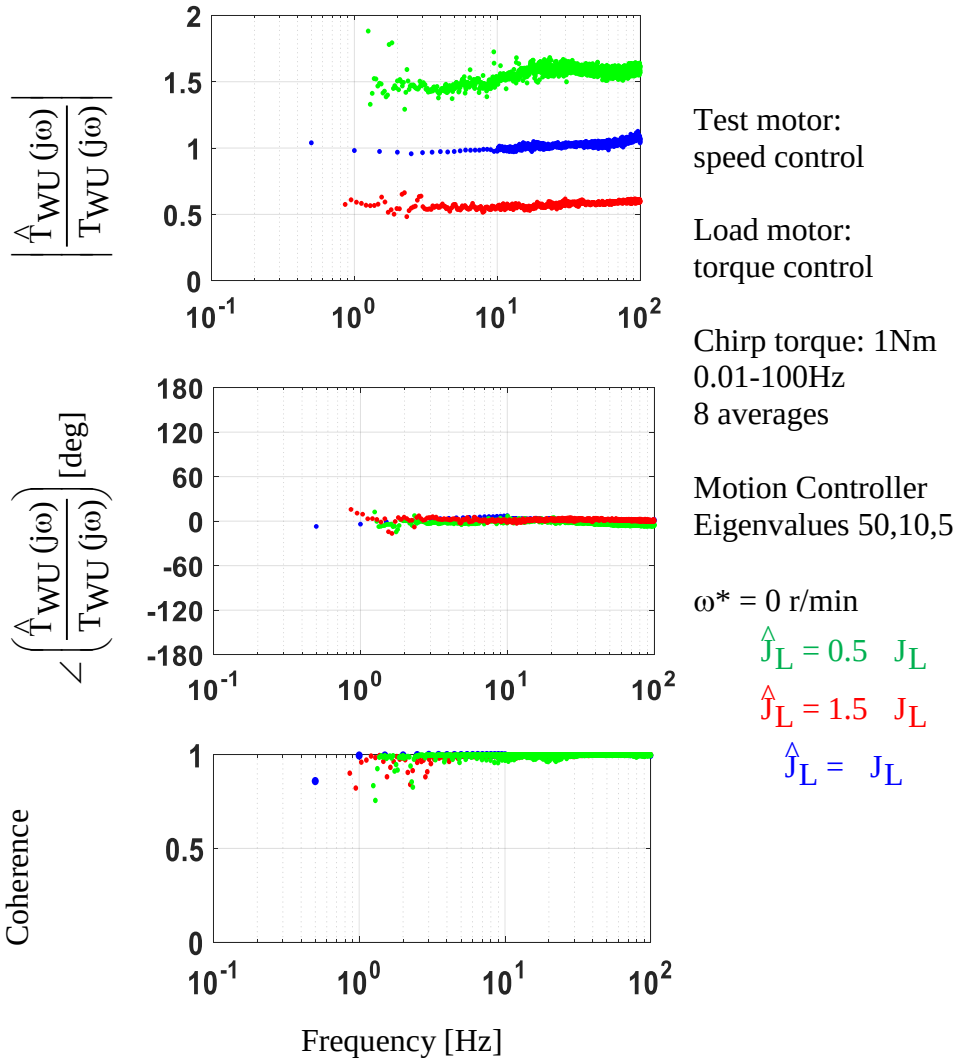

Fig. 4-28 Experimental results for windup torque estimation accuracy at different estimated motor inertia values

In order to achieve accurate torque estimation, the load motor's inertia needs to be estimated. This can be done using different techniques. for example, the authors of [114] and [115] proposed an estimator to estimate the motor inertia. The author of [116] proposed an auto-tuning algorithm for electrical drives, through this algorithm the motor inertia can be estimated. Simpler techniques can also be used to estimate the motor inertia, like the asymptote of the dynamic stiffness at high-frequency values or using the measured resonant frequency to tune the

inertia value.

4.6 Summary

This chapter presents a methodology for estimating the shaft torque during steady-state and transient speed operations using an observer structure allowing accurate transient loss measurement. This chapter documents the methodology and experimentally evaluates its accuracy when measuring transient loss on servo drives during acceleration/deceleration cycles. The key observations and conclusions from this chapter are summarized as follows.

- Standard torque transducers measure the shaft windup torque and are unable to directly consider the inertial torque that appears during transient speed operation. This limits the usage of this sensor to primarily steady state speed operation.
- The proposed observer structure emulates the physical model of the dynamometer. This observer structure can be used to estimate the load motor speed and position, windup shaft torque, and the dynamic shaft torque that include the inertial torque component with high fidelity, without the need to use any angular acceleration and/or windup torque sensors; this structure can work even with a very low-resolution encoder.
- An enhanced Luenberger style rigid body observer can be used in cascade with the proposed observer structure, this allows using the proposed observer structure with the lower resolution position sensors without the need for a high-resolution position sensor.
- The dynamic shaft torque matches the windup shaft torque for steady state speed operation, this is because the inertial torque component doesn’t appear during this

operation. With that, the measured steady-state losses using the dynamic torque match the losses measured using the windup torque.

- Accurate loss measurement during transient speed operation requires an accurate estimation of the dynamic shaft torque. This can be done using the proposed observer structure. This allows measuring the motor losses during transient speed operation accurately using standard drive sensors without the need of any extra sensor.
- The proposed observer structure is not sensitive to the estimated system stiffness. This observer also is not sensitive to the estimated system damping for frequencies lower than the resonant frequency.
- Accurate torque estimation requires a good estimation of the motor inertia, which is typically known in testing dynamometers. Auto-tuning algorithms can be used to automatically estimate the motor inertia.

Chapter 5 Dynamic Loss Minimizing Control of a PM Servo Motor Operating Even at the Voltage Limit When Using DB-DTFC

The main technical content of this chapter has been published in two technical papers in [128] and [129]. This chapter presents a methodology to design a dynamic loss minimizing controler using DB-DTFC (LMC-DB-DTFC). This controller selects the optimum feasible stator flux linkage dynamically each switching period to minimize the total motor losses without affecting the torque dynamics of the drive. The proposed controller works even at the voltage limit during flux weakening operation.

In this chapter, the DB-DTFC algorithm for PM motors is reviewed, then a simple and accurate stator flux linkage loss model is derived and verified. Then, the LMC-DB-DTFC algorithm is developed, the effectiveness of this algorithm is verified experimentally. Finally, an online inductance estimation technique is developed to reduce the impact of inductance variation on the effectiveness of the developed LMC-DB-DTFC algorithm during the low-speed operation.

5.1 Deadbeat-Direct Torque and Flux Control for PM Servo Motors

The DB-DTFC has the fastest possible response in which the commanded airgap torque or stator flux linkage can be achieved in only one switching period. With this controller, it is easy to control the actual motor states (airgap torque and stator flux linkage) directly and

independently. The DB-DTFC algorithm for PM motors was proposed in [63] and the corresponding block diagram is shown in Fig. 5-1.

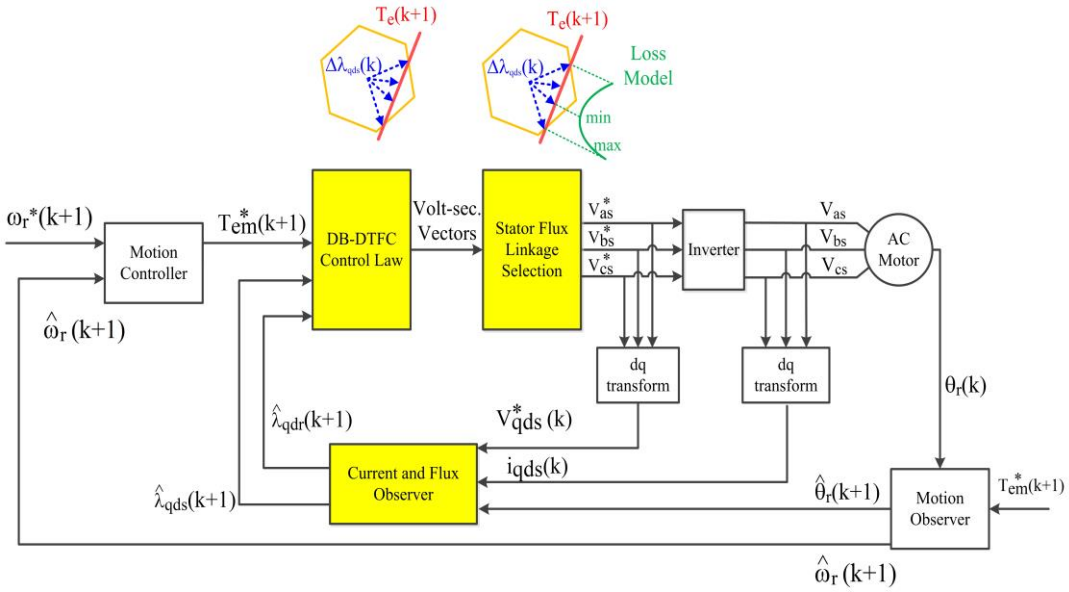

Fig. 5-1 Block diagram of DB-DTFC drive systems [63]

DB-DTFC requires estimating the motor airgap torque and stator flux linkage. This can easily be done using Gopinath style stator flux linkage observer and a Luenberger style stator current observer. Fig. 5-2 shows the block diagrams of those two observers [63]. The implementation sequence of this controller was presented in [117]. The torque line equation calculated by DB-DTFC given in (5-1).

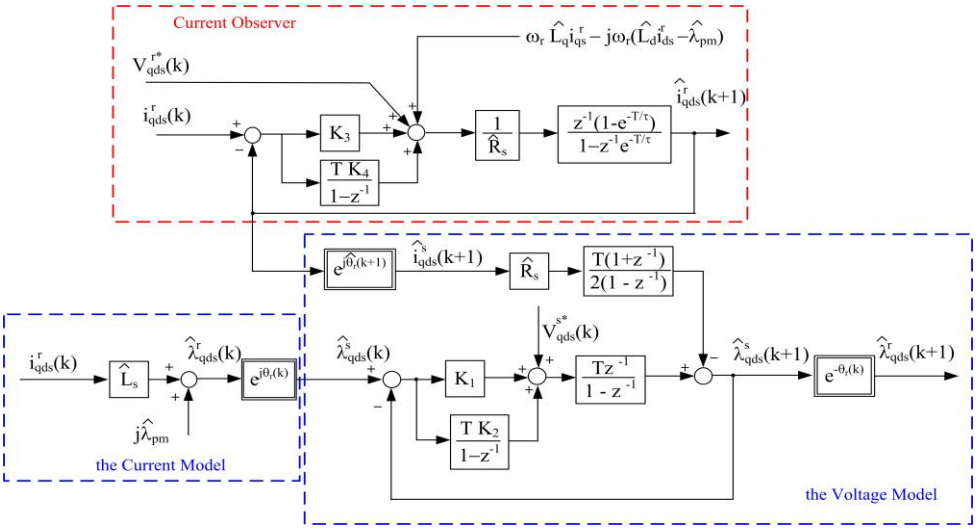

Fig. 5-2 Block diagram of discrete time current and flux observer system for PMSMs [117]

$$V_q T_s = m^* V_d T_s + b \tag{5-1}$$

where $m = \left((L_q - L_d) \cdot \hat{\lambda}^r_{qs} \right) / \left((L_q - L_d) \cdot \hat{\lambda}^r_{ds} - L_q \lambda_{pm} \right)$

$$b = \left(\frac{L_d \cdot L_q}{(L_d - L_q) \cdot \hat{\lambda}^r_{ds} + L_q \cdot \lambda_{pm}} \right) \cdot \left\{ \left[\frac{4}{3p} \cdot \Delta T_{pm} - \frac{\omega_r \cdot T_s}{L_d \cdot L_q} \left((L_q - L_d)(\hat{\lambda}^{r\,2}_{ds} - \hat{\lambda}^{r\,2}_{qs}) - L_q \cdot \hat{\lambda}^r_{ds} \cdot \lambda_{pm} \right) \right] - \left[\frac{R_s \cdot \hat{\lambda}^r_{qs} \cdot T_s}{L_d^2 \cdot L_q^2} \left((L_q^2 - L_d^2) \cdot \hat{\lambda}^r_{ds} - L_q^2 \cdot \lambda_{pm} \right) \right] \right\}$$

DB-DTFC control algorithm calculates the set of volt-sec vectors that would achieve the required torque. Different methods have been used to select the operating volt-sec vector. Fig. 5-3 shows the graphical solution for DB-DTFC in the re-aligned stationary reference frame, where the hexagon represents the volt-sec limit of the power inverter, and the yellow vectors represent the calculated set of volt-sec vectors from the DB-DTFC algorithm that would achieve the commanded torque (red line). The cyan curve represents the loss distribution for the feasible set of the calculated volt-sec vectors.

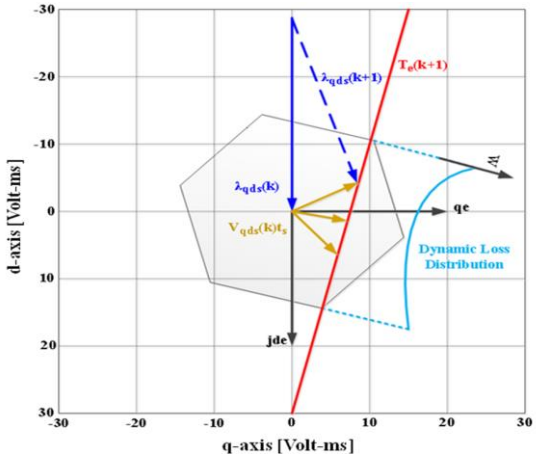

Fig. 5-3 Graphical solution of a fixed stator flux command DB-DTFC drives [118]

Different methods were used to select the operating volt-sec vector (operating flux). The simplest way is through using the existing standard flux weakening d axis current command as in [119]-[121]. In this way, a zero d-axis current command is used at low speed (this is for surface permanent magnet synchronous motors (SPMSMs), for IPMSM the calculated d axis current command from MTPA algorithm can be used), and a negative d-axis current is required to decrease the stator flux linkage during the high-speed flux weakening operation. In this case, the commanded flux could be written as shown in (5-2).

$$\lambda_s^* = \sqrt{\left(L_q \cdot T_{em}^* / K_T \right)^2 + \left(L_d \cdot I_d^* + \lambda_{pm} \right)^2} \qquad (5\text{-}2)$$

This method is similar to the standard flux weakening operation used with field-oriented control. The benefits of using this method would be controlling the airgap torque precisely with high dynamics. The selected volt-sec vector, in this case is not the optimum volt-sec vector that would minimize motor losses. This thesis presents an algorithm to select the optimum volt-sec vector that would minimize motor losses even when the motor is operating at the voltage limit, during flux weakening operation. This will be done dynamically at the switching period level.

In this thesis, the current observer was tuned to achieve 1 kHz bandwidth. This observer would capture the current precisely without any phase distortion. The used flux observer combines both current model and voltage model flux observers. Current model flux observer was implemented in the synchronous reference frame. This model is parameter sensitive, and it dominates the flux estimation at low speed below the cutoff frequency of the observer controller bandwidth. While the voltage model was implemented in the stationery reference frame, this model dominates the flux estimation at high speed above the tuned bandwidth of the flux observer controller. Generally, this model is insensitive to the estimated parameters, and it is accuracy depends on the accuracy of the commanded voltage if it is close to the actual voltage or not.

The flux observer controller is tuned to 100 Hz, which means below 1200 r/min the current model flux estimation dominates the estimated flux. At higher speed, the voltage model estimation dominates the flux estimation. The tuning process was done by first tuning the flux observer controller to 1Hz bandwidth (voltage model estimation will be dominant at very low speed) and commanding a fixed torque from the load motor. Then, the tested motor's speed was increased and estimated torque from the observed flux and current was compared to the measured torque from the torque cell. The bandwidth of the flux observer is then determined by the speed (frequency) which the estimated torque become similar to the measured torque. This bandwidth generally depends on the accuracy of the voltage command compared to the actual voltage, which is significantly affected by the inverter non-linearity and dead-time effects.

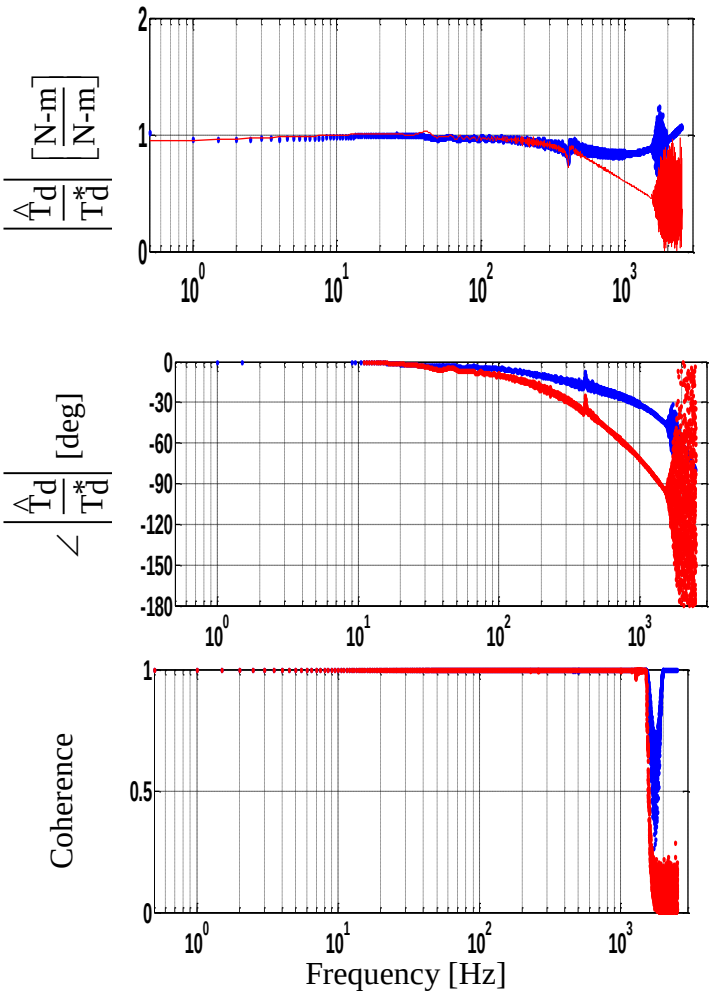

Fig. 5-4 Torque FRF comparison between CVCR and DB-DTFC for FI-SPMSM

DB-DTFC provides an infinite bandwidth of the commanded air-gap torque, not like FOC, in which the dynamic response is limited by the current regulator bandwidth. Fig. 5-4 compares the torque frequency response between FOC and DB-DTFC. It is clear that with DB-DTFC, the torque response is better than the FOC response. Around 400 Hz the response of DB-DTFC slightly drops down then increases at higher frequency, this happens due to using a single encoder and operating close to the resonance frequency (position of tested motor will be different than the load motor close to the resonance).

To explore the benefits of DB-DTFC compared to the standard FOC, a rapid acceleration test was performed on the tested motor. The tested motor is controlled using both FOC and DB-DTFC using the described flux linkage command method in (5-2). The tested motor is accelerated from 0 to 3000 r/min in 120 ms, Fig. 5-5 shows the speed calculated from the encoder for this test. Fig. 5-6 shows the commanded and estimated airgap torque that is required to accelerate the motor using FOC, while Fig. 5-7 shows the commanded and estimated airgap torque in case of using DB-DTFC.

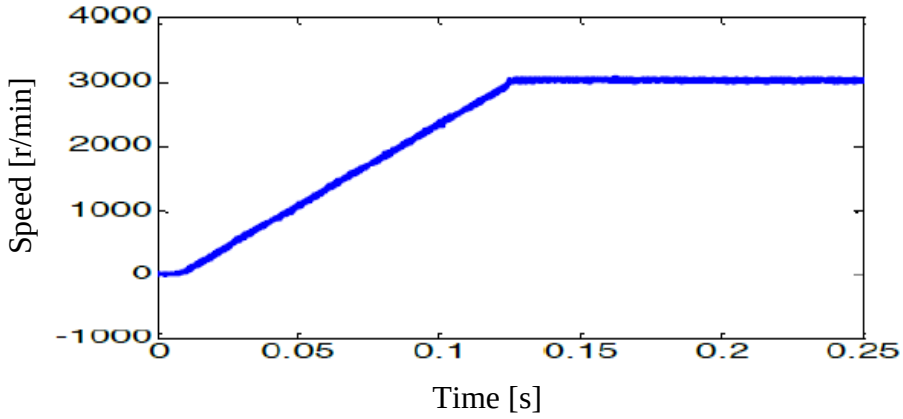

Fig. 5-5 Speed calculated from the encoder during accelration test

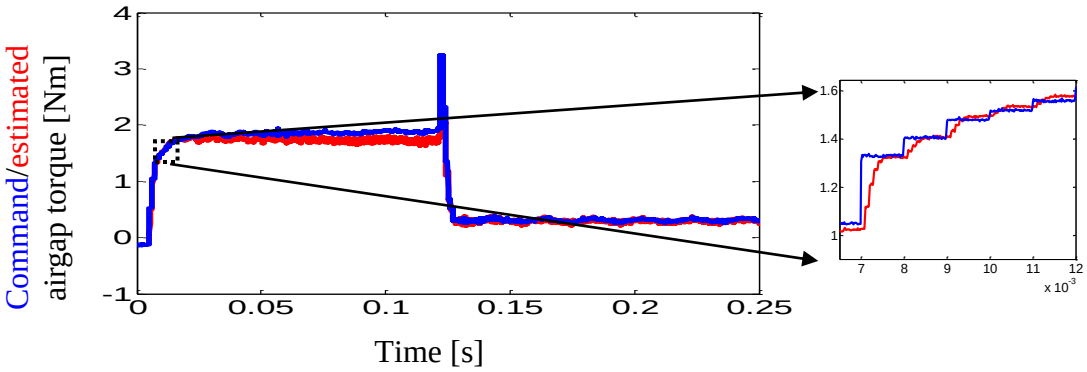

Fig. 5-6 Commanded and estimated airgap torque during rapid acceleration test using FOC-500 Hz bandwidth

Using DB-DTFC, the airgap torque was precisely controlled even during the rapid acceleration condition. While in the case of using FOC, the response does not perfectly track the

commanded airgap torque. This is because the dynamic response of FOC is limited by the bandwidth of the current regulators (500 Hz).

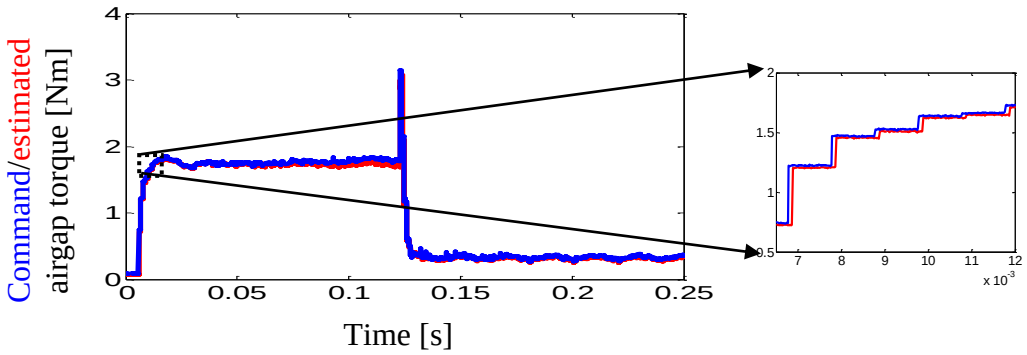

Fig. 5-7 Commanded and estimated airgap torque during rapid acceleration test using DB-DTFC

5.2 Flux Linkage Based Dynamic Loss Model

In this section, different loss models are evaluated. After that, a flux linkage-based model is proposed, which will be used in DB-DTFC to minimize motor losses dynamically at the switching period level.

In order to minimize motor losses dynamically using DB-DTFC, it is important to have an accurate loss model. This model will be expressed as a flux linkage-based model, allowing the use of a simple searching algorithm to select the optimum flux linkage.

In general, motor losses can be divided into copper loss and iron loss. Copper loss can be easily calculated from the measured currents as in (5-3). Different models were proposed to model iron loss. Generally, iron loss can be estimated using the Steinmetz model as in (5-4) or (5-5). The model in (5-4) requires less computational time in the DSP compared to the model in (5-5), this improves the real-time operation of the LMC-DB-DTFC algorithm.

$$P_{cu\_loss} = \frac{3}{2} R \cdot (\hat{I}_{ds}^{r\,2} + \hat{I}_{qs}^{r\,2}) \qquad (5\text{-}3)$$

$$P_{Iron\_loss1} = K_h \cdot \omega_e \cdot \left(\hat{\lambda}_{ds}^{r\,2} + \hat{\lambda}_{qs}^{r\,2} \right) + K_e \cdot \omega_e^{2} \cdot \left(\hat{\lambda}_{ds}^{r\,2} + \hat{\lambda}_{qs}^{r\,2} \right) \quad (5\text{-}4)$$

$$P_{Iron\_loss2} = K_c * \omega_e^{1.5} * \left(\hat{\lambda}_{ds}^{r\,2} + \hat{\lambda}_{qs}^{r\,2} \right)^{0.75} \quad (5\text{-}5)$$

where: R = motor phase resistance (Ω),
$\hat{\lambda}_{ds}^{r}$, $\hat{\lambda}_{qs}^{r}$= d, q axis estimated stator flux linkage from the flux observer in the synchronous reference frame (V-s),
K_h, Ke= eddy current, hysteresis loss coefficients,
Kc= iron loss coefficients,

Hysteresis, eddy current loss, and iron losss coefficients were calculated using the least square error method. The tested motor was controlled to run at different speeds and load conditions. Input and output power were measured using a motor drive analyzer (MDA 810 from Teledyne LeCroy). The iron loss was measured by subtracting the copper loss from the measured motor total loss (friction and windage loss are negligible for the tested motors). Fig. 5-8 compares the measured total loss with the modeled total loss, while Fig. 5-9 compares the measured and modeled Iron loss. Both models show a good accuracy.

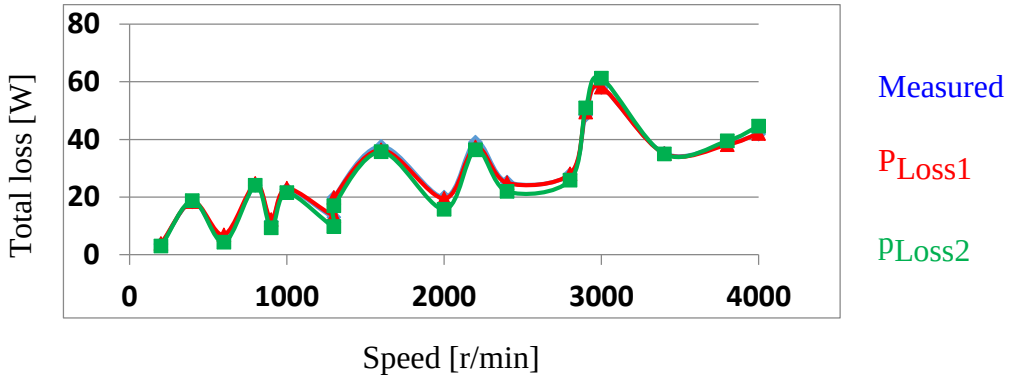

Fig. 5-8 Results of least square error and evaluation of different loss models – total loss comparison

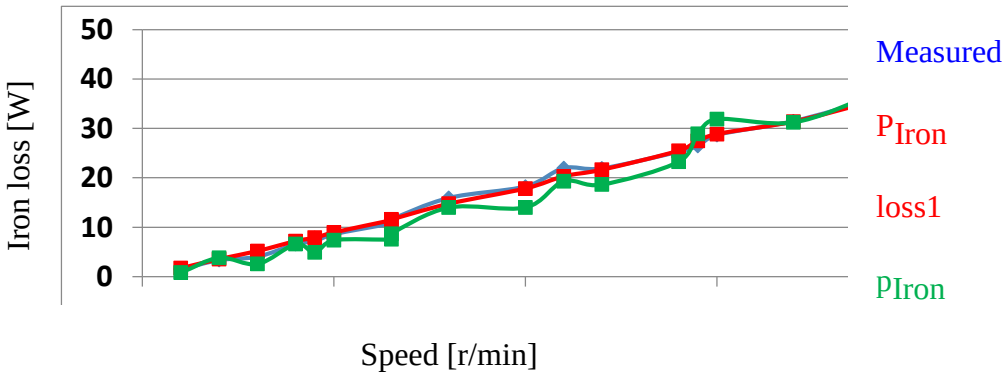

Fig. 5-9 Results of least square error and evaluation of different loss models – Iron loss comparison

The previous results were calculated offline, to make sure the models can estimate the losses accurately online. The previous models are programed in the DSP, and the tested motor was run at different speed and load conditions. Fig. 5-10 compares the measured total and iron loss, with the online estimated loss through the previously constructed models.

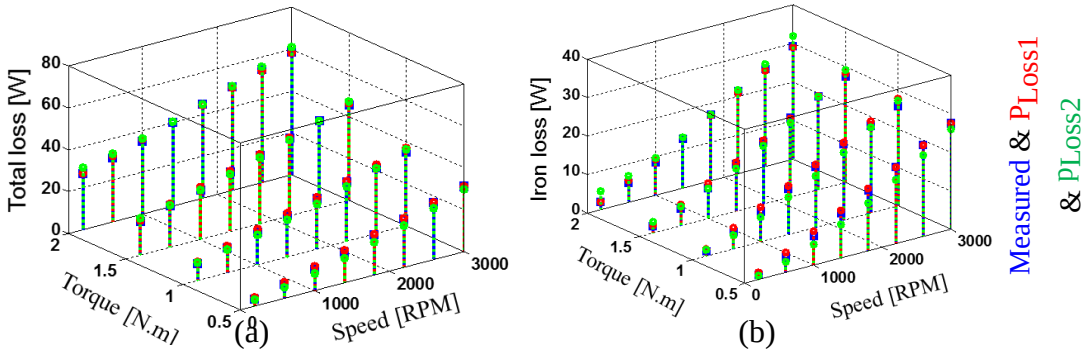

Fig. 5-10 Online loss estimation evaluation using different loss models

The model in (5-4) requires less computational time inside the DSP; the error in the estimated loss using this model is less than 5%. To be able to use this model with DB-DTFC, the loss model converted to flux linkage-based model as in (5-6).

$$P_{loss} = \frac{3}{2} R \cdot \left(\left(\frac{\hat{\lambda}^{r}_{ds\text{-}cm} - \lambda_{pm}}{L_d} \right)^2 + \left(\frac{\hat{\lambda}^{r}_{qs\text{-}cm}}{L_q} \right)^2 \right) + K_h \cdot \omega_e \cdot (\hat{\lambda}^{r\,2}_{ds} + \hat{\lambda}^{r\,2}_{qs}) + K_e \cdot \omega_e^{\,2} \cdot (\hat{\lambda}^{r\,2}_{ds} + \hat{\lambda}^{r\,2}_{qs}) \qquad (5\text{-}6)$$

where: $\hat{\lambda}^{r}_{ds\text{-}cm} = L_d \cdot \hat{I}^{r}_{d} + \lambda_{pm}$

$\hat{\lambda}^{r}_{qs\text{-}cm} = L_q \cdot \hat{I}^{r}_{q}$,

This loss model has good accuracy. It is easy to calculate the loss coefficient parameters of this model. This loss model can be used in any kind of PM motors and doesn't require huge computational efforts inside the DSP. No lookup tables are required for this loss model, only a fixed value for K_h & K_e need to be used inside the DSP.

The accuracy of this loss model depends on the accuracy of the stator flux linkage and the motor resistance estimates. The estimated flux linkages from the current model ($\hat{\lambda}^{r}_{ds\text{-}cm}$ & $\hat{\lambda}^{r}_{qs\text{-}cm}$) are used to estimate the copper loss. This will reduce copper loss estimation sensitivity to the estimated inductance, while the estimated flux linkages using the flux observer in Fig. 5-2 are used to estimate the iron loss.

The stator flux linkage observer is not sensitive to the estimated parameters during medium and high-speed operation when the voltage model dominates the flux estimation, leading to accurate motor flux and iron loss estimation. However, at low-speed operation, the current model will dominate the flux estimation; this model is sensitive to estimated motor inductance. To reduce the sensitivity to estimated motor parameters, volt-sec sensing can be used as in [69] , extending the operation of the voltage model to run at very low speed, or an online parameter estimation can be used to estimate the motor inductance. In this thesis, MRAC based online estimation technique for motor d,q inductances will be presented later in this chapter.

Stator resistance varies with the winding temperature affecting the accuracy of copper loss estimation. To accurately consider this variation, online resistance estimation can be done as in [130] and [131].

Using this simple steady-state loss model would improve the real time implementation of the dynamic loss minimizing controller during both steady-state and transient operation, even though this model is not very accurate during dynamic operation.

5.3 Dynmaic Loss Minimizing Control DB-DTFC for PM Servo Motors

LMC-DB-DTFC is a model-based loss minimization technique, this algorithm searches the feasible volt-sec domain to select the optimum volt-sec solution that satisfies the commanded torque with minimum losses. This is done at the switching period level. A golden section search method is used to search for the optimum volt-sec solution. This is similar to what the authors of [118] did, but in this case, an accurate but simple loss model is used. This makes it feasible to minimize motor loss dynamically in real-time for different operating conditions, not just when a step torque is commanded.

To find the volt-sec range for this case, a volt-sec balance equation for the motor that is not operating at the voltage limit is used. This equation is shown in (5-7).

$$V_d^2 \cdot T_s^2 + V_q^2 \cdot T_s^2 = V_m^2 \cdot T_s^2 \qquad (5\text{-}7)$$

where T_s = sampling period,

V_m = maximum achievable voltage from the inverter.

Substituting (5-1) in (5-7) and solving the resulting quadrature equation to find the range of d-axis volt-sec solutions as in (5-8) and (5-9). The q-axis volt-sec solution is calculated by using the DB-DTFC algorithm as in (5-1).

$$\text{Min.}V_d T_s = \frac{-m \cdot b - \sqrt{m^2 \cdot b^2 - (m^2+1) \cdot (b^2 - V_m{}^2 T_s{}^2)}}{(m^2+1)} \tag{5-8}$$

$$\text{Max.}V_d T_s = \frac{-m \cdot b + \sqrt{m^2 \cdot b^2 - (m^2+1) \cdot (b^2 - V_m{}^2 T_s{}^2)}}{(m^2+1)} \tag{5-9}$$

The terms m and b are the torque line slope and offset calculated by the DB-DTFC algorithm as in (5-1).

This thesis will extend LMC-DB-DTFC to work at the voltage limit during flux weakening operation. In this case, a different volt-sec balance equation will be used. The new volt-sec balance equation is shown in (5-10).

$$V_d{}^2 \cdot T_s{}^2 + V_q{}^2 \cdot T_s{}^2 = \left(\frac{V_m}{\omega_r}\right)^2 \tag{5-10}$$

where ω_r = rotor speed in electrical rad/s.

Substituting (5-1) in (5-10) and solving the resulting quadrature equation to find the range of d-axis volt-sec solutions as in (5-11) and(5-12). The q-axis volt-sec solution is calculated by using the DB-DTFC algorithm as in (5-1).

$$\text{Min. } V_d T_s = \frac{-m \cdot b - \sqrt{m^2 \cdot b^2 - (m^2+1) \cdot \left(b^2 - \left(\frac{V_m}{\omega_r}\right)^2\right)}}{(m^2+1)} \tag{5-11}$$

$$\text{Max. } V_d T_s = \frac{-m \cdot b + \sqrt{m^2 \cdot b^2 - (m^2+1) \cdot \left(b^2 - \left(\frac{V_m}{\omega_r}\right)^2\right)}}{(m^2+1)} \tag{5-12}$$

The maximum achievable voltage from the inverter depends on the modulation technique used and on the DC link voltage level. In the case of linear modulation, maximum peak line-

neutral voltage would be ($V_{dc}/\sqrt{3}$), and in the case of over modulation, the maximum peak line-neutral voltage would be ($2V_{dc}/\pi$).

5.4 Experimental Evaluation of the Proposed LMC-DB-DTFC Algorithm

The proposed controller is implemented in the testing dynamometer. Initially the algorithm was verified on the SPMSM rotor, then it is tuned and used to control IPMSM and FI-SPMSM rotors.

A golden section method is used to search the operating volt-sec space to find the optimum volt-sec solution that will minimize the motor loss that is modeled in (5-6). This is done each switching period. To verify the effectiveness of the proposed controller, the tested motor (SPMSM) was controlled to run at 3000 r/min and 0.5 Nm; motor losses and current were monitored. To find the actual optimum point at this operating condition, the motor current vector was controlled (CVC) and current magnitude was adjusted so that torque and speed were fixed, power loss was measured for different current angles as recorded in Fig. 5-11. LMC-DB-DTFC was used to control the motor at the same operating condition, whereby it found the optimum point (red) directly.

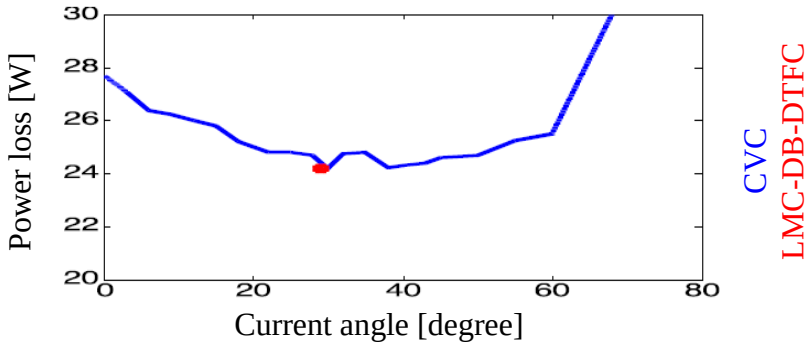

Fig. 5-11 Motor loss at 3000 r/min and 0.5 Nm using CVC & LMC-DB-DTFC

The measured losses when the motor was controlled to run at 3000 r/min and 0.5 Nm using FOC (MTPA current angle = 0 for the SPMSM servo motor) was 27.8 W, while the measured losses using LMC-DB-DTFC was 24 W (13.6% lower). Fig. 5-12 compares the measured d, q axis currents, and voltages between the two controllers. LMC-DB-DTFC commands a negative d-axis current. This will increase the copper loss of the motor but will decrease the stator flux linkage, which will minimize the iron loss to achieve lower total loss of the motor.

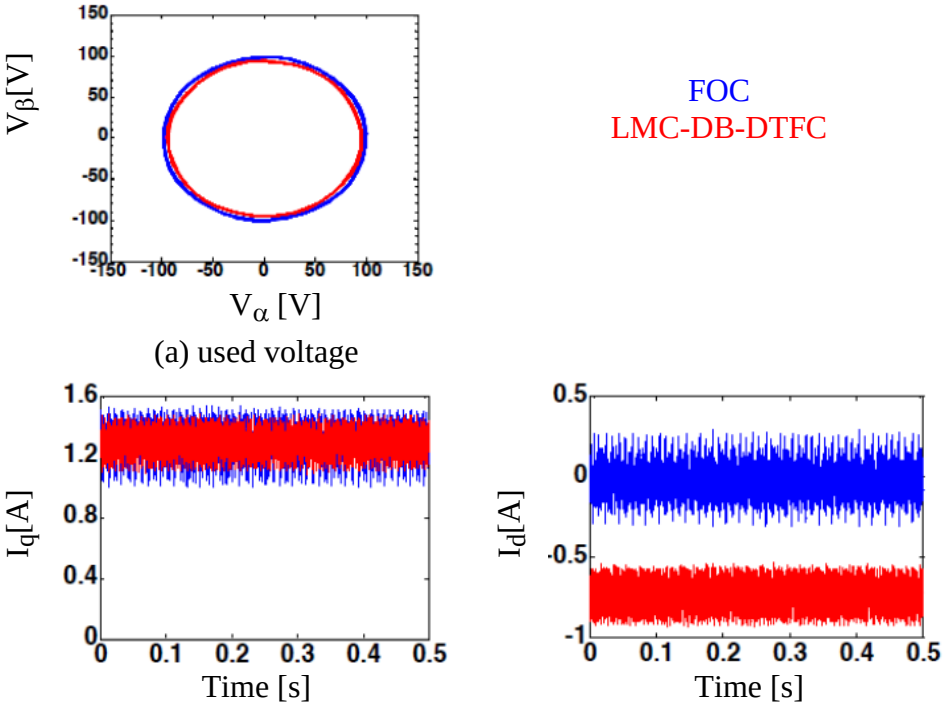

(a) used voltage

(b) q axis current

(c) d axis current

Fig. 5-12 Comparison between FOC & LMC-DB-DTFC at 3000 r/min and 0.5 Nm using 270 V DC link

To evaluate the performance of LMC-DB-DTFC when the motor run at the voltage limit during flux weakening operation, the DC link voltage reduced to 150 V. Then the tested (SPMSM) motor is controlled using LMC-DB-DTFC and flux weakening CVC to run at 2700 r/min with different load conditions.

First, the motor was controlled to run at 2700 r/min and 0.5N.m load is applied from the load motor. For this light load operation, iron loss dominates the motor total loss. LMC-DB-DTFC uses higher negative d axis current compared to flux weakening- FOC (FW-FOC) to reduce the stator flux linkage which reduces the iron loss with increasing the copper loss to decrease the total motor loss. Fig. 5-13 compares the measured d, q axis currents, and voltages between the two controllers.

The measured motor losses using LMC-DB-DTFC was found to be 13.5 W while in case of FW-FOC was 14 W (LMC-DB-DTFC achieves 3.5% lower total loss compared to FW-FOC).

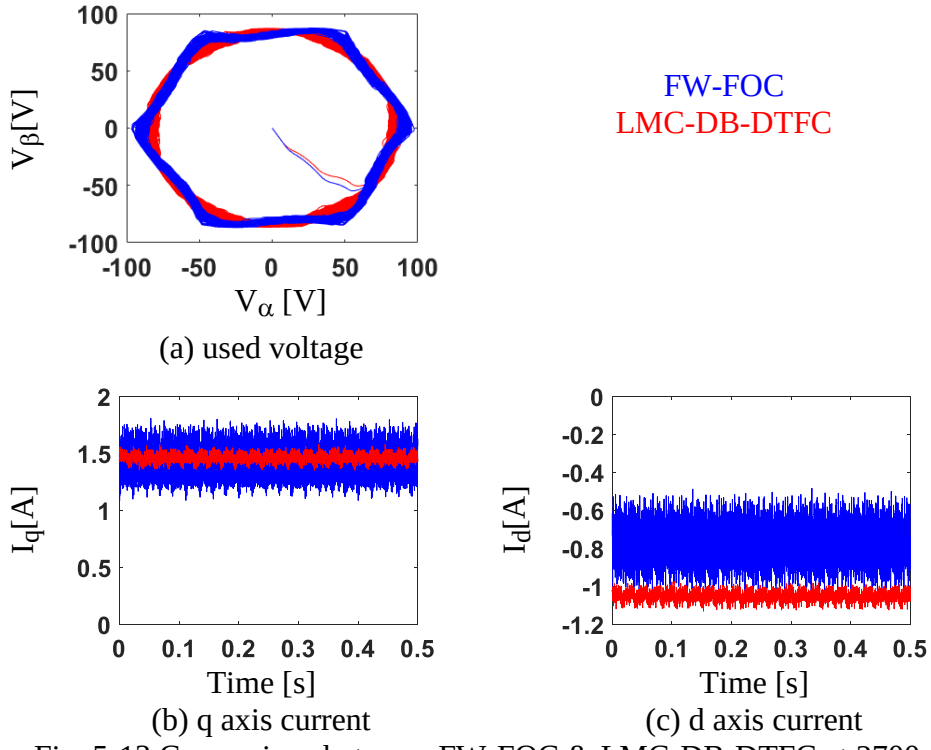

(a) used voltage

(b) q axis current

(c) d axis current

Fig. 5-13 Comparison between FW-FOC & LMC-DB-DTFC at 2700 r/min and 0.5 Nm using 150 V DC link

Then the applied load torque from the load motor was increased to 1Nm. In this case, motor copper loss become close to the iron loss, so LMC-DB-DTFC commanded lower negative d-axis current compared to the previous case, this to reduce the total motor losses, the commanded negative d- axis current is still lower than the FW-FOC case, this to reduce the iron loss and to achieve lower total motor loss. Fig. 5-14 shows the measured dq axis currents and the inverter voltage at this operating condition.

For this operating condition, LMC-DB-DTFC achieves 3.4% lower losses compared to FW-FOC.The measured motor loss at this operation using LMC-DB-DTFC was 18.5 W while using FW-FOC was 19.2 W.

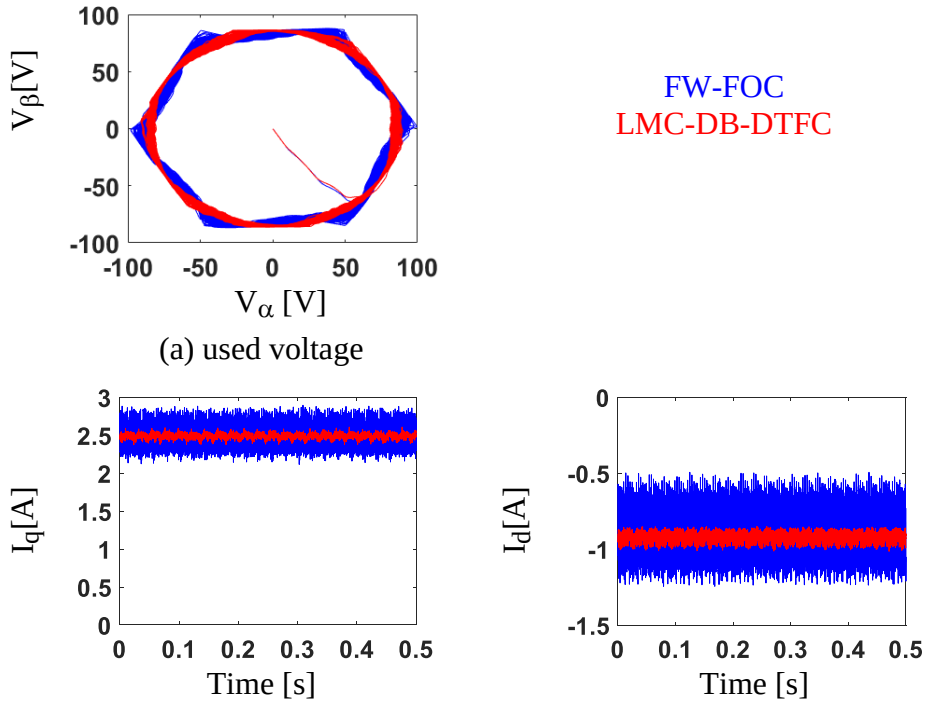

(a) used voltage

(b) q axis current

(c) d axis current

Fig. 5-14 Comparison between FW-FOC & LMC-DB-DTFC at 2700 r/min and 1 Nm using 150 V DC link

The applied load torque from the load motor was further increased to 1.5 Nm. While the motor is still running at 2700 r/min. At this operating condition, the motor copper losses become dominant compared to the iron loss. LMC-DB-DTFC utilizes the inverter voltage hexagon to reduce the motor negative d-axis current, which reduces the motor copper loss, the results of this experiment are shown in Fig. 5-15.

For this operating condition, LMC-DB-DTFC achieves 3.5% lower losses compared to FW-FOC.The measured motor loss at this operation using LMC-DB-DTFC was 26.9 W while using FW-FOC was 27.5 W.

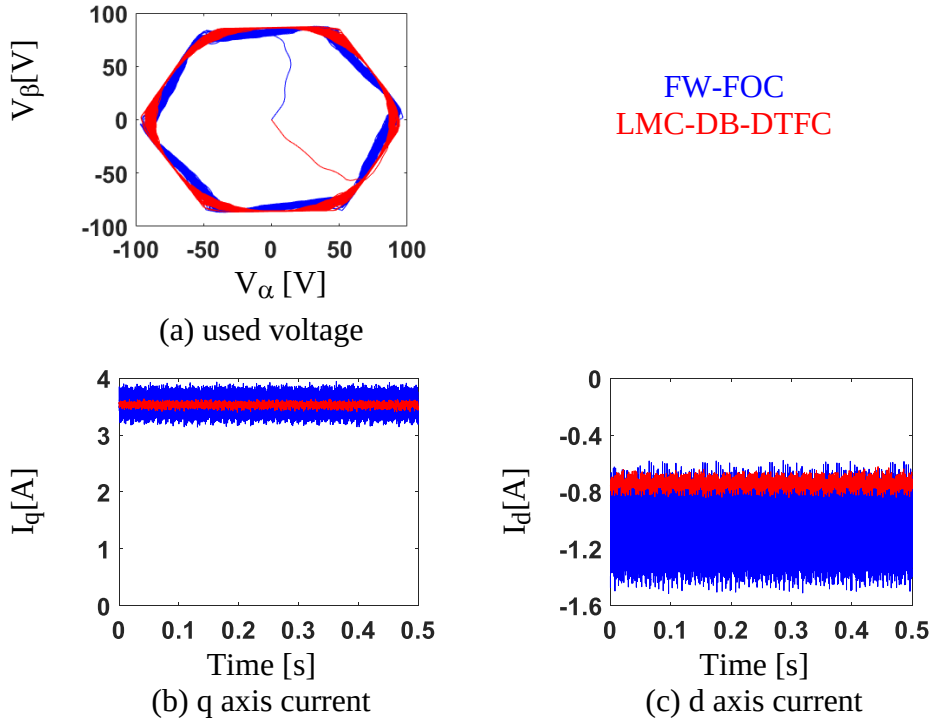

(a) used voltage

(b) q axis current

(c) d axis current

Fig. 5-15 Comparison between FW-FOC & LMC-DB-DTFC at 2700 r/min and 1.5 Nm using 150 V DC link

Fig. 5-16 and Fig. 5-17 show the step torque response for LMC-DB-DTFC during the same operating conditions as in Fig. 5-12 (not at voltage limits) and Fig. 5-13 (at voltage limits). LMC-DB-DTFC control the air-gap torque precisely even at the voltage limit.

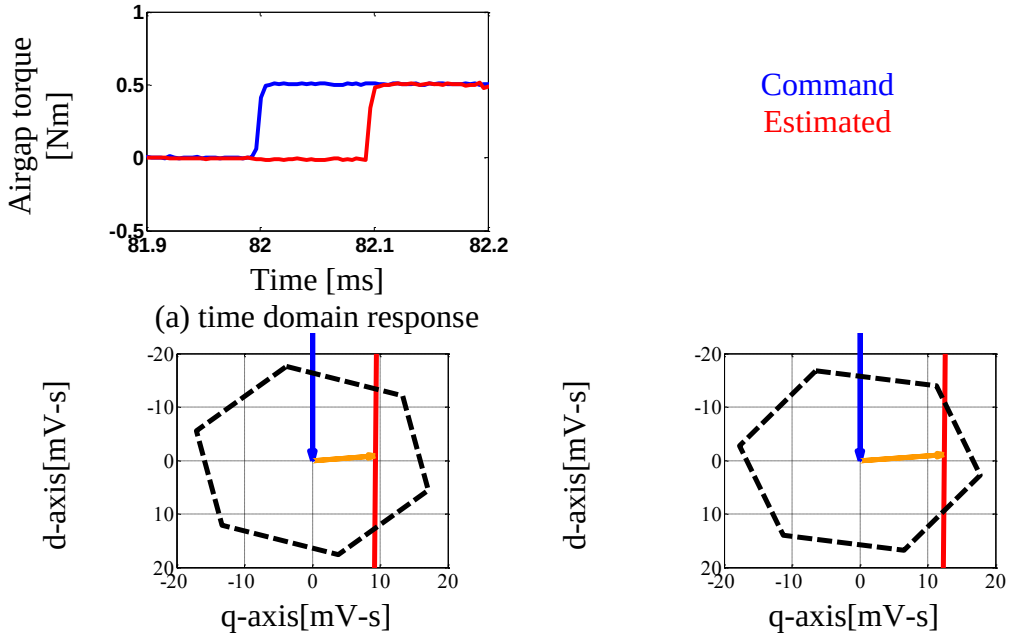

(a) time domain response

(b) graphical solution before step (c) graphical solution after step

Fig. 5-16 Step torque response for LMC-DB-DTFC at 3000 r/min using 270 V dc link

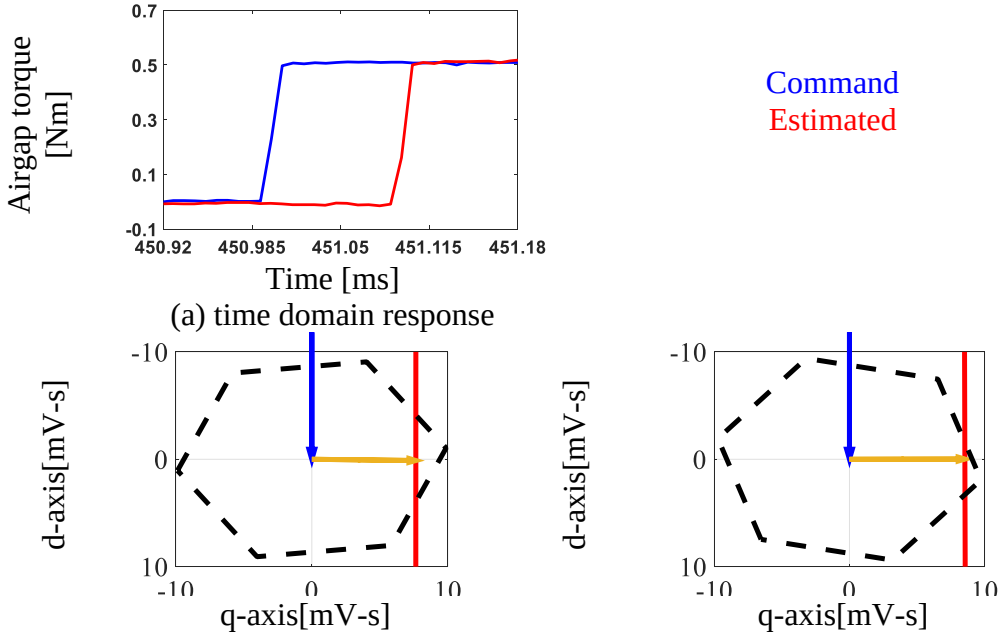

(a) time domain response

(b) graphical solution before step (c) graphical solution after step

Fig. 5-17 Step torque response for LMC-DB-DTFC at 2700 r/min using 150 V dc link – operating at the voltage limit

To evaluate the performance of the proposed LMC-DB-DTFC algorithm during rapid dynamic operation, the tested motor (SPMSM) is accelerated from 0 to 2700 r/min in only 100 ms. The DC link is set to 150 V; thus, the motor will operate at the voltage limit when the motor speed approaches from 2500 r/min. This experiment was repeated using FW-FOC algorithm. Measured torque and speed are compared in Fig. 5-18.

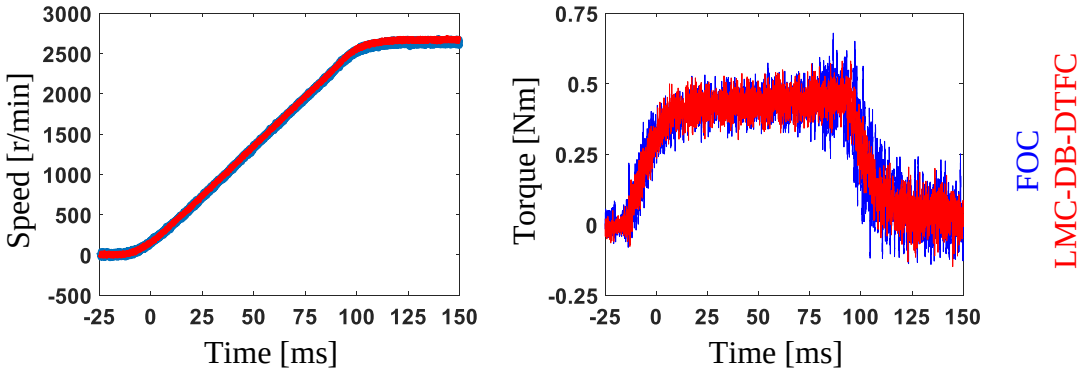

(a) calculated speed from encoder (b) dynamic shaft torque torque

Fig. 5-18 Measured speed and torque during rapid accelration using 150 V dc link – operating at the voltage limit

Fig. 5-19 compares the measured dq current when the motor controlled using FW-FOC and LMC-DB-DTFC. Q-axis current is the same in both controllers, this because the tested motor is SPMSM, and same torque is achieved using both controllers. At low speed, FOC commands zero d-axis current (MTPA solution), while LMC-DB-DTFC varies the d-axis current to achieve lower total motor losses.

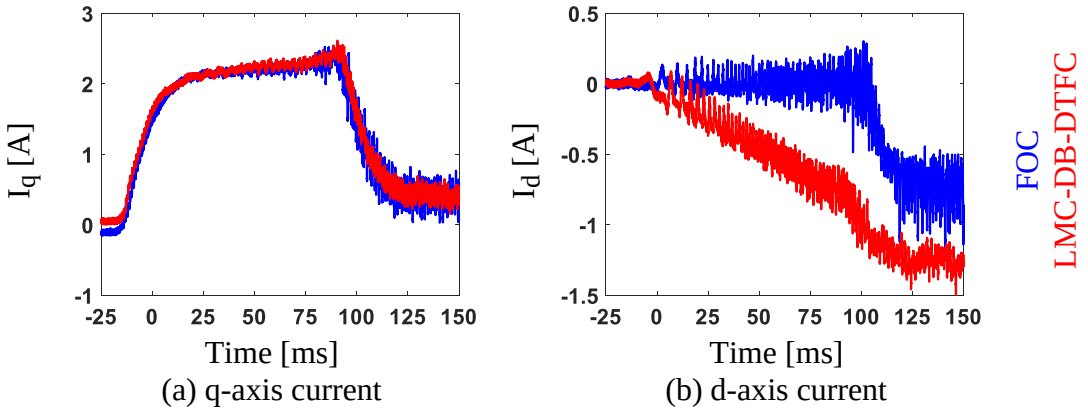

(a) q-axis current (b) d-axis current

Fig. 5-19 Measured dq current during rapid accelration using 150 V dc link – operating at the voltage limit

Fig. 5-20-b shows the measured mechanical power using both controllers during the acceleration test. Both controllers achieve same mechanical power (same speed and torque are achieved using both controllers). Fig. 5-20-a compares the measured electrical power using both controllers. LMC-DB-DTFC has lower losses during this rapid acceleration test, so lower electrical power is required during that test.

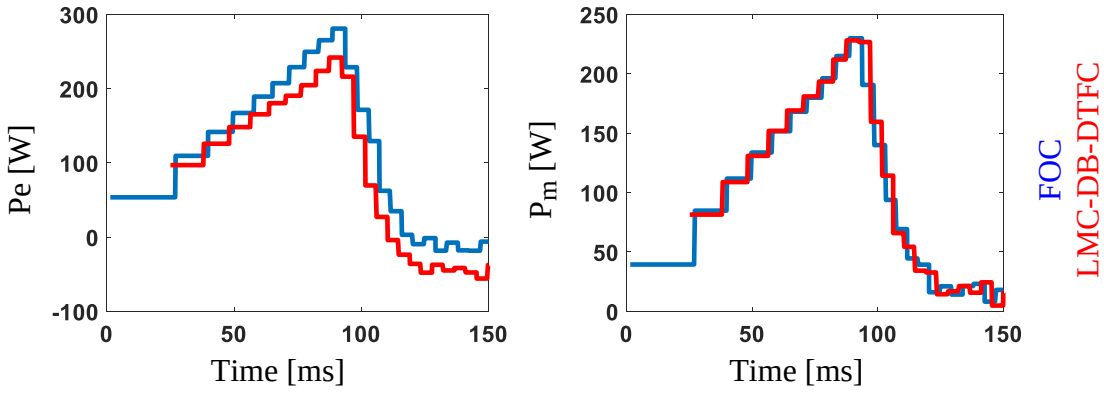

(a) electrical power (b) mechanical power

Fig. 5-20 Measured input/output power during rapid accelration using 150 V dc link – operating at the voltage limit

To explore the significance of the proposed controller, energy loss during a typical servo cycle is evaluated using the proposed controller and using the MTPA-FOC controller. Fig. 5-21 shows the measured speed during this test using both controllers.

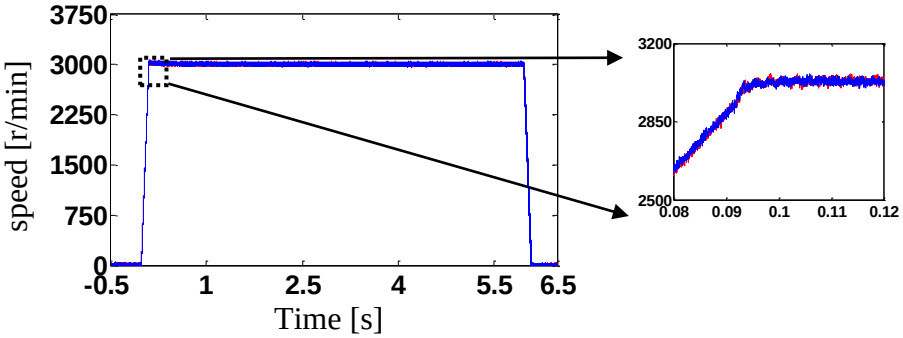

Fig. 5-21 Speed calculated from the encoder when the motor is controlled using MTPA-FOC and using LMC-DB-DTFC

To accurately measure the motor losses during acceleration/deceleration periods, the dynamic shaft torque is used to calculate the motor losses. This torque is estimated using a shaft torque observer, which was discussed in the previous chapter.

Fig. 5-22 shows the observed dynamic torque during this cycle using both FOC and LMC-DB-DTFC. Both controllers achieve the same speed-torque for the studied cycle (this is determined by the application).

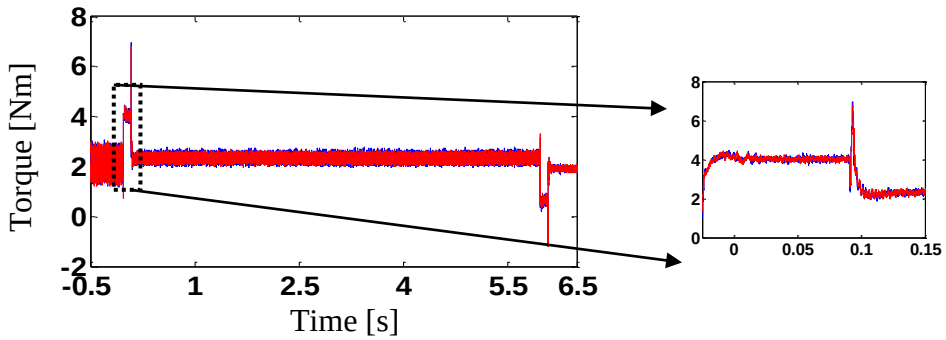

Fig. 5-22 Dynamic shaft torque when the motor is controlled using MTPA-FOC and using LMC-DB-DTFC

Fig. 5-23-a compares the measured q axis current when the system is controlled using FOC with the measured q axis current when LMC-DB-DTFC is used to control the motor. Both controllers have the same current because the controlled motor is SPMSM. The torque in this type of motors is directly proportional to the q axis current.

Fig. 5-23-b shows the measured d axis current during the studied cycle using MTPA-FOC and LMC-DB-DTFC. MTPA-FOC controls the d axis current to be zero; this will minimize the motor copper loss. However, LMC-DB-DTFC varies the d axis current to minimize total motor loss.

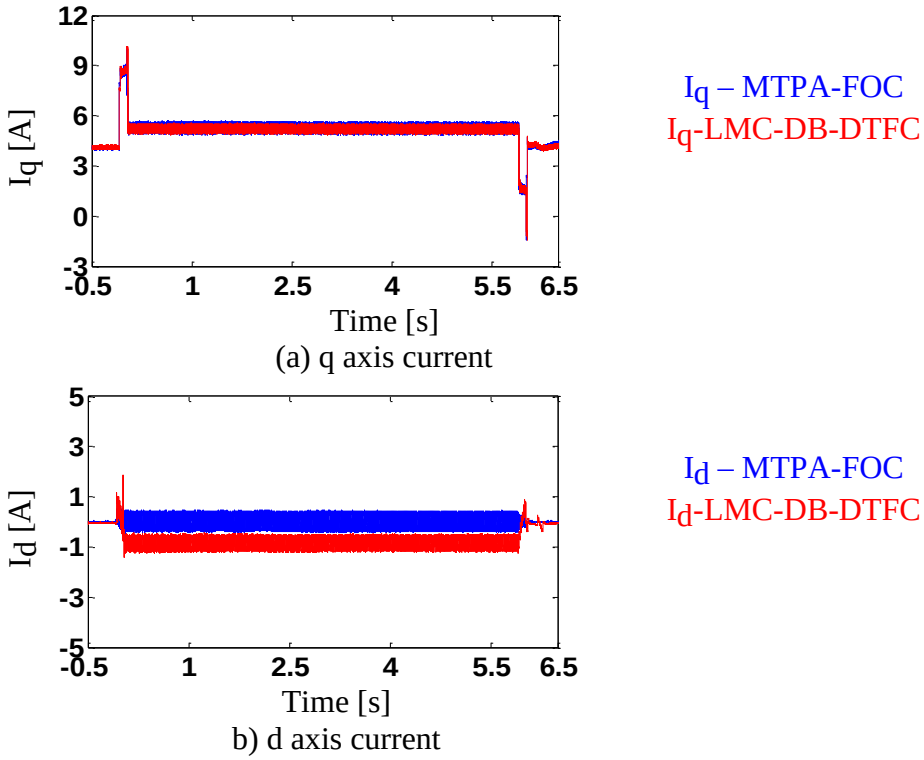

(a) q axis current

b) d axis current

Fig. 5-23 Measured q ,d axis current for the studies cycle when the motor controlled using MTPA-FOC and LMC-DB-DTFC

Fig. 5-24 shows the measured power loss for the tested motor using both MTPA-FOC and LMC-DB-DTFC. These results were obtained using a high sampling rate motor drive

analyzer (MDA 810 from Teledyne LeCroy). The tested motor has lower power losses when it is controlled using LMC-DB-DTFC compared to MTPA-FOC.

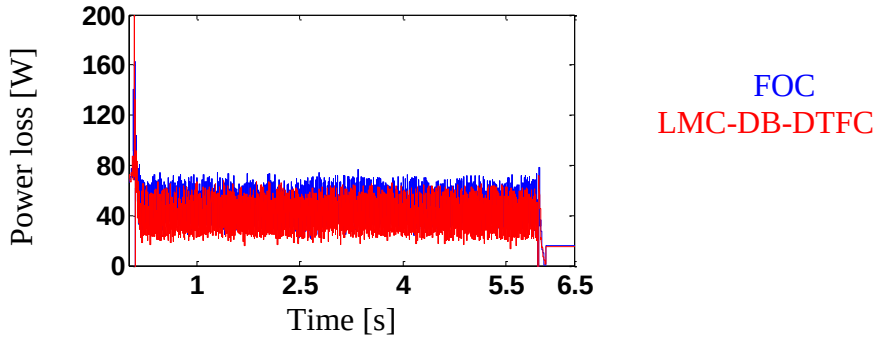

Fig. 5-24 Measured cycle loss using FOC and LMC-DB-DTFC

The measured energy loss for the studied cycle is evaluated using both controllers. Fig. 5-25 compares the measured energy loss during the studied cycle for both controllers.

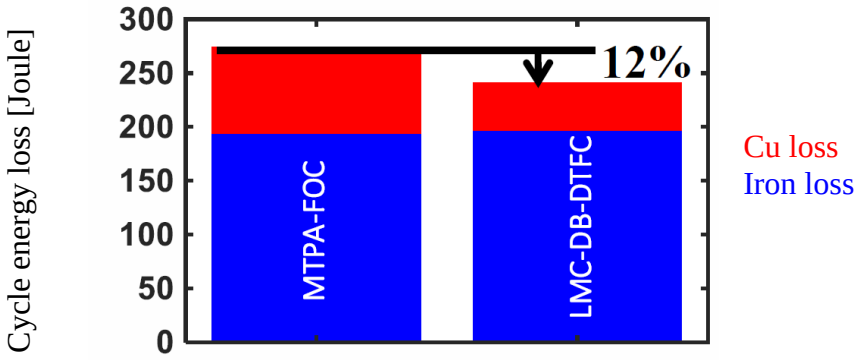

Fig. 5-25 Comparison between the cycle energy loss using MTPA-FOC woth LMC-DB-DTFC

Comparing the cycle energy loss between MTPA-FOC and LMC-DB-DTFC. LMC-DB-DTFC increases the energy loss due to copper loss by 1.5% but decreases the energy loss due to iron loss by 45%. This will decrease the total energy loss of the cycle by 12%.

LMC-DB-DTFC was also able to minimize the motor loss during acceleration/deceleration periods by 3%. A smaller amount of energy is saved. This is because

the copper loss is significant during the acceleration/deceleration period due to applying 200% of the motor rated torque during these periods.

The proposed LMC-DB-DTFC algorithm was also implemented in the other two motors. A continuous servo cycle evaluation using both CVC and LMC-DB-DTFC are performed Fig. 5-26 shows the results of the 3000r/min cycle, while Fig. 5-26 shows the results of 4000 r/min cycle. LMC-DB-DTFC could save energy in the three motors.

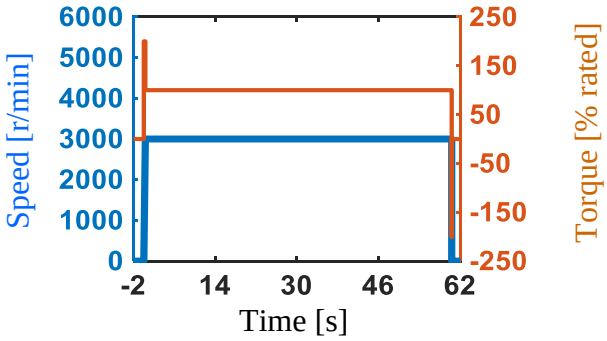

(a) 3000 r/min continuous servo cycle

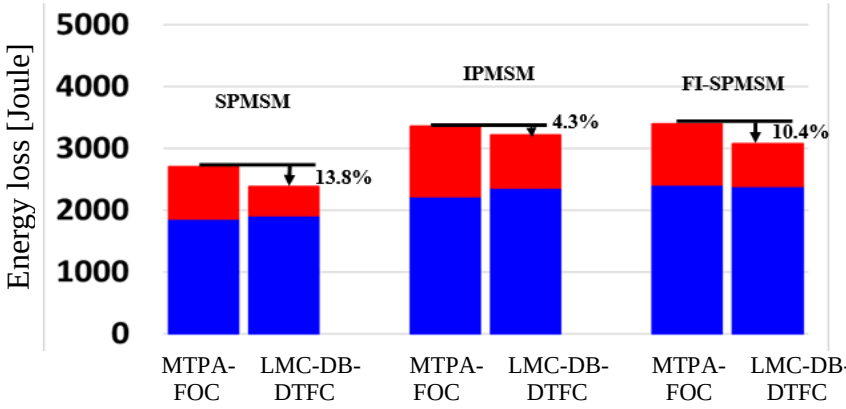

(b) Measured cycle energy loss

Fig. 5-26 Measured Energy loss for the three motors for 3000 r/min continuous servo cycle using FOC and LMC-DB-DTFC

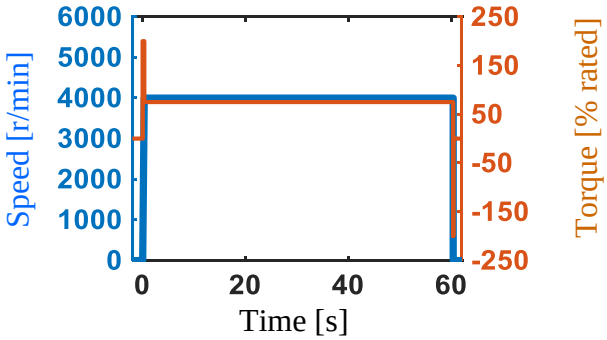

(a) 3000 r/min continuous servo cycle

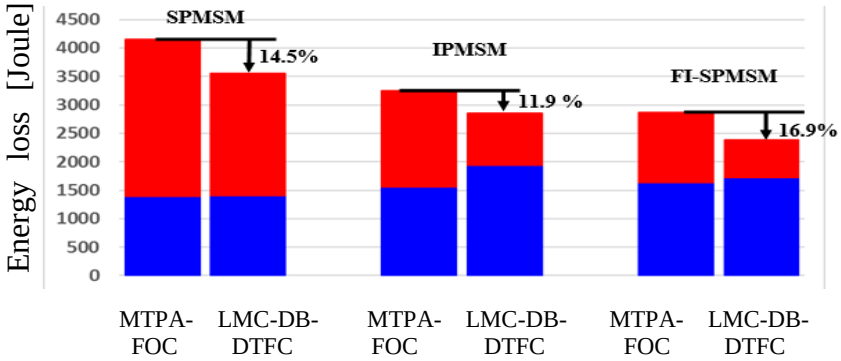

(b) Measured cycle energy loss

Fig. 5-27 Measured Energy loss for the three motors for 4000 r/min continuous servo cycle using FOC and LMC-DB-DTFC

The evaluated IPMSM servo motor has a small saliency ratio with a negligible cross-saturation. To evaluate the performance of the proposed algorithm on an IPMSM with a high saliency ratio including cross-saturation effects, a simulation was conducted using MATLAB/Simulink. The simulated motor parameters are summarized in Table II.

Table 5-1 Simulated IPMSM parameters

motor type	IPMSM	motor resistance	0.6 Ω
rated power/torque	2.39N.m / 750W	L_d/L_q	2.63/5.26 mH
motor inertia	170 μKgm^2	L_{dq}	1 mH
back EMF constant	33.9mV_{peak}/r/min		

First, the impact of inductance variations on the proposed controller performance is evaluated without including the cross-saturation effect. The motor is controlled to run at 2000

r/min and 1 Nm torque. Fig. 5-28-a compares the motor loss vs. d-axis flux calculated inside the machine model, with estimated losses calculated inside the controller using detuned estimated inductance values. The proposed technique can estimate the optimum flux linkage even with wrong estimated inductance values, due to estimating motor flux from the motor voltage using the flux observer.

Then, the cross-saturation is included in the machine model without modifying the controller. The motor is controlled to run at 2000 r/min and 1Nm. The estimated loss inside the controller is overlaid with the calculated motor loss, which includes the cross-saturation effect using (5-13), as in Fig. 5-28.

$$P_{loss\text{-}CT} = \{ \frac{3}{2} R \cdot (\hat{I}_{ds}^{r\,2} + \hat{I}_{qs}^{r\,2}) + K_h \cdot \omega_e \cdot (\lambda_{d\text{-}CT}^{r\,2} + \lambda_{q\text{-}CT}^{r\,2}) + K_e \cdot \omega_e^2 \cdot ((\lambda_{d\text{-}CT}^{r\,2} + \lambda_{q\text{-}CT}^{r\,2})\} \quad (5\text{-}13)$$

where: $\lambda_{d\text{-}CT}^{r} = L_d \cdot I_d^r + \lambda_{pm} + L_{dq} \cdot I_q^r$,

$\lambda_{q\text{-}CT}^{r} = L_q \cdot I_q^r + L_{dq} \cdot I_d^r$,

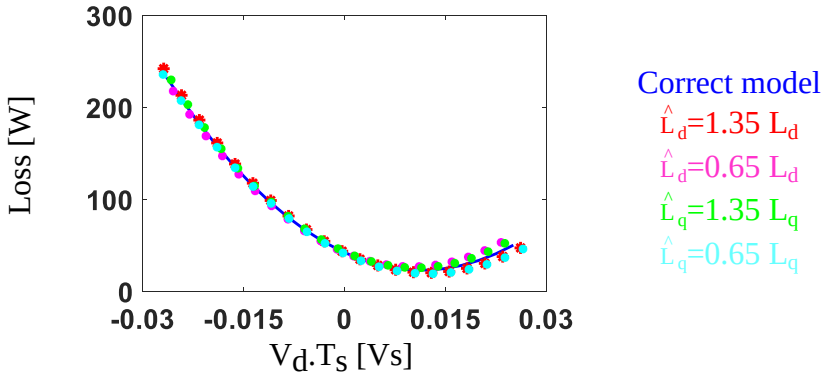

(a) Impact of inductance estimation error on the estimated loss

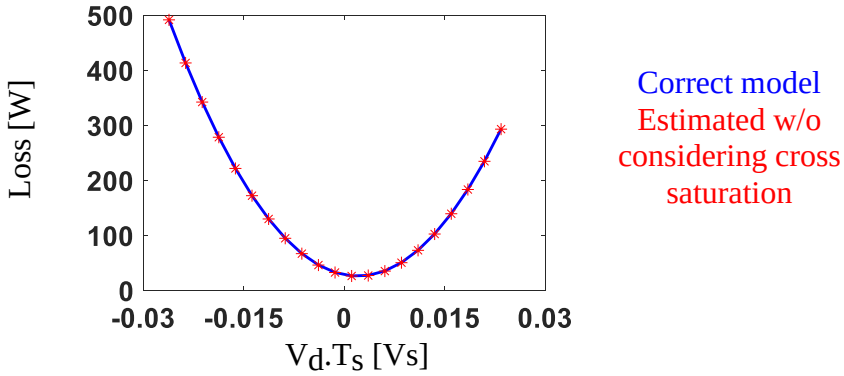

(b) Impact of cross-saturation on the estimated loss

Fig. 5-28 Impact of inductance estimation and cross-saturation on the proposed LMC-DB-DTFC perfromance

Both DB-DTFC and the proposed LMC-DB-DTFC are not sensitive to the estimated motor inductance during medium and high-speed operation, due to estimating the stator flux linkage from the motor terminal voltage. However, at low-speed operation, the flux estimation relies on the estimated motor inductance. To reduce the sensitivity of the proposed LMC-DB-DTFC to the estimated motor inductance during the low-speed operation, an online inductance estimation is developed. This technique will be presented in the following section.

5.5 Online Inductance Estimation using Model Reference Adaptive Control Technique (MRAC)

DB-DTFC and LMC-DB-DTFC are not sensitive to the estimated motor inductance during the high-speed operation, due to directly estimating the stator flux linkage from the motor stationery voltage when the voltage model flux observer doimates the closed loop flux observer estimates. This is shown in Fig. 5-2**.** However, during low-speed operation the current model flux observer dominates the closed loop flux observer estimates, making the flux estimation very sensitive to the estimated motor inductance values.

To reduce the sensitivity of the flux observer estimates during the low-speed operation, online inductance estimation can be used with both DB-DTFC and LMC-DB-DTFC. Model reference adaptive control (MRAC) technique can be used to estimate the motor d and q inductances through forcing the current model estimates to track the voltage model estimates during the high-speed operation and using the calculated values in the current model when the motor operates at low-speed.

Fig. 5-29 shows the block diagram of the MRAC technique used to estimate the motor inductance values during the high-speed operation. The PI regulator forces the current model to track the voltage model flux estimation by adjusting the initial inductance value.

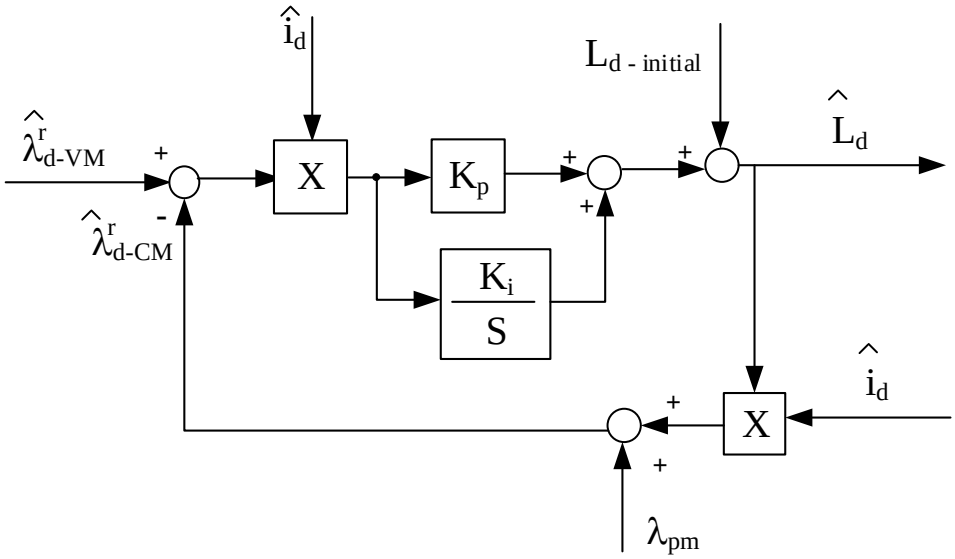

(a) d-axis MRAC based online inductance estimation

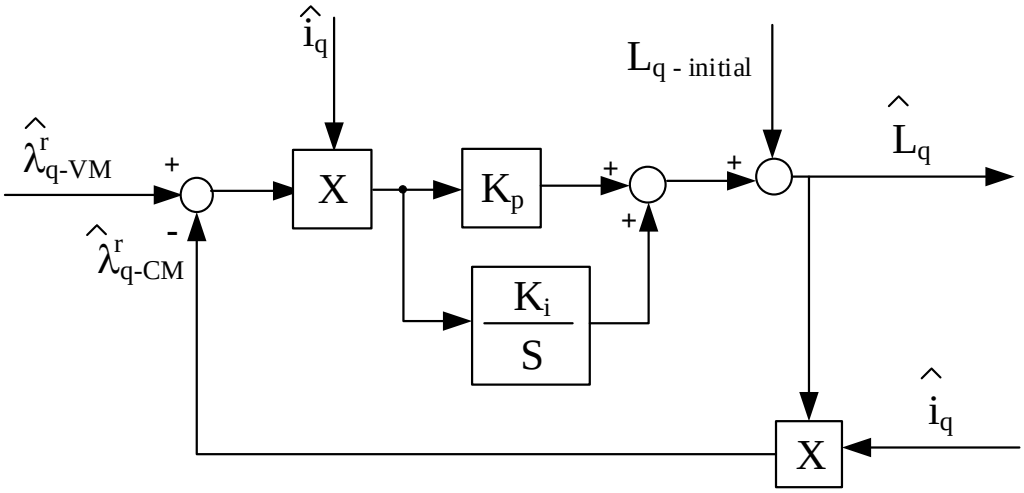

(b) q-axis MRAC based online inductance estimation

Fig. 5-29 Online estimation of the dq inductances using MRAC technique

This technique is used to estimate to the 1HP FW-SPMSM (which was discussed in chapter 2 of this thesis) d and q inductances value. The PI regulators were tuned to achieve 100 Hz leading to estimating the inductance value in less than 10 ms when the motor is spinning at 3000 r/min and 1 Nm. The results of this experiment are shown in Fig. 5-30.

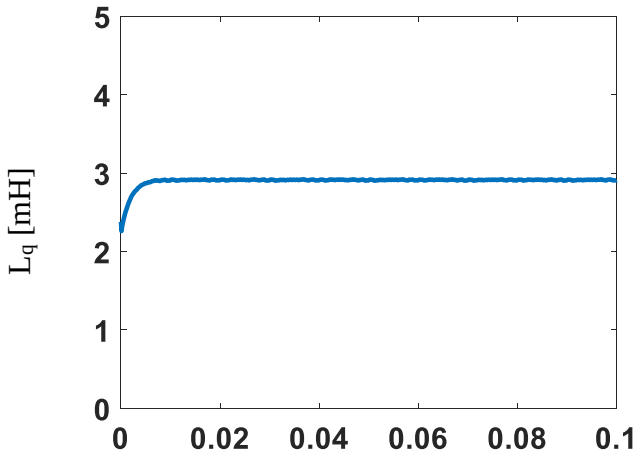

(a) q-axis inductance estimation

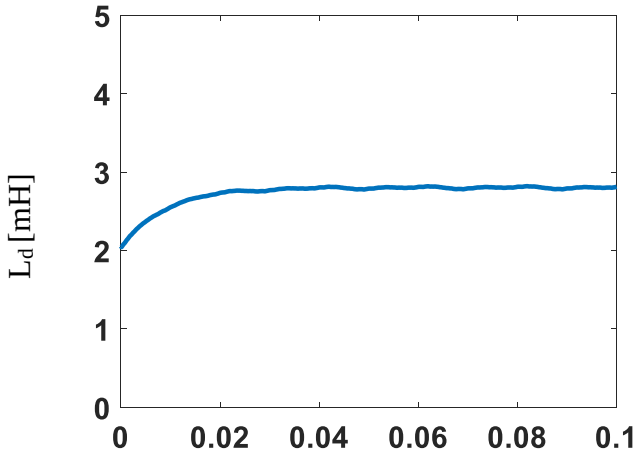

(b) a-axis inductance estimation

Fig. 5-30 Dq inductance estimation using MRAC technique for the1HP, FW-SPMSM

To verify the accuracy of this technique, the motor dq inductance values were estimated using MRAC technique at different q-axis current (load current) when the d-axis current is controlled to be zero, and the motor is controlled to run at 3000 r/min. The estimated d,q inductance values using MRAC technique are compared with the expected values from FEA. The results show a good agreement as in Fig. 5-31.

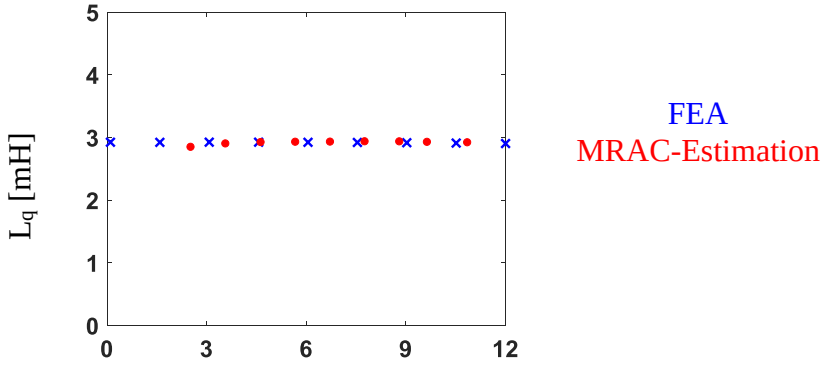

(a) q-axis inductance estimation

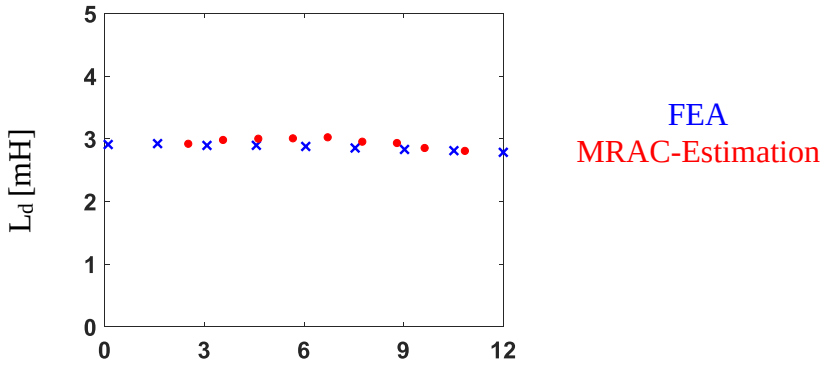

(b) a-axis inductance estimation

Fig. 5-31 Comparison between the estimated dq inductance values using MRAC technique and FEA

5.6 Summary

This chapter presents a methodology to minimize motor losses dynamically using DB-DTFC during normal and flux weakening operation. The key observations and conclusions from this chapter are summarized as follows.

- DB-DTFC provides fast, direct, and independent control of the motor airgap torque and stator flux linkage, allowing the selection of the optimum flux linkage to minimize motor

losses dynamically each switching period without affecting the torque dynamics of the drive.

- Defining the feasible volt-sec domain allows running of LMC-DB-DTFC during high speed- flux weakening operation.
- Using a simple and accurate flux linkage-based loss model and bounding the volt-sec domain to the feasible range allows running the proposed LMC-DB-DTFC in real-time for different operating conditions even during flux weakening operation without sacrificing the torque dynamics of the drive.
- The used Gopinath style stator flux linkage observer provides accurate estimation of the stator flux linkage during high-speed operation. This reduces the sensitivity of the loss model to the estimated motor inductance.
- Experimental results show the effectiveness of the proposed algorithm. LMC-DB-DTFC could minimize the energy lost in the studied servo cycle by 12%, compared to the standard MTPA-FOC, without the need for a lookup table.
- The proposed LMC-DB-DTFC algorithm is effective to minimize total motor losses during both steady-state and dynamic operations. This controller can be used in any kind of PM motors.
- The proposed LMC-DB-DTFC algorithm is not affected by unmodeled motor cross-saturation, due to estimating the stator flux linkage from the motor voltage during medium and high-speed operation.

- MRAC technique can be used to estimate the motor d,q axis inductances online by forcing the current model flux observer to track the voltage model flux observer, which is insensitive to the motor parameters during the high-speed operation.

Chapter 6 Wide-Speed Range Self-Sensing Control for PM Servo Motor

The main technical content of this chapter has been published in a technical paper in [132]. In this chapter, a self-sensing algorithm is proposed. This algorithm operates at zero, low and high-speed. The proposed algorithm has sufficient dynamic performance, allowing controlling the motor in self-sensing control even during rapid servo dynamics. The proposed algorithm doesn't degrade the torque dynamics of the servo motor.

In order to control the motor at zero and low speed operation, a high-frequency flux injection (HFFI) based self-sensing algorithm using DB-DTFC is proposed. This allows controlling the motor with ideally zero torque ripple not like standard current or voltage injection self-sensing techniques. The HFFI is combined with a back EMF self-sensing technique to control the motor during medium and high-speed operation. This chapter also proposes a method for a smooth transition between these two methods.

6.1 High-Frequency Flux Injection Based Self-Sensing Control with DB-DTFC

Self-sensing at zero and low-speed operation is feasible for salient machines through tracking the motor saliency. This requires a salient machine like an IPMSM or a specially designed SPMSM. In this thesis, the designed FI-SPMSM discussed in chapter 2 and the designed FW-SPMSM discussed in chapter 3 are used, these motors have a small, but detectable saliency.

DB-DTFC allows independent control of the motor airgap torque and stator flux linkage. This allows the use of the flux linkage as a degree of freedom to inject a high-frequency flux signal along the torque line with inherently zero torque ripple without the need to use any filters for the feedback signals, then the measured current can be used to detect the motor position. In this way, the torque dynamics will not be affected by the injected signal. Fig. 6-1 shows the block diagram of DB-DTFC with HFFI.

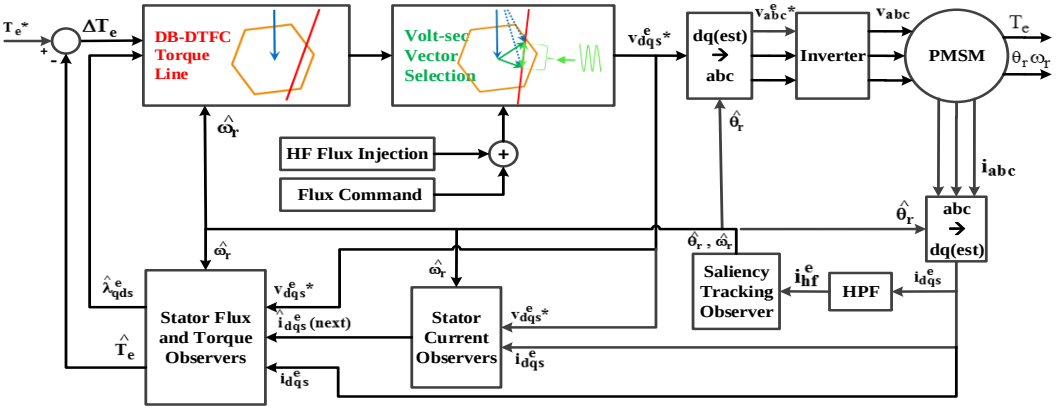

Fig. 6-1 Block diagram of DB-DTFC drive systems

To evaluate the performance of DB-DTFC with flux injection, an 850Hz flux is injected along the torque line with DB-DTFC. Then the performance is compared with a standard pulsating voltage injection with a complex vector current regulator (CVCR) and implemented on the designed FI-SPMSM. Fig. 6-2 shows the commanded d-axis voltage using both controllers. Similar d-axis voltage is achieved by injecting the appropriate voltage and flux.

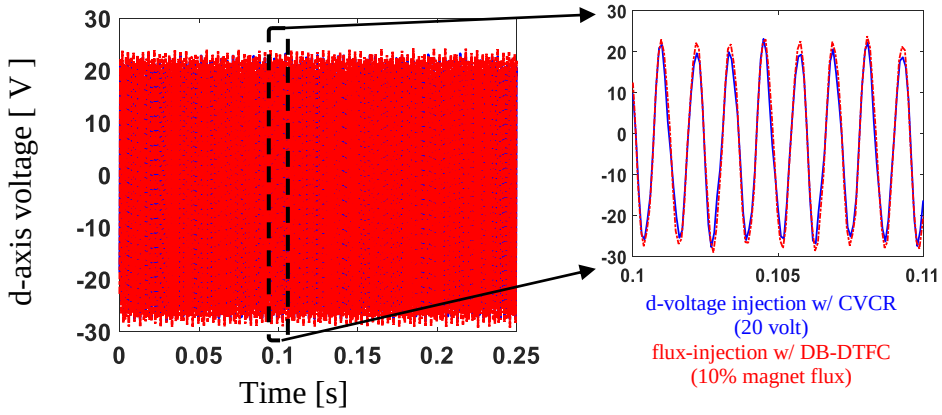

Fig. 6-2 D-axis voltage with voltage and flux injection when the motor run at 600 r/min and 0.6 Nm

Then the FI-SPM servo motor is controlled to run at 600 r/min and 0.6 Nm is applied using the load motor, the measured position from the encoder is used as a feedback position signal. Fig. 6-3 shows the calculated speed from the encoder using both controllers.

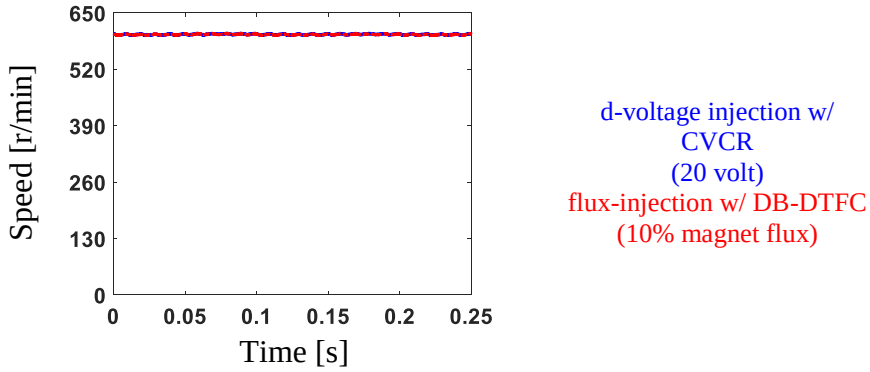

Fig. 6-3 Calculated FI-SPMSM speed from the encoder using two different injection techniques

Fig. 6-4 compares between the FI-SPMSM airgap torque using CVCR and DB-DTFC. DB-DTFC achieves smooth airgap torque compared to CVCR without any additional ripple induced by the injection.

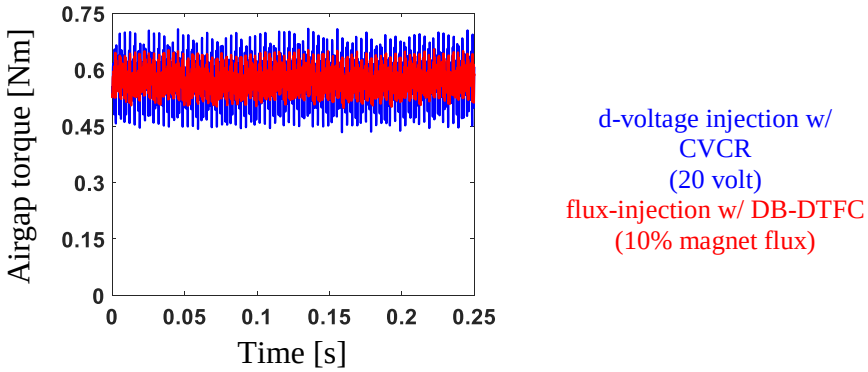

Fig. 6-4 FI-SPMSM airgap torque comparison using two different injection techniques when the motor run at 600 r/min and 0.6 Nm

Fig. 6-5 shows the FFT for the FI-SPMSM airgap torque using both controllers. With CVCR significant torque ripple appears at the injected frequency, while with DB-DTFC a negligible torque ripple is achieved with the flux injection. This allows using DB-DTFC without any low pass filters for the feedback signals to mitigate this ripple, which limits the dynamic performance of the controller as in CVCR.

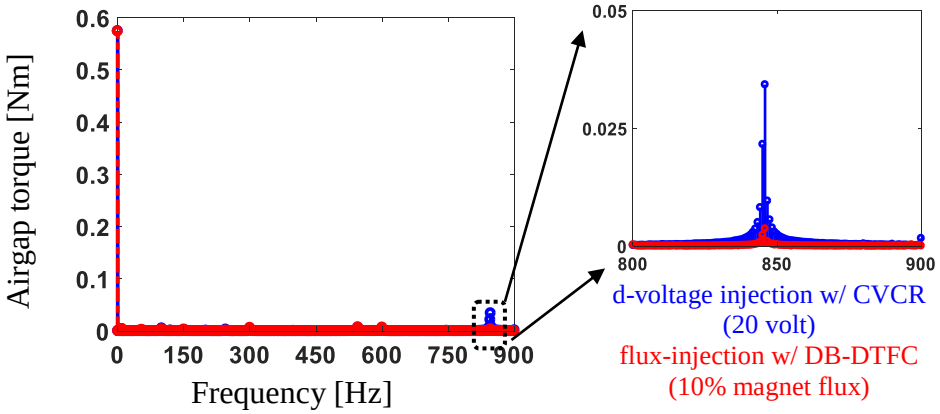

Fig. 6-5 FFT of the FI-SPMSM airgap torque using two different injection techniques when the motor run at 600 r/min and 0.6 Nm

In this thesis, HFFI along the torque line using DB-DTFC with zero torque ripple is proposed. The proposed algorithm is implemented on FI-SPMSM and FW-SPMSM designed for servo motor. These motors have a small detectable saliency. The torque line for SPMSMs, which

is calculated using DB-DTFC algorithm, is almost vertical (m≈0), similar equations to pulsating a high-frequency voltage on the d-axis (which was discussed in section 1.3.5.2 of this thesis) can be used to estimate the rotor position from the measured motor current. Equation (6-1) relates the high-frequency voltage component that appears due to injecting a high-frequency flux linkage along the torque line for a slightly salient motor.

$$\begin{bmatrix} \hat{V}^{r}_{d\text{-}hf} \\ \hat{V}^{r}_{q\text{-}hf} \end{bmatrix} = V_C \begin{bmatrix} \sin \omega_c t \\ 0 \end{bmatrix} = \frac{\lambda_c}{T_s} \begin{bmatrix} \cos \omega_c t \\ 0 \end{bmatrix} \tag{6-1}$$

where:

λ_c = injected high frequency flux amplitude [V.s],

V_c = induced high-frequency voltage by flux injection [V],

ω_c = injection frequency [rad/s],

T_s = simple period [s],

$\hat{V}^{r}_{d\text{-}hf}$, $\hat{V}^{r}_{q\text{-}hf}$= high-frequency d, q voltage components in the estimated rotor frame[V]

The induced high-frequency flux will cause two rotating current vectors. The position difference between the actual and the estimated rotor frame (θ_{err}) is used to calculate the induced high-frequency currents in the estimated frame as in (6-2).

$$\begin{bmatrix} \hat{i}^{r}_{d\text{-}hf} \\ \hat{i}^{r}_{q\text{-}hf} \end{bmatrix} = \frac{1}{2 L_d L_q} * \begin{bmatrix} \Sigma L+\Delta L \cos(2\theta_{err}) & -\Delta L \sin(2\theta_{err}) \\ -\Delta L \sin(2\theta_{err}) & \Sigma L-\Delta L \cos(2\theta_{err}) \end{bmatrix} * \frac{\lambda_c}{T_s} \begin{bmatrix} \cos \omega_c t \\ 0 \end{bmatrix} \tag{6-2}$$

where:

$\hat{I}^{r}_{d\text{-}hf}$, $\hat{I}^{r}_{q\text{-}hf}$= high-frequency d, q current in the estimated rotor frame [A],

L_d, L_q = d, q inductance [H],

$\Delta L = (L_d - L_q)/2$ [H],

$\Sigma L = (L_d + L_q)/2$ [H],

θ_{err}= position error [rad]

The high-frequency current component in the estimated q axis frame contains the spatial information as in (6-3). A heterodyning demodulation process with a position observer is then used to estimate the rotor position and speed as shown in Fig. 6-6.

$$\hat{i}^{r}_{q\text{-}hf} = \frac{\lambda_c}{T_s} * \frac{\Delta L}{2L_d\, L_q \omega_c} \sin(\omega_c t)\sin(2\theta_{err}) \tag{6-3}$$

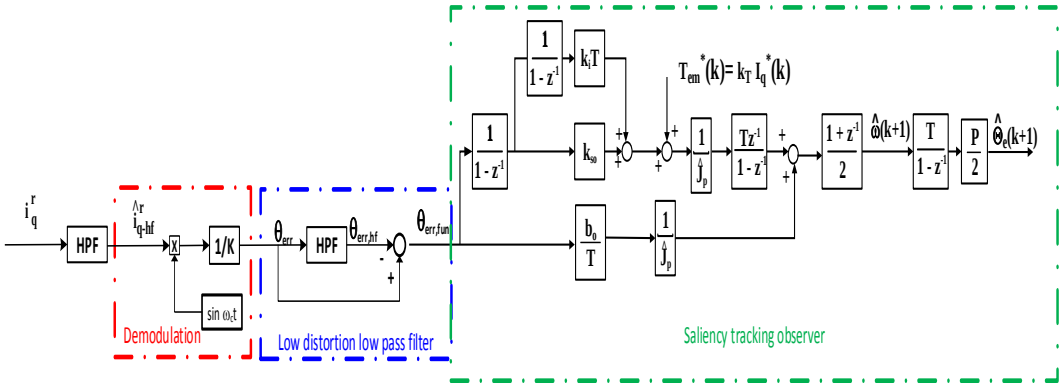

Fig. 6-6 Motor position and speed estimation from the measured q-axis current

In this thesis, 850 Hz sinewave flux is injected on the top of the commanded flux along the torque line with DB-DTFC. A 650 Hz high pass filter is used to extract the high-frequency current component. The position error is then calculated by multiplying the high-frequency current component in the q-axis with a sine function with the same injection frequency. This error is fed to a Luenberger style position observer. This observer is tuned to achieve 20 Hz bandwidth. The position observer bandwidth forms the upper limit for the feasible motion controller bandwidth.

In order to extract the fundamental position error without causing any phase distortion, a low-pass filter is designed by subtracting a high-pass filter response with 30Hz bandwidth from the position error signal. Fig. 6-6 shows the block diagram for the process of estimating the rotor

position and speed from the measured q-axis current. The constant k in this figure can be calculated as in (6-4).

$$K= \frac{T_s}{\lambda_c} * \frac{L_d\, L_q \omega_c}{\Delta L} \qquad (6\text{-}4)$$

The motion controller is tuned to achieve 20 Hz (same bandwidth as the position tracking observer). The motor is controlled using HFFI self-sensing DB-DTFC controller at a different speed and load conditions. This algorithm is then used to control the designed FI-SPMSM and the specially designed FW-SPMSM in chapter 3 of this thesis.

6.1.1 Expermental results of HFFI self-sensing on the designed FI-SPMSM

HFFI self-sensing algorithm is first implemented on the designed FI-SPMSM motor, 5 % of the magnet flux is superimposed on top of the commanded flux that achieves the MTPA solution of this motor using (5-2), minimizing the motor copper loses which dominates the motor losses during the low-speed operation when the HFFI self-sensing is used.

The steady-state performance of this technique is evaluated by running the motor at a different speed and torque conditions. The measured and estimated position when the FI-SPMSM ran at 100 r/min (0.03 pu) with 0 Nm load are shown in Fig. 6-7-a, and with 0.1 Nm load are shown in Fig. 6-7-c . The position error is higher than expected, this due to inverter non-linearity and dead-time effect (The used inverter has 3.5 μs dead-time). At this operating condition, the commanded voltage will be different than the actual one.

The FI-SPMSM then ran at 600 r/min and 0.5 Nm torque was applied from the load motor. As the speed increases, the impact of the inverter deadtime become less significant which leads to lower angular position error as shown in Fig. 6-7-h and Fig. 6-7-f when the load torque is removed.

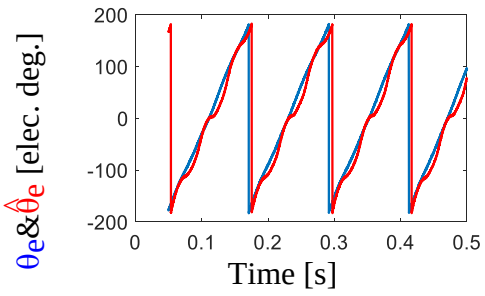

(a) Measured, estimated position at 100 r/min, 0 Nm

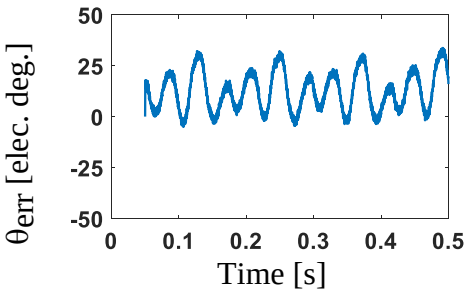

(b) Position error at 100 r/min, 0 Nm

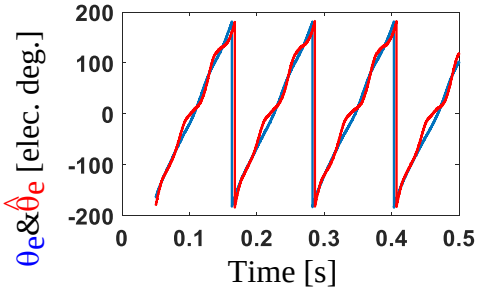

(c) Measured, estimated position at 100 r/min, 0.1 Nm

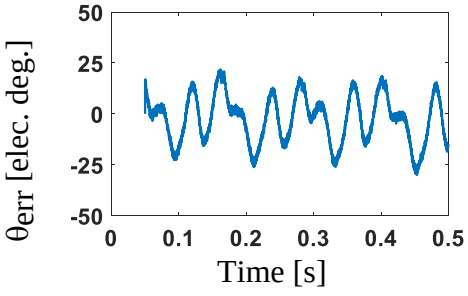

(d) Position error at 100 r/min, 0.1 Nm

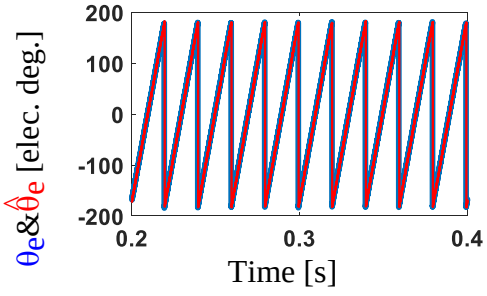

(e) Measured, estimated position at 600 r/min, 0 Nm

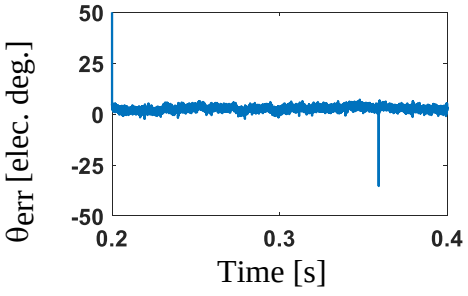

(f) Position error at 600 r/min, 0 Nm

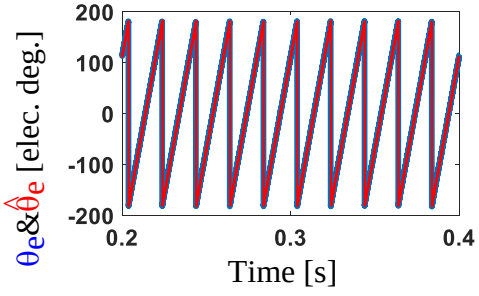

(g) Measured, estimated position at 600 r/min, 0.5 Nm

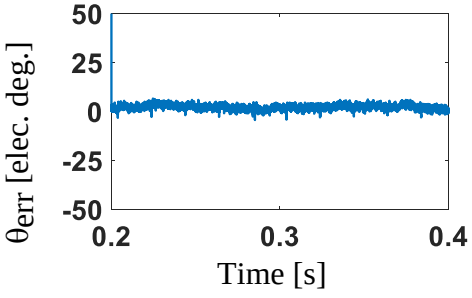

(h) Position error at 600 r/min, 0.5 Nm

Fig. 6-7 Measured, estimated, position error when the FI-SPMSM is controlled using HFFI self-sensing DB-DTFC at different speed and load conditions

The dynamic performance of the proposed technique using the designed FI-SPMSM is then evaluated during rapid acceleration. The FI-SPMSM was accelerated from 200 r/min to 1000 r/min in 40 ms. Fig. 6-8 compares the measured and estimated position and speed during this test. The proposed algorithm achieves good dynamic performance due to not using a low pass filter in the measured current as in standard voltage injection self-sensing with CVCR.

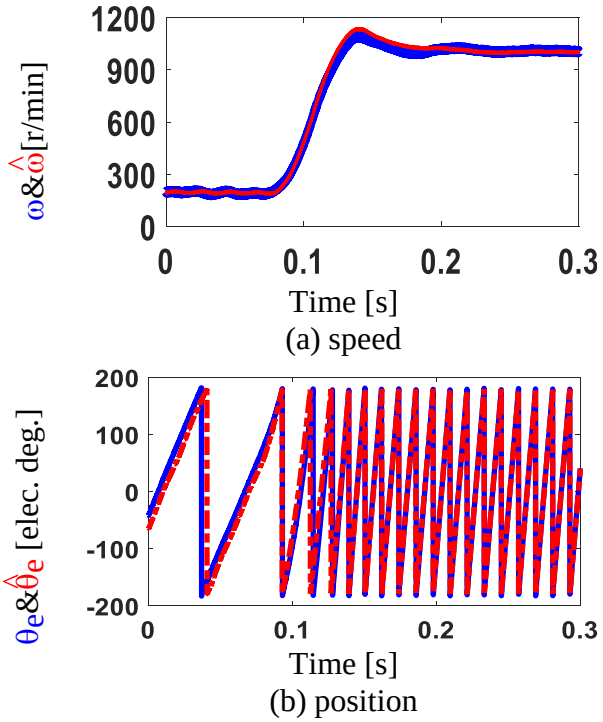

Fig. 6-8 Measured, estimated, speed and position of the FI-SPMSM during rapid acceleration using HFFI self-sensing control

The dynamic stiffness of the proposed algorithm is then evaluated and compared with the sensor-based case. Fig. 6-9 shows the comparison results. At low frequency, the dynamic stiffness of the proposed HFFI self-sensing algorithm is lower than the sensor-based case. This is because the motion controller bandwidth is reduced from 50 Hz to 20 Hz for the self-sensing case. The bandwidth is reduced to match the tuned saliency tracking observer bandwidth, which

is limited to the bandwidth of the filters used to extract the spatial information from the measured current.

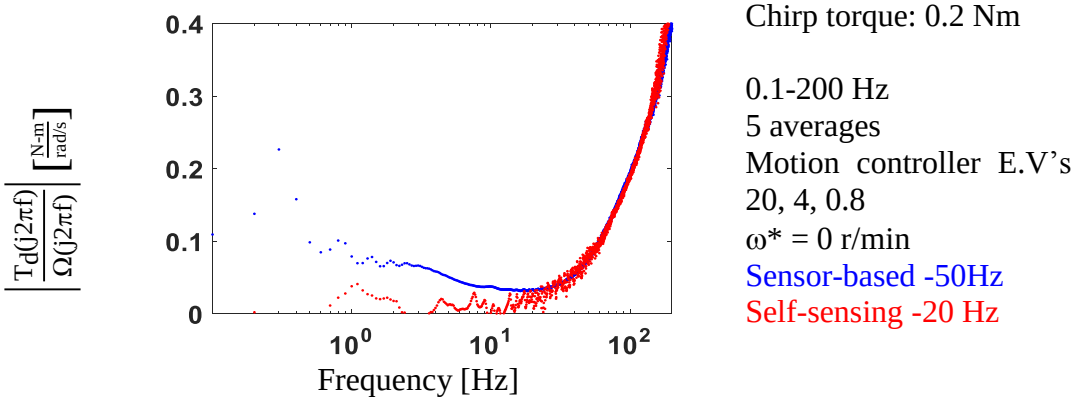

Fig. 6-9 Dynamic stiffness comparison between HFFI self-sening and sensor-based control using the FI-SPMSM

6.1.2 Expermental results of HFFI self-sensing on the designed FW-SPMSM

Then the developed HFFI self-sensing control algorithm is evaluated on the designed FW-SPMSM which was discussed in chapter 3 of this thesis. For this motor, 7.5% of the magnet flux is superimposed on the corresponding MTPA flux linkage command, which achieves the minimum losses during the low-speed operation.

The steady-state performance of the HFFI self-sensing technique on the designed FW-SPMSM is evaluated. Fig. 6-10 compares the measured and estimated position when the FW-SPMSM ran at different speed and load conditions. Larger position error than expected showed up during the low-speed operation when the motor run at 50 r/min, this is due to inverter non-linearity and dead-time effect (The used inverter has 3.5 μs dead-time). At this operating condition, the commanded voltage will be different than the actual one.

The position error decreases with increasing the speed to 500 r/min. This is because the impact of the inverter deadtime become less significant, which leads to lower angular position

error as in Fig. 6-10-f. The designed FW-SPMSM in chapter 3 is controlled using HFFI self-sensing even at overload condition when 18 Nm torque is applied. This is due to the enhanced self-sensing properties of this motor.

The position error increases with load. It increases linearly from -1.9 electrical degrees at no load to 13.5 electrical degrees at the rated torque (17 Nm) when the FW-SPMSM is controlled using HFFI self-sensing and ran at 500 r/min, **Error! Reference source not found.**-a documents the measured results. The speed error at different load condition is almost zero as shown in **Error! Reference source not found.**-b. This position error can be compensated using lookup tables to achieve low position error.

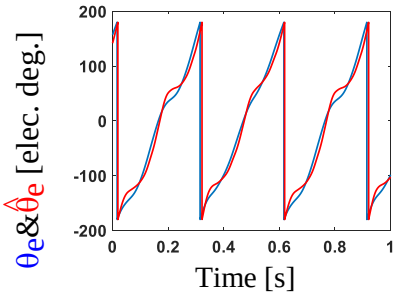

(a) Measured, estimated position at 50 r/min, 0 Nm

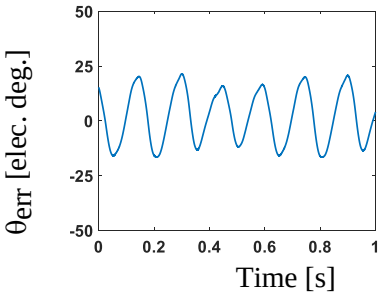

(b) Position error at 50 r/min, 0 Nm

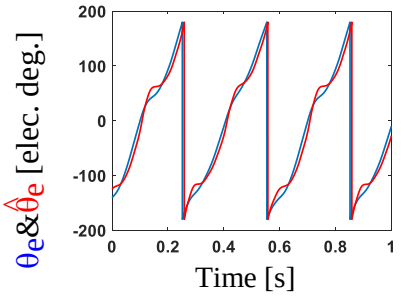

(c) Measured, estimated position at 50 r/min, 2 Nm

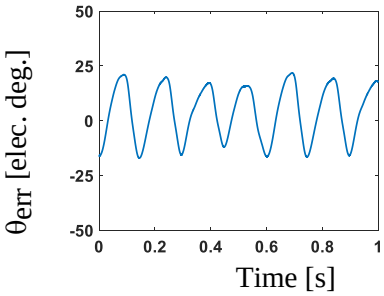

(d) Position error at 50 r/min, 2 Nm

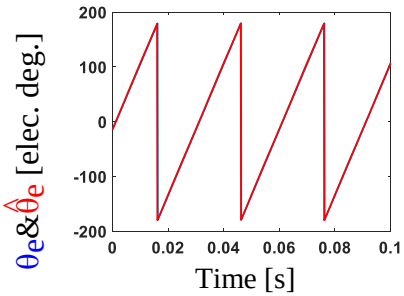

(e) Measured, estimated position at 500 r/min, 0 Nm

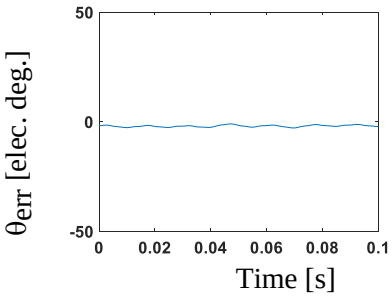

(f) Position error at 500 r/min, 0 Nm

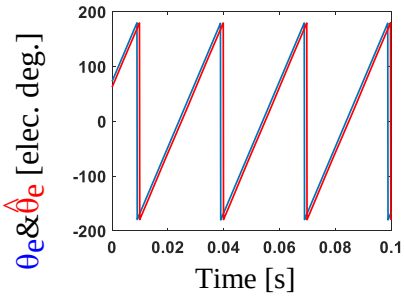

(g) Measured, estimated position at 500 r/min, 18 Nm

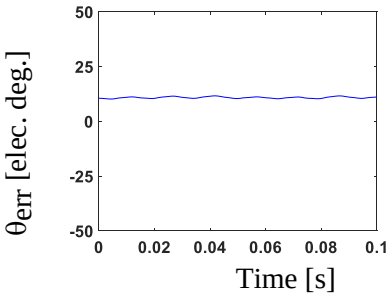

(h) Position error at 500 r/min, 18 Nm

Fig. 6-10 Measured, estimated, position error when the FW-SPMSM is controlled using HFFI self-sensing DB-DTFC at different speed and load conditions

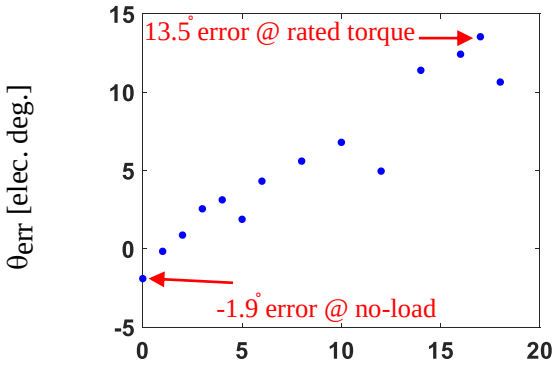

(a) position error at diffrent load

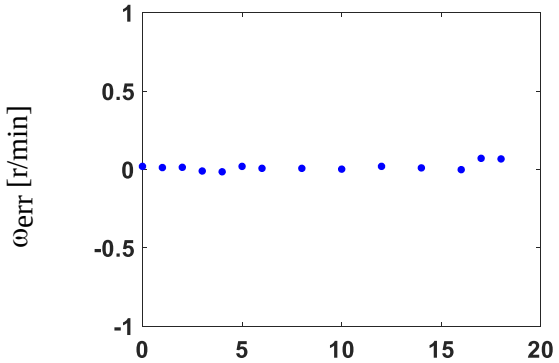

(a) speed error at diffrent load

Fig. 6-11 Speed and position error at different load levels for the FW-SPMSM controlled using HFFI self-sensing at 500 r/min

The dynamic performance of the proposed technique using the designed FW-SPMSM is then evaluated during rapid acceleration. The FW-SPMSM was accelerated from 100 r/min to 1000 r/min in 50 ms. Fig. 6-12 compares the measured and estimated position and speed during this test. 15 Nm torque is commanded from this motor to achieve this high acceleration rate. The commanded and achieved airgap torque are shown in Fig. 6-12-c.

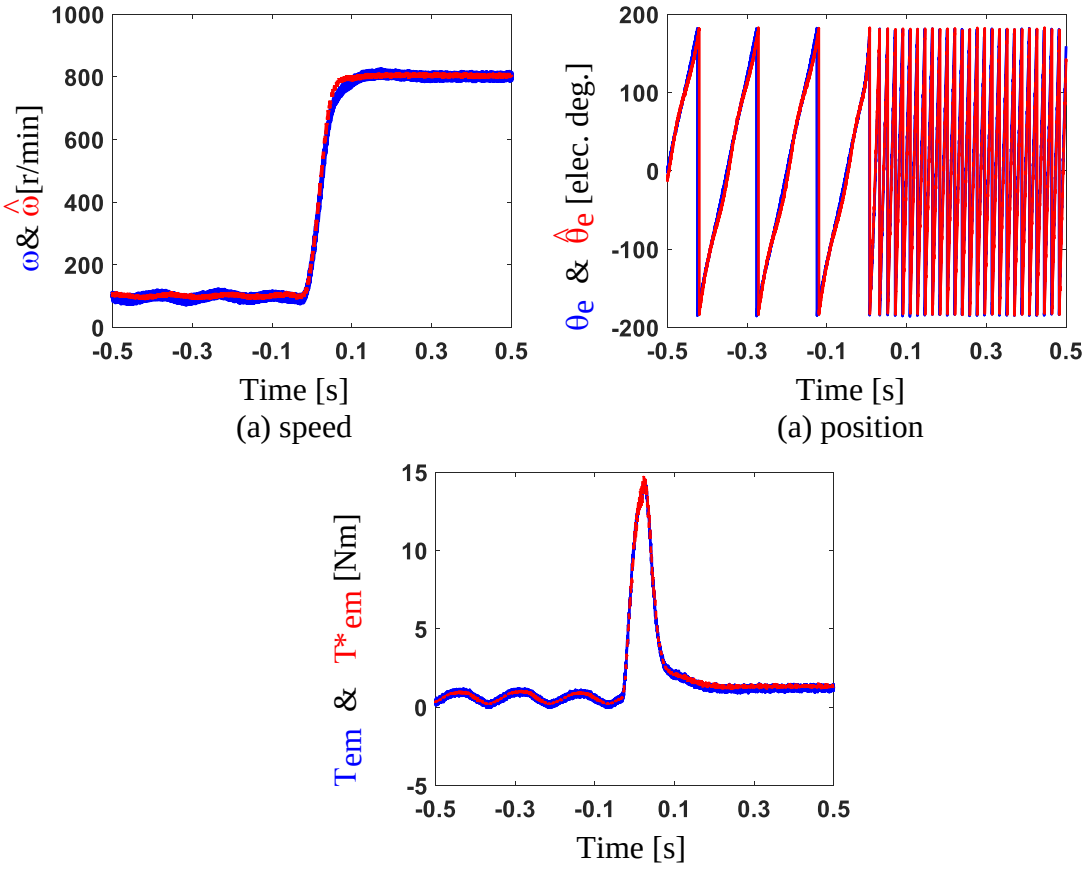

Fig. 6-12 HFFI self-sensing performance during rapid acceleration test for the designed FW-SPMSM

The developed HFFI self-sensing algorithm achieved good dynamic performance on both FW-SPMSM and FI-SPMSM. This technique will be used to control the motor at zero and low-speed operation. During the high-speed operation, back-EMF tracking self-sensing technique without any flux injection will be used.

6.2 Back-EMF Tracking Self-Sensing Control with DB-DTFC

As the motor speed increases, the signal to noise ratio in the estimated back-EMF improves, allowing the use of this signal to estimate the rotor position and speed without the need to inject any signal into the motor. A back-EMF state filter can be used to estimate the

back-EMF voltage. This filter has a similar structure to a current observer in the stationary reference frame. This filter is capable of estimating the back-EMF voltage within its bandwidth. The position is then estimated using a position observer. In this paper, two cascaded observers are used to estimate the rotor position and speed. This improves the performance of the drive when it runs at low speed, in which the estimated speed will be filtered out using the cascaded observer without any phase distortion issues. The two cascaded position observers were tuned for 20,5 Hz respectively, while the back-EMF state filter is tuned for 1 kHz bandwidth. Fig. 6-13 shows the block diagram of the constructed back EMF state filter with the two cascaded position observers.

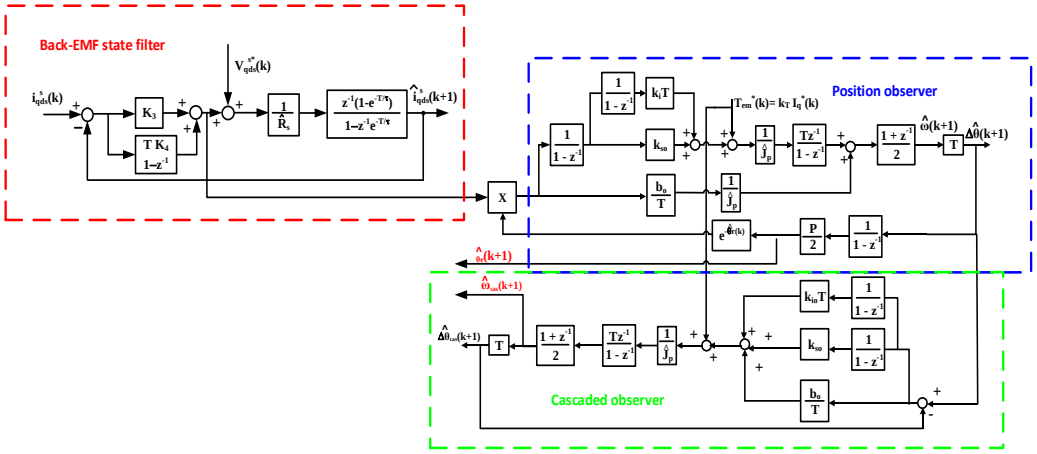

Fig. 6-13 Back-EMF state filter with a cascaded position observer structure

To validate the constructed back-EMF state filter with the constructed observers, the FI-SPMSM ran at different speed and load conditions using the encoder feedback signal, then the estimated position from the position observer is compared with the actual position measured using the encoder, the result of this experiment is shown in Fig. 6-14.

After validating the constructed state filter and observers, the motor is controlled using back-EMF self-sensing DB-DTFC. The measured position from the encoder is used to start up

the motor. When the speed is greater than 200 r/min, the estimated position through back-EMF tracking is used to control the motor. Fig. 6-15 compares the measured and the estimated position of the motor at a different speed and load conditions when the motor is controlled using back-EMF tracking self-sensing with DB-DTFC.

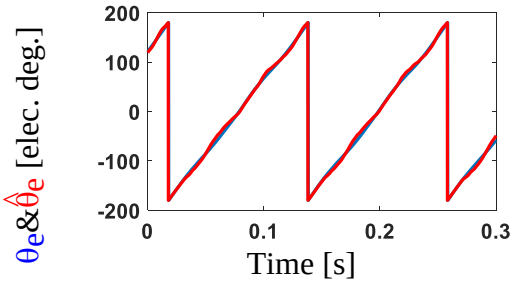

(a) Measured, estimated position at 100 r/min, 0 Nm

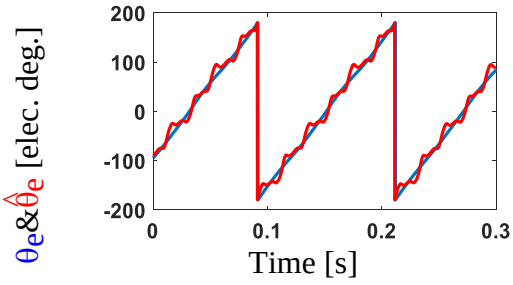

(b) Measured, estimated position at 100 r/min, 0.5 Nm

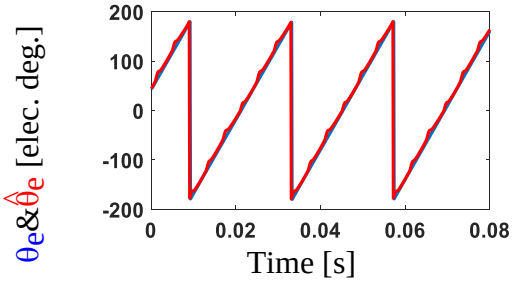

(c) Measured, estimated position at 500 r/min, 1.5 Nm

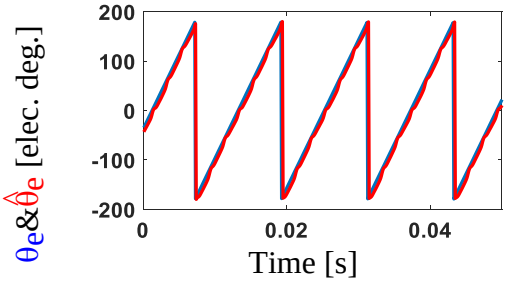

(d) Measured, estimated position at 1000 r/min, 2 Nm

Fig. 6-14 Measured, estimated position through back EMF tracking when the motor is controlled using sensor-based DB-DTFC at different speed and load conditions

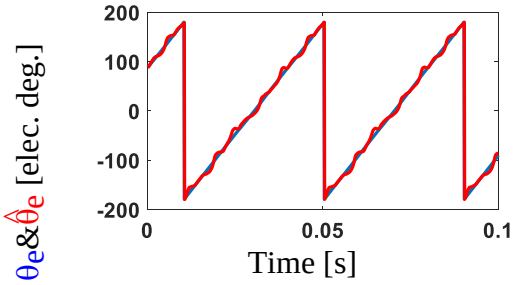

(a) Measured, estimated position at 300 r/min, 0.5 Nm

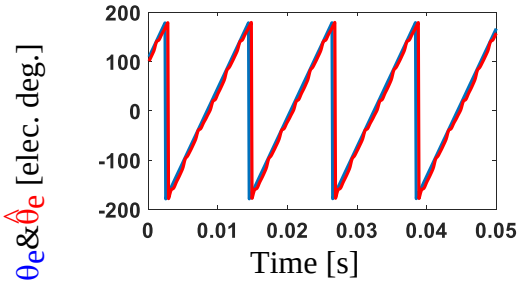

(b) Measured, estimated position at 1000 r/min, 2Nm

Fig. 6-15 Measured, estimated position using back-EMF tracking when the motor is controlled using self-sensing based DB-DTFC at different speed and load conditions

6.3 Full Speed Range Self-Sensing DB-DTFC Control during Dynamic Servo Cycles

In this section, both HFFI and back-EMF tracking self-sensing techniques are combined. When the motor is running at zero and low-speed operations, the HFFI self-sensing method is used. At higher speeds, the back-EMF tracking self-sensing method is adopted. A smooth transition between these algorithms is developed.

First, direct switching between the two algorithms is used, this method requires two separate cascaded position observers. When the speed is lower than 200 r/min, the HFFI technique is used and at a higher speed, the back-EMF tracking is used. The FI-SPM motor was accelerated to 3000 r/min in 120 ms. Fig. 6-16 compares the estimated and measured motor speed and position during the acceleration period. At the switching moment, a small error appears between the measured and estimated position (oscillation in the estimated position happens due to swithing the estimated position from the two methods); this will cause a small error in the estimated motor speed.

The direct switching technique requires using two separate observers for the two self-sensing methods. This increases the computational efforts in the DSP. To achieve smooth switching between the two self-sensing algorithms with minimum computational effort in the DSP, the same cascaded tracking position observer structure is used for both HFFI and back-EMF self-sensing. The observer controller will achieve a smooth transition between the two algorithms. The input of the tracking observer is the position error between the estimated and actual rotor position, which is obtained either from the HFFI demodulation process when the speed is less than 200 r/min (high-frequency flux is injected only when the speed is less than 200

r/min), or from the heterodyning process with the estimated back-EMF when the speed is greater than 200 r/min. Fig. 6-17 shows the block diagram of the proposed switching technique. Back EMF tracking self-sensing technique will be used to control the motor when it runs close to 200 r/min.

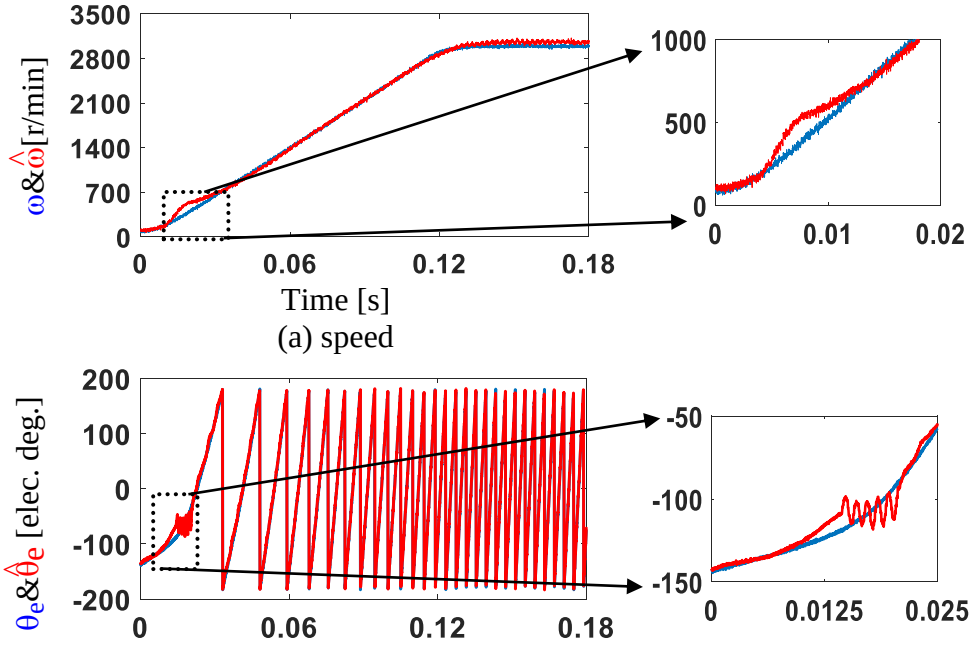

Fig. 6-16 Measured, estimated speed and position during acceleration test using direct switching between HFFI and back-EMF tracking self-sensing

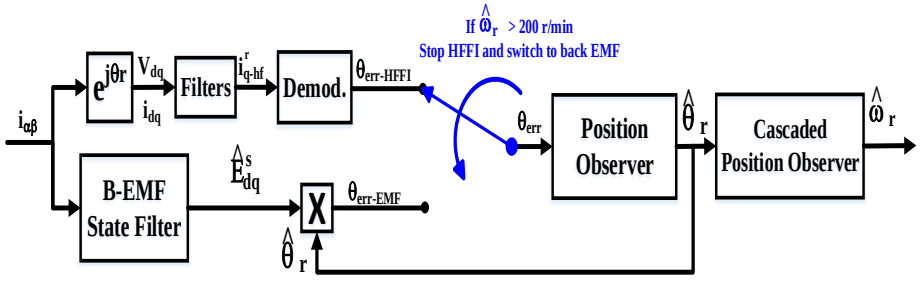

Fig. 6-17 Block diagram of the proposed smooth switching technique between HFFI and back-EMF tracking self -sensing

The same acceleration test using the proposed switching technique is performed. The results of this experiment are shown in Fig. 6-18. The proposed method achieves a smooth transition even during the rapid acceleration operation. Small position error appears during the low-speed operation, which happens due to inverter deadtime and nonlinearity effect.

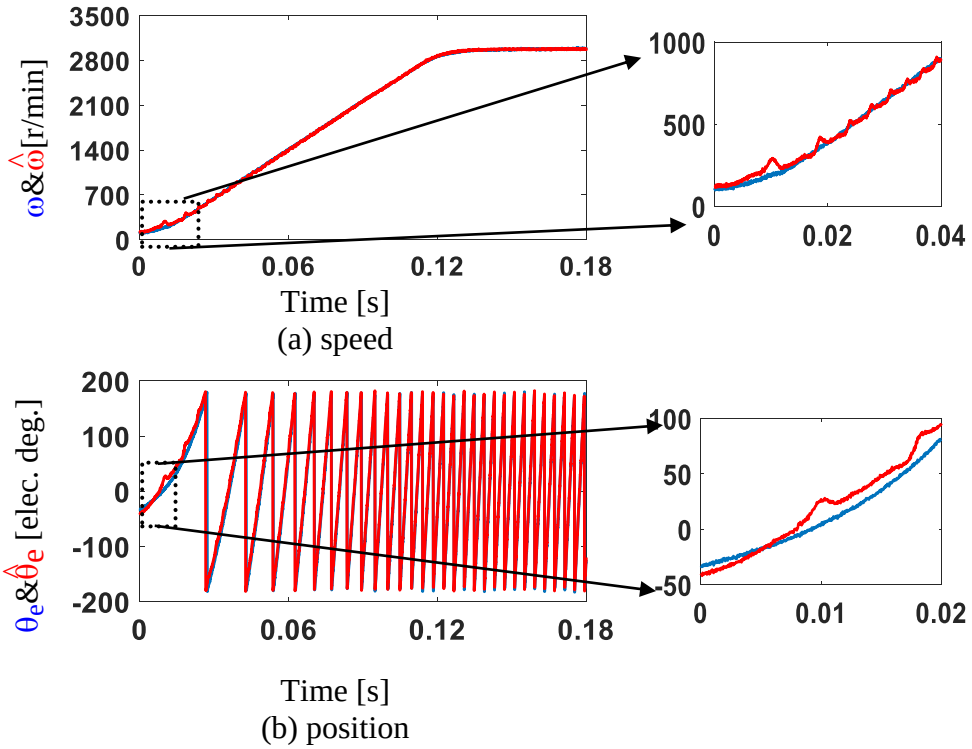

(a) speed

(b) position

Fig. 6-18 Measured, estimated speed and position during acceleration test using the proposed switching method between HFFI and back-EMF tracking self-sensing

The wide-speed range self-sensing algorithm achieved good performance. This algorithm was implemented on the designed FI-SPMSM. This algorithm would also work for the designed FW-SPMSM with enhanced self-sensing properties, and for any PM motor that is suitable for injection-based self-sensing.

6.4 Summary

This chapter presents a wide-speed range self-sensing control algorithm. This algorithm combines both flux injection-based self-sensing control with back-EMF tracking self-sensing control. A methodology for a smooth transition between these two algorithms is presented in this chapter. The key observations and conclusions from this chapter are summarized as follows.

- DB-DTFC provides direct and independent control of the actual motor states, airgap torque and stator flux linkage, allowing the use of the airgap torque to control the motor speed, while the stator flux linkage is a degree of freedom that can be utilized for loss minimization or self-sensing techniques.
- High-frequency injection-based self-sensing with zero torque ripple can be achieved using DB-DTFC. This method is based on injecting a high-frequency flux signal along the torque line using DB-DTFC which inherently has zero torque ripple while enabling estimation of rotor position and speed.
- High-frequency voltage/current injection self-sensing methods with CVCR requires using low pass filter in the measured feedback current to minimize the torque ripple that is caused by the injection. This is an effective technique during steady-state operation. However, this filter limits the dynamic performance of the motor.
- HFFI self-sensing doesn’t require any filters in the feedback signals, which maintain the high dynamic performance of the controller allowing it to be used during rapid servo dynamics. This algorithm is experimentally evaluated in flux intensifying and flux weakening PM motors.

- Wide speed range self-sensing algorithms require combining injection-based and back-EMF tracking techniques. Direct combination requires the use of dual observer structures to estimate the position, which increases the computational efforts. This method also causes undesirable speed and position error during the switching between the two methods.
- The proposed smooth switching method requires the use of only one cascaded observer structure for both self-sensing methods, which reduces the computational efforts. The position error signal, which is the input of the position tracking observer, is switched between the two methods. The observer controller enables a smooth transition between the two self-sensing algorithms.
- The proposed wide-speed range self-sensing algorithm is evaluated on a FI-SPM servo motor. This method achieves good performance during rapid servo dynamics.

Chapter 7 Conclusions, Contributions, and Recommended Future Work

7.1 Research Conclusions

The following list summarizes the key conclusions reached through this research.

7.1.1 Conclusions from review of the state-of-the-art

- FI-IPMSM has attractive self-sensing and dynamic loss minimization capabilities. However, this design has lower peak torque compared to FW-IPMSM.
- Skewing the rotor or stator, PM shifting, or selecting proper slot poles combinations can be utilized to minimize motor cogging and ripple torques.
- FW-SPMSM has an excessively low saliency making it unsuitable for injection based self-sensing.
- SPMSMs with narrow teeth tip or with ringed pole magnet have good self-sensing properties. However, these techniques are not suitable for servo motors.
- DB-DTFC provides independent and direct control of airgap torque and stator flux linkage. The command is achieved in only one switching period.
- The dynamic performance of standard current regulated drives is limited by the current regulator bandwidth.
- Motor stator flux linkage is a degree-of-freedom in servo drives, allowing its utilization for loss minimization or injection-based techniques.
- Self-sensing techniques improve motor reliability by controlling it without a physical position sensor.

- Saliency tracking (injection-based) self-sensing is effective at zero and low-speed operation, while back-EMF tracking is effective at high-speed operation.
- Standard back-to-back dynamometers are useful for evaluating steady-state performance of tested motors.
- Evaluating transient motor loss is not trivial using standard dynamometers.

7.1.2 Conclusions from PM servo motor design for dynamic loss minimization

- A significant amount of energy can be saved if the proposed FI-SPMSM servo design is adopted in high-speed duty cycle servo operations.
- The airgap flux density in the FI-SPMSM is reduced by reducing magnet span, using less magnetic material. This design has an inverted saliency by using q-axis flux barriers.
- FI-SPMSM has an inverted saliency, which is useful for flux boosting during peak torque operation or for injection-based self-sensing control.
- The proposed FI-SPMSM has lower back-EMF compared to the SPMSM. This design requires lower flux weakening current during high-speed operation.
- The designed FI-SPMSM achieves very low iron loss in both stator and rotor compared to the SPMSM and IPMSM designs.
- The designed FI-SPMSM achieves lower magnet eddy current loss compared to the standard SPMSM design.
- FW-SPMSM maximizes airgap flux per magnet volume. This motor is efficient for low-speed high-torque operation.
- FW-SPMSM has high air-gap flux, leading to high iron loss during high-speed operation.

- IPMSM servo motors havelower airgap flux for the same magnet volume compared to SPMSM, due to rotor leakage flux. This motor has higher copper loss, but lower iron loss compared to SPMSM.
- A 10 poles 12 slots configuration, and bread-loaf magnets are used in this research to achieve a sinusoidal back-EMF with low ripple and cogging torques.
- The scalability analyses performed on the FI-SPMSM shows that this design can save energy for both small and large motors.

7.1.3 Conclusions from FW-SPMSM servo motor design with enhanced self-sensing properties

- FW-SPMSMs for servo applications can be designed with shifted ring magnets or through shaping the magnets to achieve the desired ripple and cogging torques.
- FW-SPMSMs for servo applications with shifted PM's require special mechanical rotor design to move the center-of-mass back to the center of rotation.
- The designed FW-SPMSM with symmetrical rotor achieves low losses in servo applications that run at low-speed and high-torque.
- The designed FW-SPMSM with symmetrical rotor has an attractive self-sensing feature. The motor saliency ratio improves with load, allowing the use of self-sensing techniques even at overload conditions.
- Adding d-axis flux barriers with FW-SPMSM symmetric rotors helps in creating a non-degrading saliency ratio with load variations.
- Adding small iron notches between adjacent magnets slightly increases leakage flux and reduces motor torque. However, it significantly improves motor saliency.

- Using large d-axis flux barriers leads to saturation of the main flux path with increasing motor saliency. However, this reduces motor torque production.
- Bread-loaf magnets are thinner at the edges compared to the center. Demagnetization risk in these magnets needs to be evaluated when injecting q-axis current.
- The designed FW-SPMSM with symmetrical rotor achieves lower losses in the rotor, stator, and magnet compared to the designed FW-SPMSM with asymmetrical rotor.
- Scalability analysis showed superior self-sensing properties and power conversion performance of the designed FW-SPMSM with symmetrical rotor compared to asymmetric rotor. This is valid for small and large servo motors.
- Experimental evaluation of the fabricated FW-SPMSM prototypes using symmetrical and asymmetrical rotors showed the sensitivity of the asymmetrical rotor design to manufacturing tolerance, in which perfect harmonic cancellation is not achieved leading to higher back-EMF secondary harmonics, cogging and ripple torques.

7.1.4 Conclusions from dynamic shaft torque observer and transient loss measurements

- Accurate transient loss measurements require estimating motor dynamic torque including the inertial torque component.
- Standard dynamometer torque sensors measure windup shaft torque signal. This signal can be used to measure motor steady-state loss.
- The inertial torque component becomes significant during transient speed operation.
- The inertial torque can theoretically be calculated by multiplying motor inertia with rotor acceleration, which requires a rotary angular acceleration sensor which is unavailable in the market.

- The constructed shaft torque observer emulates the mechanical dynamometer physical model. This observer works with standard dynamometer sensors.
- The constructed shaft torque observer is capable of estimating shaft torque components including inertial torque with high fidelity.

7.1.5 Conclusions from dynamic loss minimizing control of PM servo motors operating even at the voltage limit

- The MTPA technique is an effective way to reduce motor copper losses, while MTPV is a good way to minimize motor iron loss.
- Standard loss minimization techniques with CVCR are based on manipulating d-axis current to reduce motor loss, affecting drive torque dynamics degrading servo motor performance.
- DB-DTFC provides naturally decoupled torque and flux dynamics. Allowing stator flux linkage to be used as a degree-of-freedom to minimize motor losses without affecting motor torque dynamics.
- Accurate iron loss estimation requires accurate estimation of motor stator flux linkage, which can be estimated from the flux observer.
- LMC-DB-DTFC is a model-based loss minimization technique. This algorithm selects a feasible optimum stator flux linkage to minimize total motor loss.
- LMC-DB-DTFC can be used to minimize copper loss (MTPA), in which the flux linkage minimizing motor current will be selected.
- LMC-DB-DTFC operates every switching period. This technique is effective during both steady-state and transient speed operation.

- Using a simple and accurate flux linkage-based loss model and bounding the volt-sec domain to the feasible range allows running the LMC-DB-DTFC in real-time.
- LMC-DB-DTFC operated even at the voltage limit during flux weakening operation, without sacrificing drive torque dynamics.
- The proposed LMC-DB-DTFC and DB-DTFC algorithms are not affected by unmodeled motor cross-saturation, due to estimation of the stator flux linkage from motor voltage during medium and high-speed operation.
- MRAC technique can be used to estimate the motor synchronous reference frame inductance online through forcing the current model flux observer to track the voltage model flux observer during high-speed operation.

7.1.6 Conclusions from wide speed range self-sensing control for PM servo motor

- Injection-based self-sensing control is an effective way to control salient motors at zero and low speed by exciting the motor saliency with a high-frequency signal and estimating the rotor position from the measured motor signals.
- A high-frequency voltage signal is usually injected with CVCR. Rotor position and speed are then estimated from the measured motor current. This method will cause an extra torque ripple to the drive due to cross-coupling between the d and q axes.
- Injection-based self-sensing with zero torque ripple can be achieved using DB-DTFC, in which a high-frequency flux is injected along the torque line.
- Inverter deadtime and non-linearity significantly affect the accuracy of self-sensing at very low speed.

- The maximum achievable motion controller bandwidth is limited by the saliency-tracking observer bandwidth.
- The saliency-tracking observer bandwidth depends on the signal-to-noise ratio level of extracted spatial information from measured current.
- The designed FI-SPMSM has a small detectable saliency that is fixed with load variations, allowing the self-sensing control of this motor without the need for lookup tables with high dynamic performance.
- The designed FW-SPMSM with symmetrical rotor has a small saliency that improves with load. This allows controlling the motor in self-sensing control even at overload conditions with high dynamic performance.
- Back-EMF is an effective way to control the motor at medium and high-speed operation. This technique doesn't require any high-frequency signal injection.
- Controlling the motor in a wide speed range in self-sensing mode requires combining both HFFI and back-EMF tracking algorithms.
- Direct switching the estimated position from HFFI to the estimated position from back-EMF tracking leads to a significant error in estimated speed and position.
- The proposed methodology for a smooth transition between HFFI and back-EMF tracking requires low computational efforts in the DSP.
- The proposed smooth transition technique uses the same cascaded observer for both HFFI and back-EMF tracking. The estimated position error is switched between the 2 algorithms. The observer controller achieves the smooth transition.

7.2 Research Contributions

The following list summarizes the key contributions made by this research.

7.2.1 Contributions in high-performance servo motor design methodology for dynamic loss minimization performance

- Developed a methodology to design FI-SPMSM for servo applications, using less magnetic material, with enhanced dynamic loss minimization and self-sensing capabilities.
- Developed a servo cycle methodology that can be used to systematically evaluate servo motor designs for loss minimization capability.
- Used the developed test cycle methodology to experimentally identify differences between the designed SPMSM, IPMSM, and FI-SPMSM servo motors.
- Investigated and evaluated the loss distribution inside the three motors.
- Investigated and evaluated the scaled motors performance, including both dynamic loss minimization performance and self-sensing properties.

7.2.2 Contributions in high-performance FW-SPMSM design methodology for servo applications with enhanced self-sensing properties

- Developed a methodology to design FW-SPMSMs with a symmetrical rotor, with attractive self-sensing features and low losses for high-torque servo applications.
- Developed a methodology and guidelines to design d-axis flux barriers and iron notches to enhance the self-sensing properties of the FW-SPMSM.

- A genetic algorithm based multi-objective optimization methodology has been adapted to bread-loaf symmetric FW-SPMSM for servo applications.
- Identified and quantified the self-sensing properties and power conversion performance of the designed FW-SPMSM with asymmetrical rotor structure.
- The motor losses and loss distribution for the designed FW-SPMSM using symmetrical and asymmetrical rotors have been identified and evaluated.
- Investigated and evaluated the performance of the scaled FW-SPMSMs for servo applications designed with symmetrical and asymmetrical rotors.

7.2.3 Contributions from the dynamic shaft torque estimation and transient loss measurements methodologies

- Developed a methodology to design an observer to estimate the shaft torque quantities, enabling accurate transient loss measurements.
- Proposed a methodology to model the mechanical connection for the testing dynamometer including the shaft couplings and the torque sensor.
- Proposed a cascaded observer structure, allowing the use of the proposed shaft torque observer structure with low-resolution position sensors.
- Experimentally identified accuracy limitations of the proposed observer in estimating the dynamic shaft torque during both steady-state and transient speed operations.
- Identified parameter sensitivity limitations of the proposed observer using experiments and simulation.

7.2.4 Contributions from the dynamic loss minimization control with DB-DTFC methodology

- Developed a methodology to minimize total motor loss dynamically, without affecting the drive torque dynamics. This algorithm operates even at the voltage limit.
- Proposed a simple and accurate loss model that is based on a methodology for identifying the effective elements of existing loss models for PM motors.
- Identified the limitations of the proposed LMC-DB-DTFC in several servo motors using the developed servo cycles.
- Developed a methodology to online estimate the PM motor d and q axis inductance using the MRAC technique.
- Identified and evaluated the performance of the developed LMC-DB-DTFC control algorithm with cross-saturated PM motors.

7.2.5 Contributions from the methodology for wide speed range self-sensing control for PM servo motors

- Developed a methodology for injection-based self-sensing control with zero torque ripple, through injecting a high-frequency flux with DB-DTFC.
- Experimentally identified the steady-state and dynamic performance of the developed HFFI self-sensing algorithm on flux intensifying and flux weakening PM motors.
- Developed a methodology for smooth switching between injection-based and back-EMF tracking self-sensing techniques, with low computational efforts inside the DSP.
- Identified the limitations of existing voltage injection self-sensing techniques. These techniques achieve limited dynamic performance.

7.3 Recommended Future Work

Following the research that has been done, the recommended future work is presented.

- **Evaluate and extend the proposed FI-SPMSM design methodology for different slot-pole combinations, different winding configuration, and different magnetic material**

The FI-SPMSM design methodology proposed in chapter 2 of this thesis was verified in a 10 poles 12 slots concentric winding configuration using neodymium iron boron. There is an opportunity to extend this methodology for motors designed using different magnetic materials like ferrite magnets, different winding types like distributed windings and different slot-pole combinations.

- **Evaluate and extend the proposed FW-SPMSM with enhanced self-sensing properties design methodology for different slot-pole combinations and for different winding configuration**

The FW-SPMSM with enhanced self-sensing properties design methodology proposed in chapter 3 of this thesis was verified in an 8 poles 24 slots distributed winding configuration using neodymium iron boron magnets. There is an opportunity to extend this methodology for motors designed using different magnetic materials like ferrite magnets, different winding types like concentric windings and different slot-pole combinations.

- **Improve the disturbance rejection response of the proposed HFFI self-sensing algorithm.**

The results presented in chapter 6 show the effectiveness of the proposed self-sensing algorithm. However, the disturbance rejection of this algorithm will be lower than the encoder

case, due to the filters used to extract spatial information from the measured current. This would limit the amount of applied torque at low speed when the HFFI self-sensing is used. It is an opportunity to combine disturbance input decoupling (DID) techniques with the proposed self-sensing algorithm. This requires constructing disturbance observers with adequate bandwidth to estimate the disturbance then decouple it.

- **Improve the proposed self-sensing algorithm estimation accuracy**

The self-sensing algorithm proposed in Chapter 6 of this thesis showed good dynamic performance even during rapid acceleration which is essential for servo motors. However, a small positional error occurred, which is not acceptable for high precision servo applications. There is an opportunity to develop techniques to enhance self-sensing estimation accuracy like decoupling this error using predefined lookup tables or adopting image tracking self-sensing techniques.

- **Integrate volt-sec sensor into the servo drive system**

The performance of the self-sensing algorithm presented in chapter 6 of this thesis degrades at very low speed due to inverter non-linearity and deadtime that causes a volt-sec error between the actual and commanded inverter volt-sec. Performance can be improved by adding a volt-sec sensor to measure the inverter output volt-sec and use it in the developed self-sensing algorithm.

Volt-sec sensor will also be useful to reduce flux observer bandwidth, in which the voltage model flux estimates will dominate the closed loop flux observer estimation at low-speed. This would reduce the sensitivity of the developed LMC-DB-DTFC algorithm to the estimated motor inductance during low-speed operation.

- **Develop a methodology to online estimate motor resistance and integrate it with the developed LMC-DB-DTFC algorithm**

The flux linkage-based loss model developed in chapter 5 models both copper and iron loss. The accuracy of copper loss estimation depends on estimated motor resistance which changes with temperature. There is an opportunity to develop a technique to online estimate the motor resistance and integrate it with the developed loss model. This will improve the accuracy of this loss model leading to reduced sensitivity of the developed LMC-DB-DTFC to estimated motor resistance.

References

[1] N. Mohan, T. Undeland and W. Robbins, Power electronics. New Delhi, India: Wiley India, 2007.

[2] T. Finken, M. Felden and K. Hameyer, "Comparison and design of different electrical machine types regarding their applicability in hybrid electrical vehicles," in *Proc. of the 18th International Conference on Electrical Machines, 2008 (ICEM 2008)*, Vilamoura, 2008, pp. 1-5.

[3] R.H. Staunton, S.C. Nelson, P.J. Otaduy, J.W. McKeever, J.M. Bailey, S. Das, R.L. Smith, "PM Motor Paramteric Design Analyses for a Hybrid Electric Vehicle Traction Application Drive", Oak Ridge National Laboratory Report, Sep 2004.

[4] Hendershot and T. Miller, Design of brushless permanent-magnet motors. Venice: Motor Design Books, 2010.

[5] A.M. EL-Refaie, "High Speed Operation of Permannet Magnet Machines," in Dept. of Electrical and Computer Engineering. vol. Ph.D. Dissertation: University of Wisconsin-Madison, 2005.

[6] E. C. Lovelace, "Optimization of Magnetically Saturable Interiror Permanent-Magnet Synchronous Machine Drive," in Dept. of Electrical and Computer Engineering. vol. Ph.D. Dissertation: Massachusetts Institute of Technology, 2000.

[7] K. Yamazaki, Y. Fukushima, and M. Sato, "Loss Analysis of Permanent-Magnet Motors With Concentrated Windings-Variation of Magnet Eddy-Current Loss Due to Stator and Rotor Shapes," Industry Applications, IEEE Transactions on, vol. 45, pp. 1334-1342, 2009.

[8] S. C. Yang, "Position Sensing of Surface Permanent Magnet Machine Using High Freuqncy Signal Injection," in Dept. of Mechanical Engineering. vol. Ph.D. Dissertation: University of Wisconsin-Madison, 2011.

[9] T. M. Jahns and W. L. Soong, "Pulsating torque minimization techniques for permanent magnet AC motor drives-a review," in IEEE Transactions on Industrial Electronics, vol. 43, no. 2, pp. 321-330, Apr 1996.

[10] S. Ruangsinchaiwanich, Z. Q. Zhu and D. Howe, "Influence of magnet shape on cogging torque and back-emf waveform in permanent magnet machines," 2005 International Conference on Electrical Machines and Systems, 2005, pp. 284-289 Vol. 1.

[11] N. Bianchi and S. Bolognani, "Design techniques for reducing the cogging torque in surface-mounted PM motors," in IEEE Transactions on Industry Applications, vol. 38, no. 5, pp. 1259-1265, Sep/Oct 2002.

[12] S. Huang, G. Wang, J. Gao, K. Huang and T. Liu, "Optimization design of permanent magnet synchronous servo motor with new high dynamic performance," *2011 International Conference on Electrical Machines and Systems*, Beijing, 2011, pp. 1-5.

[13] S. Shah, T. Lipo and B. Kwon, "Modeling of Novel Permanent Magnet Pole Shape SPM Motor for Reducing Torque Pulsation", IEEE Transactions on Magnetics, vol. 48, no. 11, pp. 4626-4629, 2012.

[14] Wenliang Zhao, T. Lipo and Byung-Il Kwon, "Material-Efficient Permanent-Magnet Shape for Torque Pulsation Minimization in SPM Motors for Automotive

Applications", IEEE Transactions on Industrial Electronics, vol. 61, no. 10, pp. 5779-5787, 2014.

[15] R. Islam, I. Husain, A. Fardoun and K. McLaughlin, "Permanent-Magnet Synchronous Motor Magnet Designs With Skewing for Torque Ripple and Cogging Torque Reduction," in IEEE Transactions on Industry Applications, vol. 45, no. 1, pp. 152-160, Jan.-feb. 2009.

[16] Y. Li, D. Bobba and B. Sarlioglu, "A Novel 6/4 Flux-Switching Permanent Magnet Machine Designed for High-Speed Operations," in *IEEE Transactions on Magnetics*, vol. 52, no. 8, pp. 1-9, Aug. 2016.

[17] T. Jahns and W. Soong, "Pulsating torque minimization techniques for permanent magnet AC motor drives-a review", IEEE Transactions on Industrial Electronics, vol. 43, no. 2, pp. 321-330, 1996.

[18] D. C. Hanselman, Brushless Permanent Magnet Motor Design, 2nd ed. New York: McGraw-Hill, 2003.

[19] A. Pouramin, R. Dutta and M. F. Rahman, "Preliminary study on differences in the performance characteristics of concentrated and distributed winding IPM machines with different rotor topologies," *2017 IEEE Energy Conversion Congress and Exposition (ECCE)*, Cincinnati, OH, 2017, pp. 3565-3570.

[20] G. Slemon, "Electrical machines for variable-frequency drives", Proceedings of the IEEE, vol. 82, no. 8, pp. 1123-1139, 1994.

[21] D. Hanselman, Brushless permanent magnet motor design. Lebanon, Ohio: Magna Physics Publishing, 2006.

[22] Z. Q. Zhu, D. Howe, and C. C. Chan, "Improved analytical model for predicting the magnetic field distribution in brushless permanent-magnet machines," *Magnetics, IEEE Transactions on*, vol. 38, pp. 229-238, 2002.

[23] A. EL-Refaie, "Fractional-Slot Concentrated-Windings Synchronous Permanent Magnet Machines: Opportunities and Challenges", IEEE Transactions on Industrial Electronics, vol. 57, no. 1, pp. 107-121, 2010.

[24] Y. Asano, Y. Honda, H. Murakami, Y. Takeda, and S. Morimoto, "Novel noise improvement technique for a PMSM with concentrated winding," in *Power Conversion Conference, 2002. PCC Osaka 2002. Proceedings of the*, 2002, pp. 460-465 vol.2.

[25] F. Magnussen and C. Sadarangani, "Winding factors and Joule losses of permanent magnet machines with concentrated windings," in Electric Machines and Drives Conference, 2003. IEMDC'03. IEEE International, 2003, pp. 333-339 vol.1

[26] A. G. Jack, B. C. Mecrow, P. G. Dickinson, D. Stephenson, J. S. Burdess, N. Fawcett, and J. T. Evans, "Permanent-magnet machines with powdered iron cores and prepressed windings," *Industry Applications, IEEE Transactions on*, vol. 36, pp. 1077-1084, 2000.

[27] H. Akita, Y. Nakahara, N. Miyake, and T. Oikawa, "New core structure and manufacturing method for high efficiency of permanent magnet motors," in Industry Applications Conference, 2003. 38th IAS Annual Meeting. Conference Record of the, 2003, pp. 367-372 vol.1.

[28] J. Cros and P. Viarouge, "Synthesis of high performance PM motors with concentrated windings," Energy conversion, IEEE transactions on, vol. 17, pp. 248-253, 2002.

[29] N. Bianchi, S. Bolognani, and M. Dai Pre, "Magnetic Loading of Fractional-Slot Three-Phase PM Motors With Nonoverlapped Coils," *Industry Applications, IEEE Transactions on,* vol. 44, pp. 1513-1521, 2008.

[30] N. Bianchi, S. Bolognani, M. D. Pre, and G. Grezzani, "Design considerations for fractional-slot winding configurations of synchronous machines," *Industry Applications, IEEE Transactions on,* vol. 42, pp. 997-1006, 2006.

[31] D. Ishak, Z. Q. Zhu, and D. Howe, "Permanent-magnet brushless machines with unequal tooth widths and similar slot and pole numbers," *Industry Applications, IEEE Transactions on,* vol. 41, pp. 584-590, 2005.

[32] M. R. Shah and A. M. El-Refaie, "End Effects in Multiphase Fractional Slot Concentrated-Winding Surface Permanent Magnet Synchronous Machines," *Energy Conversion, IEEE Transactions on,* vol. 25, pp. 1001-1009, 2010.

[33] P. B. Reddy, T. M. Jahns, and A. M. El-Refaie, "Impact of Winding Layer Number and Slot/Pole Combination on AC Armature Losses of Synchronous Surface PM Machines Designed for Wide Constant-Power Speed Range Operation," in *Industry Applications Society Annual Meeting, 2008. IAS '08. IEEE,* 2008, pp. 1-8.

[34] Z. Q. Zhu, Z. P. Xia, L. J. Wu, and G. W. Jewell, "Influence of slot and pole number combination on radial force and vibration modes in fractional slot PM brushless machines having single- and double-layer windings," in *Energy Conversion Congress and Exposition, 2009. ECCE 2009. IEEE,* pp. 3443-3450.

[35] S. Yang, T. Suzuki, R. Lorenz and T. Jahns, "Surface-Permanent-Magnet Synchronous Machine Design for Saliency-Tracking Self-Sensing Position Estimation at Zero and Low Speeds", IEEE Transactions on Industry Applications, vol. 47, no. 5, pp. 2103-2116, 2011.

[36] S. G. Min and B. Sarlioglu, "Modeling and Investigation on Electromagnetic Noise in PM Motors With Single- and Double-Layer Concentrated Winding for EV and HEV Application," in IEEE Transactions on Transportation Electrification, vol. 4, no. 1, pp. 292-302, March 2018.

[37] N. Limsuwan, "Field Intensifying Interior Permanent Magnet Synchronous Machines for Power Conversion and Self-Sensing Control," in Dept. of Electrical and Computer Engineering. vol. MS Thesis: University of Wisconsin-Madison, 2009.

[38] N. Limsuwan, "Concurrent Design of FI-FPM Machines for Self-Sensing and Electromechanical Power Conversion," in Dept. of Electrical and Computer Engineering. vol. Ph.D. Dissertation: University of Wisconsin-Madison, 2013.

[39] N. Limsuwan, Y. Shibukawa, D. Reigosa and R. Lorenz, "Novel Design of Flux-Intensifying Interior Permanent Magnet Synchronous Machine Suitable for Self-Sensing Control at Very Low Speed and Power Conversion", IEEE Transactions on Industry Applications, vol. 47, no. 5, pp. 2004-2012, 2011.

[40] M.H.A. Prins, C.W. Vorster, M.J. Kamper, "Reluctance synchronous and field intensified-PM motors for variable-gear electric vehicle drives," 2013 IEEE Energy Conversion Congress and Exposition, Denver, CO, 2013, pp. 657-664.

[41] B. Yan, X. Zhu, L. Chen, "Design and evaluation of a new flux-intensifying permanent magnet brushless motor," 2014 17th International Conference on Electrical Machines and Systems (ICEMS), Hangzhou, 2014, pp. 673-677.

[42] N. Limsuwan, T. Kato, K. Akatsu, R.D. Lorenz, "Design and Evaluation of a Variable-Flux Flux-Intensifying Interior Permanent-Magnet Machine," in IEEE Transactions on Industry Applications, vol. 50, no. 2, pp. 1015-1024, March-April 2014.

[43] A. Athavale, K. Sasaki, B. Gagas, T. Kato and R. Lorenz, "Variable Flux Permanent Magnet Synchronous Machine (VF-PMSM) Design Methodologies to Meet Electric Vehicle Traction Requirements with Reduced Losses", IEEE Transactions on Industry Applications, vol. 53, no. 5, pp. 4318-4326, 2017.

[44] M. Ibrahim, L. Masisi, P. Pillay, "Design of Variable-Flux Permanent-Magnet Machines Using Alnico Magnets," in IEEE Transactions on Industry Applications, vol. 51, no. 6, pp. 4482-4491, Nov.-Dec. 2015.

[45] B.S. Gagas, K. Sasaki, T. Fukushige, A. Athavale, T. Kato, R.D. Lorenz, "Analysis of Magnetizing Trajectories for Variable Flux PM Synchronous Machines Considering Voltage, High-Speed Capability, Torque Ripple, and Time Duration," in IEEE Transactions on Industry Applications, vol. 52, no. 5, pp. 4029-4038, Sept.-Oct. 2016.

[46] I.P. Brown, "Design Rules For Induction Machine Self-Sensing," Ph.D. Dissertation, University of Wisconsin-Madison, Madison, 2009.

[47] I.P. Brown, R.D. Lorenz, "Response Surface Methodologies for the Design of Induction Machine Self-Sensing Rotor Position Saliencies," International Conference on Electrical Machines and Systems, ICEMS., Seoul, 2007, pp. 1354-1359.

[48] I.P. Brown, R.D. Lorenz, "Induction Machine Design Methodology for Self-Sensing: Balancing Saliencies and Power Conversion Properties", IEEE Trans. on Ind. Appl., Vol. 47, No. 1, pp. 79-87, 2011.

[49] J. Cilia, G.M. Asher, K.J. Bradley, M. Sumner, "Sensorless Position Detection for Vector-Controlled Induction Motor drives Using an Asymmetric Outer-Section Cage," IEEE Trans. on Ind. Appl., Vol. 33, pp. 1162-1169, 1997.

[50] N. Bianchi, S. Bolognani, J.-H. Jang, and S.-K. Sul, "Comparison of PM Motor Structures and Sensorless Control Techniques for Zero-Speed Rotor Position Detection," Power Electronics, IEEE Transactions on, vol. 22, pp. 2466-2475, 2007.

[51] A. Faggion, N. Bianchi and S. Bolognani, "Ringed-Pole Permanent-Magnet Synchronous Motor for Position Sensorless Drives," in *IEEE Transactions on Industry Applications*, vol. 47, no. 4, pp. 1759-1766, July-Aug. 2011.

[52] N. Bianchi, S. Bolognani, and A. Faggion, "A ringed-pole SPM motor for sensorless drives - electromagnetic analysis, prototyping and tests," in Industrial Electronics (ISIE), 2010 IEEE International Symposium on, 2010, pp. 1193-1198.

[53] N. Bianchi, S. Bolognani, and A. Faggion, "Rotor design arrangement of SPM motors for the sensorless control at low speed and standstill," in Power Electronics and Motion Control Conference (EPE/PEMC), 2010 14th International, 2010, pp. S1-23-S1-28.

[54] T. A. Nondahl, C. Ray, P. B. Schmidt, and M. L. Gasperi, "A permanent-magnet rotor containing an electrical winding to improve detection of rotor angular position," Industry Applications, IEEE Transactions on, vol. 35, pp. 819-824, 1999.

[55] E.G.Strangas, "Notes for an Introductory Course on Electrical Machines and Drives," MSU Electrical Machines and Drives Laboratory.

[56] G.J. Banos, "Predictive Controller for PMSM Drive," Master Thesis, Department of Energy Technology, Aalborg University, June 2013.

[57] D. Novotny and T. Lipo, Vector control and dynamics of AC drives. Oxford: Clarendon Press, 2005.

[58] F. Briz, M. W. Degner and R. D. Lorenz, "Analysis and design of current regulators using complex vectors," in *IEEE Transactions on Industry Applications*, vol. 36, no. 3, pp. 817-825, May 2000.

[59] H. Kim, M. W. Degner, J. M. Guerrero, F. Briz and R. D. Lorenz, "Discrete-Time Current Regulator Design for AC Machine Drives," in *IEEE Transactions on Industry Applications*, vol. 46, no. 4, pp. 1425-1435, Jul 2010.

[60] B. H. Kenny, "Deadbeat direct torque control of induction machines using self-sensing at low and zero speed," University of Wisconsin--Madison, 2001., 2001, pp. x, 274 p

[61] R. D. Lorenz, "The emerging role of dead-beat, direct torque and flux control in the future of induction machine drives," in *Proc. of Optimization of Electrical and Electronic Equipment, 2008. OPTIM 2008. 11th International Conference on*, pp. XIX-XXVII.

[62] N. T. West and R. D. Lorenz, "Digital Implementation of Stator and Rotor Flux-Linkage Observers and a Stator-Current Observer for Deadbeat Direct Torque Control of Induction Machines," *Industry Applications, IEEE Transactions on*, vol. 45, pp. 729-736, 2009

[63] J. S. Lee, "Deadbeat Direct Torque & Flux control for Interior Permanent Magnet Synchronous Machines," Master's thesis, University of Wisconsin - Madison, 2009.

[64] T. R. Obermann, Z. D. Hurst, and R. D. Lorenz, "Deadbeat-direct torque & flux control motor drive over a wide speed, torque and flux operating space using a single control law," in *Proc. of Energy Conversion Congress and Exposition (ECCE), 2010 IEEE*, pp. 215-222

[65] J. S. Lee, C. Chan-Hee, S. Jul-Ki, R. D. Lorenz, "Deadbeat direct torque and flux control of interior permanent magnet machines with discrete time stator current and stator flux linkage observer," *in Energy Conversion Congress and Exposition. ECCE. IEEE*, 2009, pp. 2504-2511.

[66] T. R. Obermann, Z. D. Hurst, B. F. Bradley, and R. D. Lorenz, "Deadbeat-direct torque and flux control motor drive using a single control law to minimize motor losses," in *Proc. of Electrical Machines and Systems (ICEMS), 2010 International Conference on*, pp. 742-747

[67] W. Xu, "Dynamic loss Modeling for Loss Minimizing Control of IPMSM using DB-DTFC not Operating in Voltage or Current Limits," in Dept. of Mechanical Engineering. vol. Ph.D. Dissertation: University of Wisconsin-Madison, 2013.

[68] Y. Wang, H. Flieh, S. C. Lee and R.D. Lorenz, "Implementation issues and performance evaluation of deadbeat-direct torque and flux control drives," 2015 IEEE International Electric Machines & Drives Conference (IEMDC), Coeur d'Alene, ID, 2015, pp. 953-959.

[69] Y. Wang, "Deadbeat - Direct Torque and Flux Control Drives for High Power Applications using Low Switching Frequency Multi-level Inverters," in Dept. of Mechanical Engineering. vol. Ph.D. Dissertation: University of Wisconsin-Madison, 2016.

[70] H. Flieh, "Self-Sensing Deadbeat Direct Torque and Flux Control for Surface Mount Permanent Magnet Synchronous Machine," in Dept. of Electrical and Computer Engineering. vol. MS Thesis: University of Oviedo, 2014.

[71] C. Bouxsein, "Injection-Based Self-Sensing with Deadbeat-Direct Torque and Flux Control for Surface-Mounted PM Synchronous Machines," in Dept. of Mechancial Engineering . vol. MS Thesis: University of Wisconsin-Madison, 2015.

[72] F. Quattrone, "Dynamic Modeling of Losses in electric machines for active loss control," Master of Science thesis, Leibniz University Hannover, June, 2011.

[73] JMAG Corporation, "19 - Analysis of the Centrifugal Force in an IPM motor: Application Catalog", Jmag-international.com, 2016. [Online]. Available: http://www.jmag-nternational.com/catalog/19_IPMMotor_CentrifugalForce.html.

[74] A.M. Bazzi and P.T. Krein, "A survey of real-time power-loss minimizers for induction motors," in Electric Ship Technologies Symposium, 2009. ESTS 2009. IEEE, 2009, pp. 98-106.

[75] S. Vaez, V.I. John and M.A. Rahman, "Adaptive loss minimization control of inverter-fed IPM motor drives," in Power Electronics Specialists Conference, 1997. PESC '97 Record., 28th Annual IEEE, 1997, pp. 861-868 vol.2.

[76] D.S. Reay, C. Shang and B.W. Williams, "Efficiency improvements in switched reluctance motor position and torque control using adaptive fuzzy systems," in Fuzzy Systems, 1996., Proceedings of the Fifth IEEE International Conference on, 1996, pp. 800-805 vol.2.

[77] A.M. Bazzi and P.T. Krein, "Review of methods for real-time loss minimization in induction machines," Industry Applications, IEEE Transactions on, vol. 46, no. 6, pp. 2319-2328 2010.

[78] S. Morimoto, Y. Takeda, T. Hirasa and K. Taniguchi, "Expansion of operating limits for permanent magnet motor by current vector control considering inverter capacity," in *IEEE Transactions on Industry Applications*, vol. 26, no. 5, pp. 866-871, Sep/Oct 1990.

[79] P.M. Johnson, K. Bai and X. Ding, "Back-EMF-Based Sensorless Control Using the Hijacker Algorithm for Full Speed Range of the Motor Drive in Electrified Automobile Systems," in IEEE Transactions on Transportation Electrification, vol. 1, no. 2, pp. 126-137, Aug. 2015.

[80] S. Morimoto, K. Kawamoto, M. Sanada and Y. Takeda, "Sensorless control strategy for salient-pole PMSM based on extended EMF in rotating reference frame", IEEE Transactions on Industry Applications, vol. 38, no. 4, pp. 1054-1061, 2002.

[81] R. Hejny and R. Lorenz, "Evaluating the Practical Low-Speed Limits for Back-EMF Tracking-Based Sensorless Speed Control Using Drive Stiffness as a Key Metric", IEEE Transactions on Industry Applications, vol. 47, no. 3, pp. 1337-1343, 2011.

[82] F. Genduso, R. Miceli, C. Rando and G. R. Galluzzo, "Back EMF Sensorless-Control Algorithm for High-Dynamic Performance PMSM," in *IEEE Transactions on Industrial Electronics*, vol. 57, no. 6, pp. 2092-2100, June 2010.

[83] Hyunbae Kim, Sungmo Yi, Namsu Kim and R. D. Lorenz, "Using low resolution position sensors in bumpless position/speed estimation methods for low cost PMSM

drives," *Fourtieth IAS Annual Meeting. Conference Record of the 2005 Industry Applications Conference, 2005.*, 2005, pp. 2518-2525 Vol. 4.

[84] Y. Wang and R. D. Lorenz, "Using Volt-sec. sensing to extend the low speed range and the disturbance rejection capability of back-EMF-based self-sensing," *2016 18th European Conference on Power Electronics and Applications (EPE'16 ECCE Europe)*, Karlsruhe, 2016, pp. 1-10.

[85] F. Phlippen, "Position Estimation in PM Synchronous Machines using Signle Saliency-Tracking, Self-Sensing Methods," in Dept. of Electrical and Computer Engineering. vol. Diplomarbeit: University of Wisconsin-Madison, 1998.

[86] A. Consoli, G. Scarcella, and A. Testa, "Industry application of zero-speed sensorless control techniques for PM synchronous motors," IEEE Trans. Ind. Appl., vol. 37, pp. 513 – 521, March-April 2001.

[87] S. Shinnaka, "New 'mirror-phase vector control' for sensorless drive of permanentmagnet synchronous motor with pole saliency," IEEE Trans. on Ind. Appl., vol. 40, pp. 599-606, March-April 2004.

[88] N. Teske, "Sensorless position control of induction machines using high frequency signal injection," Ph.D. Dissertation, University of Nottingham, 2001.

[89] M.W. Degner and R.D. Lorenz, "Position estimation in induction machines utilizing rotor bar slot harmonics and carrier-frequency.

[90] S. Kim and S. Sul, 'Sensorless control of AC motor—Where are we now?', pp. 1--6, 2011.

[91] G. Zhang, G. Wang and D. Xu, "Saliency-based position sensorless control methods for PMSM drives - A review," in Chinese Journal of Electrical Engineering, vol. 3, no. 2, pp. 14-23, September 2017.

[92] S. Yang and R. Lorenz, 'Surface Permanent-Magnet Machine Self-Sensing at Zero and Low Speeds Using Improved Observer for Position, Velocity, and Disturbance Torque Estimation', Industry Applications, IEEE Transactions on, vol 48, iss 1, pp. 151--160, 2012.

[93] C. Choi and J. Seok, 'Pulsating signal injection-based axis switching sensorless control of surface-mounted permanent-magnet motors for minimal zero-current clamping effects', Industry Applications, IEEE Transactions on, vol 44, iss 6, pp. 1741--1748, 2008.

[94] C. Yu, J. Tamura, D. Reigosa and R. Lorenz, 'Position self-sensing evaluation of a FI-IPMSM based on high frequency signal injection methods', pp. 3029--3036, 2011.

[95] D. Kim, Y. C. Kwon, S. K. Sul, J. H. Kim and R. S. Yu, "Suppression of Injection Voltage Disturbance for High-Frequency Square-Wave Injection Sensorless Drive With Regulation of Induced High-Frequency Current Ripple," in *IEEE Transactions on Industry Applications*, vol. 52, no. 1, pp. 302-312, Jan.-Feb. 2016.

[96] Engineering Manual Model 1800 In-line Torque Sensor, Rev. A, Honeywell,MN 2012.

[97] H. Zhao and H. Feng, "A Novel Angular Acceleration Sensor Based on the Electromagnetic Induction Principle and Investigation of Its Calibration Tests", Sensors, vol. 13, no. 12, pp. 10370-10385, 2013.

[98] Schicker, Rainer, and Georg Wegener. Measuring Torque Correctly. 1st ed. Bielefeld: Hottinger Baldwin Messtechnik, 2002. Print.

[99] G. Ellis and R.D. Lorenz, "Resonant load control methods for industrial servo drives," Conference Record of the 2000 IEEE Industry Applications Conference. Thirty-Fifth IAS Annual Meeting and World Conference on Industrial Applications of Electrical Energy (Cat. No.00CH37129), Rome, 2000, pp. 1438-1445 vol.3.

[100] A. Tokunaga, M. Nakamura, H. Takami and T. Okamoto, "An optimal observer design for 2-inertia system via ILQ design method," Industry Applications Society Annual Meeting (IAS), 2012 IEEE, Las Vegas, NV, 2012, pp. 1-8.

[101] S. Yorozu and S. Katsura, "Vibration suppression control of 2-mass resonant system for haptic tele-operation," 2010 11th IEEE International Workshop on Advanced Motion Control (AMC), Nagaoka, Niigata, 2010, pp. 655-660.

[102] J.N. Yun, J. Su, Y.I. Kim and Y.C. Kim, "Robust Disturbance Observer for Two-Inertia System," in IEEE Trans. on Industrial Electronics, vol. 60,no.7,pp.2700-2710,July2013.

[103] D. Lindr, P. Rydlo and P. Jirásko, "Simplified inverse control method for two-mass servomechanism vibration suppression," 2014 ELEKTRO, Rajecke Teplice, 2014, pp. 186-191.

[104] T.A. Lipo, Introduction To AC Machine Design. 1st ed. [Madison, Wis.]: Wisconsin Power Electronics Research Center, University of Wisconsin, 2004. Print.

[105] J. Cros and P. Viarouge, "Synthesis of high performance PM motors with concentrated windings," in IEEE Transactions on Energy Conversion, vol. 17, no. 2, pp. 248-253, Jun 2002.

[106] S. Ruangsinchaiwanich, Z. Q. Zhu and D. Howe, "Influence of magnet shape on cogging torque and back-emf waveform in permanent magnet machines," 2005 International Conference on Electrical Machines and Systems, 2005, pp. 284-289 Vol. 1.

[107] Zhiqian Chen, M. Tomita, S. Doki and S. Okuma, "An extended electromotive force model for sensorless control of interior permanent-magnet synchronous motors," in IEEE Transactions on Industrial Electronics, vol. 50, no. 2, pp. 288-295, Apr 2003.

[108] D. Raca, P. Garcia, D.D. Reigosa, F. Briz and R.D. Lorenz, "Carrier-Signal Selection for Sensorless Control of PM Synchronous Machines at Zero and Very Low Speeds," in IEEE Transactions on Industry Applications, vol. 46, no. 1, pp. 167-178, Jan.-feb. 2010.

[109] T.S. Slininger, Y. Xu and R.D. Lorenz, "Enhancing estimation accuracy by applying cross-correlation image tracking to self-sensing including evaluation on a low saliency ratio machine," 2016 IEEE Energy Conversion Congress and Exposition (ECCE), Milwaukee, WI, 2016, pp. 1-7.

[110] Ji-Hoon Jang, Seung-Ki Sul, Jung-Ik Ha, K. Ide and M. Sawamura, "Sensorless drive of surface-mounted permanent-magnet motor by high-frequency signal injection based on magnetic saliency," in IEEE Transactions on Industry Applications, vol. 39, no. 4, pp. 1031-1039, July-Aug. 2003.

[111] Robert W. Hejny, “Degradation of Dynamic Stiffness at Low Speeds When Using Back-emf Tracking for Closed Loop Speed Control,” Master of Science thesis, University of Wisconsin, Madison, WI, 2008.

[112] R.D. Lorenz and K.W.Van Patten, "High-resolution velocity estimation for all-digital, AC servo drives," in IEEE Trans. on Industry Applications, vol. 27, no. 4, pp. 701-705, Jul/Aug 1991.

[113] B. Knight (2015,November).White paper: Understanding Inertia Ratio and Its Effect On Machine Performance. Mitsubishi Electric Automation ,INC, Vernon Hills , IL. [Online]. Available: https://us.mitsubishielectric.com/fa/en/support/technical-support/knowledge-base/getdocument/?docid=3E26SJWH3ZZR-41-13086.

[114] J.W. Choi, S.C. Lee and H.G. Kim, "Inertia identification algorithm for high-performance speed control of electric motors," in IEE Proceedings - Electric Power Applications, vol. 153, no. 3, pp. 379-386, 1 May 2006.

[115] K.B. Lee, J.Y. Yoo, J.H. Song and I. Choy, "Improvement of low speed operation of electric machine with an inertia identification using ROELO," in IEE Proceedings - Electric Power Applications, vol. 151, no. 1, pp. 116-120, 9 Jan. 2004.

[116] K.H. Kim, "Nonlinear speed control for a PM synchronous motor with a sequential parameter auto-tuning algorithm," in IEE Proceedings - Electric Power Applications, vol. 152, no. 5, pp. 1253-1262, 9 Sept. 2005.

[117] Y. Wang, H. Flieh, S.C. Lee, R.D. Lorenz, "Implementation issues and performance evaluation of deadbeat-direct torque and flux control drives," 2015 IEEE International Electric Machines & Drives Conference (IEMDC), Coeur d'Alene, ID, 2015, pp. 953-959.

[118] W. Xu and R. D. Lorenz, "Dynamic Loss Minimization Using Improved Deadbeat-Direct Torque and Flux Control for Interior Permanent-Magnet Synchronous Machines," in IEEE Transactions on Industry Applications, vol. 50, no. 2, pp. 1053-1065, March-April 2014.

[119] Y. Inoue, S. Morimoto, M. Sanada, "Comparative Study of PMSM Drive Systems Based on Current Control and Direct Torque Control in Flux-Weakening Control Region," in IEEE Transactions on Industry Applications, vol. 48, no. 6, pp. 2382-2389, Nov.-Dec. 2012.

[120] Seung-Ki Sul, "Vector Control [1 and 2]," in Control of Electric Machine Drive Systems, 1, Wiley-IEEE Press, 2011, pp.230-282.

[121] S.D. Sudhoff, K.A. Corzine, H.J. Hegner, "A flux-weakening strategy for current-regulated surface-mounted permanent-magnet machine drives," in IEEE Transactions on Energy Conversion, vol. 10, no. 3, pp. 431-437, Sep 1995.

[122] S. Yang and Y. Hsu, "Full Speed Region Sensorless Drive of Permanent-Magnet Machine Combining Saliency-Based and Back-EMF-Based Drive," in *IEEE Transactions on Industrial Electronics*, vol. 64, no. 2, pp. 1092-1101, Feb. 2017.

[123] H. Flieh, R. D. Lorenz, E. Totoki, S. Yamaguchi and Y. Nakamura, "Investigation of different servo motor designs for servo cycle operations and loss minimizing control performance," *2017 IEEE Energy Conversion Congress and Exposition (ECCE)*, Cincinnati, OH, 2017, pp. 4316-4323.

[124] H. M. Flieh, R. D. Lorenz, E. Totoki, S. Yamaguchi and Y. Nakamura, "Investigation of Different Servo Motor Designs for Servo Cycle Operations and Loss Minimizing Control Performance," in *IEEE Transactions on Industry Applications*, vol. 54, no. 6, pp. 5791-5801, Nov.-Dec. 2018.

[125] H. Flieh, E. Totoki and R. D. Lorenz, "Dynamic shaft torque observer structure enabling accurate transient loss measurements," *2017 IEEE International Electric Machines and Drives Conference (IEMDC)*, Miami, FL, 2017, pp. 1-8.

[126] H. M. Flieh, E. Totoki and R. D. Lorenz, "Dynamic Shaft Torque Observer Structure Enabling Accurate Dynamometer Transient Loss Measurements," in *IEEE Transactions on Industry Applications*, vol. 54, no. 6, pp. 6121-6132, Nov.-Dec. 2018.

[127] Barlow, T.J., Latham, S., McCrae, I.S., Boulter, P.G.: 'A reference book of vehicle driving cycles for use in the measurements of road vehicles emissions', TRL Limited, Technical Report, 2009.

[128] H. Flieh, R. D. Lorenz, E. Totoki, S. Yamaguchi and Y. Nakamura, "Dynamic loss minimizing control of a PM servomotor operating even at the voltage limit when using DB-DTFC," *2017 IEEE Energy Conversion Congress and Exposition (ECCE)*, Cincinnati, OH, 2017, pp. 3604-3611.

[129] H. Flieh, R. D. Lorenz, E. Totoki, S. Yamaguchi and Y. Nakamura, "Dynamic Loss Minimizing Control of a Permanent Magnet Servomotor Operating Even at the Voltage Limit when using DeadBeat-Direct Torque and Flux Control," in *IEEE Transactions on Industry Applications*.

[130] K. Liu, Q. Zhang, J. Chen, Z. Q. Zhu, J. Zhang, "Online Multiparameter Estimation of Nonsalient-Pole PM Synchronous Machines With Temperature Variation Tracking," in IEEE Transactions on Industrial Electronics, vol. 58, no. 5, pp. 1776-1788, May 2011.

[131] D.D. Reigosa, D. Fernandez, T. Tanimoto, T. Kato, F. Briz, "Comparative Analysis of BEMF and Pulsating High-Frequency Current Injection Methods for PM Temperature Estimation in PMSMs," in IEEE Transactions on Power Electronics, vol. 32, no. 5, pp. 3691-3699, May 2017.

[132] H. Flieh, T. Slininger, R. D. Lorenz and E. Totoki, "Self-Sensing via Flux Injection with Servo Dynamics including a Smooth Transition to Back-EMF Tracking," *2018 IEEE Energy Conversion Congress and Exposition (ECCE)*, Portland, OR, 2018, pp. 1762-1769.